



HAL
open science

Multi-scale modelling approach of a steam storage with Phase Change Materials integrated into a thermal process

Teddy Chedid

► **To cite this version:**

Teddy Chedid. Multi-scale modelling approach of a steam storage with Phase Change Materials integrated into a thermal process. Chemical and Process Engineering. Université Côte d'Azur, 2023. English. NNT : 2023COAZ4134 . tel-04426229

HAL Id: tel-04426229

<https://theses.hal.science/tel-04426229v1>

Submitted on 30 Jan 2024

HAL is a multi-disciplinary open access archive for the deposit and dissemination of scientific research documents, whether they are published or not. The documents may come from teaching and research institutions in France or abroad, or from public or private research centers.

L'archive ouverte pluridisciplinaire **HAL**, est destinée au dépôt et à la diffusion de documents scientifiques de niveau recherche, publiés ou non, émanant des établissements d'enseignement et de recherche français ou étrangers, des laboratoires publics ou privés.

$$\rho \left(\frac{\partial v}{\partial t} + v \cdot \nabla v \right) = -\nabla p + \nabla \cdot T + f$$

$$e^{i\pi} + 1 = 0$$

THÈSE DE DOCTORAT

Approche multi-échelles pour la modélisation d'un
stockage thermique de vapeur par matériau à
changement de phase intégré dans un système

Teddy CHEDID

Laboratoire Polytech'Lab (POLYTECH'LAB)

**Présentée en vue de l'obtention
du grade de docteur en sciences pour
l'ingénieur**

d'Université Côte d'Azur

Dirigée par : Erwin FRANQUET, Jean-
Pierre BÉDÉCARRATS

Encadrée par : Jérôme POUVREAU

Soutenue le : 13 décembre 2023

Devant le jury, composé de :

Cathy CASTELAIN, Directrice de recherche, Nantes
Université

Erwin FRANQUET, Professeur, Université Côte d'Azur

Gilles FRAISSE, Professeur, Université Savoie Mont Blanc

Jean-Pierre BÉDÉCARRATS, Professeur, Univ. Pau et
Pays de l'Adour

Jérôme POUVREAU, Docteur-Ingénieur, CEA – LITEN

Marie DUQUESNE, Professeur, La Rochelle Université
(Présidente du jury)

Pascal BIWOLE, Professeur, Université Clermont Auvergne

Pierre GARCIA, Docteur-Ingénieur, NewHeat Bordeaux



Approche multi-échelles pour la modélisation d'un stockage thermique de vapeur par matériau à changement de phase intégré dans un système

Jury :

Rapporteurs

Cathy CASTELAIN, Directrice de recherche, Nantes Université
Pascal BIWOLE, Professeur, Université Clermont Auvergne

Examineurs

Gilles FRAISSE, Professeur, Université Savoie Mont Blanc
Marie DUQUESNE, Professeur, La Rochelle Université

Directeurs

Erwin FRANQUET, Professeur, Université Côte d'Azur
Jean-Pierre BÉDÉCARRATS, Professeur, Univ. Pau et Pays de l'Adour
Jérôme POUVREAU, Docteur-Ingénieur, CEA – LITEN

Invités

Pierre GARCIA, Docteur-Ingénieur, NewHeat Bordeaux

Résumé – Abstract

Résumé

Dans le cadre de la transition énergétique, le stockage de vapeur est un élément essentiel pour la récupération de la chaleur fatale sous forme de vapeur ainsi que pour les procédés industriels dépendants de l'énergie solaire où il permet d'adapter la puissance produite par la source de chaleur aux besoins du procédé. Le stockage de vapeur revêt par ailleurs une importance primordiale dans le contexte des centrales solaires thermiques à génération directe de vapeur. Dans cette thèse, les systèmes de stockage de type tubes-calandre par Matériau à Changement de Phase (dit MCP) sont étudiés. Dans ces systèmes, la chaleur est stockée à une température quasi-constante via la chaleur latente de changement de phase des MCP. La plupart des MCP ont pour inconvénient d'avoir une faible conductivité thermique, ce qui limite la puissance thermique du stockage. Pour cela des ailettes ou inserts ayant des formes géométriques spécifiques sont disposées sur la surface externe des tubes afin d'intensifier les échanges thermiques entre le fluide caloporteur et le MCP. En outre, plusieurs phénomènes physiques sont en jeu dans ce type de stockage. Dans le MCP, les transferts de chaleur sont souvent influencés par la transition de phase solide/liquide, ainsi par les mouvements de convection naturels du MCP liquide. L'objectif principal de cette thèse est d'étudier l'influence des différents phénomènes physiques et des configurations géométriques du stockage sur la performance du module de stockage à partir d'un modèle mécanique des fluides numériques (*Computational Fluid Dynamics* ou CFD). Ensuite, le développement d'une approche de modélisation multi-échelles ouvrirait la voie à l'établissement de lois génériques régissant les transferts de chaleur au sein du système de stockage. Ces lois, exprimées sous forme de corrélations, seraient ensuite intégrées dans un modèle système, facilitant ainsi le dimensionnement rapide et efficient d'un système de stockage à l'échelle industrielle. Dans un premier temps, deux approches de modélisation du problème de changement de phase à l'échelle des systèmes ont été développées. La première approche implique une discrétisation du domaine contenant le MCP et les ailettes dans la direction radiale (modèle 1D radial). La seconde approche, en revanche, ne procède pas à une telle discrétisation de ce volume (modèle 0D radial), mais évalue directement les transferts thermiques au sein du stockage à partir des corrélations issues de la CFD. Ces deux modèles ont été couplés à un modèle représentant les

écoulements diphasiques eau liquide/vapeur à l'intérieur des tubes, et ont été validés au moyen de données expérimentales provenant d'un prototype installé au CEA Grenoble. Dans un second temps, un modèle 3D CFD à maille fine a été développé pour simuler sur une géométrie représentative du module de stockage les différents phénomènes physiques en jeu. Les simulations à l'échelle CFD ont permis de quantifier l'impact de la convection naturelle sur les performances thermiques du stockage en phase de charge. En outre, des études paramétriques sur la configuration géométrique et les propriétés thermiques des ailettes radiales ont été réalisées. Les paramètres investigués sont le pas, l'épaisseur, la longueur, et la conductivité thermique des ailettes. L'influence de chaque paramètre géométrique sur les transferts thermique (conductifs et convectifs) a été investiguée et a permis d'établir des corrélations génériques sur la puissance du stockage. Ces corrélations ont ensuite été intégrées dans le modèle système 1D capable de reproduire les résultats des modèles CFD, tout en permettant une significative réduction des ressources informatiques requises. Notamment, la simulation d'une phase de charge complète requiert généralement de 2 à 3 jours de calcul par le modèle CFD. Toutefois, grâce au modèle système, cette durée est réduite à quelques secondes.

Mots clés : Stockage thermique, Vapeur, MCP, CFD, système, multi-échelles

Abstract

In the context of energy transition, steam storage is a crucial element for recovering waste heat in the form of steam and for solar-dependent industrial processes, where it allows adjusting the power generated by the heat source to the process's needs. Furthermore, steam storage plays a vital role in the context of direct steam generation in solar thermal power plants. In this thesis, shell-and-tube Latent Heat Thermal Energy Storage (LHTES) systems using Phase Change Material (PCM) are studied. In these systems, heat is stored at nearly constant temperature using the latent heat of PCM phase change. Most PCM suffer from low thermal conductivity, limiting the thermal power of the storage. To address this issue, metallic fins or inserts with specific geometrical shapes are generally placed on the external surface of the tubes to enhance the thermal exchange between the heat transfer fluid and the PCM. Additionally, various physical phenomena are at play in this type of storage. In the PCM region, the solid/liquid phase transition and the natural convection movements of the liquid PCM often influence heat transfers. The main objective of this thesis is to investigate the influence of different physical phenomena and storage geometries on the module's performance using a Computational Fluid

Dynamics (CFD) model. Subsequently, the development of a multi-scale modeling approach would pave the way for establishing generic laws governing heat transfer within the storage system. These laws, expressed as correlations, would then be integrated into a system model, facilitating the rapid and efficient design of an industrial-scale storage system. Initially, two modeling approaches to the phase change problem at the system level were developed. The first approach involves discretizing the domain containing the PCM and fins radially (1D radial model). The second approach, on the other hand, does not discretize this volume (0D radial model) but directly evaluates heat transfers within the storage using correlations derived from CFD. Both models were coupled with a model representing two-phase liquid water / steam flow inside the tubes and validated using experimental data from a prototype installed at CEA Grenoble. Subsequently, a fine-mesh 3D CFD model was developed to simulate the various physical phenomena at play in a representative storage module geometry. CFD-scale simulations quantified the impact of natural convection on the thermal performance during the charging phase. Furthermore, parametric studies on the geometric configuration and thermal properties of radial fins were conducted. The investigated parameters include pitch, thickness, length, and thermal conductivity of the fins. The influence of each geometric parameter on thermal transfers (conductive and convective) was investigated and led to the establishment of generic correlations regarding the storage power. These correlations were then integrated into the 1D system model, capable of reproducing CFD model results while significantly reducing computational resources. Notably, simulating a complete charging phase typically requires 2 to 3 days of calculations using the CFD model. However, thanks to the system model, this duration is reduced to a few seconds.

Keywords: Thermal storage, Steam, PCM, CFD, System, Multi-scale

Table of Contents

Résumé – Abstract.....	II
Table of Contents	V
List of Figures.....	IX
List of Tables.....	XIX
Nomenclature.....	XXI
Chapter I – General Introduction	1
I.1. Thermal Energy Storage (TES)	2
I.2. Steam storage.....	4
I.3. Thermal energy storage using PCM	5
I.4. Objectives of the thesis	7
Chapter II – State of the Art	11
II.1. Steam storage technologies	11
II.1.1. Steam accumulators.....	11
II.1.2. Steam storage using Phase Change Materials	13
II.1.2.1. Concept and overview of different technologies.....	14
II.1.2.2. Shell-and-tube systems	17
II.1.2.2.1. Concept.....	17
II.1.2.2.2. Existing prototypes.....	19
II.2. Modelling of various factors influencing the thermal performances of shell-and-tube LHTES	21
II.2.1. Phase change problem	22
II.2.1.1. Stefan problem.....	22
II.2.1.2. Advanced models	23
II.2.1.2.1. Front-tracking methods.....	24
II.2.1.2.2. Front fixing methods	24
II.2.1.2.3. Fixed-domain methods.....	24
II.2.1.2.3.1. Heat capacity method	24
II.2.1.2.3.2. Level-set method.....	25
II.2.1.2.3.3. Volume Of Fluid method (VOF)	25
II.2.1.2.3.4. Phase-field method	26
II.2.1.2.3.5. Enthalpy method	26

II.2.1.2.3.6.	Enthalpy-porosity method.....	26
II.2.1.2.3.7.	Dumping of velocity in solid regions	27
II.2.2.	Natural convection in the liquid phase	28
II.2.2.1.	Various approaches for modelling natural convection	29
II.2.2.1.1.	Variable density	29
II.2.2.1.2.	Effective thermal conductivity	35
II.2.2.1.3.	Boussinesq approximation	36
II.2.2.2.	Influence of natural convection on the melting process of PCM.....	37
II.2.2.3.	Comparison of different approaches accounting for natural convection.....	40
II.2.3.	Addition of fins	42
II.2.3.1.	Types.....	43
II.2.3.2.	Comparison between different types of fins.....	45
II.2.3.3.	Parametric studies in fin configuration	48
II.2.3.4.	Fin material.....	51
II.3.	Multi-scale modelling approach.....	53
II.4.	Conclusion	56
Chapter III – System modelling of LHTES.....		59
III.1.	Introduction.....	59
III.2.	Description of the prototype.....	60
III.3.	Determination of the heat transfer correlations	65
III.3.1.	CFD model	65
III.3.2.	Heat transfer correlations	67
III.4.	Description of the system models.....	70
III.4.1.	Two-phase flow	71
III.4.2.	Tube.....	73
III.4.3.	PCM + fins: 1D radial	73
III.4.3.1.	Central tubes	73
III.4.3.2.	Peripheral tubes	78
III.4.4.	PCM + fins: OD radial	79
III.5.	Application case.....	84
III.5.1.	working conditions	84
III.5.2.	Energy stored	86
III.5.2.1.	Experimental trial	86
III.5.2.2.	System models.....	89

III.5.2.3. Comparison of the energy stored predicted by the ‘system’ model with the experimental case	91
III.5.3. Water level	93
III.6. Conclusion	99
Chapter IV – CFD investigations on the effects of natural convection and fin parameters of a LHTES	103
IV.1. Introduction.....	103
IV.2. Description of the CFD model	105
IV.2.1. Physical model.....	105
IV.2.2. Governing Equations	107
IV.3. Smooth-tube TES.....	109
IV.4. Tube with fins: effect of fin type (radial vs longitudinal)	115
IV.4.1. Validation of the domain reduction for radial fins: 22.5 ° vs 360 °	116
IV.4.2. Melted fraction.....	118
IV.4.3. Temperature distribution.....	120
IV.5. Tube with circular fins: effect of the geometry.....	123
IV.5.1. Effect of fin length	124
IV.5.2. Effect of fin pitch and thickness	127
IV.5.2.1. Melted fraction.....	129
IV.5.2.2. Influence of natural convection: melting time ratio	132
IV.5.2.3. Temperature and velocity distributions.....	134
IV.5.2.4. Heat Flux distribution	136
IV.5.2.5. Enhanced fin design: Triangular-shaped fin	139
IV.5.2.5.1. Design proposal	139
IV.5.2.5.2. Melted fraction.....	140
IV.5.2.5.3. Temperature and velocity distributions	141
IV.5.3. Effect of fin material.....	142
IV.6. Conclusion	147
Chapter V – Multi-scale modelling approach.....	151
V.1. Introduction.....	151
V.2. Calculation of the heat transfer correlation.....	152
V.2.1. Introduction.....	152
V.2.2. Parameters of the correlation	152

V.2.3.	Influence of the geometric configuration on the dimensionless numbers.....	155
V.2.4.	Formulation of the heat transfer correlation.....	157
V.3.	System modelling	163
V.3.1.	Results	165
V.3.1.1.	RMSE.....	165
V.3.1.2.	Non-uniform temperature boundary condition.....	176
V.4.	Conclusion	178
Chapter VI – General conclusion and perspectives.....		181
VI.1.	Conclusions.....	181
VI.2.	Perspectives.....	187
Appendix A		191
Appendix B		196
References.....		203

List of Figures

Figure 1. Temperature-enthalpy diagram for TES for DSG. (a) purely sensibly storage (b) three-stage storage [34]	6
Figure 2. Schematic representation of the Ruths accumulator [13]	12
Figure 3. Steam accumulator with integrated latent heat storage material [13].....	15
Figure 4. Capsules filled with $\text{NaNO}_3\text{-KNO}_3$ used for laboratory-scale test [30].....	15
Figure 5. Design concepts to increase effective thermal conductivity: composite of expanded graphite and PCM [29]	15
Figure 6. Single segment made of PCM/composite material used for the laboratory-scale storage unit. Holes are intended for steam pipes. [30]	15
Figure 7. Design concepts to increase effective thermal conductivity: graphite foils as layers between PCM [29]	16
Figure 8. Schematic diagram of the RHTS concept [25]	16
Figure 9. A double screw heat exchanger (SHE): material can be transported (transport direction left to right) and simultaneously heated/cooled by a heat transfer fluid [26].....	17
Figure 10. Horizontal PCMflux design [32].....	17
Figure 11. Top photo of the PCMflux experimental apparatus [24]	17
Figure 12. Drawing of a shell-and-tube LHTES [internal document CEA]	18
Figure 13. Insulated PCM test module at the test site in Carboneras, Spain [17].....	19
Figure 14. Finned-tube assembly showing an assembled tube with a euro-coin to show scale [27]	20
Figure 15. Layout of LHASSA test facility and storage test section [23]	20
Figure 16. Photo of tubes with circular radial fins with metallic inserts constructed at CEA Grenoble	21

Figure 17. Photo of a tube with serrated radial fins constructed at CEA Grenoble	21
Figure 18. Common methods to simulate a phase-change problem. [41].....	23
Figure 19. Illustrations of the PCM’s volume expansion/shrinkage during phase change with a gaseous volume in the domain (a) the gas can enter and exit the domain (b) the gas is compressed inside the domain.....	30
Figure 20. Schematic of the cylindrical domain with PCM and a volume of air opened to the surrounding [80].....	31
Figure 21. Comparison of shapes of numerical solid and liquid fractions with experiment [80]	32
Figure 22. Computational domains of the investigated cases: (a) truncated cone (axisymmetric), (b) sphere (axisymmetric), (c) cut-off sphere (axisymmetric), (d) cylinder (axisymmetric), (e) cylinder (3D) and (f) cube (3D). Black: emitter surface (adiabatic during melting), green: axis, red: walls.[78].....	33
Figure 23. Illustrations of the PCM’s volume expansion/shrinkage during phase change without a gaseous volume in the domain	34
Figure 24. Comparison of the solid fraction between numerical and experimental results [84]	35
Figure 25. Shell and tube configuration of the PCM heat storage: (a) complete system; and (b) single module considered for simulations [89], [90].....	37
Figure 26. Time series of the stored heat percentage. Convective case (continuous line) and conductive case (dotted line). [89]	38
Figure 27. A vertical single unit cylindrical shell-and-tube LHTES system [74].....	39
Figure 28. Effect of natural convection on melting fraction: (a) LHTHS unit without fin; (b) LHTHS unit with annular fins (N = 19).....	40
Figure 29. Schematic representation of the state of the domain at $t > 0$ s. [75].....	41

Figure 30. Evolution of the phase front for Octadecane. The upper row corresponds to the constant density Boussinesq approximation model. The lower one to the variable density model. The snapshots are taken at the same time. [75].....	42
Figure 31. A set of photos and illustrations of different types of radial fins (a) annular [91] (b) perforated [95] (c) pinned [96](d) helical [98].....	43
Figure 32. A set of photos and illustrations of different types of axial fins (a) longitudinal (b) Y-shaped [103] (c) snowflake-shaped [106].....	44
Figure 33. The variation of PCM liquid fraction in terms of time for the finned double-pipe heat storage system compared with the non-finned case during the melting process.[111].....	45
Figure 34. Specifications of (a) non-finned tube (b) longitudinal-finned tube (c) Circular-finned tube.[113]	45
Figure 35. Evolution of the cumulative energy stored during charging process.[113].....	46
Figure 36. Photograph and the schematic views of the unfinned, solid finned and perforated finned HXs: (a) Photograph of the HXs, (b) Schematic views and dimensions of the HXs (all dimensions are in mm). [95]	47
Figure 37. Typical schematic of (a) pinned tube, (b) finned tube [96]	48
Figure 38. a) Schematic of the shell-and-tube LHTES unit with annular fins; (b) computational domain [91]	48
Figure 39. Effect of fin number on the full melting time.[91]	49
Figure 40. Evolution of the solidification time with different fin thermal conductivities. [120]	52
Figure 41. Structure and characteristics of the proposed multi-scale model. [35].....	55
Figure 42. Photograph of the prototype module	60
Figure 43. Photograph of the finned tubed (a) prototype module (b) fraction of the tube’s length	61
Figure 44. Arrangement of the tubes within the shell of the prototype module	62

Figure 45. Diagram of the arrangement of three neighboring tubes	63
Figure 46 Diagram showing the passive PCM volume at the periphery of the shell	63
Figure 47. Diagram illustrating the axial positions, ranging from N1 to N7, at which the thermocouples are placed within the PCM of the prototype module	64
Figure 48. Diagram of the thermocouple placement within the PCM of the prototype module, at a specific level and around a designated tube.	64
Figure 49. Bottom of the computational CFD model domain [35]	66
Figure 50. Illustration of the cross-sectional hexagonal tiling to associate PCM zones with various tubes [35]	66
Figure 51. (Ra,Nu) scatter points obtained from CFD results for the definitions of lc and T_{cold} presented in Equations (35) and (36) [35]	69
Figure 52. Diagram of the possible discretization of the system models (a) 1D radial (b) 0D radial	71
Figure 53. Cross-sectional view of the discretized active PCM + fins domain used in the 1D radial model	74
Figure 54. Illustrations of the presence of fins in a given sub-domain (a) radial cross-section view (b) axial cross-section view	75
Figure 55. Illustration of the trapezoidal method	76
Figure 56. Cross-sectional view of the discretized active PCM + fins and the passive PCM domains used in the 1D radial model	78
Figure 57. Cross-sectional view of the 0D radial domain for $Tt, ext < TPC$ and $fm = 0$	80
Figure 58. Cross-sectional view of the 0D radial domain for $Tt, ext > TPC$ and $0 < fm < 1$	82
Figure 59. Evolution of the average temperature of the liquid PCM phase according to the melted fraction for both the CFD results and the correlation of Equation (77)	83
Figure 60. Cross-sectional view of the 0D radial domain for $Tt, ext > TPC$ and $fm = 1$	84

Figure 61. Distribution of the temperature of the HTF along the heat transfer tube	85
Figure 62. Sankey diagram of the distribution of energy in various parts of the prototype module (thickness of different fractions is not to scale)	87
Figure 63. Evolution in time of the energy accumulated in various parts of the prototype module	89
Figure 64. Evolution in time of the stored energy predicted by both numerical models compared to experimental data curve	92
Figure 65. Illustration of the water level within the tubes (a) film condensation (b) water content in each elementary volume (c) calculated water level using Equation (96).....	94
Figure 66. Evolution in time of the water level predicted by both system models compared to the experimental data curve.....	95
Figure 67. Illustrations of the water level inside the tubes and the PCM's melting front predicted by both 0D and 1D radial models at three instants (a) $t = 0.3$ h (b) $t = 1$ h (c) $t = 1.7$ h.....	96
Figure 68. Variation of the heat flux of the two models according to the PCM's melted fraction	98
Figure 69. Variation of the average temperature of the liquid PCM phase of the two models according to the PCM's melted fraction	99
Figure 70. Cross-sectional view of the basic geometry for the CFD model	106
Figure 71. Smooth-tube domain represented in the CFD.....	109
Figure 72. Evolution in time of the PCM's melted fraction for smooth-tube configurations	111
Figure 73. Variation of the melting time of a given PCM's fraction according to the tube's height.....	112
Figure 74. Temperature distribution within the tube + PCM domains for different smooth-tube heights	114
Figure 75. Geometric domains for circular and longitudinal fins used in the CFD model	116

Figure 76. Geomtries of circular fins following a helical pattern for different angular sectors. (a) 360° (b) 22.5°	117
Figure 77. Evolution in time of the PCM’s melted fraction for different angular sectors	118
Figure 78. Evolution in time of the PCM’s melted fraction for circular and longitudinal fins	119
Figure 79. Temperature distribution within the tube, fins and PCM regions for circular and longitudinal fins at three instants (a) $t = 0.25$ h (b) 0.75 h (c) 1.25 h.....	122
Figure 80. Geometric domain with circular fins used in the CFD model	124
Figure 81. Evolution in time of the PCM’s melted fraction for different fin length values ..	125
Figure 82. Distribution of the PCM’s melted fraction along the domain for different fin length values.....	127
Figure 83. Studied fin configurations, e : thickness, p : pitch.....	128
Figure 84. Comparison of the PCM’s melted fraction, fm , at different instants for the two models, ‘C’ (on the left) and ‘CC’ (on the right)	131
Figure 85. Distribution of the time ratio to melt a PCM fraction with and without natural convection	133
Figure 86. Comparison of the temperature and velocity distributions in the tube + fins + PCM domains for different fins’ thickness for a given pitch of 25 mm. ‘C’ model (left), ‘CC’ model (right).....	134
Figure 87. Variation of the total heat flux per meter of tube with respect to the melted fraction for case 38	137
Figure 88. Heat flux distribution on the tube’s outer wall and fins surface for case 38. Semi-transparent gray surfaces correspond to the isosurface of $fm = 0.5$. Different scales are used in each case.....	138
Figure 89. Description of triangular fins geometry. (a) Fraction domain represented in CFD modelling pattern (b) Computational domain	140

Figure 90. Evolution in time of the PCM’s melted fraction for triangular and rectangular fins	140
Figure 91. Comparison of the temperature and velocity distributions in the tube + fins + PCM domains for two fins geometries (a) rectangular section (b) triangular section.....	142
Figure 92. Evolution in time of the energy stored in the tube’s wall, fins and PCM regions for different ρ_{cp} values.....	144
Figure 93. Retained geometric configurations for study of the influence of the thermal conductivity.....	145
Figure 94 variation of the time required to melt 98 % of the PCM volume according to the pitch p for different e/p ratios and thermal conductivities. $\lambda =$ (a) $50 \text{ W.m}^{-1}.\text{K}^{-1}$ (b) $100 \text{ W.m}^{-1}.\text{K}^{-1}$ (c) $200 \text{ W.m}^{-1}.\text{K}^{-1}$ (d) $400 \text{ W.m}^{-1}.\text{K}^{-1}$	146
Figure 95. Illustration showing the position of lc according to the state of the PCM	154
Figure 96. Evolution of the Rayleigh and Nusselt numbers with lc . $p =$ (a) 2.5 mm (b) 10 mm (c) 17.5 mm (d) 25 mm.	156
Figure 97. Evolution of the average temperature of liquid PCM as function of lc	157
Figure 98. Combination of different sets of configurations used in the construction of the Nusselt correlation. Number of configurations: (a) 4 (b) 10 (c) 12 (d) 20 (e) 32 (f) 50	159
Figure 99. Distribution of the Nusselt number resulted from both CFD and heat transfer correlation.....	162
Figure 100. Computational domain represented in the “system” model.....	163
Figure 101. Illustrations of the presence of circular fins in a given sub-domain (a) radial cross-section view (b) axial cross-section view.....	164
Figure 102. RMSE values for all the tested correlations. (a) for $fm = 0.2$ (b) $fm = 0.5$ (c) $fm = 0.8$ (d) $fm = 0.98$	167
Figure 103. Evolution of the RMSE values with the melted fraction for the correlations obtained from 12 geometric configurations	168

Figure 104. Distribution of the charging time ratio between both ‘system’ and CFD models for Nusselt correlations constructed using data from 4 geometric configurations (a) 4 coefficients (b) 5 coefficients (c) 7 coefficients (d) 8 coefficients.	170
Figure 105. Distribution of the charging time ratio between both ‘system’ and CFD models for Nusselt correlations constructed using data from 10 geometric configurations (a) 4 coefficients (b) 5 coefficients (c) 7 coefficients (d) 8 coefficients.	171
Figure 106. Distribution of the charging time ratio between both ‘system’ and CFD models for Nusselt correlations constructed using data from 12 geometric configurations (a) 4 coefficients (b) 5 coefficients (c) 7 coefficients (d) 8 coefficients.	172
Figure 107. Distribution of the charging time ratio between both ‘system’ and CFD models for Nusselt correlations constructed using data from 20 geometric configurations (a) 4 coefficients (b) 5 coefficients (c) 7 coefficients (d) 8 coefficients.	173
Figure 108. Distribution of the charging time ratio between both ‘system’ and CFD models for Nusselt correlations constructed using data from 32 geometric configurations (a) 4 coefficients (b) 5 coefficients (c) 7 coefficients (d) 8 coefficients.	174
Figure 109. Distribution of the charging time ratio between both ‘system’ and CFD models for Nusselt correlations constructed using data from 50 geometric configurations (a) 4 coefficients (b) 5 coefficients (c) 7 coefficients (d) 8 coefficients.	175
Figure 110. Evolution with time of the energy stored in the storage predicted by both the ‘system’ and CFD models for a charge with a non-uniform temperature along the tube’s height.	177
Figure 111. Distribution of the liquid PCM layer along the domain obtained by both ‘system’ and CFD models at different instants for a charge with a non-uniform temperature along the tube’s height.	178
Figure 112. Evolution in time of the PCM’s melted fraction for circular radial fins with a pitch of 2.5 mm.	191
Figure 113. Evolution in time of the PCM’s melted fraction for circular radial fins with a pitch of 5 mm.	191

Figure 114. Evolution in time of the PCM’s melted fraction for circular radial fins with a pitch of 7.5 mm.	192
Figure 115. Evolution in time of the PCM’s melted fraction for circular radial fins with a pitch of 10 mm.	192
Figure 116. Evolution in time of the PCM’s melted fraction for circular radial fins with a pitch of 12.5 mm.	193
Figure 117. Evolution in time of the PCM’s melted fraction for circular radial fins with a pitch of 15 mm.	193
Figure 118. Evolution in time of the PCM’s melted fraction for circular radial fins with a pitch of 17.5 mm.	194
Figure 119. Evolution in time of the PCM’s melted fraction for circular radial fins with a pitch of 20 mm.	194
Figure 120. Evolution in time of the PCM’s melted fraction for circular radial fins with a pitch of 22.5 mm.	195
Figure 121. Evolution in time of the PCM’s melted fraction for circular radial fins with a pitch of 25 mm.	195
Figure 122. Evolution in time of the PCM’s melted fraction for circular radial fins with $p=2.5$ mm and $e/p=5\%$	196
Figure 123. Evolution in time of the PCM’s melted fraction for circular radial fins with $p=10$ mm and $e/p=5\%$	196
Figure 124. Evolution in time of the PCM’s melted fraction for circular radial fins with $p=17.5$ mm and $e/p=5\%$	197
Figure 125. Evolution in time of the PCM’s melted fraction for circular radial fins with $p=25$ mm and $e/p=5\%$	197
Figure 126. Evolution in time of the PCM’s melted fraction for circular radial fins with $p=2.5$ mm and $e/p=15\%$	198

Figure 127. Evolution in time of the PCM's melted fraction for circular radial fins with $p=10\text{mm}$ and $e/p=15\%$	198
Figure 128. Evolution in time of the PCM's melted fraction for circular radial fins with $p=17.5\text{mm}$ and $e/p=15\%$	199
Figure 129. Evolution in time of the PCM's melted fraction for circular radial fins with $p=25\text{mm}$ and $e/p=15\%$	199
Figure 130. Evolution in time of the PCM's melted fraction for circular radial fins with $p=2.5\text{mm}$ and $e/p=25\%$	200
Figure 131. Evolution in time of the PCM's melted fraction for circular radial fins with $p=10\text{mm}$ and $e/p=25\%$	200
Figure 132. Evolution in time of the PCM's melted fraction for circular radial fins with $p=17.5\text{mm}$ and $e/p=25\%$	201
Figure 133. Evolution in time of the PCM's melted fraction for circular radial fins with $p=25\text{mm}$ and $e/p=25\%$	201

List of Tables

Table 1. Studies containing an investigation of geometric parameters of radial fins	50
Table 2. Material properties studied in [118]	51
Table 3. Material properties for steel and sodium nitrate.....	67
Table 4. Parameters of the system model for the prototype module	86
Table 5. Summary of the shared characteristics and distinctions between the 1D radial and the 0D radial models	100
Table 6. General design parameters of the CFD model	106
Table 7. Domain height values studied in the case of a smooth-tube TES	110
Table 8. Design parameters for circular and longitudinal fins	116
Table 9. Study parameters	129
Table 10. PCM's melted fraction and maximum velocity for different fins' thickness for a given pitch of 25 mm	136
Table 11. Material properties to study the influence of the thermal inertia of fins on the behavior of the storage	143
Table 12. Values of the studied thermal conductivity.....	145
Table 13. Combination of parameters used in the Nusselt correlation (Equation (114)).....	158
Table 14. Coefficients of Nusselt correlation when constructed using data from 4 geometric configurations.....	160
Table 15. Coefficients of Nusselt correlation when constructed using data from 10 geometric configurations.....	160
Table 16. Coefficients of Nusselt correlation when constructed using data from 12 geometric configurations.....	160
Table 17. Coefficients of Nusselt correlation when constructed using data from 20 geometric configurations.....	161

Table 18. Coefficients of Nusselt correlation when constructed using data from 32 geometric configurations..... 161

Table 19. Coefficients of Nusselt correlation when constructed using data from 50 geometric configurations..... 161

Nomenclature

A	Factor in the damping term of the momentum equation	$[\text{kg.m}^{-3}.\text{s}^{-1}]$
A_i	Coefficients of the Nusselt correlation	$[-]$
A_{mush}	Mushy zone constant	$[\text{kg.m}^{-3}.\text{s}^{-1}]$
b	Constant in the damping term	$[-]$
Bi	Biot number	$[-]$
C	Product coefficient of the Nusselt vs Rayleigh correlation	$[-]$
c_p	Specific heat capacity	$[\text{J.kg}^{-1}.\text{K}^{-1}]$
d	Distance	$[\text{m}]$
D_{th}	Thermal diffusivity	$[\text{m}^2.\text{s}^{-1}]$
e	Thickness	$[\text{m}]$
E	Energy	$[\text{J}]$
F_i	Combination of various parameters used in the Nusselt correlation	$[-]$
f_m	Melted fraction	$[-]$
$\overline{f_m}$	Average melted fraction	$[-]$
g	Acceleration of gravity	$[\text{m.s}^{-2}]$
h	Enthalpy	$[\text{J}]$
H	Total enthalpy	$[\text{J}]$
h_{tube}	Domain height	$[\text{m}]$
k_x	Effective spring constant	$[\text{N.m}^{-3}]$
l	Length	$[\text{m}]$
L	Latent heat	$[\text{J.kg}^{-1}]$
l_c	Characteristic length	$[\text{m}]$
m	Mass	$[\text{kg}]$
\dot{m}	Mass flow rate	$[\text{kg.s}^{-1}]$
n	Exponent of the Nusselt vs Rayleigh correlation	$[-]$
\mathbf{n}	Normal vector	$[-]$
N	Number of tubes	$[-]$
Nu	Nusselt number	$[-]$
Nu_1	Nusselt number during the charging of latent energy	$[-]$

Nu_2	Nusselt number during the charging the sensible heat in liquid PCM	[–]
p	Pitch	[m]
P	Pressure	[Pa]
ΔP	Pressure difference	[Pa]
r	Local volume ratio	[–]
R	Radius	[m]
Ra	Rayleigh number	[–]
S_e	Heat transfer surface	[m ²]
Ste	Stefan number	[–]
S_v	Source term added to the momentum equation	[kg.m ⁻² .s ⁻²]
t	Time	[s]
T	Temperature	[°C]
$\overline{T_{PCM_i}}$	Average temperature of liquid PCM	[°C]
\mathbf{u}	Velocity vector	[m.s ⁻¹]
\mathbf{v}	Velocity vector	[m.s ⁻¹]
V	Volume	[m ³]
WL	Water level	[m]
x	Cartesian coordinates	[m]
x_m	Mass fraction	[–]
x_v	Volume fraction	[–]
x_{vap}	Vapor mass fraction	[–]
Δx	Deformation	[m]
z	Cylindrical coordinates, axial position	[m]

Greek symbols

α	Heat transfer coefficient	[W.m ⁻² .K ⁻¹]
α_n	Volume fraction of each fluid in VOF	[–]
β	Thermal expansion coefficient	[K ⁻¹]
γ	Inclination angle	[°]
Δ	Difference	
ϵ	Void fraction	[–]
θ	Angular sector	[°]

λ	Thermal conductivity	[W.m ⁻¹ .K ⁻¹]
μ	Dynamic viscosity	[kg.m ⁻¹ .s ⁻¹]
ρ	Density	[kg.m ⁻³]
φ	Heat flow	[W]
Ω_{loss}	Heat loss	[W.K ⁻¹]

Superscript and subscript

0D	0D radial model
acc	Accumulated
ambient	Ambient
central	Central tubes
CFD	Computational Fluid Dynamics
cold	Cold
cont	Containment parts
eff	Effective
eq	Equivalent
exp	Experimental
ext	External boundary
fins	Fins
h	Homogenous material
hot	Hot
HTF	Heat Transfer Fluid
in	In
ini	Initial
l	Liquid
lat	Latent
liq	Liquidus
loss	Loss
lw	Liquid water
m	Metallic
out	Out
p	Passive PCM

PC	Phase change
PCM	Phase Change Material
PCM_l	Liquid Phase Change Material
PCM_s	Solid Phase Change Material
peripheral	Peripheral
ref	Reference
s	Solid
sat	Saturation
sens	Sensible
shell	Shell
sol	Solidus
sys	System model
t,ext	External tube wall
t,int	Internal tube wall
tot	Total
tube	Tube

Abbreviations

C	Conduction only
CC	Conduction + Convection
CFD	Computational Fluid Dynamics
CSP	Concentrated Solar Power
DSG	Direct Steam Generation
FTM	Front-Tracking Methods
HTF	Heat Transfer Fluid
LHTES	Latent Heat Thermal Energy Storage
PCM	Phase Change Material
RHTS	Reflux Heat Transfer Storage
RMSE	Root-Mean-Square Error
SHE	Screw Heat Exchanger
TES	Thermal Energy Storage
VOF	Volume Of Fluid

Chapter I – General Introduction

In recent decades, planet earth has experienced a profound transformation. The term ‘climate change’ has become synonymous with an emerging environmental crisis that threatens the delicate balance of this world. Human activities, especially through the emissions of greenhouse gases, have undeniably been the driving force behind global warming, resulting in a global surface temperature increase of 1.1 °C above pre-industrial levels during the period from 2011 to 2020 [1]. This has also led to a significant rise in global mean sea levels, increasing by 0.2 m between 1901 and 2018, with an accelerating rate of sea level rise. In the near term (by 2040), global warming is set to intensify, primarily driven by the increase in the cumulative CO₂ emissions. It is highly likely to exceed 1.5 °C even under relatively low greenhouse gas emission scenarios. Therefore, mitigating global warming and achieving net-zero carbon emissions are critical imperatives for humanity.

Renewable resources play a pivotal role in achieving our energy transition objectives. Renewable sources like solar, wind, and hydropower provide clean, sustainable energy that reduces our reliance on fossil fuels, mitigates climate change, and fosters energy independence. In France, ambitious goals in the realm of sustainable energy and environmental responsibility has been set as outlined in the 2015 energy transition for green growth law [2]. This includes a commitment to reduce greenhouse gas emissions by 40 % by 2030 and 85 % by 2050. An additional target consists of cutting the final energy consumption by 50 % between 2012 and 2050, aiming to integrate 32 % of renewable and recovered energy sources into final energy consumption by 2030.

However, the intermittent nature of renewable resources necessitates effective energy storage solutions. Energy storage systems enable the capture and efficient utilization of surplus renewable energy, ensuring a stable and reliable power supply. This synergy between renewables and energy storage not only supports grid resilience but also accelerates the transition to a greener, more sustainable energy landscape, ultimately driving us closer to a carbon-neutral future.

Beyond their critical role in ensuring a reliable and stable power supply for renewable energy sources, energy storage systems serve multiple purposes regarding the efficient energy utilization. Among various technologies, Thermal Energy Storage (TES) systems have the

ability to recover industrial waste heat effectively. Many industrial processes rely heavily on heat as a crucial component in their process, with a significant portion of it dissipating into the atmosphere as waste. In France, approximately 30% of the energy consumed in industrial processes is lost in the form of this waste heat [3]. The integration of TES systems into these processes presents a valuable opportunity to capture and store the energy contained within this waste heat. This, in turn, contributes to reducing the overall energy consumption of these processes and enhances their efficiency. Furthermore, TES systems can be integrated into buildings and linked to urban heat networks, playing a vital role in balancing energy production and demand. During periods of low demand, surplus heat production is stored, while in times of heightened consumption, these stored heat reserves are readily deployed, ensuring a balanced and efficient energy ecosystem. This also helps avoid relying on polluting sources during peak periods and prevents the need for over-sizing certain infrastructure.

I.1. Thermal Energy Storage (TES)

TES systems become particularly interesting technologies when the energy to be stored takes the form of heat. Such systems deal with the storage of energy by heating, melting or vaporizing a material or through thermochemical reactions. Consequently, the stored energy raises the temperature of the storage material and, in some technologies, induces a physical or chemical transformation in its phase. The thermal energy stored can be later recovered when the process is reversed. Generally, TES technologies are classified in three categories: sensible heat storages, latent heat storages and thermochemical thermal storages.

Sensible heat TES consists of storing heat by increasing the temperature of the storage medium, which can be solid (bedrock, brick, concrete, etc.), liquid (water, oil) or even gas (air). This stored energy can then be extracted during the discharging phase when the material's temperature is reduced. The selection of the material depends on several criteria, such as the density, the specific heat capacity and the thermal conductivity, as well as non-thermal criteria, including chemical compatibility, hazardousness, cost, and availability. The amount of energy E required to increase the temperature of a medium from T_1 to T_2 is calculated as follows:

$$E = m \int_{T_1}^{T_2} c_p dT \quad (1)$$

Where m is the mass of the storage material and c_p is its specific heat. Sensible TES are the most common method for heat storage due to their relative simplicity and reliability compared to other TES methods. For instance, water storage tanks, which are a common form of sensible TES, are used in almost all residential buildings to store hot water for domestic use. Finally, in some sensible TES cases, the Heat Transfer Fluid (HTF) is the same as the storage material, as seen in cases like a non-dual thermocline or a steam accumulator. Conversely, in other situations, a HTF is employed alongside a separate storage material, such as in a dual-media thermocline using a solid storage material.

Latent heat TES (LHTES) is a concept where heat is absorbed or released during the phase change of a material. Solid-liquid phase transitions are most often considered due to their higher latent capacity compared to solid-solid transitions. The storage materials used in such systems are referred to as Phase Change Materials (PCM). The solid-liquid phase transition enables to store (release) a significant amount of heat by melting (solidifying) a PCM. The phase transition process is characterized by small temperature changes. The ability of PCM to store energy at an almost constant temperature via the latent heat of phase change results in high energy stored per unit volume of the storage material, leading to a significant energy density in the storage system. For a PCM initially solid at T_1 changing phase at T_m (melting temperature), the amount of energy stored in the PCM at T_2 (where $T_1 < T_m < T_2$) is expressed as the sum of the contributions of the sensible and latent heats, and is expressed as follows:

$$E = m \left(\int_{T_1}^{T_m} c_{p_s} + L + \int_{T_m}^{T_2} c_{p_l} dT \right) \quad (2)$$

Where L corresponds to the PCM's latent heat during phase transition. For LHTES, the HTF can be either single-phase or two-phase.

Another way to store heat is the use of *Thermochemical storages* where materials store heat through reversible chemical reactions. During the charging phase, an endothermic reaction takes place where the storage material absorbs heat and undergo a chemical transition. The heat is then discharged through an exothermic reaction with the storage material returning to its initial chemical state. Thermochemical storages are characterized by a high storage density and minimal to negligible thermal losses. Additionally, they are an interesting solution for long-

term storage duration. However, the technological maturity of such storages is low in comparison to sensible and LHTES.

TES technologies can bridge the disparity between the available energy source and demand, enabling efficient utilization of intermittent renewable sources as needed. Additionally, a TES system can be integrated in industrial processes to improve the efficiency of the industry by recovering waste heat otherwise lost in the process, yielding economic and reliable advantages. Finally, TES systems have a wide range of applications, including heavy electronic equipment cooling, solar TES, building application to provide thermal comfort, HVAC applications and several medical and agricultural applications.

I.2. Steam storage

Steam is the gaseous phase of water that forms when water is heated to its boiling point and undergoes vaporization. It consists of water vapor molecules that are in a highly energetic state, characterized by high temperature and pressure. Steam is a common source of energy in many industrial processes due to its ability to transport a large amount of energy per unit mass via latent heat resulted by the liquid / vapor phase transition. Additionally, two-phase flows offer significant heat transfer coefficients with surrounding boundaries, which improves the efficiency of the process [4].

Steam plays a vital role in energy production from renewable resources. For example, in Concentrated Solar Power (CSP) plants with Direct Steam Generation (DSG), solar energy is concentrated using mirrors into a receiver, heating water that produces high-pressure steam. The produced steam is then utilized to drive steam turbines, generating electricity. Such power plants help reduce reliance on fossil fuels and therefore reduce the impact on climate change. However, the steam production is based on renewable energy resources, which are intermittent by nature, the integration of a storage technology is essential to tackle this variability, offering a stable and reliable energy supply [5]. The role of a steam storage system in CSP plants can be described as follows: during periods with high steam generation from the renewable resource, the excess energy, in the form of heat, is stored in a storage system. When energy demand exceeds supply or during low-resource periods, the stored energy can be released to reproduce steam that can be used to drive turbines and respond to discrepancy between supply and demand. Therefore, steam storage systems smooth out the fluctuations in energy production

from renewable resources, enabling better grid stability and enhancing the overall efficiency of the energy generation [6]. They also enable CSP plants to generate electricity during nighttime and under low sunlight conditions.

Apart from energy production from renewable resources, steam storage systems can also be integrated into industrial processes to recover waste heat in the form of steam [7], [8]. This reduction in energy waste enhances the overall efficiency of industrial operations, contributing to both cost savings and a reduced environmental footprint. Some known processes include paper manufacturing, pharmaceutical, food and beverage processing and metallurgical industry [9]–[12]. Generally, two approaches exist for steam storage energy. The first and most used approach to date involves the use of steam accumulators [9]–[19], where steam is stored under pressure with a volume of saturated liquid. The second approach consists of storing steam energy within a PCM [13], [14], [17], [20]–[33].

I.3. Thermal energy storage using PCM

Using PCM for TES presents an intriguing approach with numerous advantages. As elaborated in Section I.1, LHTES systems offer the distinct capability to store a substantial amount of energy within a narrow temperature range, thereby achieving high energy densities. Moreover, in the context of steam storage applications, it is important to consider the behavior of the HTF, which undergoes a two-phase transformation: steam condensation during the charging phase and liquid water evaporation during discharge. Throughout this process, the steam undergoes a phase transition while maintaining an almost constant temperature. When paired with a latent storage material that similarly maintains a nearly constant temperature during these phases, it effectively minimizes temperature and pressure differences between the stored and recovered steam. For instance, during the charging phase, steam is introduced at a slightly higher temperature than the PCM's melting point. This temperature differential ensures the heat transfer from the steam to the PCM. Conversely, during the discharge phase, the saturation temperature of the liquid water should be lower than the PCM's solidification point to assure the transfer of heat from the PCM to the liquid water (Figure 1 (b)). Achieving this temperature differential can be accomplished by regulating the pressure of the HTF, thereby altering the saturation temperature at which the liquid-vapor phase transition takes place. In contrast, when employing sensible storage material, the saturation temperature of the steam must remain higher than the maximum temperature experienced by the sensible material during charging, and lower

than the minimum temperature during discharge (Figure 1 (a)). This results in a significant temperature difference of the steam between charging and discharging phases.

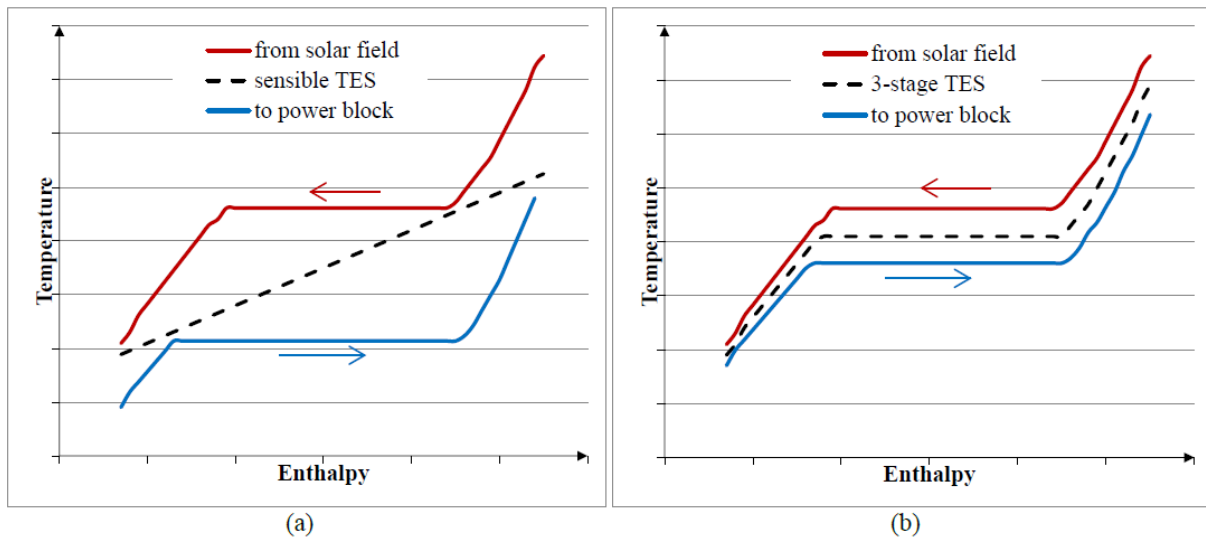


Figure 1. Temperature-enthalpy diagram for TES for DSG. (a) purely sensibly storage (b) three-stage storage [34]

The primary challenge in the field of LHTES lies in effectively regulating and improving the thermal performance of the system. A significant limitation derives from the inherently low thermal conductivity of most PCM. This constrains the heat transfer between the HTF and the PCM within the storage unit, consequently diminishing the thermal power of the system. Moreover, the thermal power of the storage system is dependent upon several complex physical phenomena that occur during operation, including the PCM's phase change problem, natural convection induced by movements within the liquid phase, and PCM volume expansion/shrinkage.

Several technologies exist where PCM is used to store steam energy, with the shell-and-tube LHTES being the most common among them [17], [22], [23], [27], [28]. In these systems, the PCM occupies a shell traversed by HTF tubes through which water flows. Heat exchange between the HTF and the PCM volume occurs at the tube walls. During the charging phase, the initially solid PCM absorbs the steam energy to be stored, initiating a melting process around the tubes, creating a melting front that propagates away from the heat transfer tubes. The discharge phase reverses this process, with the initially liquid PCM releasing its energy as heat, transforming liquid water back into steam. In the shell, the PCM solidifies, and a solidification front evolves away from the tubes.

To address the limitation of low thermal conductivity in PCM and enhance the storage thermal performance, metallic fins are commonly added to the external tube walls. These fins, along with their geometric shapes, configurations, and material properties, significantly influence heat exchange within the storage system. Consequently, their influence must be carefully considered when sizing such storage systems. Furthermore, within the PCM, the solid-liquid phase transition and temperature gradients in the liquid phase can induce natural convection movements, directly contributing to heat exchange. Therefore, their impact must also be evaluated during system sizing.

At CEA Grenoble, several prototype shell-and-tube LHTES modules have been designed, constructed, and tested, applying to either single-phase HTF or two-phase liquid water/steam flows. These experimental modules serve various crucial objectives: firstly, they aid in perfecting the practical implementation of energy storage within a system; secondly, they facilitate the examination of storage behavior during charging, discharging, cycling, and aging. Lastly, they furnish reliable experimental data to validate numerical models. Nevertheless, conducting these experimental trials is a time-intensive and costly endeavor.

The accurate sizing of shell-and-tube LHTES systems demands the prediction of various physical phenomena, geometric configurations, and material properties that affect system behavior. Given the inherent complexity of storage geometry and the diverse scales of physical phenomena involved, Computational Fluid Dynamics (CFD) codes are indispensable. However, transient simulations of complete charging or discharging phases using CFD typically demand substantial computational resources. Furthermore, such simulations may span several days or even weeks, rendering them impractical for design purposes, where multiple design points require assessment. Consequently, the development of a rapid and efficient modelling tool is imperative to facilitate the integration of this technology into the industrial sector.

I.4. Objectives of the thesis

The primary objective of this thesis is the development of a numerical methodology adapted for sizing industrial-scale shell-and-tube LHTES systems. The focus lies on achieving two key attributes: speed and precision. First, the planned model must succeed in its capacity to provide relatively precise predictions of the storage system's behavior. It does so by incorporating the

impact of various physical phenomena, including the phase transition of the PCM, heat conduction within different components of the system, and natural convection within the liquid phase of PCM. Moreover, the model must take into account the influential role that the geometric characteristics and material properties of fins play in contributing to the thermal performance of the storage system. Furthermore, it is imperative that this model conducts these precise predictions within reasonable computational time and resource constraints.

As discussed in the previous section, the challenge arises from the need to model the complex physical phenomena on a representative geometry of the storage system, which often necessitates expensive CFD simulations. Conversely, simplified models, while faster, tend to oversimplify the underlying physics, leading to less accurate results. Therefore, the objective of this research is to develop and generalize a comprehensive multi-scale modelling approach; able to combine advantages of each method.

In this approach, in-depth CFD simulations are executed to comprehend how the system behaves under the influence of the aforementioned physical phenomena and geometries. Then, from the rich dataset gathered through these CFD simulations, general heat transfer laws are established in the form of correlations. These heat transfer laws are subsequently integrated into a reduced numerical model, effectively replicating the precision of the CFD results, while concurrently optimizing computational efficiency, thereby providing balance between accuracy and computational resources and time.

Chapter II presents a state-of-the-art of various steam energy storage technologies, with a particular focus on shell-and-tube LHTES systems. It examines various factors that influence the behavior of these systems and dedicates specific attention to the array of mathematical methods available to account for each influential factor. Additionally, it showcases an array of parametric studies from existing literature that examine how the geometric configurations of fins impact system performance. The insights gained from this chapter lay the foundation for informed decisions in the subsequent studies.

In **Chapter III**, reduced numerical approaches are developed for modelling the transient behavior of shell-and-tube LHTES systems. These models are tested and validated according to experimental data obtained from trials involving a shell-and-tube LHTES prototype module installed at CEA Grenoble. The prediction of the behavior of the storage by these models relies

upon the integration of heat transfer correlations, which are derived from the extensive CFD simulations conducted by Beust et al. [35] on the specific prototype module's geometry.

The correlations used in Chapter III are unique to the distinct geometry and working conditions of the prototype module installed at CEA Grenoble. To extend this approach's applicability, a step back to the CFD scale is taken in **Chapter IV**. This chapter is dedicated to in-depth CFD investigations with the objective of providing comprehensive insights into how different fin shapes, configurations, and material properties impact various heat transfer mechanisms within the storage system. Multiple parametric studies are conducted, and the knowledge gained will serve as the basis for establishing more generalized heat transfer laws.

Finally, **Chapter V** is dedicated to the generalization and assessing of a multi-scale modelling approach. The knowledge acquired from CFD investigations will serve in the formulation of generalized heat transfer correlations that incorporate the behavior of the storage system. Ultimately, these correlations must be integrated into a simplified numerical model, which must enable both accurate and rapid predictions of the storage system's performance.

Chapter II – State of the Art

This chapter delves into the state of the art in the field of thermal energy storages applied for steam applications. After presenting various technologies that allow storing steam energy, a focus will be drawn to shell-and-tube storages with PCM. In particular, the influence of different factors on the behavior of the operation of such storage systems is explained. Through a comprehensive exploration of existing literature, this chapter seeks to provide a complete overview of the various modelling approaches employed to analyze, optimize and size a shell-and-tube LHTES. By examining the strengths and limitations of these approaches, this study aims to construct a multi-scale modelling approach that will serve in the advancement of innovative strategies in the design, operation, and integration of LHTES systems within the context of sustainable energy systems.

II.1. Steam storage technologies

II.1.1. Steam accumulators

Steam accumulators are devices used in steam-based energy systems to store excess steam generated during periods of low demand or high steam production. They act as a buffer storage, providing saturated steam at pressures up to 100 bar [13]. Given their low volumetric energy density, the direct storage of steam, by keeping the water in vapor state in pressurized vessels, is not economically viable. Alternatively, the energy from steam is stored in as sensible heat in pressurized saturated liquid water used in steam accumulators. Liquid water is characterized with high density and high specific heat capacity, which makes it possible to reduce the volume of the storage compared to storing steam solely in its gaseous form. Therefore, the storage capacity is defined by the latent heat due to steam condensation and the specific heat capacity of liquid water.

Figure 2 shows the scheme of a steam accumulator where both liquid and gaseous phases are under pressure. During the charging process, hot steam is injected within the cooler liquid phase. The steam's energy content in the form of latent heat is transferred to the liquid phase. As a result, the steam condenses and the heat recovered by the liquid water will increase its temperature. Consequently, a new thermodynamics equilibrium characterized with higher pressure and temperature is attained. Occasionally, in specific scenarios, it may be necessary to

introduce or remove liquid water from the system during operation, as depicted in Figure 2. This action is taken to mitigate the rise in system pressure.

During the discharging process, pressure within the system is reduced, ensuring the generation of steam from liquid water. Such systems are also called *Ruths storage systems* [13], [14]. By decreasing the pressure in the system, steam is produced from liquid water. Consequently, the energetic capacity of such systems is determined by the pressure difference between the start and the end of the discharging phase.

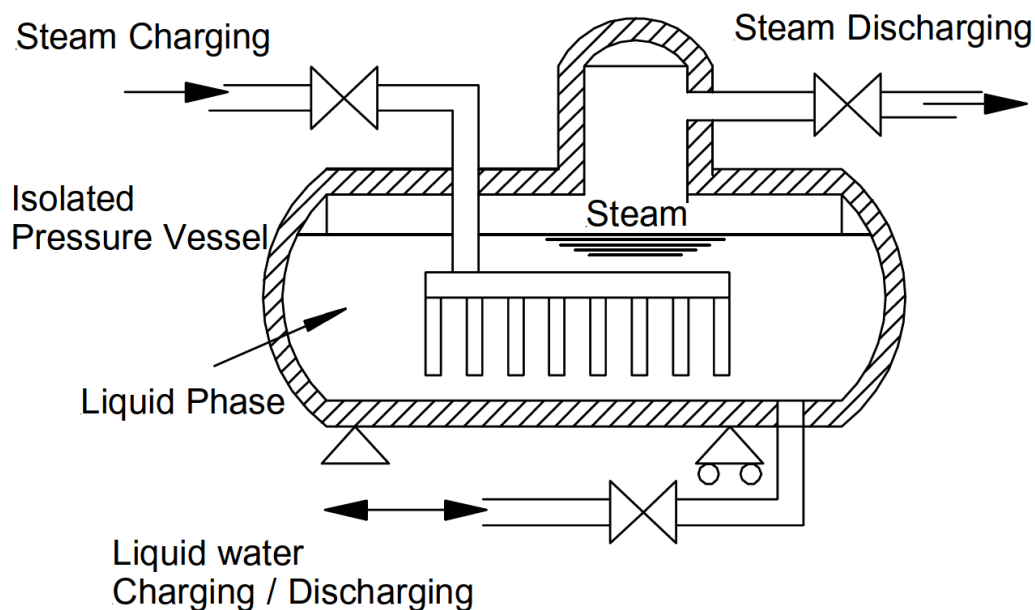


Figure 2. Schematic representation of the Ruths accumulator [13]

Steam accumulators are widely used in the industry for several reasons, as they offer numerous advantages and benefits to industrial processes. For instance, since water is used as both a storage and a working medium, high discharge rates are possible. As a result, a steam accumulator can provide a rapid response to sudden changes in demand or system failures, ensuing continuous process operations. Additionally, given that such systems are considered relatively simple on the technical side, they succeeded in finding their way into various industrial processes where steam plays a crucial role. Some common processes include food and beverage processing [9], where accumulators help maintain a stable steam supply for cooking, sterilization and other processes, in paper manufacturing [10], metallurgical industry [11], pharmaceutical [12] and in power generation plant to balance steam supply and demand. Additionally, steam accumulators help to store thermal energy for continuous power generation in CSP plants based on DSG [18], [19].

Despite their aforementioned advantages, steam accumulators are not cost-competitive for larger storage capacities [15]–[17]. Storing steam at a very high pressure imposes mechanical constraints to its design that increases the cost of each single storage system and makes it difficult to construct accumulators with large storage capacity. For example, the total capacity of the four accumulators employed in the PS-10 plant in Spain is 20 MWh [18]. During the plant operation, a part of the steam generated by the receiver at 250 °C and 40 bar is used to charge the TES. The Khi Solar One plant in South Africa houses a set of 19 steam accumulators offering an estimated storage capacity of 100 MWh. Such capacities are indeed limited when compared to thermal solar power plants with sensible storages based on molten salts that have a storage capacity that can exceed 1000 MWh [19].

Another drawback of the *Ruths* basic steam accumulator arises from the state of steam produced during the discharge phase. In fact, some processes require steam at constant pressure over time, while others demand superheated steam. Therefore, relying on a steam accumulator alone may not be sufficient to meet the requirements imposed by these processes.

II.1.2. Steam storage using Phase Change Materials

Steam storage using PCM is a method of storing thermal energy in the form of latent heat. During the charging process, highly energetic steam releases its energy in the form of heat and condenses. The heat is then recovered by the PCM that will undergo a solid-liquid phase transition. For the discharge phase, the heat transfer process is reversed. The hot melted PCM will transfer its energy to heat the water and produce steam that can again be used in the process.

Storing steam energy using PCM offers several advantages over traditional steam accumulators. Firstly, the PCM is not maintained under pressure, which reduces the mechanical constraints of the storage system allowing the increase of the storage capacity relative to steam accumulators. Secondly, during the phase change, PCM absorb or release a significant amount of heat energy without experiencing a significant change in temperature. This ability is ideal when dealing with a two-phase HTF such as steam. By choosing a suitable PCM that undergoes its solid-liquid phase transition at a temperature near the saturation temperature of the steam, the pressure and temperature differences of the steam used to charge the storage and the one produced during the discharge are reduced. Therefore, the choice of PCM depends on the desired working conditions of the application [31]

Despite the many advantages of PCM, this technology faces several challenges. Since the steam energy is stored by heating a material, the thermal performances of the storage system depend on several factors that influence the heat transfer mechanism between the HTF and the PCM. Generally, most PCM have a low thermal conductivity, which limits the heat transferred by conduction within the storage and hence reduces the thermal power of the system [20]. Additionally, the thermal power of the storage system can be affected by the physical phenomena occurring within the PCM. For example, during the charging phase, the PCM's solid-liquid phase transition is accompanied by a density variation (most PCM are less dense when in liquid state). This density difference as well as the temperature gradient within the melted PCM induce motion in the liquid phase that can influence the dynamics of the charging process of the storage. The enhancements of the thermal power of the storage due to natural convection are less significant when discharging the storage. During discharge, static solid PCM is formed around the wall that separates the PCM from the steam. Due to the aforementioned low thermal conductivity, this can decrease the heat transfer rate since this latter is then only conductive. Consequently, one should carefully study the design of the storage in order to regulate and optimize the heat transferred within the storage for both charging and discharging phases.

II.1.2.1. Concept and overview of different technologies

Several technologies that use PCM to store the energy contained in steam already exist, one example is the encapsulation where the PCM is packed into capsules in contact with the steam [13]. This solution was proposed to respond to the steam pressure drop during discharge in *Ruths*-type steam accumulators. As shown in Figure 3, the PCM capsules are integrated into the storage vessel partly replacing the liquid water. In order to ensure a sufficient heat transfer rate and to compensate for the low thermal conductivity of PCM, the capsules must be small and thin. Steinmann and Eck [13] indicated that using encapsulated PCM increases the volume-specific storage capacity from around 20-30 kWh/m³ to about 100 kWh/m³ compared to the simple use of water. Steinmann and Tamme [30] presented cylindrical capsules with a length of 0.5 m and diameters of 15-25 mm that were filled with eutectic NaNO₃-KNO₃ (Figure 4). The challenge facing such solutions resides in variation of the specific volume of PCM during phase change. Steinmann and Tamme [30] proposed two options to compensate the volume variation :

- A flexible capsule is filled completely with PCM,
- A stiff capsule contains both PCM and gas.

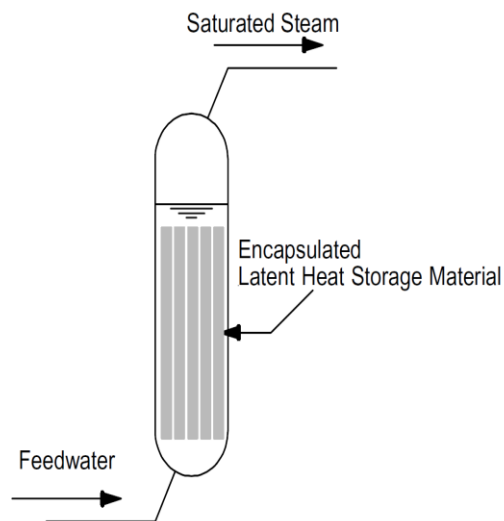


Figure 3. Steam accumulator with integrated latent heat storage material [13]

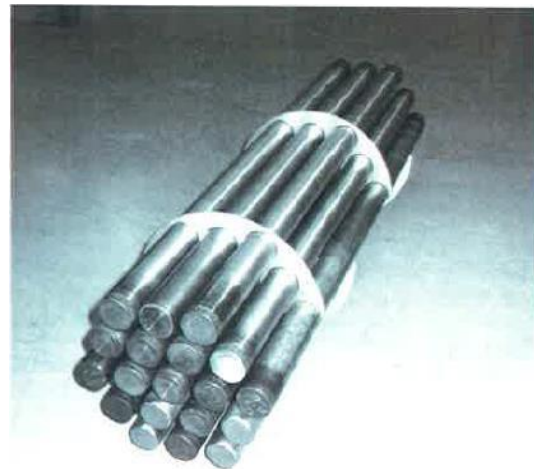


Figure 4. Capsules filled with $\text{NaNO}_3\text{-KNO}_3$ used for laboratory-scale test [30]

Other approaches exist where the focus is on increasing the effective thermal conductivity of the PCM instead of increasing the heat transfer area between the steam and the PCM. The use of highly conductive composite materials is one of them (Figure 5 and Figure 6).

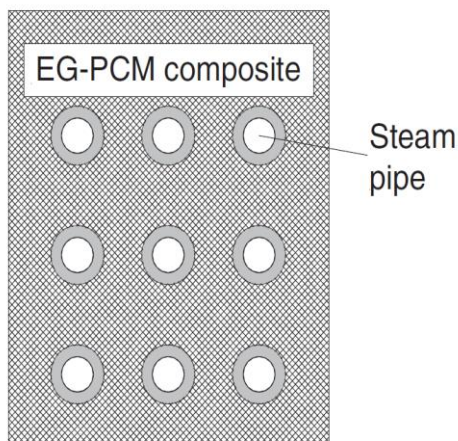


Figure 5. Design concepts to increase effective thermal conductivity: composite of expanded graphite and PCM [29]



Figure 6. Single segment made of PCM/composite material used for the laboratory-scale storage unit. Holes are intended for steam pipes. [30]

An alternative approach to increase the effective thermal conductivity is to add layers of highly conductive materials into the PCM. Graphite can be used either to form the composite material or to create foils [29] (Figure 7).

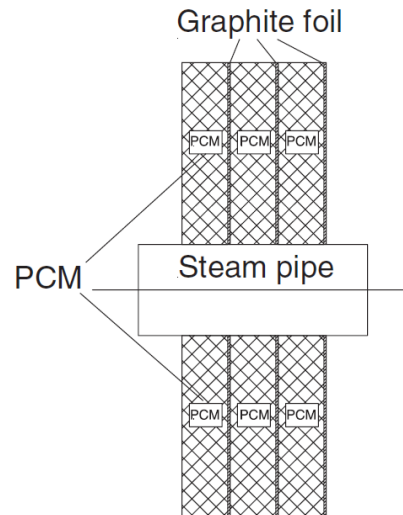


Figure 7. Design concepts to increase effective thermal conductivity: graphite foils as layers between PCM [29]

In addition to encapsulation and composite materials, there are other concepts that utilize PCM for storing steam energy, including:

- The addition of high-temperature HTF to the storage medium [25]: the Reflux Heat Transfer Storage (RHTS) concept is based on a synergistic utilization of phase change effects of melting and vaporization occurring in the thermal energy storage medium (Figure 8).
- Non-static PCM: the PCM can be transported during the heat exchange leading to high heat transfer coefficients. Examples of such active storages are the Screw Heat Exchanger (SHE) [26] (Figure 9) and the PCMFlux design [24], [32] (Figure 10 and Figure 11)

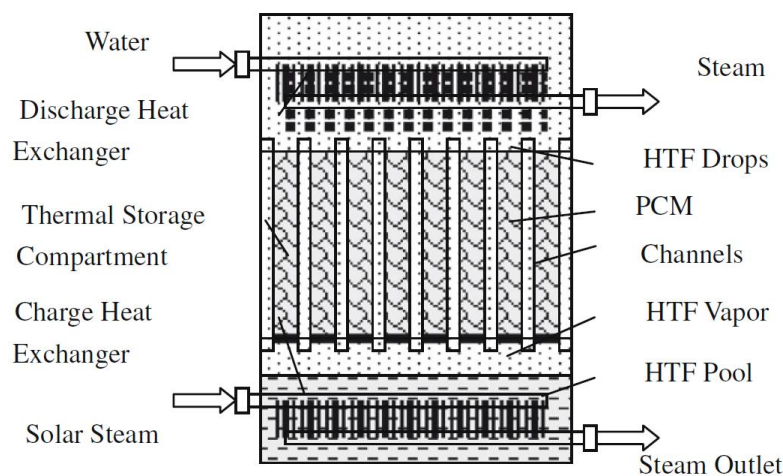


Figure 8. Schematic diagram of the RHTS concept [25]

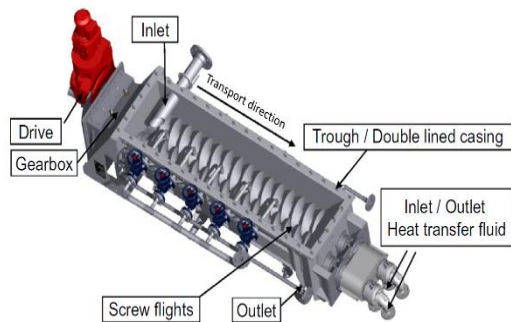


Figure 9. A double screw heat exchanger (SHE): material can be transported (transport direction left to right) and simultaneously heated/cooled by a heat transfer fluid [26]

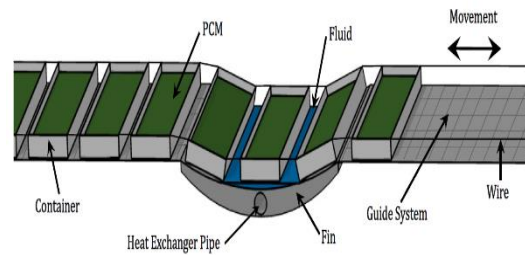


Figure 10. Horizontal PCMflux design [32]



Figure 11. Top photo of the PCMflux experimental apparatus [24]

In this section, several latent heat storage concepts were presented, each having its own advantages. However, the most intensely analyzed LHTES unit is the shell-and-tube system, accounting for more than 70 % of the studies carried out in the field of thermal storage by PCM [20]. The concept and the existing prototypes of such system are detailed in the following section.

II.1.2.2. Shell-and-tube systems

II.1.2.2.1. Concept

Shell-and-tube latent heat thermal energy storage is a concept derived from the shell-and-tube heat exchanger configuration. It consists of a shell with an array of tubes placed inside (Figure 12). The HTF (steam in this case) flows through the tubes, while the PCM occupies the volume of the shell surrounding them. For steam storage application, during the charging phase, the steam flowing inside the tubes transfers its energy in the form of heat to the PCM via the tube's wall. As a result, the steam undergoes condensation. The heat recovered by the PCM will increase its temperature and change its phase from solid to liquid. Consequently, a melting front is produced and propagates away from the tubes in the radial direction. Then for the discharging phase, which occurs at lower pressure and temperature compared to the charging phase, the process is reversed, the hot melted PCM releases its energy to heat up the water within the tubes

producing steam. The PCM solidifies in the shell and the produced steam could be used again in the process.

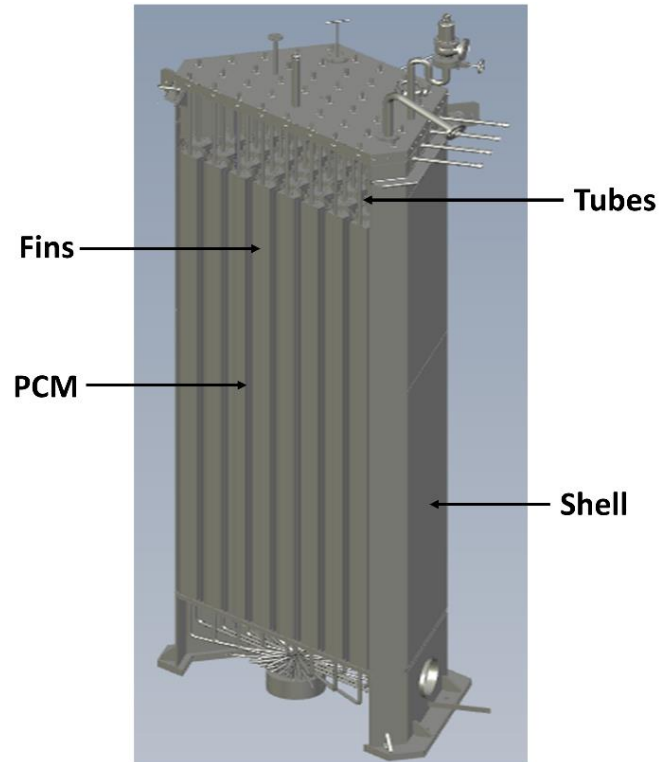


Figure 12. Drawing of a shell-and-tube LHTES [internal document CEA]

The thermal power of shell-and-tube LHTES is defined by the rate of heat transferred between the HTF and the PCM through the tube's wall. For steam storage applications, the two-phase flow inside the tubes results in a high heat transfer coefficient along most of the tube's inner wall. This means that the thermal performances of the storage are primarily affected by the thermal resistances within the PCM. As mentioned earlier, most PCM are poor conductor of heat. Additionally, with the melting progress during the charging phase, hot liquid PCM is surrounding the heat transfer tubes resulting in a decrease in the temperature gradient between the steam and the PCM, which affect the thermal performances of the storage system. Generally, in almost all existing prototypes, highly conductive metallic fins are added to the tube's outer wall within the PCM. The primary role of the fins is to enhance the heat transferred to and from the PCM by extending the heat transfer area between the metal and the PCM. Consequently, questions arise regarding the choices of the best type of fins to be used for each application, the optimal geometric configuration, as well as the fins' material to be retained. Further elaboration on these questions will be addressed in detail later in this chapter (Section II.2).

II.1.2.2.2. Existing prototypes

Laing et al. [17], [22] described a shell-and-tube steam storage using PCM (Figure 13). The PCM storage was accompanied by concrete storage in a three-part storage system developed by the German Aerospace Center DLR and tested in Carboneras, Spain. The role of the concrete storage was to store sensible heat for preheating of water and superheating of steam, while the PCM storage was used for the two-phase evaporation. The latent heat TES consisted of 152 tubes with a length of 6 m each resulting in storage capacity of 700 kWh. The PCM used was sodium nitrate NaNO_3 that changes its phase at around 305 °C. Radial fins made of aluminum were added to the tubes to enhance the heat transfer in the storage.



Figure 13. Insulated PCM test module at the test site in Carboneras, Spain [17]

Another shell-and-tube latent heat TES is designed by Johnson et al. [27], [28]. The storage system with a capacity of over 1.5 MWh is intended for the production of superheated steam at a pressure greater than 21 bar and 300 °C. The design includes 852 tubes with a length of 6 m each. Extruded longitudinal aluminum fins are mounted on the tubes, as shown in Figure 14. The hexagonal fin structure in addition to a small tube spacing of 70 mm allows for the high power level in the system. Sodium nitrate NaNO_3 was used as PCM. The storage system is integrated in a cogeneration plant in Saarland, Germany and serves as a backup to a gas turbine for steam generation.

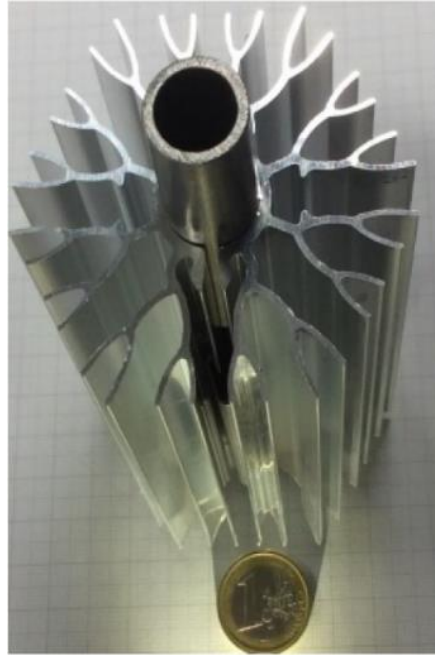


Figure 14. Finned-tube assembly showing an assembled tube with a euro-coin to show scale [27]

Garcia et al. [23] built and tested a steam shell-and-tube LHTES at CEA on the LHASSA experimental facility (Figure 15). The module is formed by 61 tubes surrounded by 6350 kg of sodium nitrate NaNO_3 used as PCM. Circular radial fins made of aluminum are used to enhance the thermal performances of the storage (Figure 16). Additionally, aluminum inserts are used to ensure an efficient heat transfer exchange with PCM regions away from the heat transfer tube.

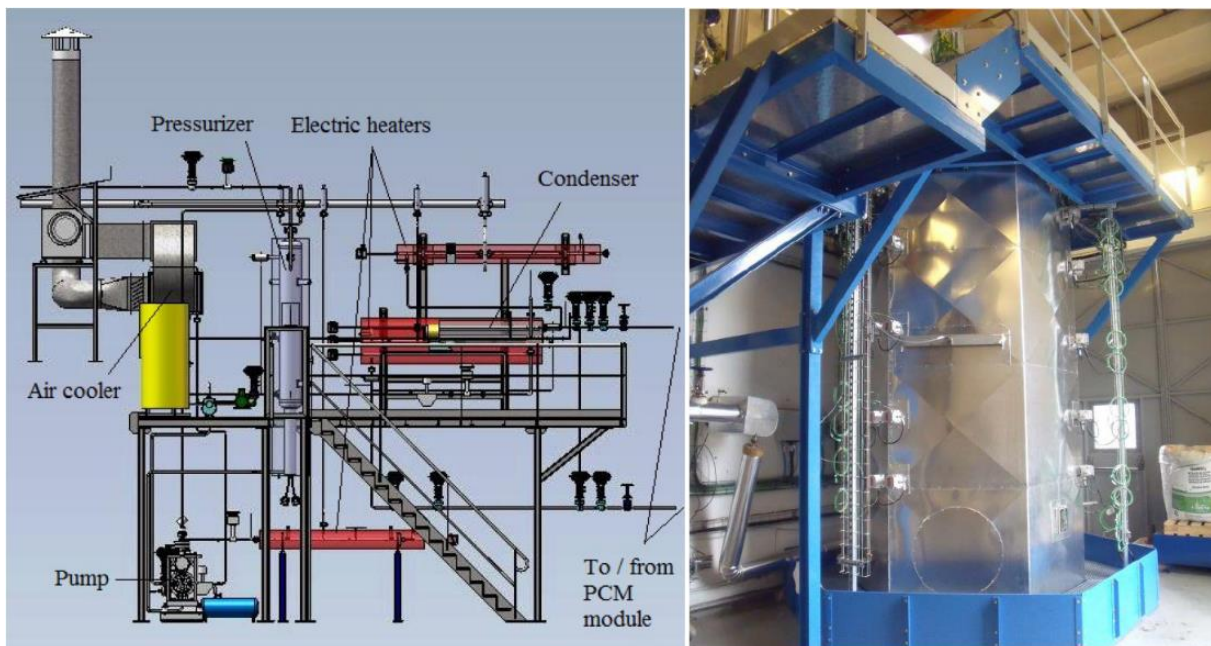


Figure 15. Layout of LHASSA test facility and storage test section [23]



Figure 16. Photo of tubes with circular radial fins with metallic inserts constructed at CEA Grenoble



Figure 17. Photo of a tube with serrated radial fins constructed at CEA Grenoble

Another prototype was also constructed by CEA for storing steam energy. The module contained 19 tubes occupied by serrated radial fins made out of steel, as shown in Figure 17. Further details about this prototype will be presented in the next chapter that will presents numerical studies that revolve around the geometry and working conditions of this prototype, in addition to the experimental data that will be used for the validation of the numerical approaches

II.2. Modelling of various factors influencing the thermal performances of shell-and-tube LHTES

In the previous section, several technologies to store steam energy were presented. A special attention was directed toward shell-and-tube LHTES which will be the main focus of the following study. As mentioned earlier, the power of such storage systems relies on the heat transfer efficiency between the steam flowing inside the tubes and the PCM region surrounding it. Consequently, the comprehension of the effects of each physical phenomena is essential to optimize the sizing of the corresponding storage system. In this section, the underlying physical phenomena during the PCM's phase transition that influences the heat transferred in the storage will be discussed. A special focus will be drawn to the different existing methods to take into account each phenomenon in 3D transient models. Furthermore, a literature review on the characteristic of metallic fins (types, configurations and materials) will be provided.

II.2.1. Phase change problem

The phase change problem revolves around the transition of a material between different states of matter. These transitions include processes like freezing, melting, evaporation and condensation. In shell-and-tube LHTEs, the PCM undergoes a phase transition at a slightly lower / higher temperature than the steam / liquid water used to charge / discharge the storage. During the charging/discharging phases, a melting/solidification front is formed that separates the solid from the liquid phases. The evolution of the solid-liquid front requires a significant amount of energy to be absorbed or released accordingly by the PCM. Consequently, the mathematical problem at the interface presents both physical and numerical challenges linked to the evolving front and the energy accompanied at solid-liquid interface. Physically, the solid liquid interface is governed by the temperature and velocity of the PCM. Mathematically, it may be seen as a boundary condition where a significant amount of energy is absorbed or released.

Such problems are known as *moving boundary problems* and are generally nonlinear and therefore more difficult to solve with respect to single-phase problems [36]. The analytical solutions of such problems are usually over simplified as they do not consider constant thermo-physical properties of PCM, they do not include natural convection in the liquid phase and they are usually based on one-dimensional analysis. As a result, the development of numerical models that can deal with the complex phenomena occurring during phase change becomes essential. Several approaches exist to study the solid-liquid phase change problem. Before presenting them, the mathematical formulation of the moving boundary problem, also known as the Stefan problem, is described.

II.2.1.1. Stefan problem

The solid-liquid phase change problem that evolves with time during the solidification/melting process of PCM is known as the Stefan problem (named after Josef Stefan 1835-1893). In its basic formulation, natural convection in the liquid phase is neglected and conduction is the sole heat transfer mechanism. Consequently, the energy equation, which is solved separately for both solid and liquid phases, is the only equation governing the medium. At the solid-liquid interface where no additional heat sources/sinks are present, the Stefan condition applies:

$$\lambda_s \nabla T_s \cdot \mathbf{n} - \lambda_l \nabla T_l \cdot \mathbf{n} = \rho L v \cdot \mathbf{n} \quad (3)$$

where L stands for the latent heat per unit mass and \mathbf{v} and \mathbf{n} are respectively the velocity vector of the interface and the unit normal of the moving interface. Consequently, in the 1D form, the Stefan condition becomes:

$$\lambda_s \frac{\partial T_s}{\partial x} - \lambda_l \frac{\partial T_l}{\partial x} = \rho L v \quad (4)$$

Some analytical solutions exist for the Stefan problem, but their applicability remains limited for situation featuring simplified geometries and boundary conditions. [37]

II.2.1.2. Advanced models

In reality, most problems including a phase transition cannot be simplified to the 1D pure conductive Stefan problem described above. In addition, in many cases, the solid-liquid transition is not isothermal and the phase change is instead spread on a temperature interval. As a result, the sharp solidification/melting front between the solid-liquid phases is transformed into what is called a *mushy region*. Additionally, natural convection occurring in the liquid phase cannot be always neglected. In reality, natural convection can significantly affect the shape and propagation of the moving boundary, especially during the melting phase [38]. These cases can be treated using specific models.

The existing strategies that deal with these various features of solidification/melting of PCM can be classed into three distinct categories Figure 18:

- The front tracking method [39], [40] with a fixed or an adaptive grid, in which the solidification/melting front position is tracked explicitly.
- The front fixing method
- The fixed domain method, in which the melting front is tracked implicitly.

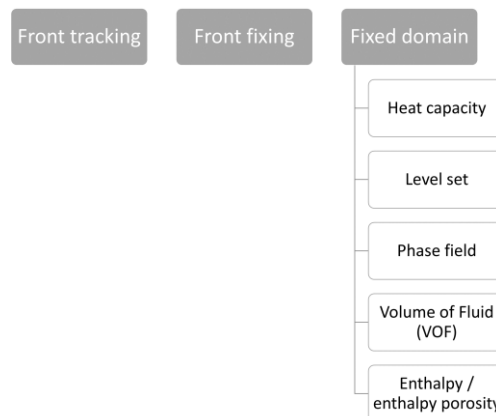


Figure 18. Common methods to simulate a phase-change problem. [41]

II.2.1.2.1. Front-tracking methods

In front-tracking methods (FTM), the location of the phase-change boundary is calculated at each time step. As a result, the position of the solidification/melting front is tracked explicitly. The numerical solution of FTM can be obtained with finite difference [42]–[44], finite element [45], finite volume [46], boundary element [47], and mesh-free methods [48]. Despite providing better accuracy in predicting the solid-liquid interface compared to fixed domain methods, the implementation of FTM is complicated for complex and 3D domains. Furthermore, in the case of shell-and-tube storages, the solidification/melting front is subject to deformations caused by the presence of fins within the PCM region. This complexity poses additional challenges in effectively incorporating FTM for the simulations and analysis of the charging/discharging stages in shell-and-tube LHTES.

II.2.1.2.2. Front fixing methods

As for the FTM, the moving solid-liquid interface is tracked explicitly in the front fixing methods. However, the moving boundary is fixed by changing the coordinates of the problem by introducing a new space variable. This approach is recommended for simple geometries and its numerical solution can be achieved with finite difference method [49]–[52], finite element method, Chebyshev spectral method [53] and with the spectral element method [48], [54].

II.2.1.2.3. Fixed-domain methods

Fixed-domain methods are the most used in the literature. In these methods, the melting front is tracked implicitly and the solidification/melting processes may occur on a temperature interval. These methods are simple for numerical simulations since both solid and liquid phases can be represented using the same equation. Some examples of the fixed-domain methods are the heat capacity method, the level set method, the phase field method and the enthalpy / enthalpy porosity methods. These methods are briefly presented in the following subsections.

II.2.1.2.3.1. Heat capacity method

In the heat capacity method [55]–[60], the latent heat of phase change is taken into account by modifying the expression the PCM's specific heat capacity. Consequently, the temperature dependent heat capacity is correlated with the enthalpy-temperature curve of the PCM.

$$c_p = \frac{dH}{dT} \quad (5)$$

In this method, the phase change occurs on a range between two temperatures $[T_{sol}, T_{liq}]$. To achieve accurate prediction of the energy stored or released within the PCM, the evolution of the heat capacity must be correctly evaluated. This is generally achieved by using specific formulations of this type:

$$c_p = \begin{cases} c_{p_s} & \text{for } T < T_{sol} \\ \frac{\int_{T_{sol}}^{T_{liq}} c_p(T) dT + L(T)}{T_{liq} - T_{sol}} & \text{for } T_{sol} \leq T \leq T_{liq} \\ c_{p_l} & \text{for } T > T_{liq} \end{cases} \quad (6)$$

where, c_{p_s} and c_{p_l} are the specific heat capacities for the solid and liquid phases, respectively. $L(T)$ represents the contribution of latent heat during the PCM's phase change and $c_p(T)$ is the temperature-dependent heat capacity.

Or more simply:

$$c_p = \begin{cases} c_{p_s} & \text{for } T < T_{sol} \\ \frac{L}{T_{liq} - T_{sol}} + \frac{c_{p_s} + c_{p_l}}{2} & \text{for } T_{sol} \leq T \leq T_{liq} \\ c_{p_l} & \text{for } T > T_{liq} \end{cases} \quad (7)$$

II.2.1.2.3.2. Level-set method

In this method [61]–[64], the moving front is captured implicitly based on addition of an artificial equation in the mathematical model. At the interface, the function (denoted D) is zero and is defined as follows:

$$D = \begin{cases} -d, & \text{solid} \\ 0, & \text{interface} \\ +d, & \text{liquid} \end{cases} \quad (8)$$

where d is the shortest distance to the front. Consequently, the solidification/melting front is located inside the elements that have both positive and negative nodal values.

II.2.1.2.3.3. Volume Of Fluid method (VOF)

In the VOF method, the solid-liquid dynamic front is implicitly tracked, relying on the volume fraction of one phase within each cell of a discretized domain. This approach possesses the advantage of ensuring total volume conservation. However, its primary drawback lies in increasing model complexity and should be chosen primarily when dealing with multiphase issues.

 II.2.1.2.3.4. Phase-field method

In phase-field methods [61], [65], the phase change can occur on a temperature range leading to an interface region having a thickness instead of a sharp interface as resulted from the level-set method. A phase field function $D(x, t)$ is used to track the position of the interface region, and is defined as follows:

$$D(x, t) = \begin{cases} -1, & \text{solid} \\ +1, & \text{liquid} \end{cases} \quad (9)$$

Consequently, the interface region can be found for values of D within the range $[-1,+1]$.

 II.2.1.2.3.5. Enthalpy method

The enthalpy method is one of the most used methods to solve the moving boundary problem. It was first proposed by Voller and Cross [66]. In this formulation, the solid-liquid moving front is tracker implicitly in a fixed-domain. The latent heat of phase change is considered using a source / sink term in the energy equation. Consequently, the energy equation is similar to the single-phase formulation making this approach relatively simple to use. Another advantage of this approach is that it is valid for both PCM undergoing phase change at a constant temperature point or over a temperature range. In each cell, the sensible heat (h_{sens}) and the latent heat of phase change (h_{lat}) are defined as function of the temperature, respectively, as follows:

$$h_{sens} = h_{ref} + \int_{T_{ref}}^T c_p dT \quad (10)$$

$$h_{lat} = f(T) \quad (11)$$

where h_{ref} is the PCM's enthalpy at the reference temperature T_{ref} . Consequently, the specific enthalpy is defined as the sum of both the sensible enthalpy and latent heat:

$$H = h_{sens} + h_{lat} \quad (12)$$

Due to its simplicity, many researchers have retained this approach to simulate the phase change problem and it has shown relatively good results and some capacity to represent industrial cases [67], [68].

 II.2.1.2.3.6. Enthalpy-porosity method

The enthalpy-porosity method is a particular case of the enthalpy method, where the latent heat is uniformly distributed along the phase change temperature interval. In this approach, the latent heat is defined as follows:

$$h_{lat} = f_m L \quad (13)$$

where f_m is the PCM's melted fraction, it is defined according to the temperature as follows:

$$f_m = \begin{cases} 0 & \text{for } T < T_{sol} \\ \frac{T - T_{sol}}{T_{liq} - T_{sol}} & \text{for } T_{sol} \leq T \leq T_{liq} \\ 1 & \text{for } T > T_{liq} \end{cases} \quad (14)$$

Consequently, the energy equation is formulated as follows:

$$\rho c_p \left(\frac{dT}{dt} + \mathbf{u} \cdot \nabla T \right) = \nabla(\lambda \nabla T) - \rho L \left(\frac{df_m}{dt} + \mathbf{u} \cdot \nabla f_m \right) \quad (15)$$

The enthalpy-porosity method is characterized by its fast convergence and high accuracy. It is the most used approach for modelling the phase change problem and was successfully validated against experimental data. Due to its simplicity and integration into the ANSYS Fluent commercial code, this approach stands as the preferred choice for modelling the phase change phenomenon in this thesis. However, for fixed-grid methods, since the same set of equations governs both solid and liquid phases, a special attention should be issued to handle the velocity within the solid phase. Consequently, an additional technique should be coupled with this methodology in order to overcome such a problem.

II.2.1.2.3.7. Dumping of velocity in solid regions

In fixed-domain methods, the PCM phase is defined according to the temperature, and a single set of equations governs both solid and liquid phases. However, when in solid state, the PCM should be static and the momentum equation requires special modification to ensure a zero velocity. Several approaches are found in the literature for this purpose:

- *Switch-off method*: as the name suggests, a zero velocity is imposed in cells occupied with the solid phase. However, the sudden change in velocity can cause discontinuities in the flow fields at the solid-liquid interface. Some proposed solutions consist of ramping the velocity at the interface to ensure a smooth transition from liquid velocity to zero. Such approach known as *Ramped switch-off method*. [69], [70]
- Another approach consists of varying the viscosity of the fluid according to the phase present in the cell. This approach is known as *Variable viscosity method* [69], [71]. In this method, the solid phase is characterized by a very high viscosity which induces deceleration resulted from the increase in the diffusive terms of the momentum

equation. The viscosity can be varied depending on temperature, liquid or solid fractions.

- The third and most used approach is the *Source term method* [72]. In this method, a source term is introduced into the momentum. Much like the variable viscosity method, the introduced term assumes very high values when in solid state and decreases until it nullifies while transitioning to the liquid state. The source term is proportional to the velocity, and is defined as follows:

$$S_v = A\mathbf{u} \quad (16)$$

The most used expression of the term A is the one derived from the Darcy's law [72]. It is defined so that the momentum equation replicates the Carman-Kozeny equation in the mushy region. The mushy region refers to a transitional zone that exists during the phase change process, it is an intermediate region where both solid and liquid phases coexist, and it is characterized by a mixture of both phases. Consequently, A is defined as follows:

$$A = A_{mush} \frac{(1 - f_m)^2}{f_m^3 + b} \quad (17)$$

With $b = 10^{-3}$, a small value added to prevent division by zero when in solid state ($f_m = 0$). A_{mush} is the mushy zone constant which has to be large enough to reduce to a negligible value the flow in the solid phase. In the literature, the values of A_{mush} depend on the studied case and they generally range between 10^3 and $10^8 \text{ kg.m}^{-3}.\text{s}^{-1}$ [73]. The Darcy source term method is the most widely used technique to annihilate the velocity in the solid phase and is directly implemented in the commercial CFD code ANSYS Fluent. Consequently, this technique was the one adopted in the simulations performed during this thesis.

II.2.2. Natural convection in the liquid phase

In the previous section, the solid-liquid phase change problem was introduced, along with various approaches for its modelling. In this section, the discussion revolves around natural convection, which is another physical phenomenon that currently occurs during the solidification/melting process of PCM. By definition, natural convection is a heat transfer process in a fluid that occurs due to density differences caused by temperature variations. It is

called natural since it relies on the buoyancy of the fluid without the need of any external mechanical forces. Additionally, when a solid-liquid phase change occurs and since most PCM (except for water) tend to have lower density in their liquid state when compared to their solid state. A PCM undergoing melting/solidification experiences a volumetric expansion/shrinkage. As a result, the solid-liquid phase transition contributes to the generation of movements in the liquid phase.

During the charging phase of a LHTES, natural convection occurring in the melted PCM can significantly enhance the heat transfer mechanisms within the storage [74]. Therefore, if the sizing of the storage is determined by its performance during the charging phase, disregarding the potential enhancements due to natural convection on the thermal exchange between the HTF and the PCM could lead to an oversized system [74]. Several approaches are found in literature to handle natural convection due to density differences between phases or where density variations occur in the liquid phase.

II.2.2.1. Various approaches for modelling natural convection

II.2.2.1.1. Variable density

The most intuitive way to account for natural convection in the liquid phase is by considering the PCM's expansion/shrinkage. Therefore, the PCM's density is varied according to the temperature in each cell.

$$\rho = \rho(T) \quad (18)$$

Typically, a constant density is assumed for the solid state, whereas a temperature dependent density is considered in the liquid state. Then, to avoid numerical instabilities, a linear interpolation is often applied in the mushy zone:

$$\rho = \begin{cases} \rho_s & \text{for } T < T_{sol} \\ f_m \rho_l(T_{liq}) + (1 - f_m) \rho_s & \text{for } T_{sol} \leq T \leq T_{liq} \\ \rho_l(T) & \text{for } T > T_{liq} \end{cases} \quad (19)$$

This formulation of the PCM's density is found across several studies in the literature [75]–[79].

Despite its accurate representation of the density variation according to the temperature and state of the PCM, the variable density formulation poses a challenging problem regarding the expansion/shrinkage in volume. Consequently, special numerical approaches are required to

treat the variation in volume of PCM during melting and solidification. Several techniques for dealing with this phenomenon are found in literature.

The first and most used method consists of simulating a layer of gas in addition to the PCM region. For a melting process, the physical model is formed by a container partially filled with solid PCM at initial temperature. The remaining volume of the container is occupied by a gas (usually air is used). When the PCM melts, its volume increases and occupies the volume previously occupied by the gas. Two methods exist, which are differentiated by how they handle the volume of gas (Figure 19). In the first one (Figure 19(a)), the container is opened from above and the gas is at atmospheric pressure. During the PCM's melting process, the PCM expands and pushes the gas outside of the domain. The process is reversed in solidification, the gas re-enter the domain due to the shrinkage of the PCM. In the second method (Figure 19(b)), the container is sealed from the top. Consequently, the gas is compressed or expanded during the PCM volume changes.

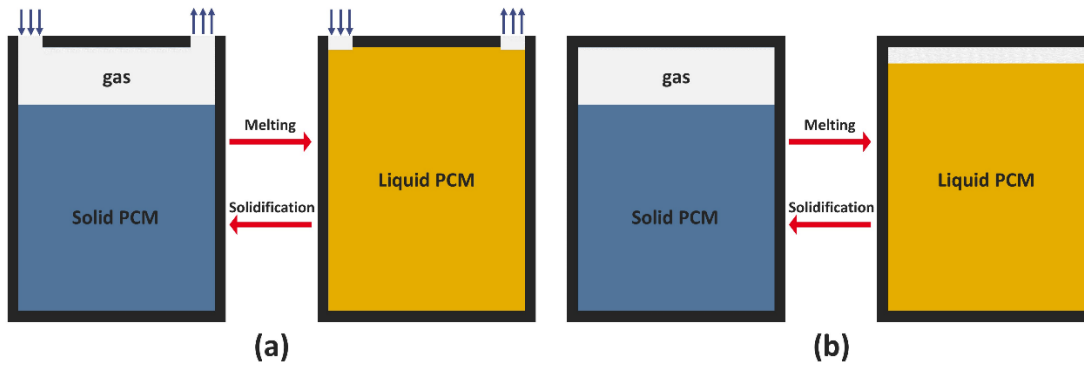


Figure 19. Illustrations of the PCM's volume expansion/shrinkage during phase change with a gaseous volume in the domain (a) the gas can enter and exit the domain (b) the gas is compressed inside the domain

Numerically, the VOF model is used to describe the PCM-gas interactions with the moving interface between the two media. In each cell, an additional property regarding the volume fraction of each fluid is considered:

$$\alpha_n = \frac{\text{volume of the } n^{\text{th}} \text{ phase in the cell}}{\text{volume of the cell}} \quad (20)$$

Where

$$\alpha_n = \begin{cases} 0 & \text{the cell does not contain the } n^{\text{th}} \text{ fluid} \\ 1 & \text{the cell is full of the } n^{\text{th}} \text{ fluid} \\ \text{between 0 and 1} & \text{the cell contains the fluid interface} \end{cases} \quad (21)$$

Consequently, the sum of the volume fraction of all fluids in each cell is one:

$$\sum_n \alpha_n = 1 \quad (22)$$

As a result, the coupling of the VOF model with the enthalpy-porosity model leads to the following governing mass, momentum and energy equations:

$$\frac{\partial(\alpha_n \rho_n)}{\partial t} + \nabla \cdot (\alpha_n \rho_n \mathbf{u}_n) = 0 \quad (23)$$

$$\frac{\partial(\alpha_n \rho_n \mathbf{u}_n)}{\partial t} + (\mathbf{u}_n \cdot \nabla)(\alpha_n \rho_n \mathbf{u}_n) = -\alpha_n \nabla P + \alpha_n \rho_n \mathbf{g} + \alpha_n \mu (\nabla \cdot \nabla) \mathbf{u}_n - A \mathbf{u} \quad (24)$$

$$\frac{\partial(\alpha_n \rho_n H)}{\partial t} + \nabla \cdot (\alpha_n \rho_n \mathbf{u}_n H) = \alpha_n \nabla \cdot (\lambda_n \nabla T) \quad (25)$$

Where H is the specific enthalpy defined by Equation (12).

The main advantage of this approach is that it offers an accurate representation of the physical behavior of the PCM during phase change. VOF method coupled with the enthalpy-porosity approach were adopted by Bechiri et Mansouri [80] to numerically investigate the melting of a PCM in a vertical cylindrical tube. At initial stage, the vertical tube is partially filled with solid PCM and the remaining volume is occupied by air at atmospheric pressure (Figure 20). The tube is insulated from the bottom side and open from above, allowing air to exist the domain. The PCM is commercial paraffin RT27 with a melting temperature interval of 28-30 °C.

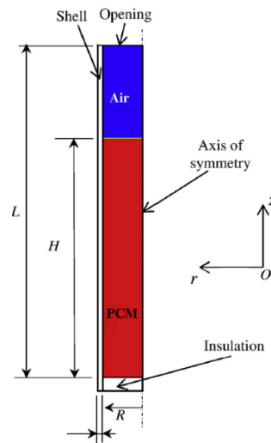


Figure 20. Schematic of the cylindrical domain with PCM and a volume of air opened to the surrounding [80]

Figure 21 shows a comparison of the density, streamlines and solid fraction contours obtained by the numerical simulation with experimental results at three different instants during the melting process. To ensure the melting of the PCM, the outer wall temperature is fixed at 20 °C above the PCM melting temperature. With the melting progress, natural convection due to the density variation leads to a more advanced melting at the top of the domain. Consequently, the

melting front evolves in both radial and axial directions. At $t = 24$ minutes, almost all of the PCM has melted, the lower density of the liquid state increases the level of the domain occupied by the PCM (0.2 m after 24 minutes compared to ~ 0.19 m at $t = 8$ minutes). Additionally, at different stages of the melting process, the solid fraction shape as well as the PCM expansion obtained by the numerical simulations are close with those obtained experimentally.

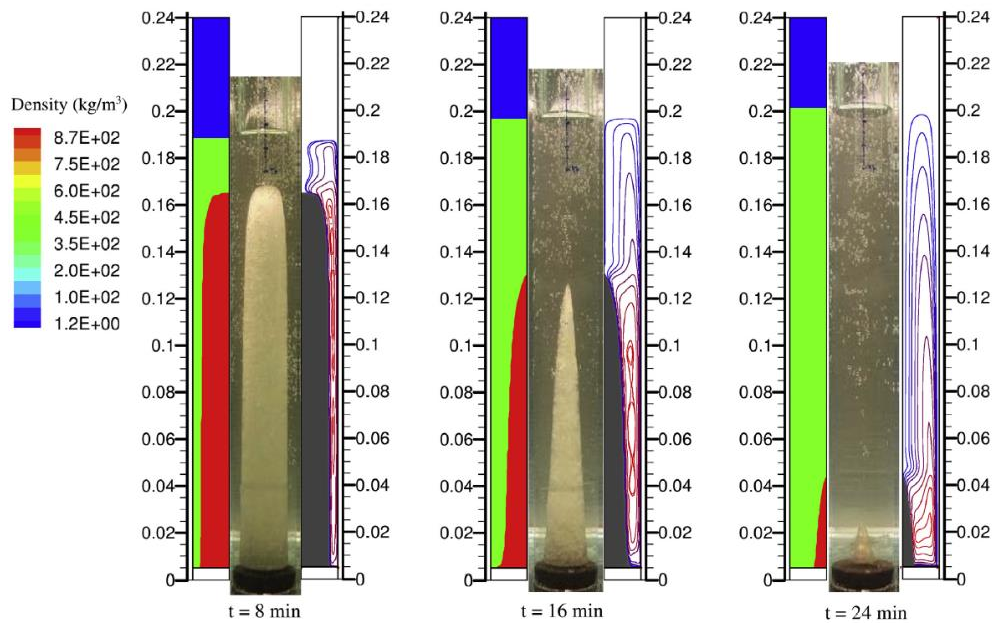


Figure 21. Comparison of shapes of numerical solid and liquid fractions with experiment [80]

A similar study was previously conducted by Shmueli et al. [81] who performed a numerical analysis on the melting process of PCM with variable density. Their study focused on investigating the influence of the mushy zone constant (Equation (17)) on the outcome of the numerical model. By comparing the results with experimental data, they concluded that there should exist an optimum value of the mushy zone constant A_{mush} (10^8 in their case).

Zeneli et al. [78] adopted the sealed container approach to numerically investigate the effect of the vessel design and operating conditions on the melting rates of a silicon-based LHTES at ultra-high temperature (~ 1410 - 2000 °C). Figure 22 illustrates the different shapes under investigation, along with the respective boundary conditions representing imposed temperatures in each case. In all cases, the inert gas is treated as a compressible fluid, by solving the Tait equation [82]. It was concluded that the heated surface plays a crucial role on the PCM melting rate when the heating of the container is from its sidewall. As a result, the cubic shape lead to the highest melting rate. However, the truncated cone resulted in the most preferable solution for melting rates, design flexibility (height can easily be modified) and heat losses.

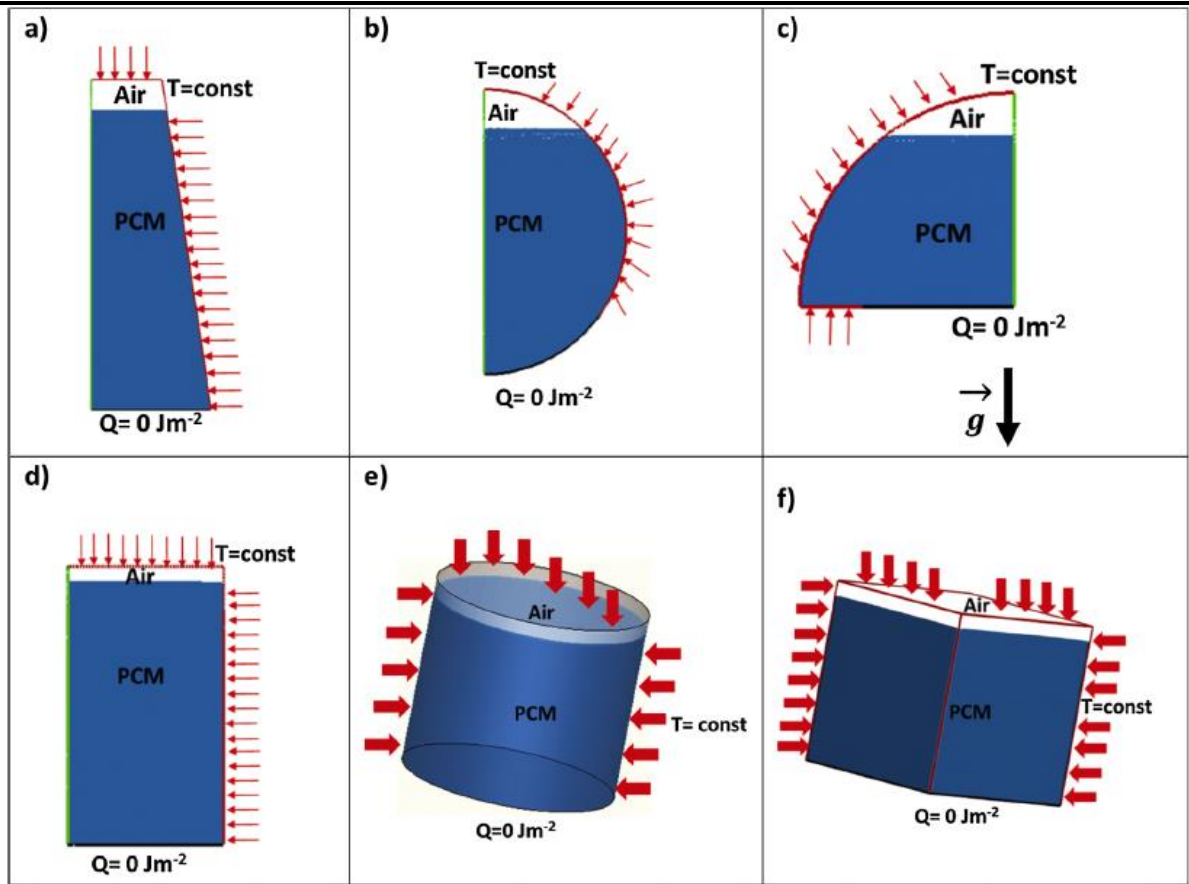


Figure 22. Computational domains of the investigated cases: (a) truncated cone (axisymmetric), (b) sphere (axisymmetric), (c) cut-off sphere (axisymmetric), (d) cylinder (axisymmetric), (e) cylinder (3D) and (f) cube (3D). Black: emitter surface (adiabatic during melting), green: axis, red: walls. [78]

Another approach to handle the PCM's expansion/shrinkage due to the density variation is to treat the container's wall as elastic. The expansion of the PCM during the melting process exerts a force on the wall. The opposing force applied by the wall will result in a rise of pressure within the PCM. Consequently, there is no need to simulate a gaseous phase in addition to the PCM (Figure 23). However, one should note that pressure can affect both the latent heat and the melting temperature of PCM [83]. For an elastic wall assumption, the pressure rise is given by Hooke's law:

$$\Delta P = k_w \Delta x \quad (26)$$

Where Δx corresponds to the deformation caused by the volumetric expansion of the PCM. k_x is the effective spring constant of the elastic wall that can be linked to the geometry and the mechanical properties of the wall [83].

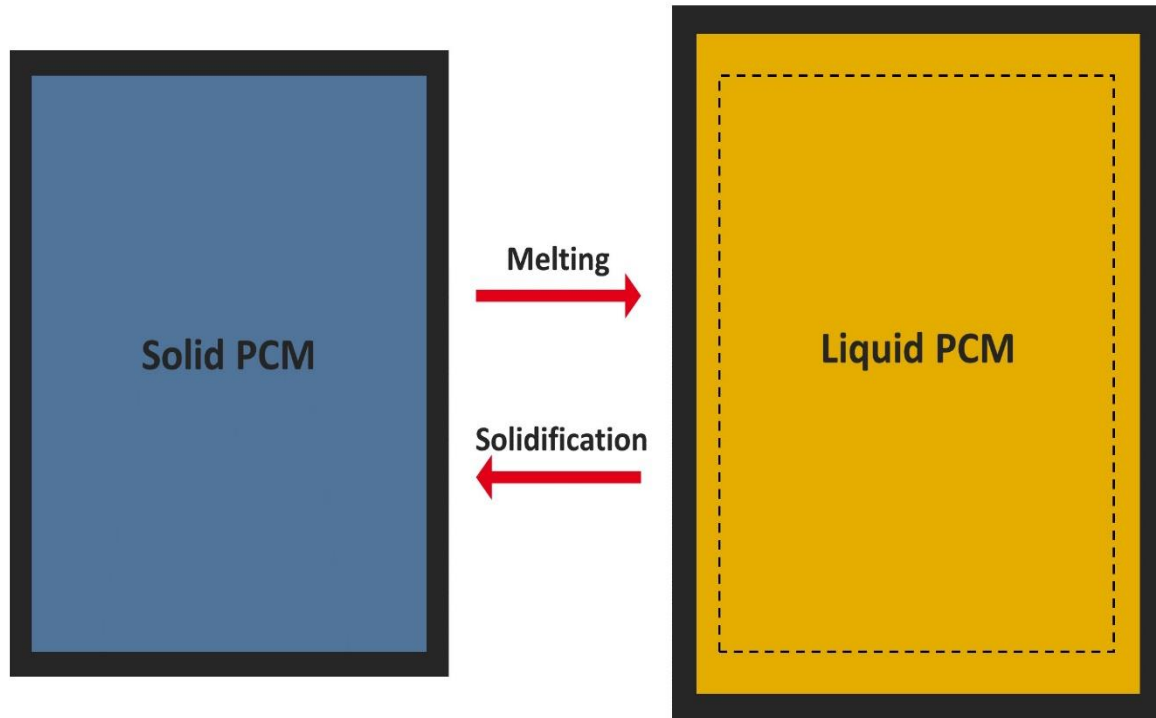


Figure 23. Illustrations of the PCM's volume expansion/shrinkage during phase change without a gaseous volume in the domain

Archibold et al. [84] used this approach to simulate the melting of sodium nitrate NaNO_3 encapsulated in a closed spherical shell. The model was validated with experimental results of the melting process of n-octadecane inside a spherical glass capsule [85]. Figure 24 shows the evolution of the solid fraction obtained from both the numerical simulation and experimental test for an imposed temperature as a boundary condition. Initially the PCM is in a solid state, after which melting initiates from the uppermost point of the spherical shell. Then, as time progresses, a melting front emerges within the shell separating the liquid from the solid phases, and gradually descends. The numerical model succeeds in reproducing the same melting front evolution obtained in experience. The numerical model was then used to perform parametric studies on the effects of the different parameters, such as the radius of the spherical shell, its thermal conductivity and temperature, as well as other non-dimensional numbers such as the Stefan number, Grashof number and the Prandtl number.

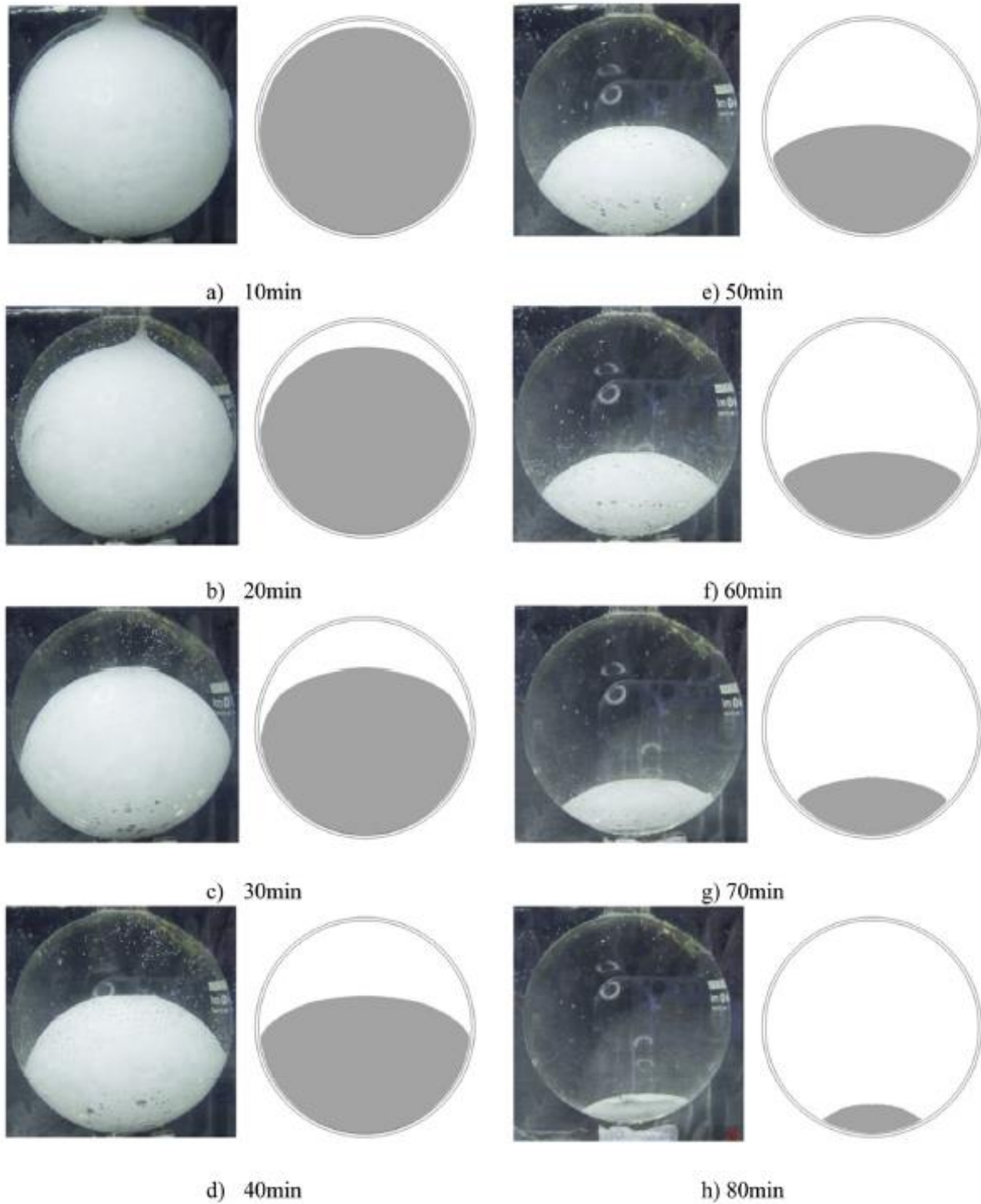


Figure 24. Comparison of the solid fraction between numerical and experimental results [84]

II.2.2.1.2. Effective thermal conductivity

The variable density method necessitates specialized treatments to accommodate to volume expansion or contraction of the PCM, which can introduce complexity and high computational

costs. Some simplifications can be employed to address convective effects, without considering the temperature and phase dependent density of the PCM.

The first method consists of taking into account the effects of natural convection in the melted phase by simply using an equivalent thermal conductivity. This means that, instead of simulating the velocity field caused by the PCM's density variation, heat is transferred by conduction within a static PCM regardless of its state. The thermal conductivity of the PCM is then varied according to the conditions within the storage to account for the potential enhancements due to natural convection that are not directly represented. Generally, an effective thermal conductivity correlation is formulated as follows:

$$\frac{\lambda_{eff}}{\lambda_l} = CRa^n \quad (27)$$

Where λ_l and λ_{eff} are respectively the liquid and the effective thermal conductivities. Ra denotes the dimensionless Rayleigh number, while C and n are experimentally determined constants. As a result, this technique relies on the availability of experimental data to accurately predict the effective thermal conductivity. This prediction enables the replication of the precise heat transfer that would have occurred, had natural convection been directly considered. Due to its simplicity and relatively low computational costs (as it eliminates the need to solve the momentum equations), this method has been employed in prior studies found in the literature [86]–[88].

II.2.2.1.3. Boussinesq approximation

Boussinesq approximation consists of taking into account the effects that variable density has on the velocity field in the liquid phase without varying the PCM's density. As a result, the volume expansion/shrinkage of the PCM is neglected and density change is only considered in the buoyancy term of the momentum equation:

$$\rho = \rho_{ref} \left(1 - \beta(T - T_{ref}) \right) \quad (28)$$

where β stands for the thermal expansion coefficient. T_{ref} is a reference temperature at which the reference density ρ_{ref} is measured. The Boussinesq approximation coupled with the enthalpy-porosity is the most widely used approach found in literature to simulate the phase change problem with natural convection. This is mainly due to its computational efficiency and

simplicity compared to variable density approaches. The mass, momentum and energy equations governing the PCM domain are as follows:

$$\nabla \cdot \mathbf{u} = 0 \quad (29)$$

$$\rho \left(\frac{d\mathbf{u}}{dt} + \mathbf{u} \cdot \nabla \mathbf{u} \right) = -\nabla P + \mu \nabla (\nabla \mathbf{u}) - \rho \beta (T - T_{ref}) \mathbf{g} - A \mathbf{u} \quad (30)$$

$$\rho c_p \left(\frac{dT}{dt} + \mathbf{u} \cdot \nabla T \right) = \nabla (\lambda \nabla T) - \rho L \left(\frac{df_m}{dt} + \mathbf{u} \cdot \nabla f_m \right) \quad (31)$$

II.2.2.2. Influence of natural convection on the melting process of PCM

Fornarelli et al. [89] performed CFD analysis of melting process in a shell-and-tube LHTES for CSP plants. The enthalpy-porosity method was coupled with the Boussinesq approximation to numerically investigate the effect of natural convection on the performances of the storage during the charging phase. The outcome of the numerical model was compared and validated with experimental data issued by Trp [90]. The experimental unit consisted of two concentric tubes as shown in Figure 25.

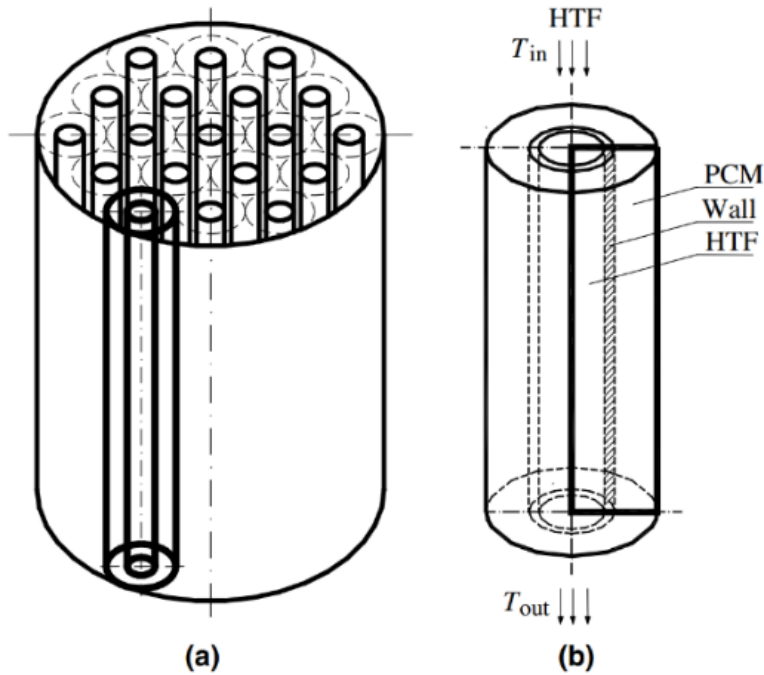


Figure 25. Shell and tube configuration of the PCM heat storage: (a) complete system; and (b) single module considered for simulations [89], [90]

The influence that natural convection has on the melting process was investigated by comparing the outcome of the convective numerical model to a pure conductive model, in which the buoyancy is neglected. The results confirmed that natural convection enhances the heat flux between the HTF and the PCM during the melting process resulting in an overall reduced charging time. Figure 26 shows the evolution with time of the percentage of heat stored. At

initial stages of the charging process, natural convection has little to no impact on the amount of energy accumulated in the PCM. However, with the melting progress, the increase in volume of the melted phase generates movements that increases the heat exchange in the storage. As a result, the charging phase is completed three hours earlier when natural convection is activated compared to a pure conductive simulation.

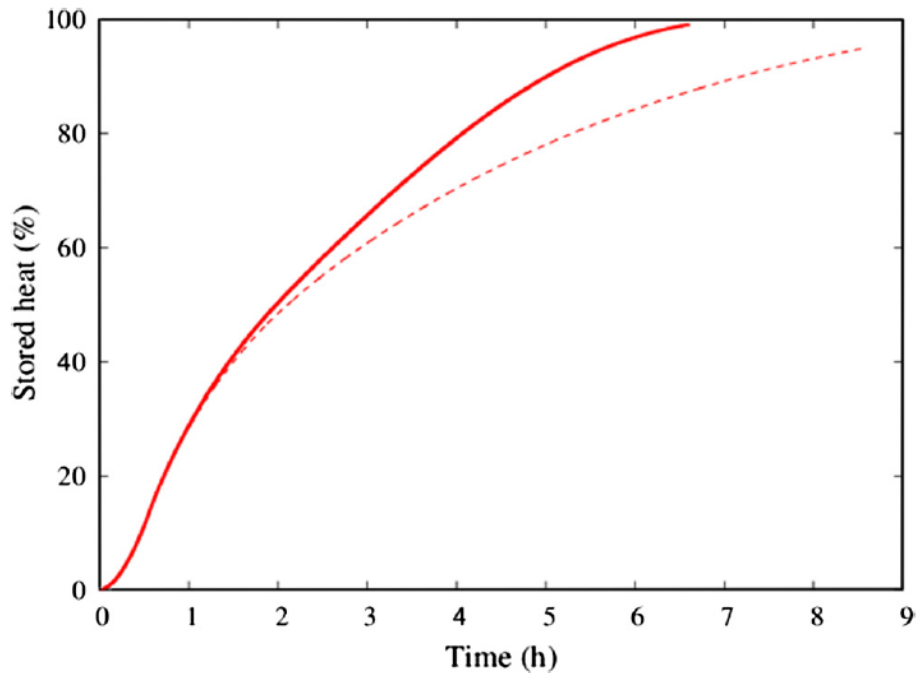


Figure 26. Time series of the stored heat percentage. Convective case (continuous line) and conductive case (dotted line). [89]

Tehrani et al. [74] applied the enthalpy-porosity method coupled with the Boussinesq approximation to numerically investigate the error of neglecting natural convection in high temperature vertical shell-and-tube LHTES systems (Figure 27). To do so, a comparative analysis was conducted between the outcomes of the model that considers natural convection effects, and simulations wherein natural convection was disregarded, and heat solely transferred by conduction through the PCM. The investigation was carried on nine distinct geometric configurations, each obtained from the permutations of three values for both the tube's length L and radius ratio $\frac{R}{r_0}$, as illustrated in Figure 27. As a result, it was found that, for the studied cases, the error of neglecting natural convection on the charging/discharging ratio of the storage were significantly higher during the melting process compared to solidification. Additionally, the effect of natural convection varied according to the geometric parameters. The error of neglecting natural convection increased with the decrease of the tube's length L and the increase

of radius ratio $\frac{R}{r_o}$. Finally, correlations were obtained to quantify this error as function of geometry and other non-dimensional numbers (Stefan number (Ste), Biot number (Bi) and the Rayleigh number (Ra)) for both melting and solidification.

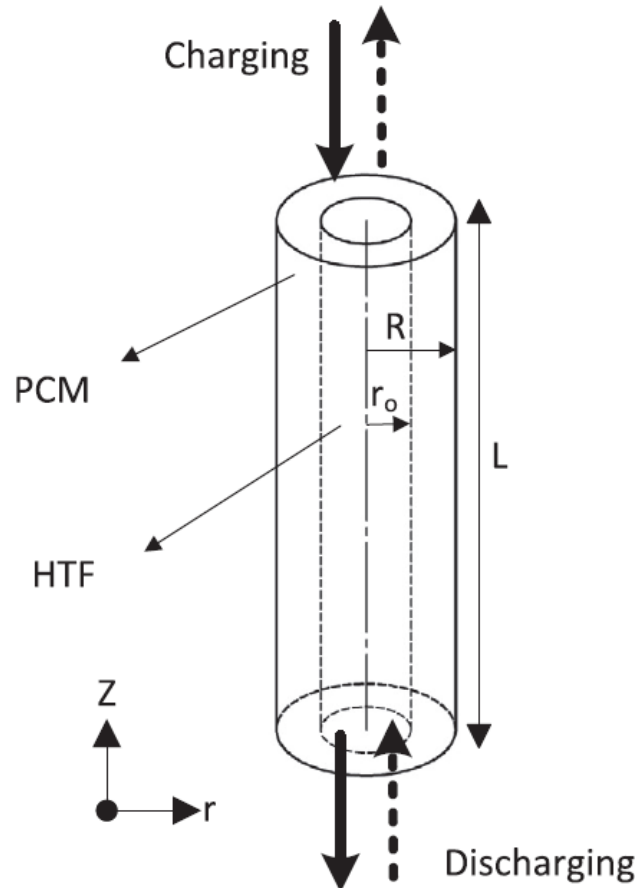


Figure 27. A vertical single unit cylindrical shell-and-tube LHTES system [74]

Yang et al. [91] also coupled the enthalpy-porosity method with Boussinesq approximation to investigate the thermal performance of a shell-and-tube LHTES unit. The outcome of the numerical model was validated with experimental results issued by Longeon et al. [92]. In line with earlier research, the role of natural convection was investigated by comparing the results with a pure conductive model. However, their study investigated the impact of natural convection with and without the presence of radial fins around the heat transfer tube. The evolution with time of the PCM's melted fraction is shown in Figure 28 for two cases, the first one corresponds to a the tube without fins (Figure 28(a)) while the second one corresponds to the case where 19 circular fins with a pitch of 20 mm are added to the tube's outer wall (Figure 28(b)). In both cases, natural convection enhances the melting progress resulting in a faster charging process.

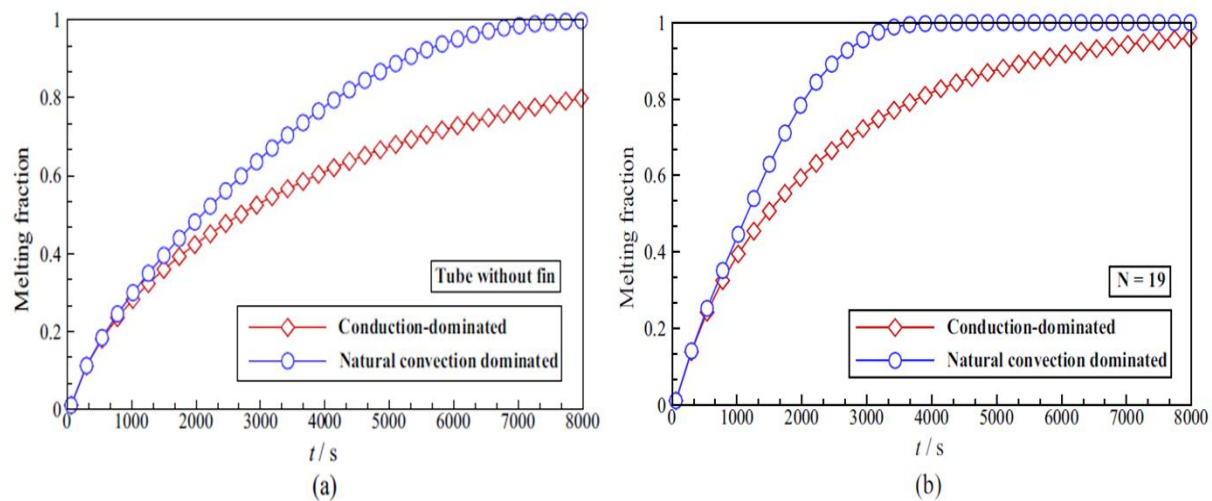


Figure 28. Effect of natural convection on melting fraction: (a) LHTHS unit without fin; (b) LHTHS unit with annular fins ($N = 19$).

II.2.2.3. Comparison of different approaches accounting for natural convection

As discussed earlier, the advantage of the variable density method lies in the accurate representation of the phase and temperature dependent density of the PCM. However, a special numerical treatment should be considered to tackle the PCM's volume expansion/shrinkage. The modelling of an additional gaseous phase requires the coupling of the VOF method with the enthalpy-porosity approach, which adds complications to the numerical models. On the other hand, the Boussinesq approximation provides an efficient and simple solution to account for natural convection due to buoyancy effects in the liquid phase. However, the PCM's density remains constant and the volume expansion/shrinkage is not represented in the numerical simulations.

Faden et al. [75] compared the outcome of both the constant density Boussinesq approximation model and the variable density model on the melting process of PCM in a rectangular capsule. The dimensions of the capsule was kept the same for both models. In the variable density case, no additional gaseous phase was modelled with the PCM. Instead, the excess PCM volume resulted from the expansion due to melting leaves the capsule through a small outlet at the upper left corner, as illustrated in Figure 29. Consequently, the PCM's mass available within the capsule is not conserved. This approach allows the investigation of the effect of the density variation on natural convection in the melted phase without the need of modelling an additional phase. Initially, the PCM is in solid state and is heated at the left capsule wall at a uniform and constant temperature higher than the melting temperature of the PCM.

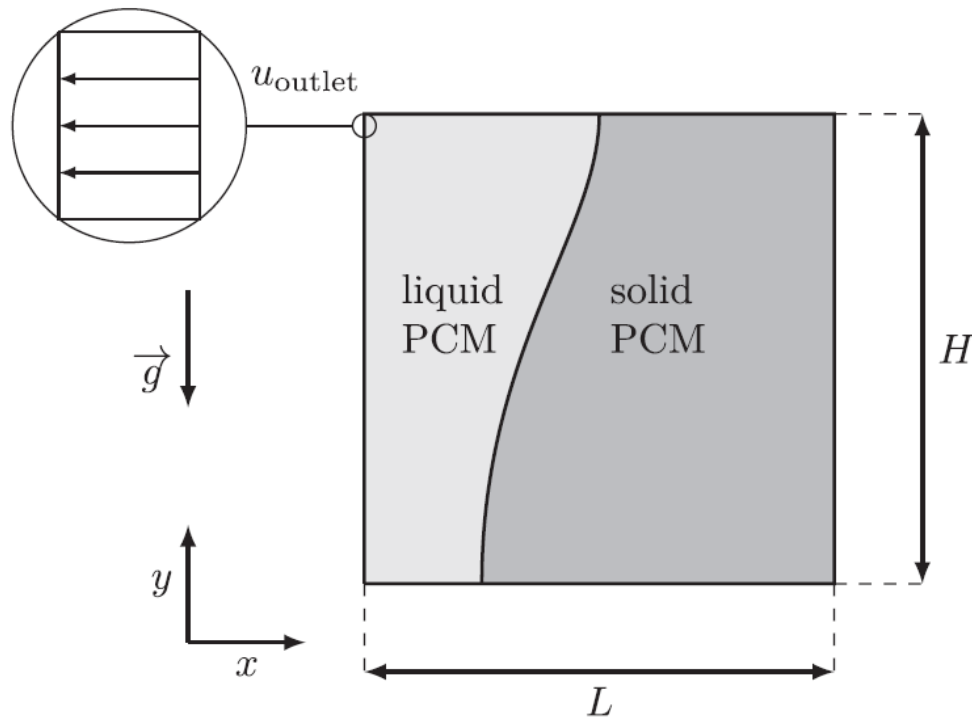


Figure 29. Schematic representation of the state of the domain at $t > 0$ s. [75]

Figure 30 shows a graphical representation of the melting process resulted from both the constant density Boussinesq model (upper row) and the variable density model (lower row). For the studied case, the authors distinguished the PCM's melting process into four regimes:

1. Diffuse regime: at initial stages, most of the PCM is on solid state (blue contour in Figure 30). Due to the small liquid fraction, the effects of natural convection are negligible and heat is mainly transferred by conduction through the PCM.
2. Convective regime: with the increase in the liquid fraction, natural convection role becomes more significant. As a result, the melting process is more advanced at the top of the domain.
3. Fluid reaches wall: the impact of natural convection on the melting process increases. The liquid PCM reaches the right wall near the top of the domain.
4. Shrinking solid: all the PCM is melted at the top of the domain, the melting process progresses in both horizontal and vertical direction.

By comparing the results shown in Figure 30, it can be observed that both numerical approaches yield a very similar melting front. However, the Boussinesq approximation model results in a relatively faster melting process. As seen in Figure 30(c), the melting front is more advanced in the Boussinesq model where it has reached the right wall, while a fraction is still to be melted

in the variable density model. This delay can be linked to heat lost by the liquid PCM exiting the domain in the variable density model. Furthermore, the authors demonstrated that the deviation between both models is predicted by the scaling theory and the relative deviation depends on the solid/liquid density ratio.

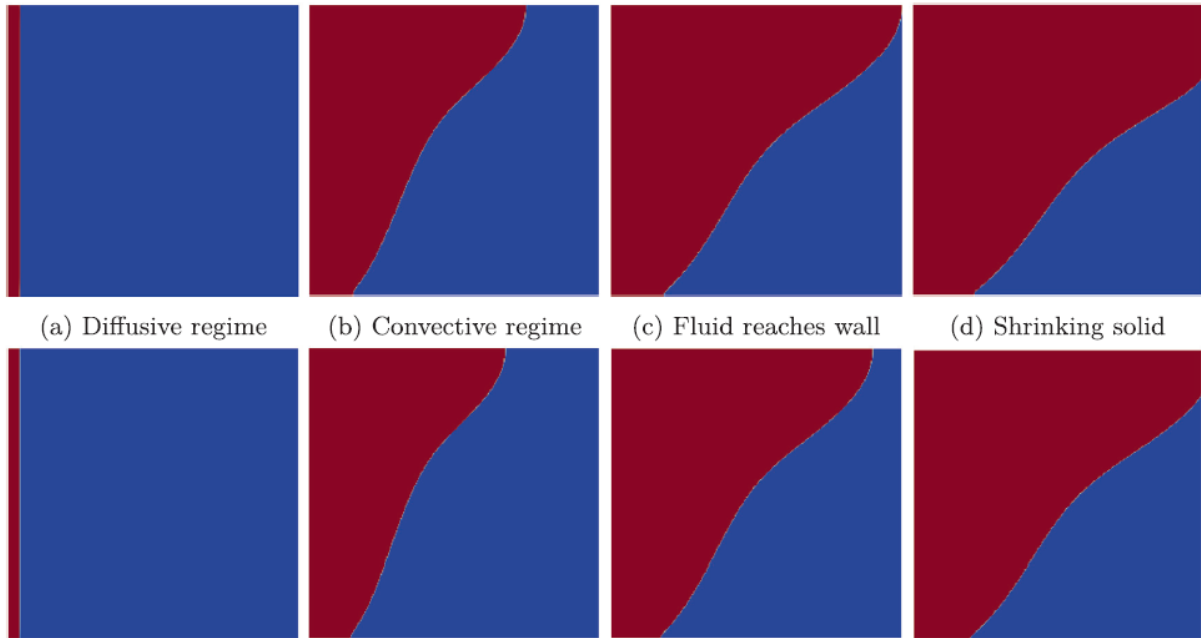


Figure 30. Evolution of the phase front for Octadecane. The upper row corresponds to the constant density Boussinesq approximation model. The lower one to the variable density model. The snapshots are taken at the same time. [75]

Finally, natural convection is an important physical phenomenon that occurs during the melting process of PCM and its influence on the heat exchanged in a LHTES cannot be overlooked while sizing a storage system. The Boussinesq approximation is the most used, most simple and most validated approach in literature to account for natural convection and was adopted in most CFD simulations performed during this thesis.

II.2.3. Addition of fins

The previous section focused on the physical phenomena occurring during the phase change process of PCM that influences the thermal behavior of shell-and-tube LHTES. A particular attention was given to explore the available numerical approaches to accurately model each phenomenon. In this section, the focus is placed on another aspect that is crucial to the performances of shell-and-tube LHTES: the addition of fins. By definition, fins refer to extended metallic surfaces that are added within the PCM region to the tube's outer wall. The role of these fins is to increase and regulate the heat transfer surface between the HTF inside

the tubes and the PCM in the shell. Consequently, the main purpose of using fins in a LHTES is to enhance the overall thermal power of the storage that is affected by the low thermal conductivities of the PCM. Fins can take various shapes, configurations, and can be made from a side array of materials. The influence of each parameter on the behavior of the storage should be carefully studied according to the application. The following sub-sections detail and compare different types of pre-existing fins, analyze the parametric studies conducted on the fin geometry configuration, and explore the influence of materials used on the thermal performances of the storage system.

II.2.3.1. Types

Fin types used in LTHES can be classified into two categories: axial and radial types. As their names suggest, axial fins are typically oriented parallel to the main axis of the cylindrical heat transfer tube, while radial fins are oriented radially or perpendicular to the main axis of the tube. A variety of axial and radial fins has been studied in the literature. The most commonly used radial fins include annular profiles [91], [93], perforated [94], [95], pinned [96] and helical fins [97]–[99]. While longitudinal [100]–[102], Y-shaped [103], [104] and snowflake-shaped fins [105], [106] are examples of axial fins. Some examples reported in literature of such fin types are shown in Figure 31 for radial fins and Figure 32 for axial fins.

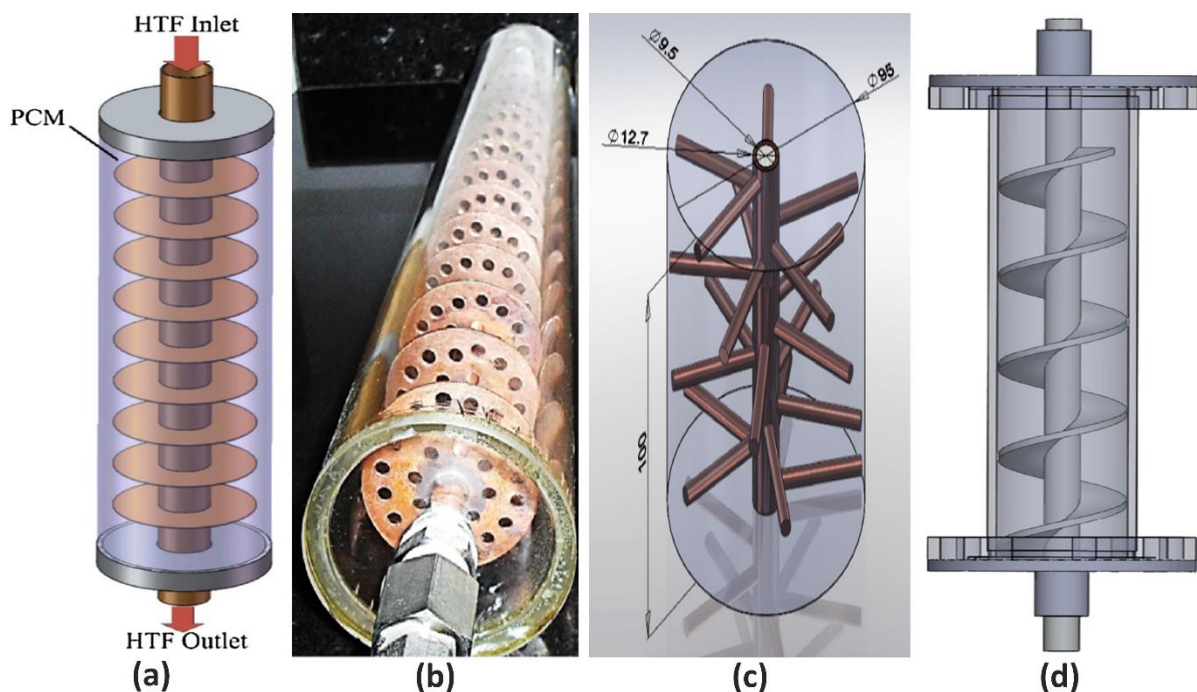


Figure 31. A set of photos and illustrations of different types of radial fins (a) annular [91] (b) perforated [95] (c) pinned [96] (d) helical [98]

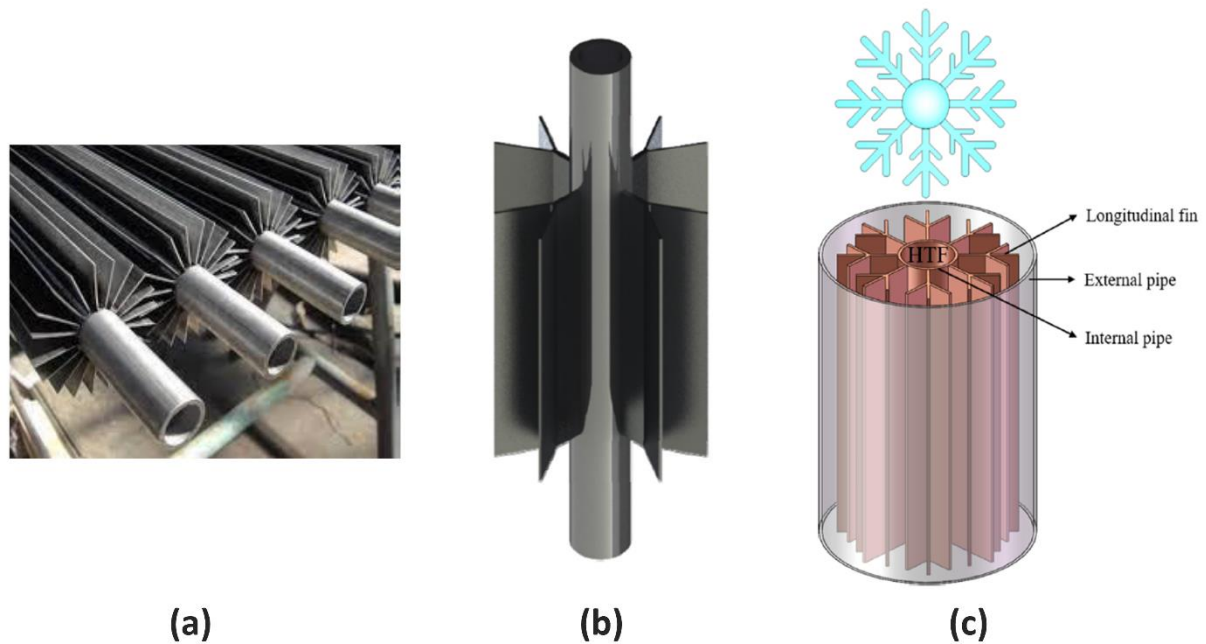


Figure 32. A set of photos and illustrations of different types of axial fins (a) longitudinal (b) Y-shaped [103] (c) snowflake-shaped [106]

The influence of the addition of fins on the thermal performances of LHTES systems was widely demonstrated experimentally [95], [107], [108] and numerically [91], [109]–[112]. This effect has been consistently observed by comparing the results obtained from different configurations with fins to those with smooth tubes LHTES. A smooth-tube TES is a system where no metallic fins are employed to compensate for the low thermal conductivity of the PCM. Therefore, the storage consists of only a heat transfer tube surrounded by a PCM region and the heat is exchanged between the two via the surface area of the tube.

Yang et al. [91] performed a numerical investigation on the influence of annular radial fins on the melting process of a shell-and-tube LHTES (Figure 31(a)). By comparing the outcomes with those of a smooth-tube TES, it was demonstrated that by adding annular fins around the heat transfer tube, the total melting time of the PCM is reduced by 65 %. The enhancement on the thermal performances of the storage during the charging phase due to the addition of annular radial fins was also investigated by Shahsavari et al. [111]. Figure 33 shows the evolution in time of the PCM's liquid fraction obtained by both cases (with and without fins). At any given instant during the melting process, the configuration containing fins results in a higher melted fraction compared to the one with no fins. As a result, the use of finned unit reduces the melting time from 225 minutes to 137 minutes, representing a reduction of approximately 40 %.

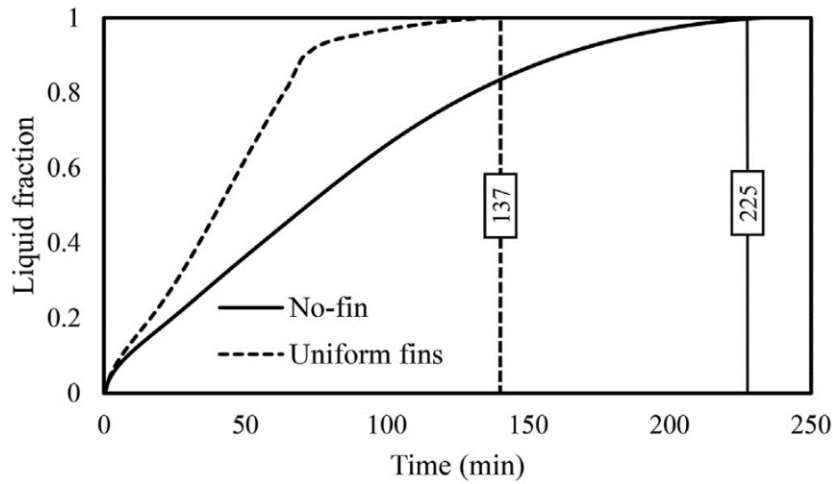


Figure 33. The variation of PCM liquid fraction in terms of time for the finned double-pipe heat storage system compared with the non-finned case during the melting process.[111]

II.2.3.2. Comparison between different types of fins

The use of metallic fins proved to be a reliable technique to improve the heat exchanged in a storage system. Nonetheless, the choice of optimal fin type may vary based on the specific requirements of each application. Numerous comparative studies in the existing literature have examined the thermal performances achieved through the utilization of different types of fins [95], [96], [113], [114]. In an experimental study, Hassan et al. [113] compared the melting process in a vertical LHTES based on two geometric fin profiles, namely, longitudinal and annular. An additional non-finned tube design is considered to assess the improvements due to the addition of fins. Figure 34 provides the main characteristic of the three proposed designs. In all cases, the heat transfer tube is made of steel and has the same dimensions. Additionally, to ensure a comprehensible comparative evaluation, a distinct number of fins was selected for each fin type, ensuring an equal overall fin volume and surface area in both scenarios.

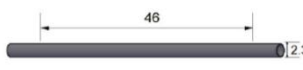

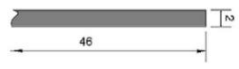
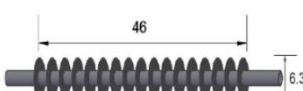

Configuration	Internal tube dimension (cm)	Fins detail		
		Dimensions (cm)	Number	Surface area (cm ²)
Bare tube		-	-	-
Longitudinal finned tube			5	460
Circular finned tube			17	459.1

Figure 34. Specifications of (a) non-finned tube (b) longitudinal-finned tube (c) Circular-finned tube.[113]

Figure 35 shows the evolution in time of the energy released by the HTF during the charging process of the storage. CF and LF stands respectively for circular and longitudinal fins. The same observations made in previous studies discussed earlier about the enhancements due to the addition of any type of fins stands here. Indeed, the integration of fins improves significantly the rate of heat transfer within the storage. Additionally, circular fins results in higher melting rate compared to longitudinal fins. At any given instant during the charging process, the energy released by the HTF in the case where circular fins are used is higher than the corresponding one with longitudinal fins. As a conclusion, despite that longitudinal axial fins being preferable in most engineering systems due to their simple structure and low manufacturing and assembly cost, the thermal performances can be greatly enhanced by switching to circular radial fins.

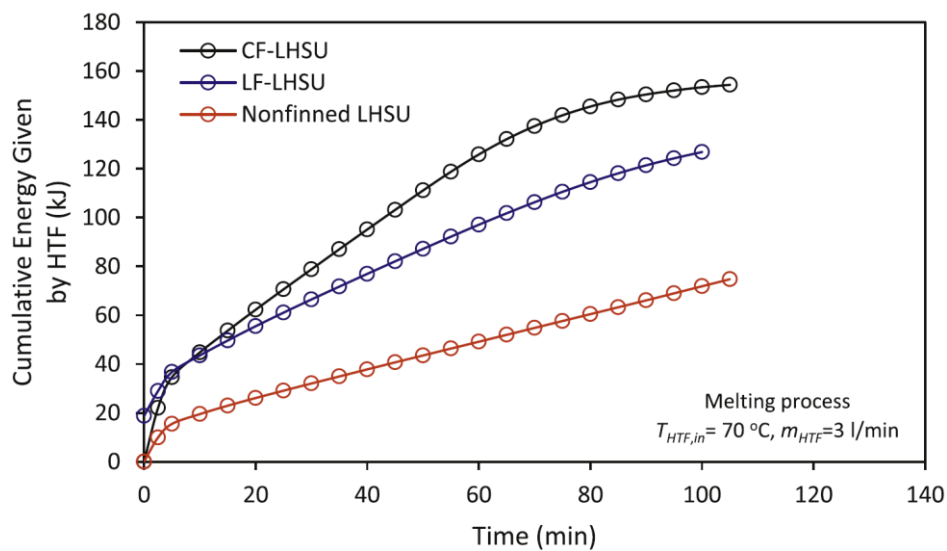


Figure 35. Evolution of the cumulative energy stored during charging process.[113]

In another study, Karami et Kamkari [95] experimentally investigated the effect of perforated fins on the thermal performances of vertical shell-and-tube LHTES systems. The experimental setup was built to study three different configurations as shown in Figure 36: unfinned tube, solid circular and perforated fins. The study focused on the charging phase of the storage (i.e. melting of the PCM) for different working conditions (inlet temperature and flow rate) on the HTF side. The results demonstrated that at initial stages of the melting process, solid circular fins lead to higher heat transfer rate compared to perforated fins, this is mainly due to the higher heat transfer surface conducting heat to the PCM. However, with the melting progress, the effect of natural convection is higher for perforated fins and the heat transfer rate exceeds the one of solid circular fins. As a result, for a fixed working condition, the time-average heat transfer rate of perforated fins is about 10 % higher than that of the solid fins.

Another comparative study of different types of radial fins was carried out by Tay et al. [96]. The performances of annular fins were compared to pinned fins (Figure 37). The investigation was performed using an experimentally validated CFD model. Unlike previous studies, the comparison was conducted based on the solidification process of the PCM. During this process, the influence of natural convection is negligible and heat is mainly transferred by pure conduction. Consequently, annular fins, possessing a greater heat transfer surface compared to pinned fins, yielded a shorter phase change duration.

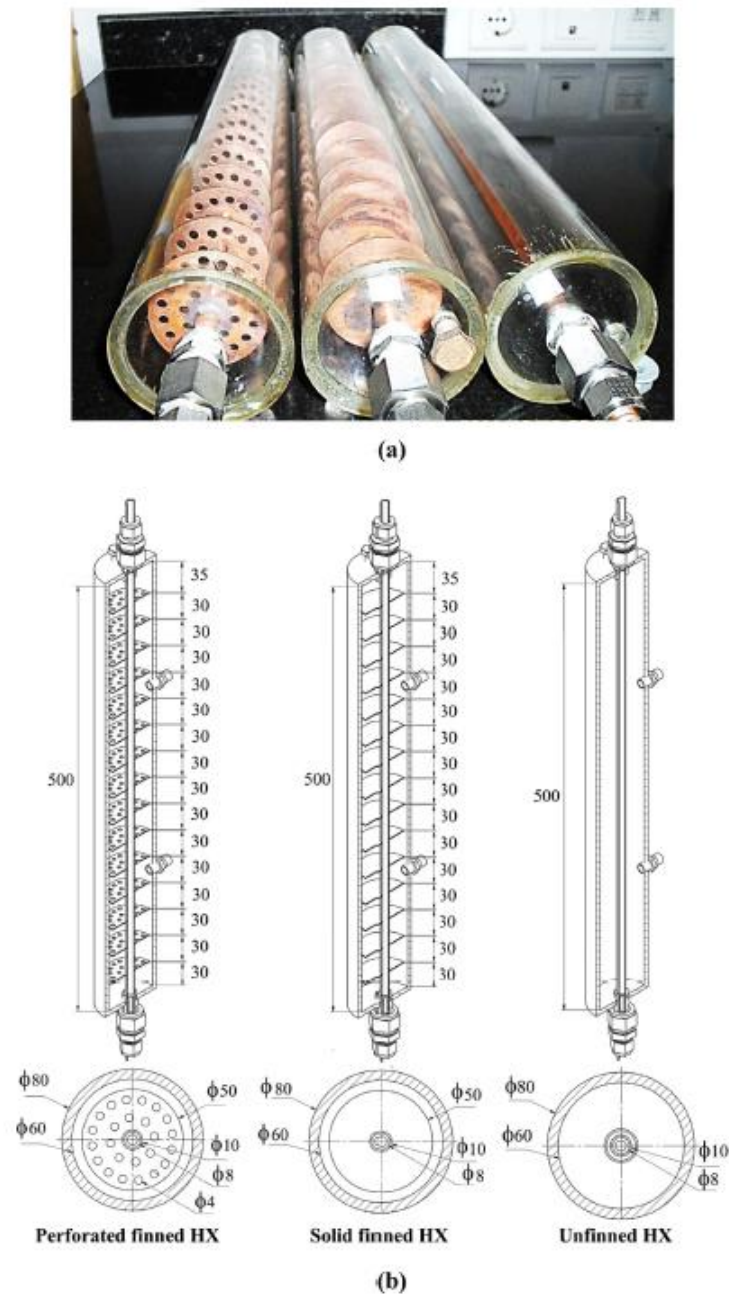


Figure 36. Photograph and the schematic views of the unfinned, solid finned and perforated finned HXs: (a) Photograph of the HXs, (b) Schematic views and dimensions of the HXs (all dimensions are in mm). [95]

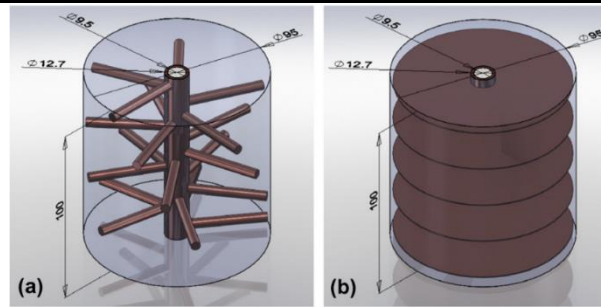


Figure 37. Typical schematic of (a) pinned tube, (b) finned tube [96]

In conclusion, different types of radial fins lead to distinct phase change behavior and thus, affect the thermal power of the storage system. Consequently, the choice of the geometric configuration of fins should be carefully studied to maximize the heat exchange within the storage. Several parametric studies exist in literature with the aim of searching for the optimized fin configuration that leads to the fastest solidification/melting processes.

II.2.3.3. Parametric studies in fin configuration

Yang et al. [91] performed a parametric numerical investigation on the geometric configuration of annular fins. Several geometric parameters were varied for a given fin volume ratio and height. The parameters include:

- Fin number: the number of fins added to the heat transfer tube.
- Pitch: the distance between the centers of two fins in the axial direction (denoted l in Figure 38).
- Thickness: the thickness of each fin (denoted t in Figure 38).

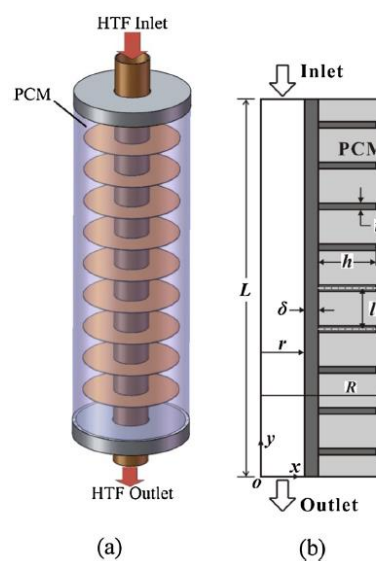


Figure 38. a) Schematic of the shell-and-tube LHTES unit with annular fins; (b) computational domain [91]

The study involved the simulation of the melting process where natural convection is accounted for using the Boussinesq approximation (Section II.2.2.1.3). Figure 39 shows the variation of the total melting time according to the fin number. By definition, the total melting time is time taken to melt the entire PCM volume available in the storage. The results show that, the increase of the fin number from 3 to 31 reduces the total melting time and consequently improves the heat transfer rate and the thermal performances of the storage. In fact, the increase of the fin number leads to higher heat transfer area that enhances heat transferred by conduction between the HTF and the PCM and therefore improve the power of the storage. However, since the fins volume fraction is conserved, this increase in fin number is accompanied by a decrease in thickness and pitch. The decrease in pitch means that the fins are brought closer together leading to a limitation of the enhancements due to natural convection in the melted phase. Consequently, the excessive increase in fin number declines the overall heat transfer rate in the storage and increases the total melting time, as shown in Figure 39 for fin number above 31. In conclusion, the results demonstrated that it is possible to obtain an optimal fin configuration (fin number, pitch and thickness) that maximizes the thermal performances of the storage. This optimal configuration compromises the benefits of increasing the number of fins and natural convection enhancements.

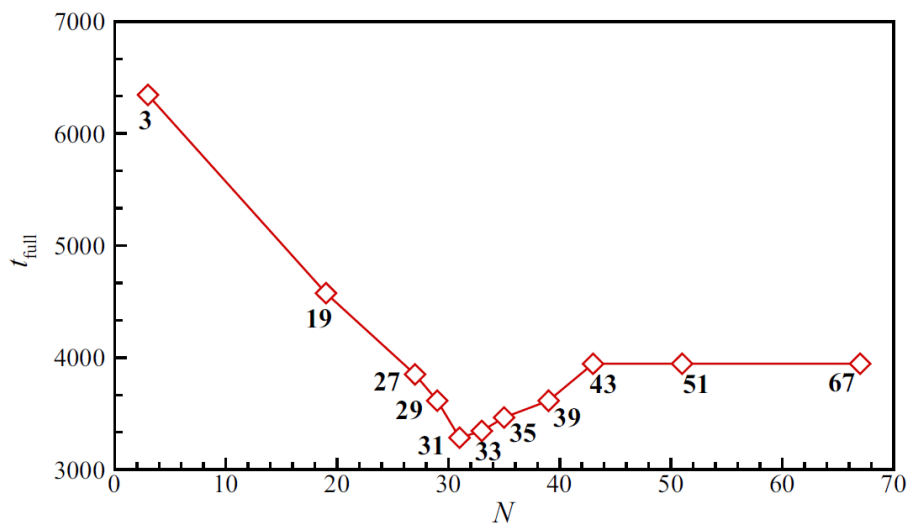


Figure 39. Effect of fin number on the full melting time.[91]

Various parametric studies exist in literature investigating the effect of the configuration of annular fins on the performances of a LHTES. The geometric parameters usually studied are: the fin number, pitch, thickness, diameter, angle and distribution. Table 1 summarizes some of these studies as well as the main observations made.

Study	Tube layout	Parameters investigated	Main observations
Erek et al. [115]	Horizontal	Diameter and pitch	The stored energy increases with increasing fin diameter and decreasing pitch
Guelpa et al. [116]	Vertical	Fin number, fin distribution (uniform vs non-uniform)	The system performance can be improved by either increasing the fin number or by adapting a non-uniform distribution of fins along the heat transfer tube.
Pu et al. [112]	Vertical	Diameter and pitch	By varying the diameter of fins for a constant fin volume fraction and thickness, an optimal diameter is obtained
Shasavar et al. [111]	Vertical	Diameter, thickness and distribution	For non-uniformly distributed radial fins on a vertical tube, the increase of the fins' length over a certain value has no contribution on the PCM's total melting time. This observation suggests that longer fins obstruct the fluid circulations within the melted PCM, which restrains the enhancements of natural convection
Parsazadeh et Duan [117]	Vertical	Pitch and angle	The variation in pitch has no significant effect on the heat transfer rate. However, a positive fin angle with the heat transfer tube enhances natural convection, leading to a faster melting process.
Zhang et al. [118]	Vertical	Pitch	The decrease in fin pitch reduces the total melting time. However, further decrease below a threshold value (10 mm in the study) results in little to no impact on the performances of the storage

Table 1. Studies containing an investigation of geometric parameters of radial fins

II.2.3.4. Fin material

Another essential element that should be carefully studied when designing shell-and-tube LHTES systems is the selection of fin material. In fact, the choice of fin material can hold an influence over the durability, cost-effectiveness as well as the overall thermal performances of the storage system. Different metallic materials possess distinct physical properties, which directly influence the efficiency, heat transfer rate, and overall effectiveness of storage. Therefore, understanding how the choice of fin material affects the thermal performance is essential for optimizing LHTES systems. For instance, the thermal conductivity of the fin material determines how effectively it can transfer heat between the HTF and the PCM region. Therefore, materials with higher thermal conductivity facilitate faster heat transfer, enabling quicker charging and discharging of the TES system. The literature presents several comparative studies on the choice of fin material in a LHTES [106], [118]–[121]. Generally, the most used materials are steel [106], [118]–[120], aluminum [106], [118]–[120] and copper [106], [118]–[121]. Additional materials that could possibly be used include iron [120], graphite [119] and high density polyethylene (HDPE) [118].

Zhang et al. [118] coupled the enthalpy-porosity approach (Section II.2.1.2.3.6) with the Boussinesq approximation (Section II.2.2.1.3) to numerically investigate the effect of fin material on the melting process of a vertical shell-and-tube TES with annular radial fins. The fin materials chosen were copper, aluminum, steel and HDPE. The physical properties, including the thermal conductivity λ , the density ρ and the heat capacity c_p , of the material used are grouped in Table 2.

Properties	HDPE	Steel	Aluminum	copper
λ (W.m ⁻¹ .K ⁻¹)	0.4	16.3	202.4	387.6
ρ (kg.m ⁻³)	950	8030	2719	8978
c_p (J.kg ⁻¹ .K ⁻¹)	2301	502.5	871	381

Table 2. Material properties studied in [118]

For each of the fins material in question, several simulations are performed where in each the pitch between the centers of two fins in the axial direction is varied. As a result, it was found that for a fin pitch larger than 40 mm, fin material has a very little effect on the melting process. Therefore, cheap nonmetallic fins could be used to reduce the cost of investment. However, for lower pitch values, the increase in thermal conductivity of the fin material improves the overall

fin surface efficiency. Although, aluminum and copper fins resulted in similar efficiency, meaning that both materials could achieve almost the same heat transfer rate.

Liu et al. [120] studied the effect of fin materials on the solidification performance of the PCM. Four types of materials were used: stainless steel, iron, aluminum and copper with respective conductivities of 16.2, 47, 202.4 and 387.6 $\text{W}\cdot\text{m}^{-1}\cdot\text{K}^{-1}$. The variation of the solidification time with respect to the thermal conductivity of the fin material is shown in Figure 40. As expected, the solidification time is reduced by around 71.4 % with the increase in the thermal conductivity from that of stainless steel to copper. Consequently, the materials with higher thermal conductivities are preferential in practical applications to enhance the thermal exchanges within the storage.

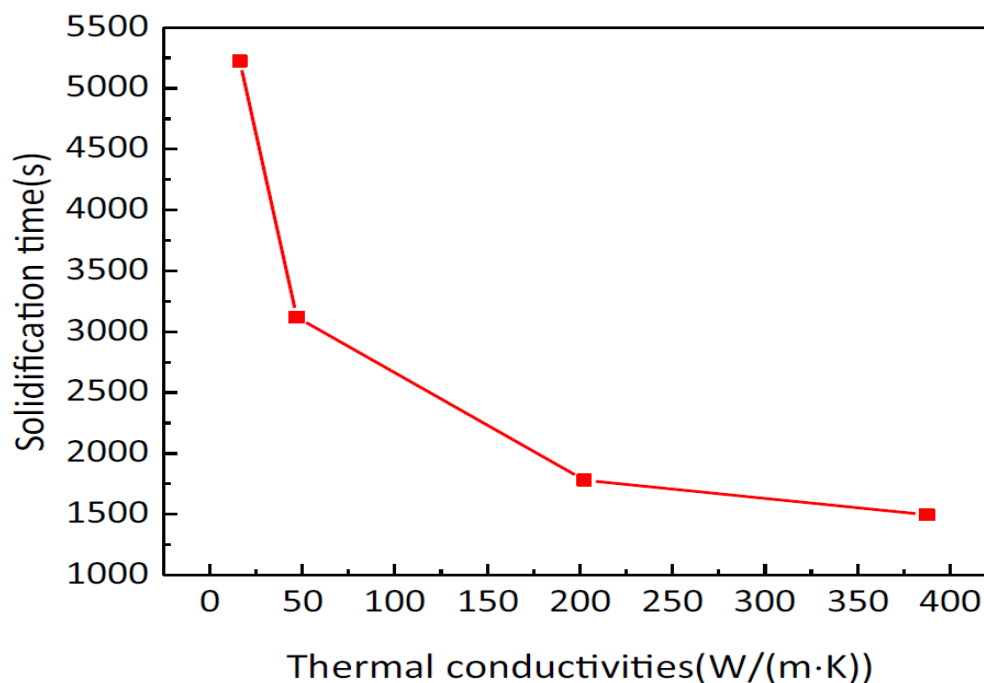


Figure 40. Evolution of the solidification time with different fin thermal conductivities. [120]

Pizzolato et al. [119] argued that the pursue of optimal LHTES systems is a coupled design-material challenge. For an optimal fins configuration, the effect of four distinct materials on the charging/discharging time of the unit was investigated. The fin materials used are steel, copper graphite and aluminum. As a result, by coupling the key thermal properties with the amount of material employed and the specific cost, they were able to rank the four materials accordingly. Consequently, by considering several factors, such as the thermal diffusivity, the volume fraction and the cost per unit volume, it was found that fins made of aluminum outperformed other materials, even the ones with higher thermal conductivities.

Finally, for an optimized thermal performance of LHTES systems, the careful choice of fin type, configuration and material is an essential task that should consider various factors. The literature review established the crucial role of radial metallic fins in improving the thermal performance of vertical LHTES systems. The parametric studies concerning the geometries of radial fins are usually centered on one-dimensional optimization, including the fins' pitch, thickness, height and angle. Additionally, the studies revealed that the impact of natural convection enhancements is substantial and should not be overlooked. However, little research has been devoted to perform a complete parametric investigation on the key factors affecting the thermal behavior of a LHTES. These questions will be further addressed in the following chapters by performing in-depth and complete CFD parametric studies investigating the influence of the physical phenomena within the PCM and coupling the effects of the design and material of fins on the melting process of a vertical shell-and-tube TES.

II.3. Multi-scale modelling approach

Previously in this chapter, several concepts to store steam energy were presented and discussed. Additionally, a special focus was drawn to shell-and-tube storages with PCM. In these systems, the thermal performance during charging and discharging phases depends on various factors, related to both physical phenomena within the PCM and geometric configurations of the storage system. Consequently, an accurate prediction of the behavior of the storage system is essential to ensure an efficient and properly scaled sizing. Generally, the modelling of various physical phenomena within the PCM volume, such as the solid/liquid phase transition, natural convection in the liquid phase and the PCM's volume expansion/shrinkage, on a representative geometry of the storage system (heat transfer tube + fins) is achieved using complex CFD simulations. However, due to their detailed representation of both the physics and the geometry of the storage, transient numerical modelling of the storage operation using CFD codes require, in general, very high computational costs. Such constraint makes it complicated to optimize the performances of shell-and-tube LTHES systems and thus facilitate the integration of this technology in the industry.

One can directly rely on basic numerical models where the complexity of simulating the proper transient operation of the storage is simplified by making assumptions regarding the influence of different factors on the thermal performances of the storage. However, such simplifications can be easily overestimated and might quickly lead to inaccurate predictions of the storage

behavior, resulting in either undersized storages that do not provide the desired performances or oversized storages that are not economically competitive. Therefore, a compromised solution is much needed that couples both aspect: a quick and accurate prediction of the behavior of the storage. Several propositions exist in literature for such numerical models [23], [35], [122]–[129]. In these models, the actual geometry of the PCM and fins domain is generally represented by an effective material with equivalent thermos-physical properties derived from the volume fractions of both the PCM and fins in the corresponding domain. Additionally, heat is assumed to be transferred by pure conduction within the effective material formed by PCM + fins. The effects of physical phenomena involved in the PCM, such as natural convection in the liquid phase, are indirectly taken into account by modifying the thermal conductivity of the PCM (Section II.2.2.1.2). To accurately estimate the corresponding equivalent thermal conductivity for a given case, one needs to rely on data obtained either from experimental studies [23], [125], [128] or from more exhaustive CFD simulations [35], [122]. Thus, a multiscale approach consists of providing information about the heat transferred between the HTF and the PCM during the operation of the storage to a simplified numerical model that can be used to make further predictions on the behavior of the storage. In the following, a brief literature review on different studies that considered a multi-scale approach is presented as well as the limitations they involve.

In an investigation of a pilot scale LHTES at CEA Grenoble, Garcia et al. [23] relied on heat transfer calculations to determine an equivalent thermal resistance that accounts for the effect of fins and inserts on the performances of the storage. However, their approach was based on a pure conductive approach and neglected the effect of natural convection. Vogel et al. [127] developed a pure conductive effective fin model for both radial plate and branched axial fins. In their study, the effective thermal conductivity was estimated from the corresponding volumes of PCM and fins in the domain using a factor of parallelism optimized using trial and error with respect to a discretized model of the representative geometry of fins. The effective thermal conductivity method was also applied by Lacroix [128] to account for the effect of natural convection in the melted phase. The heat transfer correlation considered in the study relied on experimental data and the storage system lacked the presence of metallic fins. Tehrani et al. [122] generalized the effective thermal conductivity method for LHTES systems with no fins while taking into account enhancements due to natural convection in the charging phase. In their study, the investigated parameters were the tube's length, and the external radius of the

PCM domain. Beust et al. [35] developed a predictive approach for the modelling of LHTES with radial fins. The study relied on CFD simulations to calculate heat transfer correlations that takes into consideration the effects of both natural convection and the presence of fins in the PCM domain (Figure 41). By carefully studying the definition of the parameters used in the dimensionless correlation, their approach enabled a local and continuous prediction of the thermal behavior of the storage during charging phase. The calculated correlations are then integrated into a reduced ‘system’ model (Figure 41) to calculate an equivalent thermal conductivity of a purely conductive equivalent material representing the PCM + fins volume. The heat transfer correlations considered different working conditions on the HTF side; however, these correlations were proper for a given geometric configuration of the metallic fins. This approach will be retained as the basis of the studies carried out during this thesis. The following chapters will include further details concerning the corresponding multi-scale modelling approach.

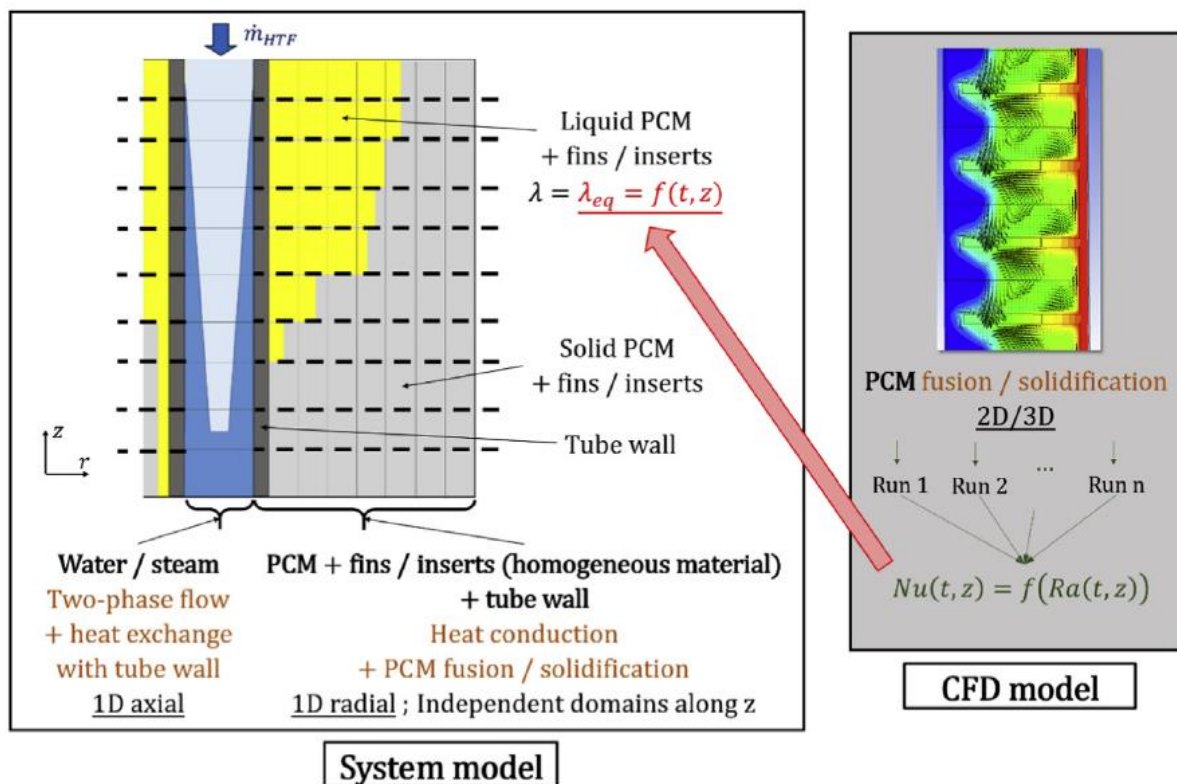


Figure 41. Structure and characteristics of the proposed multi-scale model. [35]

In conclusion, various numerical models exist in the literature to predict the thermal performances of LHTES with convenient computational costs. Despite their utility, those models are often limited in their scope of applicability. Typically, one of three cases applies:

(1) natural convection effects in the liquid phase are not accounted for in the base CFD model [23], [124], (2) the PCM domain does not include metallic fins [122], [128], or (3) the approach is developed for a unique configuration of fins [35], [125].

II.4. Conclusion

Steam is widely used as a heat transfer fluid in industrial processes, as well as for electricity production from renewable resources. Therefore, storing steam energy is essential to achieve carbon neutrality and accomplish the energy transition objectives. Indeed, storing steam is important since it ensures an energy grid stability by providing a buffer during peak demand periods or when energy generation fluctuates. It can also lead to economic benefits by recovering waste heat at high temperatures.

Several technologies for steam storage already exist with steam accumulators being the most mature and widely applied in industrial processes. Steam accumulators carry the advantage of being a relatively simple technology that was extensively been studied over the years. However, this technology has its limitations when it comes to steam generation at constant pressure and for large-scale storages. Alternatives methods consist of storing steam energy via the latent heat of phase change of PCM. The ability of PCM to store and release energy on a narrow temperature range is ideal for two-phase steam applications since it reduces the temperature and pressure differences between charging and discharging phases. Additionally, the significant amount of energy presented in the form of latent heat results in high storage density. Several concepts are proposed to store steam energy in PCM, the most adopted one being the shell-and-tube LHTES systems.

Shell-and-tube LHTES technology is currently at the pre-industrial stage with several prototypes that has been built and tested. In order to ensure its full passage to the industry, several challenges need to be addressed including the various factors influencing the behavior of the storage system during its functioning. Consequently, an accurate prediction of the thermal power of the storage using numerical models is essential for studying and sizing a large-scale storage module. In this chapter, different numerical approaches to simulate the physical phenomena in play on a representative geometry of the storage were presented. For the following investigations, at a CFD scale, the enthalpy-porosity method is retained to model the PCM's solid-liquid phase change problem. This method will be coupled with the Darcy source term method to ensure a zero velocity in the solid state. Additionally, the literature review

demonstrated the influence of natural convection on the melting process. Subsequently, the impact of convective heat transfer will be extensively investigated by comparing the outcomes of CFD simulations with a pure conductive model. In a first place, natural convection will be considered using the Boussinesq approximation in the momentum equation. On the geometric aspect, since a vertical layout is under investigation, radial fins will be the main focus of study. A thorough analysis on the effect of different geometric parameters of fins, such as the length, pitch and thickness will be conducted coupled with different materials.

Finally, a multiscale approach is essential to ensure, at the same time, an accurate and fast prediction of the behavior of the storage. Different approaches existing in literature were presented. In most cases, the equivalent thermal conductivity method is adopted where data from either experimental studies or CFD simulations are collected and used to estimate an equivalent thermal conductivity that can be applied in a computationally simpler pure conductive model to reproduce the exact heat transfer rate within the storage. This approach will be further generalized based on the numerical modelling on two distinct scales each characterized by its own detailed level of representation of the factors influencing the thermal behavior of the storage.

Chapter III – System modelling of LHTES

III.1. Introduction

As discussed in the previous chapter, the thermal performances of shell-and-tube LHTES depend on several factors ranging from diverse physical phenomena within the PCM region, such as natural convection, to the geometry and material properties of highly conducting metallic fins. Hence, to ensure an accurate and reliable sizing of a storage module, the numerical model must consider with precision the contribution of metallic fins on storage system's performance during operation. According to the parametric studies performed in literature and presented in Section II.2.3.3, this contribution is directly influenced by the geometric shape of the fins. Therefore, given the size and complexity of the geometry of fins, numerical models with fine discretization are essential to simulate the influence of fins on the heat transfer process within the storage. Additionally, an equally important factor is the enhancements due to natural convection. During the charging phase, small natural convection loops are formed in the liquid phase that grows during the melting process. The characteristic scale of such loops may be small relative to the dimensions of the storage module. Consequently, the numerical simulation of such phenomenon is only possible using CFD models.

CFD simulations require, generally, substantial computational resources and the development of alternative techniques to accurately size the storage systems seems essential to ensure the integration of such technology in the industry. In this chapter, reduced numerical models of a shell-and-tube steam storage using PCM are developed and tested according to experimental data from a steam storage prototype available at CEA Grenoble. The reduced numerical models are characterized with a less refined mesh compared to the CFD model and they will be tested for a charging phase only, where superheated steam releases its energy in the form of heat to melt the PCM in the shell. In the following, they will be referred to as “system models”. For an accurate prediction of the storage behavior, the system models will rely on the heat transfer data resulted from CFD simulations performed on the corresponding storage module by Beust et al. [35]. Using the results from several CFD simulations, they were able to construct dimensionless heat transfer correlations that accounts for the influence of natural convection as well as the geometry of the fins. The resulted correlation will be used in this study to predict the heat transfer rate between the HTF and the PCM.

In the subsequent sections, the prototype module used in this study will be described, followed by a detailed presentation of the CFD simulations that led to the calculation of heat transfer correlations. Then, two distinct approaches to reproduce the behavior of the storage at the system scale are described. The system models are then tested for the same operating conditions as the prototype. Finally, a comparison is drawn among the outcomes of the numerical models, both internally and against experimental data.

III.2. Description of the prototype

The shell-and-tube LHTES prototype module used in this study is described in detail in this section. Figure 42 shows the module installed at CEA in Grenoble. This prototype is used to store steam energy in the form of latent heat of phase change of a PCM. It is therefore linked to a high pressure and temperature steam generation loop. Consequently, it is possible to experiment on similar working conditions as in DSG solar power plants, as well as in different industrial processes.



Figure 42. Photograph of the prototype module

Teddy CHEDID – 2023

The storage system is composed of a vertical metallic cylindrical shell standing at a height of 5.3 m with a diameter of 55.9 cm. The shell contains a set of 19 heat transfer tubes which are sealed at the top and bottom using metallic plates. During the charging phase, superheated steam is injected from the top into a collector, which ensures an even distribution of the total flow rate within the tubes. A similar collector to the one at the top recovers the water condensed inside tubes at the bottom of the module. The PCM occupies the remaining volume of the shell around the heat transfer tubes. In this module, the PCM used consists of sodium nitrate (NaNO_3) that changes its phase from solid to liquid around 305 °C. The phase change temperature of sodium nitrate makes it a compelling option for electricity production in DSG solar power plants. In these facilities, steam is produced under high pressure of approximately 100 bar; corresponding to a saturation temperature of about 311 °C. Consequently, the selection of an appropriate PCM featuring a phase transition slightly below the steam's saturation temperature is essential for facilitating effective heat transfer mechanisms within the storage system. The module available at CEA contains 1700 kg of NaNO_3 . Additionally, due to the volume expansion/shrinkage that occurs during the PCM's solid-liquid phase transition, the PCM occupies a height of 3.672 m in its solid state and expands to 4.08 meters when in its liquid state.



Figure 43. Photograph of the finned tube (a) prototype module (b) fraction of the tube's length

Figure 43 shows a photo of the finned heat transfer tubes. The cylindrical tubes are made of carbon steel and exhibit an internal diameter of 27.17 mm and a thickness measuring 2.29 mm. Serrated rectangular fins made out of the same material as the tube are inserted at its outer surface. The fins follow a helical pattern with a pitch of 20 mm between the centers of two fins in the axial direction. Each rectangular branch has a thickness of 2.5 mm and occupies an

angular sector of 22.5° around the tube. As a result, a complete pitch around the tube consists of 16 fins. In the radial direction, the total length of the fins spans 30 mm, with 10 mm consisting of a cylindrical base and an additional 20 mm constituting the length of the rectangular extension.

Figure 44 shows the arrangement of the 19 tubes inside the shell. A central tube (numbered 1 in Figure 44) is surrounded by an intermediate crown of six tubes (numbered 2 to 7 in Figure 44). Then, an additional set of 12 tubes (numbered from 8 to 19 in Figure 44) form an external crown. This arrangement ensures a consistent space between the centers of any two tubes.

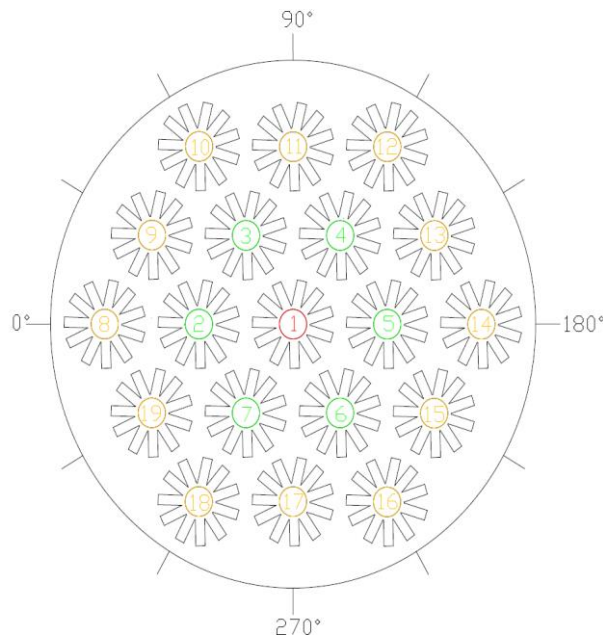


Figure 44. Arrangement of the tubes within the shell of the prototype module

Figure 45 shows the spacing between three adjacent tubes. The distance between the centers of two tubes is 97.2 mm. The PCM volume can be divided into two categories, namely, active and passive PCM. On one hand, active PCM consists of the PCM volume that is around the highly conductive fins. This PCM volume will be the first to undergo melting/solidification during the charging/discharging of the storage. As it is shown in Figure 45, fins are exposed to a substantial portion of the PCM volume situated between the tubes. Additionally, a minor portion of PCM that is not reached by the fins is situated at the central region between adjacent tubes (the orange surface in Figure 45). On the other hand, a passive PCM volume occupies the domain beyond the external crown of tubes, situated at the periphery of the shell (Figure 46). This volume will be the last to melt/solidify during the storage's operating cycle. The total mass of this passive PCM (Figure 46) is about 672 kg, i.e. about 40 % the total PCM mass available in the system.

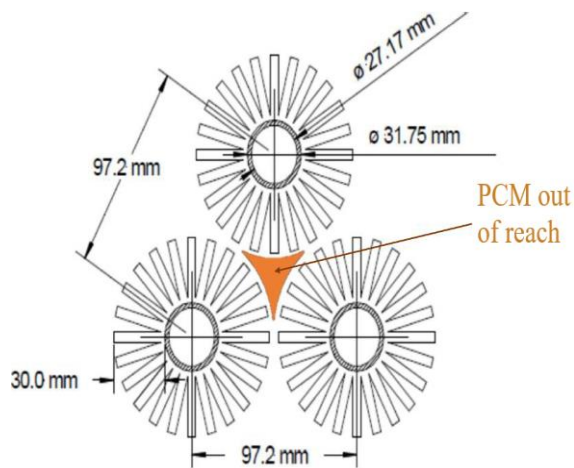


Figure 45. Diagram of the arrangement of three neighboring tubes

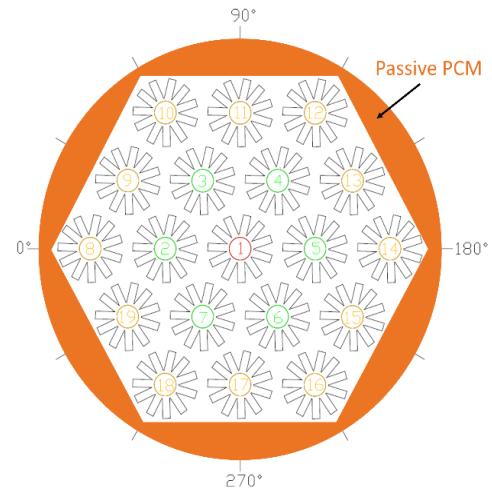


Figure 46 Diagram showing the passive PCM volume at the periphery of the shell

As mentioned earlier, the module is linked to a high pressure and temperature steam loop. The steam pressure can vary between 50 to 120 bar with a maximum possible temperature of 335 °C. Two strategies are considered according to the operation of such storages in industrial processes. The first one corresponds to charging at a *sliding pressure*. As the name suggests, the pressure of steam increases during the charging process. The reason behind this increase is to maintain a uniform thermal power of the storage. In fact, during the charging phase, a PCM melted phase at a relatively higher temperature relative to the initial solid phase is formed around the heat transfer tubes. As a result, the thermal resistance increases in the storage due to the decrease of the thermal gradient between the steam and the surrounding PCM. Therefore, the increase in steam pressure, and accordingly in its saturation temperature compensates for the increase in thermal resistance on the PCM side and ensures a uniform thermal performance in the storage. Consequently, a two-phase liquid water/steam medium occupies the whole length of the tube. The second strategy consists of charging the storage at a *fixed pressure*. The pressure, temperature and mass flowrate of steam is maintained constant throughout the charging phase. As a result, due to the increase in thermal resistance between the HTF and the PCM, the local heat exchanged between HTF and PCM at the top of the tubes decreases progressively. Therefore, a higher length of the heat transfer tube is required in order to condense the steam. Consequently, the water level decreases during a charging process at a fixed pressure.

To evaluate the behavior of the storage, a set of type K temperature sensors are disposed to measure the temperature at different locations. These thermocouples are distributed on seven

horizontal planes along the length of the tubes (Figure 47). At each level, four thermocouples are mounted in the radial direction in the PCM volume at the center plane between two fins, as shown in Figure 48. Among these sensors, three are positioned within the active PCM volume, while the fourth is situated in the portion of PCM between multiple tubes that is not reached by fins. In total, 123 thermocouples are positioned in the PCM volume and can be placed at different angular positions around the same tube.

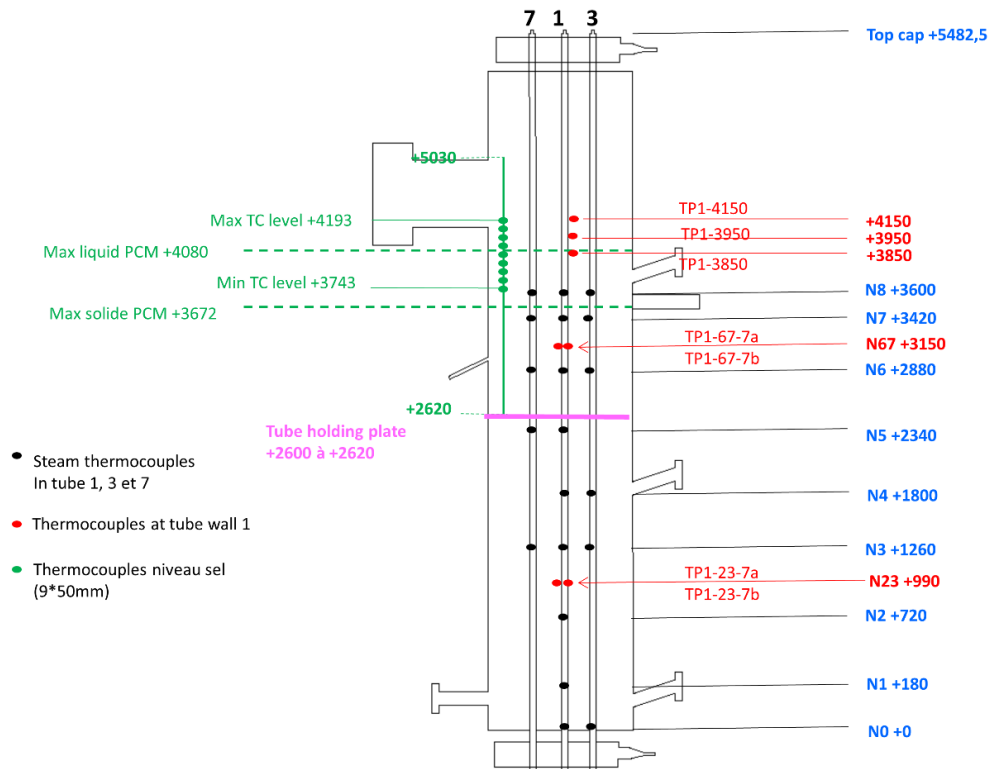


Figure 47. Diagram illustrating the axial positions, ranging from N1 to N7, at which the thermocouples are placed within the PCM of the prototype module

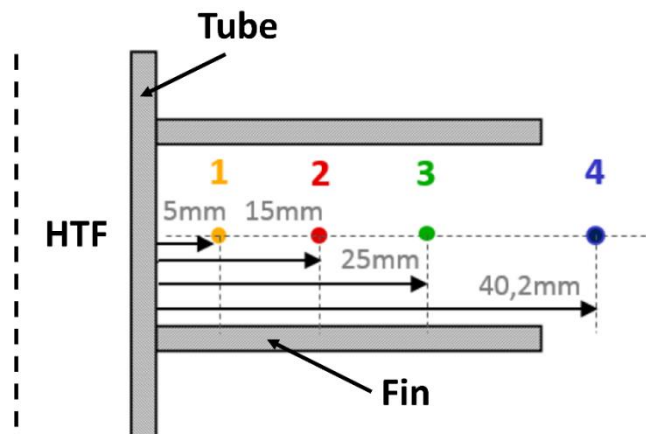


Figure 48. Diagram of the thermocouple placement within the PCM of the prototype module, at a specific level and around a designated tube.

In order to calculate the amount of energy stored or released during the operation of the system, thermocouples are positioned to measure the temperature of heat transfer fluid (liquid water/steam) at the entry and exit of the module. Additionally, temperature measurements are performed inside the central tube and for two other tubes of the intermediate crown (tubes number 3 and 7 Figure 46), at the same level as the temperature measurement within the PCM. Finally, temperature measurements are also carried out at the shell wall, as well as top and bottom plates and collectors.

III.3. Determination of the heat transfer correlations

To successfully predict the behavior of the storage in a pure conductive reduced ‘system’ model, comprehensive insights into the heat transfer mechanism within the system are essential. This information can be obtained either through experimental studies or by performing exhaustive CFD simulations. Heat transfer correlations are required for the corresponding geometry and working conditions of the prototype module described in the previous sections. Such correlations were established in the work of Beust et al. [35], [130] through CFD simulations. The following sub-sections will provide a detailed explanation of both the CFD calculations and the derivation of heat transfer correlations. These correlations will subsequently find application in the ‘system’ models.

III.3.1. CFD model

Figure 49 shows the 3D domain of the prototype module used in the CFD simulations. To reduce computational costs, the domain is constrained to a singular tube along with a single set of fins, selected from the 16 fins encircling the tube's circumference. Consequently, the computational domain consists of an angular section of 22.5° in the azimuthal direction, centered around a serrated fin. In the axial direction, a total of 27 fins are taken into account, corresponding to a tube height of 54 cm.

In the radial direction, the domain is limited between the tube's inner wall and external border on the PCM side. The domain considered is calculated in a way to integrate the volume of the PCM situated between the tubes (cf. orange surface in Figure 45). Consequently, the PCM volume represented in the model correspond to the one occupying the hexagonal layouts in Figure 50. As a result, the radius obtained for the external cylindrical boundary in the CFD model is that for which the cross-section is the same as the hexagon cross-section: 51 mm.

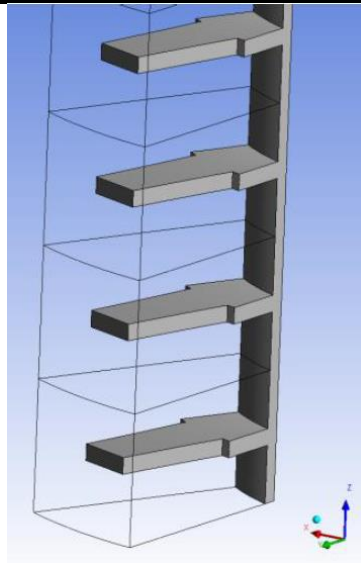


Figure 49. Bottom of the computational CFD model domain [35]

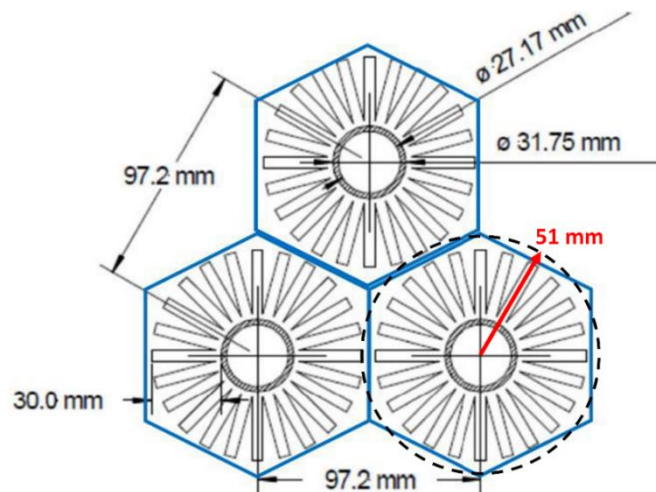


Figure 50. Illustration of the cross-sectional hexagonal tiling to associate PCM zones with various tubes [35]

The domain was discretized using mainly hexahedral meshes, featuring an average characteristic length of 0.83 mm. Mesh independence was assessed by comparing the outcomes with those derived from finer meshes with an average dimension of 0.63 mm [35].

The 3D phase change problem was modeled using the enthalpy-porosity model described in Section II.2.1.2.3.6. The PCM's volume expansion was not taken into account; the density of the PCM was set equal to its value in the liquid state. However, natural convection motions within the liquid phase were factored in using the Boussinesq approximation. Both the cylindrical tube and the radial fins are constructed using carbon steel SA344 Grade 6. The PCM selected is sodium nitrate NaNO_3 . The thermo-physical properties of both carbon steel and sodium nitrate can be found in Table 3, where ρ , β and μ stand for the density, the coefficient

of thermal expansion and the dynamic viscosity of the PCM respectively. L , T_{sol} and T_{liq} are the latent heat of phase change, the solidus and the liquidus temperatures of PCM respectively. While the properties of both materials are assumed to be independent of temperature, the specific heat capacity (c_p) and thermal conductivity (λ) values are dependent on the state of the PCM.

Material	Steel	NaNO ₃ [131]–[134]
ρ [kg.m ⁻³]	7764	1927
β [K ⁻¹]	-	3.8 10 ⁻⁴
c_p [J.kg ⁻¹ .K ⁻¹]		
solid	542.8	1813
liquid	-	1704
λ [W.m ⁻¹ .K ⁻¹]		
solid	50.33	0.72
liquid	-	0.515
μ [Pa.s]	-	2.8 10 ⁻³
L [kJ.kg ⁻¹]	-	173.3
T_{sol} [°C]	-	303.3
T_{liq} [°C]	-	306.6

Table 3. Material properties for steel and sodium nitrate

Initially, the heat transfer tube, the fins and the PCM region are at the same temperature of 290°C. Consequently, the PCM is in solid state. The HTF flow inside the tube is not directly simulated in the CFD model: to simulate the charging process of the storage, constant and uniform temperature boundary conditions, exceeding the melting temperatures of the PCM are imposed on the internal wall of the heat transfer tube. Finally, simulations were performed using ANSYS Fluent v.17.2 [135]. Three cases were studied to establish the heat transfer correlations, each characterized by a distinct temperature at the tube's inner wall. The chosen temperatures are 310 °C, 318 °C and 328 °C.

III.3.2. Heat transfer correlations

Generally, convective heat transfers are described using correlations between dimensionless numbers such the Nusselt number (denoted Nu) and the Rayleigh number (denoted Ra). By definition, the Nusselt number represents a ratio of convective to conductive heat transfer at a boundary in a fluid. The Rayleigh number is associated with buoyancy-driven flow. Numerous

studies concerning natural convection flows consider a correlation between those two dimensionless numbers structured as follows:

$$Nu = CRa^n \quad (32)$$

where C and n are coefficients with values depending on the studied system. For the heat transfer between the metallic parts formed by the tube's wall and fins with the PCM region, Nu and Ra are respectively calculated as follows:

$$Nu = \frac{\varphi}{S_e(T_{hot} - T_{cold})} \frac{l_c}{\lambda_{PCM,l}} \quad (33)$$

$$Ra = g \left(\frac{\beta}{\mu D_{th}} \right)_{PCM} (T_{hot} - T_{cold}) l_c^3 \quad (34)$$

Where $\lambda_{PCM,l}$ is the thermal conductivity of the liquid phase of the PCM. φ , S_e and T_{hot} are respectively the total heat flux, area and temperature of the heat transfer tube's inner wall. The definition of the characteristic length l_c and temperature T_{cold} should be carefully selected in order to assure a correlation between Nu and Ra as proposed in Equation (32). Beust et al. [35] investigated the outcome using several definitions of l_c and T_{cold} and they demonstrated that during the charging phase of the storage, l_c and T_{cold} should be defined as the average thickness and temperature of the liquid PCM layer and are therefore, calculated respectively as follows:

$$l_c = -R_{t,ext} + \sqrt{R_{t,ext}^2 + (R_{ext}^2 - R_{t,ext}^2) \overline{f_m}} \quad (35)$$

$$T_{cold} = \overline{T_{PCM,l}} = \frac{\sum_{i=1}^{nb \text{ PCM cells}} f_{m,i} \rho_i V_i c_{p,i} T_i}{\sum_{i=1}^{nb \text{ PCM cells}} f_{m,i} \rho_i V_i c_{p,i}} \quad (36)$$

Where $R_{t,ext}$ and R_{ext} are, respectively, the radii of the tube's outer and the external domain. $\overline{f_m}$ is the average PCM's melted fraction in a given volume. It is calculated according to the local melted fraction in each cell:

$$\overline{f_m} = \frac{\sum_{i=1}^{nb \text{ PCM cells}} f_{m,i} \rho_i V_i}{\sum_{i=1}^{nb \text{ PCM cells}} \rho_i V_i} \quad (37)$$

The definition of l_c does not distinguish between both PCM and fins volumes, and it assumes a cylindrical shape for the melting front separating the liquid from the solid phase. A more generalized definition, adapted for different shape and configurations of fins is developed in

the subsequent chapter V. The average temperature \overline{T}_{PCM_l} is determined by dividing the enthalpy of the liquid PCM within all the cells of the representative domain by its thermal capacity.

Both l_c and T_{cold} depend on the PCM's melted fraction and their values vary during the melting process. As a result, a continuous relationship between the dimensionless numbers Nu and Ra can be established throughout the entire charging phase. This facilitates the development of a correlation that accurately replicates the heat transfer rate based on the real-time condition of the storage, rather than relying on an averaged estimate.

The three CFD simulations with different temperature boundary conditions on the tube's inner wall result in the evolution of Nu values with respect to Ra values plotted in Figure 51. The collection of points appears to cluster around two curves, with some points between their bounds. The observations made by Beust et al. [35] can be summarized as follows. During the melting process, Nu and Ra values increase from zero tracing the trajectory of 'Curve 1' in Figure 51. Then, upon the end of PCM's melting, the entire PCM is in liquid state in a given sub-domain around the fins, the data points (Ra, Nu) transition to follow 'Curve 2'. The charging of the sensible heat in the liquid PCM continues until the temperature of the PCM reaches the imposed temperature on the tube's inner wall. During this phase, thermal resistance increases within the storage, resulting in a decline of both Nu and Ra values until they converge at zero as the charging phase concludes.

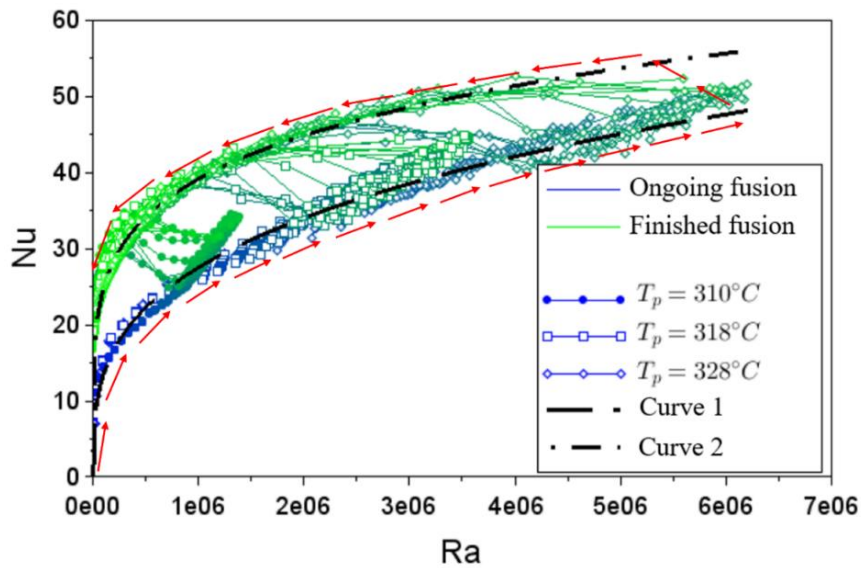


Figure 51. (Ra, Nu) scatter points obtained from CFD results for the definitions of l_c and T_{cold} presented in Equations (35) and (36) [35]

The respective equations for both curves are given as follows [35]:

$$Nu_1 = 0.402 Ra^{0.306} \quad (38)$$

$$Nu_2 = 2.614 Ra^{0.196} \quad (39)$$

Finally, to ensure a continuous formulation of the heat transfer correlation and to avoid oscillations and unstable behaviors in the reduced numerical models, the transition between the two proposed expressions is obtained through a linear interpolation between Nu_1 and Nu_2 :

$$Nu = \begin{cases} Nu_1 & \text{for } \bar{f}_m < 0.98 \\ \frac{1 - \bar{f}_m}{0.02} Nu_1 + \frac{\bar{f}_m - 0.98}{0.02} Nu_2 & \text{for } 0.98 < \bar{f}_m < 1 \\ Nu_2 & \text{for } \bar{f}_m = 1 \end{cases} \quad (40)$$

Finally, this correlation will be integrated to the system models to reproduce the exact heat transfer rate predicted by the CFD model. In the following sub-sections, two distinct approaches to solve the phase change problem and integrate the heat transfer correlation to estimate the impact of the geometry of fins and natural convection enhancements in the liquid will be described, tested and validated with experimental data from the prototype module described earlier in this chapter.

III.4. Description of the system models

The main feature of system models lies in their representation of the entire storage system. Unlike the CFD model described in the previous section, wherein a temperature boundary condition at the inner wall of the tube substituted the two phase liquid water / steam flow, the system models represent and account for the effects of this flow. Furthermore, system simulations encompass the complete length of the storage rather just a segment, as in the case of the CFD model.

Figure 52 shows the different parts of a system model that will be described in this section. The inside volume of the heat transfer tubes is discretized in the axial direction. For each elementary volume, a connected sub-domain is considered to account for the heat transfer mechanisms within the storage. Consequently, a mesh representing the thickness of the tube's wall is linked to each elementary volume of the two-phase flow. However, these sub-domains remain unconnected in the axial direction. Regarding the PCM + fins region, two distinct approaches are developed to address the PCM's phase change problem, including the related latent heat,

the influence of natural convection, and the impact of fins' geometry effects on the heat exchanged occurring within the storage system. The first one denoted '1D radial' Figure 52(a), involves discretizing the domain in the radial direction. Within each mesh, an equivalent material represents both the PCM and fins in the region. The effects of natural convection and geometry of fins is taken into account by adjusting the thermo-physical properties of the equivalent material accordingly. On the other hand, the second approach, denoted '0D radial' (Figure 52 (b)), revolves around predicting the heat flux exchanged at the tube's wall between HTF and PCM region without the need to discretize the domain.

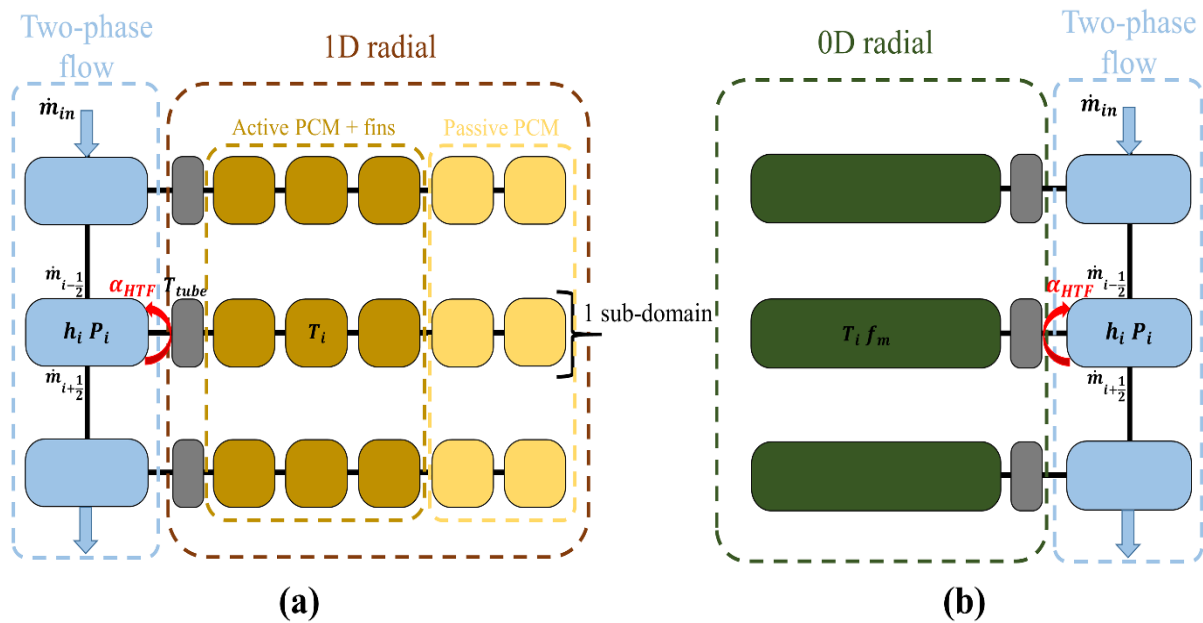


Figure 52. Diagram of the possible discretization of the system models (a) 1D radial (b) 0D radial

Both the '1D radial' and '0D radial' approaches will be coupled with the two-phase flow model to simulate the performance of the prototype storage system outlined in section III.2. Each of these models will be elaborated in further detail in the subsequent sections.

III.4.1. Two-phase flow

A two-phase liquid water/steam flow is present within the tubes. During charging phase, superheated steam is injected from the top that condenses inside the tubes. The interior of the tube is discretized in the axial direction (blue cells in Figure 52). The two-phase flow is modelled using a homogeneous approach. In each mesh, both liquid and gaseous phases are supposed to have the same temperature and the same velocity. Additionally, heat transfer by conduction in the axial direction, as well as the effects of the gravity, viscosity and pressure

drops are neglected. In fact, pressure drops were measured on the prototype module that will be used to validate this model. Experimental measures resulted in a pressure difference of less than 0.4 bar between the entry and exit of the tube. For the working pressure levels ranging from 60 to 120 bar, this pressure drop corresponds to less than 0.6 % and less than 0.4 °C regarding the variation of the saturation temperature, which makes it reasonable to neglect pressure drop to simplify the numerical model. Consequently, the partial differential equations system solved for the two-phase flow constitutes the mass and energy conservations, which are defined respectively as follows:

$$\pi R_{t,int}^2 \frac{\partial \rho_{HTF}}{\partial t} + \frac{\partial \dot{m}_{HTF}}{\partial z} = 0 \quad (41)$$

$$\pi R_{t,int}^2 \rho_{HTF} \frac{\partial h_{HTF}}{\partial t} + \dot{m}_{HTF} \frac{\partial h_{HTF}}{\partial z} = 2\pi R_{t,int} \alpha_{HTF} (T_{t,int} - T_{HTF}) \quad (42)$$

Where \dot{m}_{HTF} is the mass flow rate of the two-phase flow. T_{HTF} and h_{HTF} are the temperature and enthalpy of the heat transfer fluid (liquid water/steam in this case) respectively. And $R_{t,int}$ and $T_{t,int}$ are respectively the radius and temperature of the tube's inner wall. ρ_{HTF} is the density of the heat transfer fluid, and it is calculated according to the densities and fractions of each phase present in the volume:

$$\rho_{HTF} = \epsilon \rho_v^{sat} + (1 - \epsilon) \rho_l^{sat} \quad (43)$$

With ϵ being the local void fraction. By supposing equal velocities for both liquid and gaseous phases, the void fraction ϵ can be obtained from the vapor mass fraction x_{vap} as follows:

$$\epsilon = \frac{1}{1 + \frac{1 - x_{vap}}{x_{vap}} \frac{\rho_v^{sat}}{\rho_l^{sat}}} \quad (44)$$

In Equation (42), α_{HTF} corresponds to the heat transfer coefficient between HTF and the inner wall of the heat transfer tube. In order to account for the effect of the two-phase flow regime on the heat transfer at the inner wall level, α_{HTF} is calculated using adapted correlations [136]–[142].

Finally, the assumption that both liquid water and steam phases have the same speed may not be physically accurate. Indeed, during the charging phase, steam starts condensing near the tube's wall leaving a gaseous phase in the middle of the tube, this phenomenon is called *film condensation*. Consequently, both phases may move at different speeds. The same applies for discharging, where gaseous bubble that are less dense than neighboring liquid molecules are

formed and may have different velocities. Here, the difference in velocities is not represented in order to be able to use a homogenous model that is simple and sufficient to estimate the water level inside the tubes and the heat transferred to the PCM via the tube's wall.

III.4.2. Tube

The metallic tube (gray cells in Figure 52) may be discretized to multiple radial volumes, where the initial volume is linked to the HTF, and the final one connected to the PCM. Heat transfer is neglected in the axial direction. The height of each element within its respective sub-domain matches the height of the corresponding HTF volume. As a result, the only equation to solve is the following conductive heat equation:

$$\rho_{tube} c_{p_{tube}} \frac{\partial T_{tube}}{\partial t} = \lambda_{tube} \Delta T \quad (45)$$

III.4.3. PCM + fins: 1D radial

The first approach toward modelling the heat transfer mechanisms in the PCM and fins regions consists of discretizing the domain into elementary volumes in the radial direction (Figure 52). However, within the prototype module detailed in section III.2, a distinction was made between two types of tubes. The first type, referred to as central tubes, consists of those encircled by six adjacent tubes (cf. tubes 1 to 7 in Figure 44). The second type, called peripheral tubes, constitutes the outermost crown of tubes positioned near the shell boundary (cf. tubes 8 to 19 in Figure 44). Regarding the central tubes, the CFD model (Figure 49) encompassed the fins, the active PCM region, and even the smaller passive PCM region between the tubes (Figure 50). As a result, the correlation derived in (40) can be employed for estimating the heat transfer rate between HTF and the storage region. On the other hand, the peripheral tubes are enveloped by a passive PCM volume, which remained unaccounted for in the CFD simulations (refer to Figure 46). To ensure an accurate prediction of the overall storage system's behavior, it is essential to introduce this distinction into the numerical system model. This distinction allows for the inclusion of both central and peripheral tube categories, contribution to a comprehensive representation of the system's dynamics.

III.4.3.1. Central tubes

In the case of central tubes, an equivalent material, formed by both PCM (solid and/or liquid) and fins, fills the annular space encircling the heat transfer tube. This annular space is characterized by an internal radius, denoted as $R_{t,ext}$ in Figure 53 and an external radius

represented by R_{ext} . The specific values of $R_{t,ext}$ and R_{ext} remain consistent with those employed in the CFD model, that is to say 13.587 mm and 51 mm, respectively. Heat transfer along the axial direction has been disregarded, so the sub-domains within the system are not interconnected along this direction. Consequently, the domain is discretized to ‘m’ elementary volume in the radial direction.

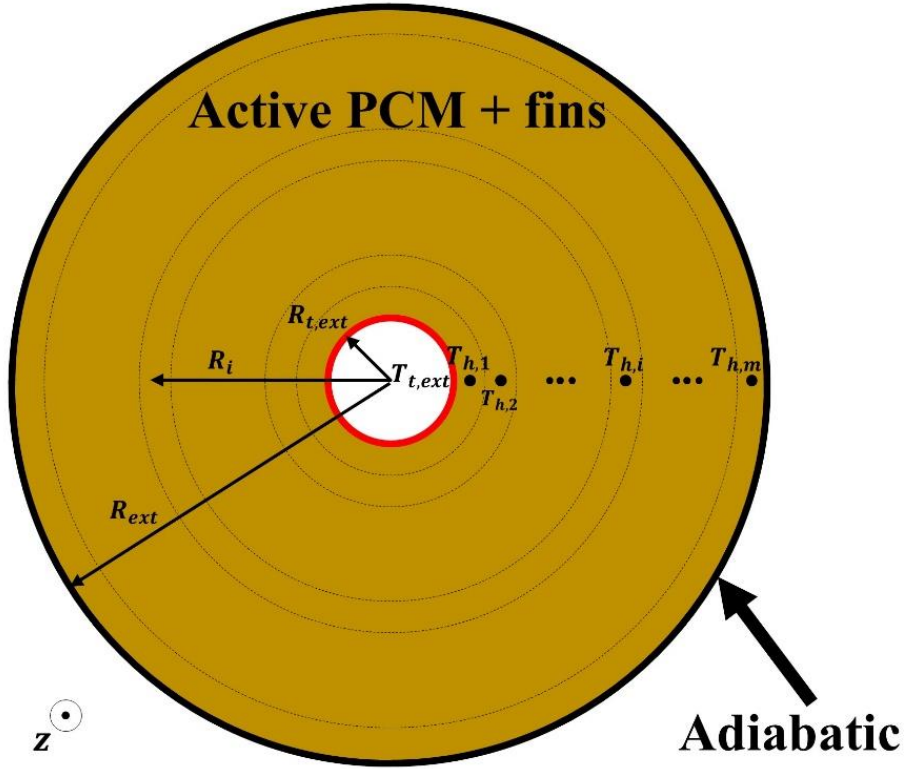


Figure 53. Cross-sectional view of the discretized active PCM + fins domain used in the 1D radial model

Energy equation is solved using a conductive approach, with an equivalent thermal conductivity to account for convective effects in the homogeneous material formed by PCM and fins. Consequently, the only equation to solve is the following heat equation:

$$\rho_h c_{p_h} \frac{\partial T_h}{\partial t} = \nabla(\lambda_{eq} \nabla T_h) \quad (46)$$

In each volume, the PCM and fins are supposed to have the same temperature T_h . ρ_h and c_{p_h} denote the density and specific heat of the equivalent (PCM + fins) material. Their expressions take into account the corresponding mass and volume fraction of each material and are calculated as follows:

$$\rho_h = x_v \rho_{PCM} + (1 - x_v) \rho_{fins} \quad (47)$$

$$c_{p_h} = x_m c_{p_{PCM}} + (1 - x_m) c_{p_{fins}} \quad (48)$$

Where ρ_{PCM} and ρ_{fins} are respectively the densities of the PCM and the fins, their values are identical to the ones used in the CFD model (Table 3). x_v and x_m are respectively the volumetric and mass fraction of the PCM within the corresponding volume. The values of these parameters can be calculated according to the distribution of both fins and PCM volumes along the radial direction. For the serrated fins presented in section III.2, three distinct regions represent the computational domain, according to the radial position ‘ R ’ (Figure 54):

1. $R_{t,ext} < R < R_{t,ext} + 0.01 \text{ m}$: The fins are composed of a cylindrical base with a length of 1 cm and a thickness of 0.25 cm. The thickness of the domain around the fins in the axial direction is 2 cm. Consequently, the PCM volume fraction ‘ r ’ in this space is:

$$r = \frac{7}{8} \quad (49)$$

2. $R_{t,ext} + 0.01 < R < R_{t,ext} + 0.03 \text{ m}$: the fins are made of a rectangular section with a height of 2 cm, width of 0.8 cm and a thickness of 0.25 cm. Given the cylindrical geometry of the domain, the PCM volume fraction is calculated as follows:

$$r(R) = 1 - \frac{16 \times 0.008 \times 0.0025}{0.02 \times 2\pi R} \quad (50)$$

3. $R_{t,ext} + 0.03 < R < R_{ext}$: this region corresponds to the annular space exceeding the tip of the fins, where only PCM occupying the volume, therefore:

$$r = 1 \quad (51)$$

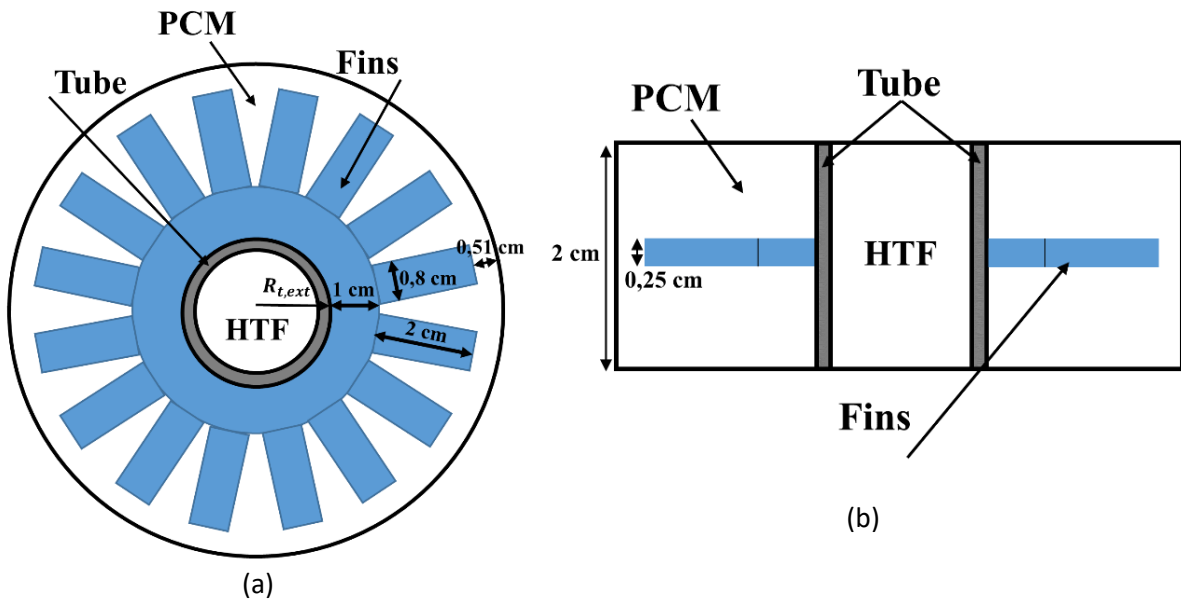


Figure 54. Illustrations of the presence of fins in a given sub-domain (a) radial cross-section view (b) axial cross-section view

In the numerical model, the calculation of the volumetric fraction of PCM x_v is achieved for every elementary volume using the trapezoidal method (Figure 55). Given the small thickness of each annular cell, a linear approach is adopted. This approach enables the computation of the average PCM volume fraction in each elementary volume x_{v_i} based on the ratio r , that varies in the radial direction.

$$x_{v_i} = \sum_{k=1}^m \frac{1}{m} (R_{1_k} r(R_{1_k}) + R_{2_k} r(R_{2_k})) \quad (52)$$

with $m = 10$, R_{1_k} and R_{2_k} are calculated respectively as follows:

$$R_{1_k} = R_{i-\frac{1}{2}} + \frac{k-1}{m} (R_{i+\frac{1}{2}} - R_{i-\frac{1}{2}}) \quad (53)$$

$$R_{2_k} = R_{i-\frac{1}{2}} + \frac{k}{m} (R_{i+\frac{1}{2}} - R_{i-\frac{1}{2}}) \quad (54)$$

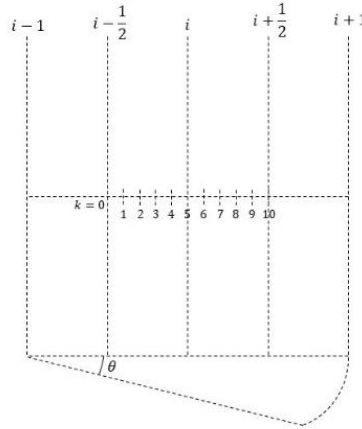


Figure 55. Illustration of the trapezoidal method

Finally, the PCM's mass fraction is calculated as follows:

$$x_m = \frac{\rho_{PCM}}{\rho_h} x_v \quad (55)$$

The phase change problem is modelled using the equivalent specific heat capacity method. To keep the consistency with the modelling of the phase change in the CFD model, this equivalent capacity is in accordance with Equations (7) and (14) from the previous Chapter. Therefore, the specific heat capacity of PCM used in Equation (48) is defined as follows:

$$c_{p_{PCM}} = \begin{cases} c_{p_{PCM_s}} & \text{if } T_h < T_{sol} \\ \frac{L}{T_{liq} - T_{sol}} + \frac{c_{p_{PCM_s}} + c_{p_{PCM_l}}}{2} & \text{if } T_{sol} \leq T_h \leq T_{liq} \\ c_{p_{PCM_l}} & \text{if } T_h > T_{liq} \end{cases} \quad (56)$$

$c_{p_{PCM_s}}$, $c_{p_{PCM_l}}$ and L are the specific heat capacity of the solid and liquid phases of PCM and its pure latent heat (energy required to change the phase of the PCM at an isothermal temperature).

Lastly, as mentioned before, the influence of the fins geometry and of natural convection enhancements on the behavior of the storage is taken into account by introducing an equivalent thermal conductivity λ_{eq} to the heat equation (46). In each elementary volume, λ_{eq} accounts for the presence of both solid and liquid phases according to a parallel arrangement. Consequently, it is calculated as follows:

$$\lambda_{eq} = f_m \lambda_{eq_l} + (1 - f_m) \lambda_{eq_s} \quad (57)$$

The PCM's melted fraction f_m varies between 0 and 1 and is calculated according to the temperature of the homogeneous material PCM + fins in the volume T_h :

$$f_m = \frac{T_h - T_{sol}}{T_{liq} - T_{sol}} \quad (58)$$

λ_{eq_s} accounts for the volumetric fraction of each material in the solid volume.

$$\lambda_{eq_s} = x_v \lambda_{PCM_s} + (1 - x_v) \lambda_{fins} \quad (59)$$

λ_{eq_l} is calculated from the correlation developed using CFD simulations (Equation (40)). The main principle relies in equating the total heat flux predicted by the correlation to the one transferred by conduction through the liquid PCM layer around the tube. This layer constitutes the space between the tube's outer surface and the melting front, which is characterized by a temperature T_{PC} matching the phase change temperature of the PCM. Additionally, this melting front resides at a radial distance l_c from the tube's wall. Therefore:

$$\varphi = \frac{Nu S_e (T_{tube} - \overline{T_{PCM_l}}) \lambda_{PCM_l}}{l_c} \quad (60)$$

$$\varphi = 2\pi dz \lambda_{eq_l} \frac{T_{tube} - T_{PC}}{\ln\left(1 + \frac{l_c}{R_{t,ext}}\right)} \quad (61)$$

Where dz corresponds to the length of the domain in the axial direction. T_{PC} is the average phase change temperature. The characteristic length l_c and temperature $\overline{T_{PCM_l}}$ are calculated using the same expressions as those utilized in CFD model, defined by equations (35) and (36). As a result, the equivalent thermal conductivity λ_{eq_l} is expressed as follows:

$$\lambda_{eq,l} = \lambda_{PCM1} \frac{T_{tube} - \overline{T_{PCM1}}}{T_{tube} - T_{PC}} \frac{R_{t,ext}}{l_c} \ln \left(1 + \frac{l_c}{R_{t,ext}} \right) Nu \quad (62)$$

Finally, in the case of central tubes, the external boundary of the domain situated at the radius R_{ext} is treated as adiabatic.

III.4.3.2. Peripheral tubes

The prototype module presented in section III.2 contains 672 kg of passive PCM at the periphery of the shell. To simplify the geometry occupied by this fraction of PCM in the numerical model, the passive PCM volume is uniformly distributed around the 12 peripheral tubes resulting in an annular layer of thickness 13.83 mm (Figure 56). In terms of volume, this additional layer corresponds to around 49 % of the total PCM + fins volume occupying the domain in peripheral tubes. Within the active PCM + fins region, an identical homogeneous material is considered, mirroring the approach adopted for central tubes. Furthermore, the equivalent governing equation and numerical approaches used to address the influences of fin geometry and natural convection are upheld, just as in the case of central tubes.

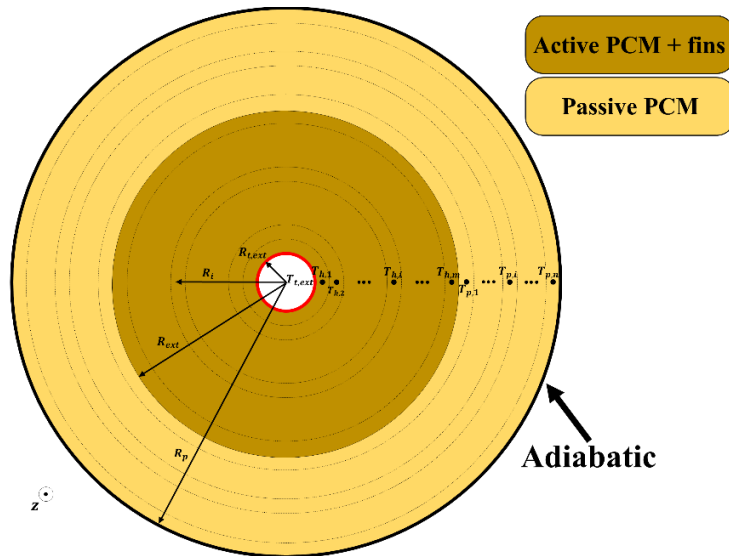


Figure 56. Cross-sectional view of the discretized active PCM + fins and the passive PCM domains used in the 1D radial model

The passive PCM layer is discretized in radial direction to ‘n’ elementary volumes as shown in Figure 56. Since there are no available data on the heat transfer in this region, it is supposed that heat is only transferred by conduction and the only equation to be solved is the following heat equation in cylindrical coordinates:

$$\rho_{PCM} c_{pPCM} \frac{\partial T_{PCM}}{\partial t} = \nabla(\lambda_{PCM} \nabla T_{PCM}) \quad (63)$$

Where $c_{p_{PCM}}$ is calculated using the same expression adopted for central tubes (Equation (56)).

Finally, the external boundary of the domain situated at the radius R_p (Figure 56) is considered adiabatic and heat losses are not taken into account in the numerical model.

III.4.4. PCM + fins: 0D radial

The 1D radial model was obtained by discretizing in the radial direction the annular domain around the heat transfer tubes, and formed by an equivalent material representing the PCM and fins. Then, the influence of natural convection and the presence of fins on the heat transfer rate is taken into account by modifying the thermo-physical properties of the equivalent material according to data collected from fine CFD simulations. However, it is important to remember that the primary purpose of conducting numerical simulations at the system scale is to predict the heat flux exchanged between the HTF and the PCM. Furthermore, considering that the heat transfer correlation derived from CFD simulations (referred to as Equation (40)) relies on the Nusselt number, which enables a straightforward prediction of the heat flux at the tube's wall, one could envision a simplified 0D approach radially in the storage. This approach eliminates the need for discretization of the PCM + fins region.

This approach introduces a unique set of challenges. For instance, accurately calculating the Nusselt number using the correlation of Equation (40) requires precise computation of the Rayleigh number. This value is directly linked to characteristic parameters like the average thickness of the liquid PCM layer (l_c) and the average temperature ($\overline{T_{PCMl}}$). By definition, these parameters vary during the charging process, and their variations depends on the storage state. Consequently, the ability to anticipate their values from general data within each sub-domain becomes crucial for effectively using the heat transfer correlation in a 0D approach. This, in turn, enables an accurate replication of the heat transfer rate within the storage system. In the following, a 0D approach in the radial direction to predict the heat exchanged at the tube's wall during the charging phase of the storage is thus described. Unlike the 1D radial approach, this model does not account for the presence of passive PCM located at the shell's periphery. This is because in this model, the heat exchanged between the HTF and the PCM + fins region is directly computed at the tube's wall using heat transfer correlations. The CFD model used to derive these correlations overlooks the passive PCM volume located at the shell's periphery. Consequently, the impact of this passive PCM volume's melting on the thermal power of the

storage is not encompassed within the correlation, making its representation challenging within a 0D approach.

In this approach, the charging process is segmented into multiple phases, each defined by the temperature at the tube's external surface and the local melted fraction of the PCM within each sub-domain, signifying the state of the storage.

1. For $T_{t,ext} < T_{PC}$ and $\overline{f_m} = 0$: the charging phase is in its initial stage, the entire volume of the PCM is in solid state (Figure 57). The temperature level of the tube's outer surface remains insufficient to initiate the PCM melting process. Therefore, the energy exchanged between the HTF and the PCM + fins region is transferred by pure conduction in the radial direction and serves in increasing the average temperature of the solid phase $\overline{T_{solid}}$.

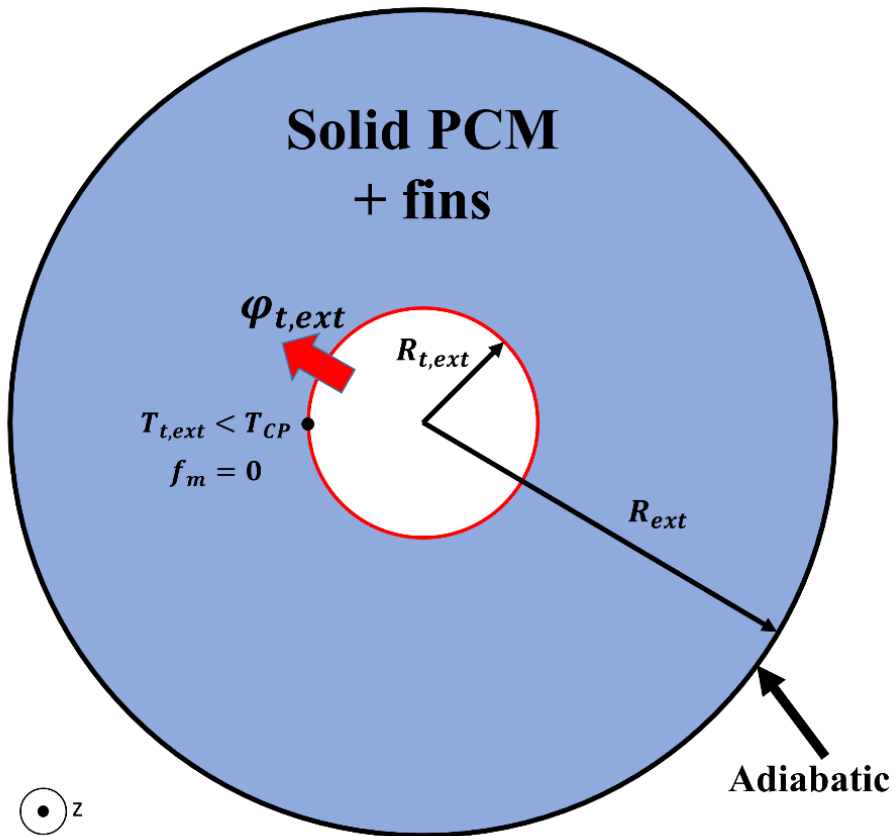


Figure 57. Cross-sectional view of the 0D radial domain for $T_{t,ext} < T_{PC}$ and $\overline{f_m} = 0$

As a result, the corresponding equations of state are written as follows:

$$\varphi_{t,ext} = \frac{2\pi dz \lambda_{h,s}}{\ln \frac{R_{ext} - R_{t,ext}}{2R_{t,ext}}} (T_{t,ext} - \overline{T_s}) \quad (64)$$

$$\varphi_{t,ext} = m_h c_{p_{h,s}} \frac{\partial \bar{T}_s}{\partial t} \quad (65)$$

$$\varphi_s = \varphi_{t,ext} \quad (66)$$

$$\varphi_l = 0 \quad (67)$$

$$\varphi_{latent} = 0 \quad (68)$$

Where $\varphi_{t,ext}$ corresponds to the total heat flux exchanged at the external tube surface. φ_s and φ_l are the heat fluxes within the PCM solid and liquid volumes, respectively. These fluxes correspond to the sensible heat associated with the temperature increase of the PCM in accordance with its state. φ_{latent} is the latent heat flux related to the PCM's solid-liquid phase transition.

In Equation (65), m_h and $c_{p_{h,s}}$ are respectively the total mass of PCM + fins and the average specific heat capacity of the equivalent storage material. Consequently, m_h is calculated according to the overall mass fraction of each material in the domain:

$$m_h = \frac{x_v}{x_m} \rho_{PCM} \pi (R_{ext}^2 - R_{t,ext}^2) dz \quad (69)$$

x_v and x_m are respectively the overall PCM volume and mass fraction. In the 1D radial approach, these factors were calculated individually within each cell, accounting for the presence of PCM and fins. In the 0D radial approach, a global approach is adopted. Therefore, in the geometric domain considered in both the CFD model and the 0D radial system model, the values of X_v and X_m are 0.9362 and 0.7847 respectively. $c_{p_{h,s}}$ is calculated in the same way by considering the mass fraction of both PCM and fins:

$$c_{p_{h,s}} = x_m c_{p_{PCM_s}} + (1 - x_m) c_{p_{fins}} \quad (70)$$

2. For $T_{t,ext} > T_{PC}$ and $0 < \bar{f}_m < 1$: charging of the latent energy. The temperature at the tube's external wall exceeds the PCM's phase change temperature: it initiates the melting process of the PCM. As a result, both solid and liquid phases of PCM, separated by a melting front, are present in the domain (Figure 58). During this phase, the total heat flux $\varphi_{t,ext}$ can be directly determined using the correlation of Equation (40). However, this heat flux is split into a sensible component, responsible for heating the solid and liquid fractions of the domain, and a latent component that drives the progression of the melting front along the radial direction from the tube's outer wall towards the farthest external boundary of the computational domain.

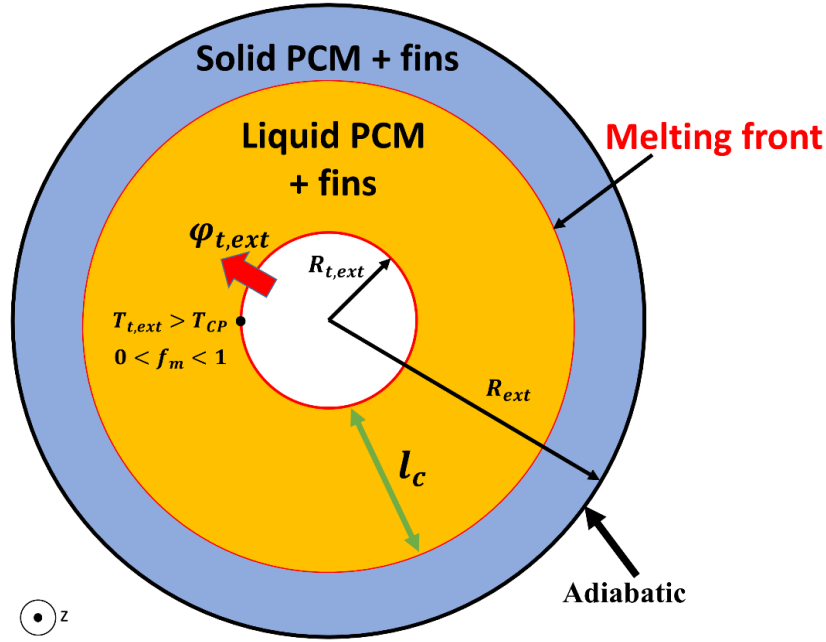


Figure 58. Cross-sectional view of the 0D radial domain for $T_{t,ext} > T_{PC}$ and $0 < f_m < 1$

Consequently, the equations of state are represented as follows:

$$\varphi_{t,ext} = 2\pi dz R_{t,ext} (T_{t,ext} - \overline{T_{PCM_l}}) \frac{\lambda_{PCM_l}}{l_c} Nu \quad (71)$$

$$\varphi_s = \frac{2\pi dz \lambda_{h,s}}{\ln \frac{R_{ext} + R_{t,ext} + l_c}{2R_{t,ext} + l_c}} (T_{PC} - \overline{T_s}) \quad (72)$$

$$\varphi_s = m_h (1 - \overline{f_m}) c_{p,h,s} \frac{\partial \overline{T_s}}{\partial t} \quad (73)$$

$$\varphi_l = m_h \overline{f_m} c_{p,h,l} \frac{\partial \overline{T_{PCM_l}}}{\partial t} \quad (74)$$

$$\varphi_{latent} = \varphi_{t,ext} - \varphi_s - \varphi_l \quad (75)$$

$$\varphi_{latent} = \frac{\partial}{\partial t} (x_m m_h L \overline{f_m}) \quad (76)$$

As shown in Figure 58, the solid fraction is limited between the melting front and the external boundary of the domain where an adiabatic condition is applied. Consequently, the average temperature $\overline{T_{solid}}$ can be calculated from the heat flux in the solid region φ_{solid} . However, on the liquid phase side, the average temperature $\overline{T_{PCM_l}}$ remains unknown, requiring the introduction of an additional equation for its prediction. Therefore, saying it differently, it is worth highlighting that the development of a non-discretized model in the radial direction calls for the integration of a secondary heat transfer correlation. The aim of such correlation is to

estimate the heat flux exchanged between the liquid fraction and the melting front. In this study, the progression of the average temperature of the liquid state $\overline{T_{PCM_l}}$ throughout the melting process is derived from a correlation (6th degree polynomial) that has been developed using prior CFD simulations:

$$\overline{T_{PCM_l}} = 234.2\overline{f_m}^6 - 564.9\overline{f_m}^5 + 492\overline{f_m}^4 - 181.6\overline{f_m}^3 + 29.6\overline{f_m}^2 - 2.8\overline{f_m} + 308.69 \quad (77)$$

The evolution of the average temperature of the liquid PCM phase according to the melted fraction $\overline{f_m}$ obtained by CFD simulations and the correlation presented in Equation (77) is shown in Figure 59.

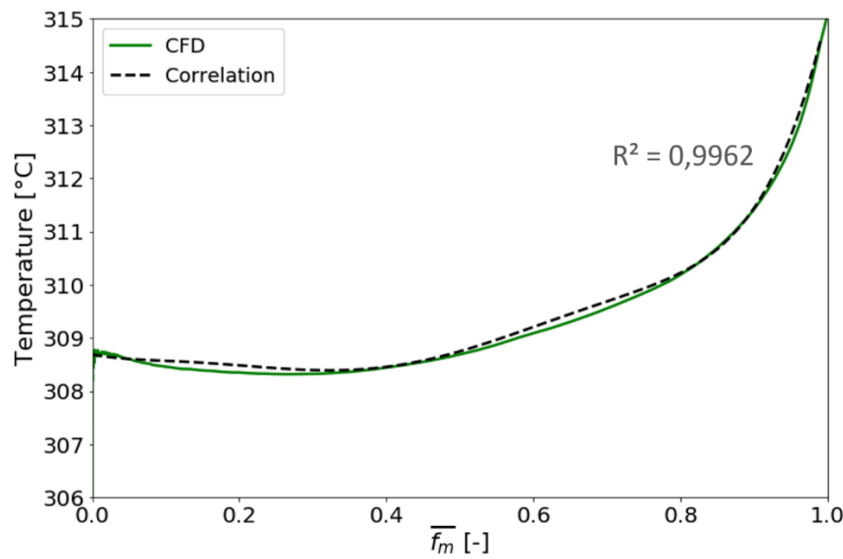


Figure 59. Evolution of the average temperature of the liquid PCM phase according to the melted fraction for both the CFD results and the correlation of Equation (77)

In Equation (75), the latent heat φ_{latent} is determined by subtracting the solid and liquid heat fluxes φ_s and φ_l from the total heat flux $\varphi_{t,ext}$. The resulting flux contributes to the evolution of the PCM's melted fraction $\overline{f_m}$. This fraction is subsequently employed in the next iteration to estimate the average length of the liquid phase l_c , as per Equation (35), which in turn leads to the computation of the updated heat flux values.

3. For $T_{t,ext} > T_{PC}$ and $\overline{f_m} = 1$: the entire PCM volume has melted. The characteristic length l_c is equal to the radial thickness of the PCM + fins domain defined by $R_{ext} - R_{t,ext}$. The charging of sensible energy continues within the remaining liquid PCM until its temperature reaches the threshold temperature of $T_{t,ext}$ (Figure 60). The total heat flux $\varphi_{t,ext}$ can still be determined using the Nusselt correlation (Nu_2 in Equation (40)):

$$\varphi_{t,ext} = \varphi_l = 2\pi dz R_{t,ext} (T_{t,ext} - \overline{T_{PCM_l}}) \frac{\lambda_{PCM_l}}{l_c} Nu \quad (78)$$

$$\varphi_l = m_h c_{p,h,l} \frac{\partial \overline{T_{PCM_l}}}{\partial t} \quad (79)$$

$$\varphi_l = \varphi_{t,ext} \quad (80)$$

$$\varphi_s = 0 \quad (81)$$

$$\varphi_{latent} = 0 \quad (82)$$

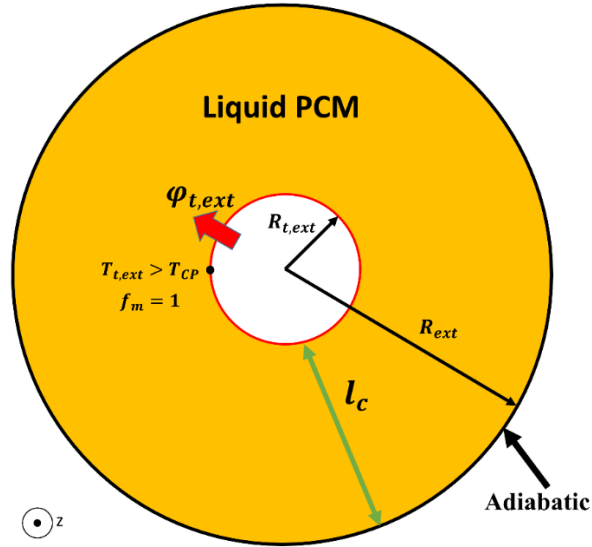


Figure 60. Cross-sectional view of the 0D radial domain for $T_{t,ext} > T_{PC}$ and $f_m = 1$

III.5. Application case

III.5.1. working conditions

Both 1D radial and 0D radial approaches were coupled with the two-phase flow model to form two system models. These models were tested according to the charging phase of the prototype module described in section III.2.

The testing case corresponds to a charging phase at a constant pressure (105.1 bar). The corresponding saturation temperature at this pressure is around 315 °C. Initially, the tube is filled with liquid water at a temperature of 286 °C. During the charging phase, superheated steam, at a slightly higher temperature than the saturation temperature is injected in the tubes from the top at a constant mass flow rate of 0.02 kg/s. The superheated steam releases its energy to melt the PCM situated around the tubes at the top of the shell. With the melting progress, thermal resistance increases within the storage. This rise in thermal resistance leads to a reduction in the heat transfer rate from the steam to the PCM. Consequently, due to the lack of

corresponding increases in pressure, flow rate, or temperature of the injected steam, which would otherwise counterbalance this rise in thermal resistance, the length of tube required so that the steam releases all its energy and condensate increases.

Figure 61 shows the distribution of the HTF temperature at different instants along central tubes of the tested prototype module. The values are recovered at different levels from the set of thermocouples shown in Figure 47. One should recall that thermocouples are positioned at the center of the tubes. This means that, in the case of film condensation, they measure the temperature of the steam rather than that of the liquid water in the film. At initial stages, at $t = 0.1$ h, the two thermocouples positioned above the tube's height of 3 m provide a HTF temperature of around 315 °C, which underlines the existence of superheated steam in the fraction of the tube. Then, a transition to liquid water occurs at a tube's height of around 3 m where the temperature of the HTF is around 285 °C for the entire volume below this level. With the melting progress, the fraction of tube occupied by steam (resp. liquid water) increases (resp. decreases), as shown by the drop in water level within the tube. Finally, at $t = 2.5$ h, the thermocouple positioned at the bottom of tube registers a temperature of 315 °C, indicating that the entire volume of the tube has become occupied with superheated steam. This measurement implies that the heat transfer rate towards the PCM is insufficient to ensure the condensation of the steam. Usually, this is because the charging process has ended and the PCM is in liquid state at the threshold temperature of the injected steam.

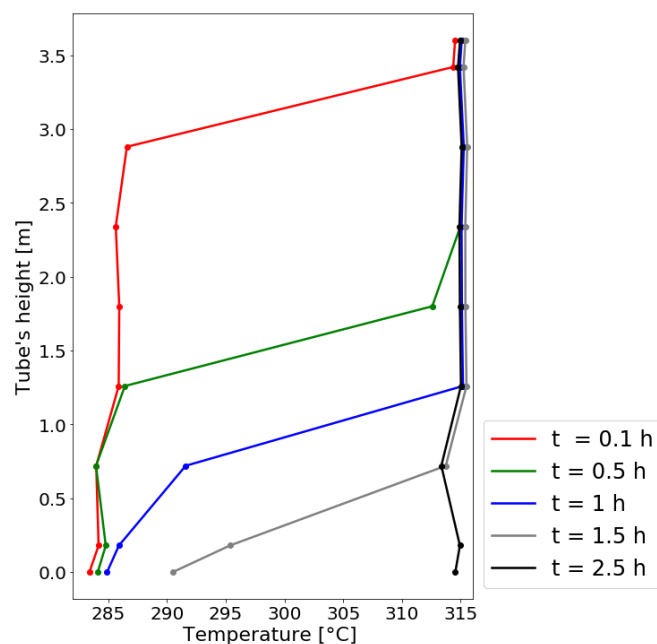


Figure 61. Distribution of the temperature of the HTF along the heat transfer tube

Finally, numerical simulations were performed using the Dymola software. For both system models, the two-phase flow inside the tubes is discretized to 20 elementary volumes. The numerical settings, as well as the geometric parameters for the system models are summarized in Table 4.

Two-phase flow inside the tubes		
Tube length		4.08 m
Discretization	Number of meshes	20
	Length in axial direction dz	0.204 m
Initial temperature		286.1 °C
Pressure		105.1 bar
Thickness of the tube's wall		
Internal radius $R_{t,int}$		13.585 mm
External radius $R_{t,ext}$		15.875 mm
Discretization	Number of meshes	1
	Length in radial direction dr	2.29 mm
1D radial		
External radius of fins + active PCM R_{ext}		51 mm
External radius of passive PCM R_p		69.83 mm
Discretization of fins + active PCM	Number of cells 'm'	20
	Length in radial direction dr	2.55 mm
Discretization of passive PCM	Number of cells 'n'	3
	Length in radial direction dr	6.276 mm

Table 4. Parameters of the system model for the prototype module

III.5.2. Energy stored

The thermal power of the storage system during the charging phase is a crucial factor for assessing the performance of a LHTES. This information can be obtained by examining the changes in overall stored energy within various components of the system. The following subsections detail the methods for calculating accumulated energy in the storage system, both in the experimental trial and with the numerical models, as well as a detailed comparison between the outcomes of the different approaches.

III.5.2.1. Experimental trial

In the experimental trial of the prototype module available at CEA Grenoble, the total energy released by steam during a charging phase is distributed according to the Sankey diagram shown in Figure 62. A considerable share of the steam energy is accumulated as latent heat in active

and passive PCM, as well as sensible heat in both the PCM and the metallic part formed by the tube and fins. An additional amount of energy is accumulated within various solid containment parts existing in the storage, including the plates, the top and bottom collectors and the shell material. Finally, a proportion of energy is dissipated and lost due to unavoidable heat exchanges with the surroundings.

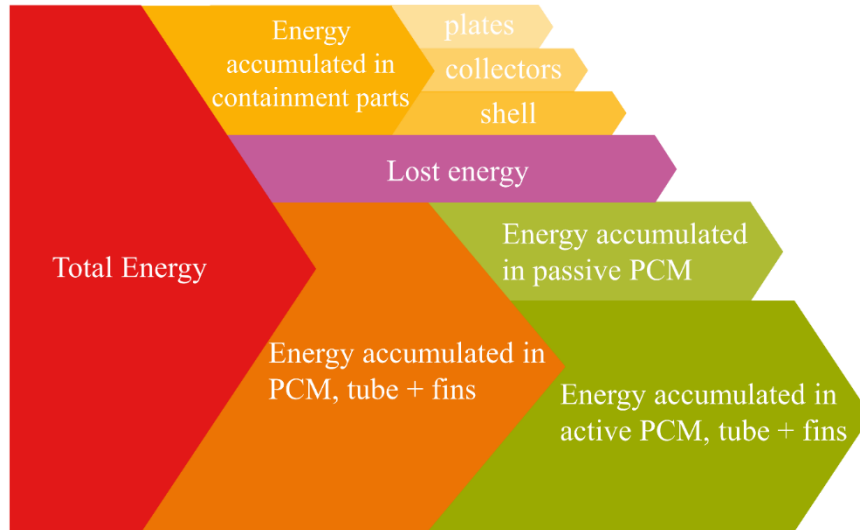


Figure 62. Sankey diagram of the distribution of energy in various parts of the prototype module (thickness of different fractions is not to scale)

Experimentally, the *total energy* is derived by applying an energy balance between the inlet and outlet of the HTF. This technique enables the calculation of the thermal power transferred within the modules, therefore leading to an estimation of the overall energy released by the steam. Consequently, the total energy transferred from the HTF (E_{tot}) between $t = 0s$ and an instant t is expressed as follows:

$$E_{tot} = \int_0^t \dot{m}_{HTF}(h_{in} - h_{out})dt \quad (83)$$

Where \dot{m}_{HTF} is the mass flow rate of the HTF. h_{in} and h_{out} are the enthalpy of the HTF at the inlet and outlet of the module, respectively.

The *lost energy* refers to the energy that the module dissipates into its surrounding environment. To quantify this heat loss, the module is equipped with heating elements strategically placed on the exterior of its shell. These heating elements generate heat by converting electrical energy, warming both the PCM and the module itself—achieving this without the need for steam circulation through the tubes. Despite the presence of thermal insulation on the outer shell,

notable heat losses occur due to the substantial temperature difference between the module's shell and the ambient air. To measure these losses, specialized tests were conducted. In these tests, the module's temperature remains constant through precise regulation of the dissipated electrical power. Once a state of equilibrium is attained, the thermal power lost to the external environment equals the electrical power required to uphold that temperature. For the entire module, a thermal loss coefficient of $\Omega_{loss} = 11.5 \text{ W} \cdot \text{K}^{-1}$ was determined. This coefficient is based on the temperature difference between the shell and the surrounding air. Consequently, the lost energy between $t = 0\text{s}$ and an instant t is calculated as follows:

$$E_{lost} = \int_0^t \Omega_{loss} (T_{shell} - T_{ambient}) dt \quad (84)$$

The *energy accumulated in containment parts* is determined from the temperature measurements of these elements. For each element, the accumulated energy between $t = 0\text{s}$ and an instant t is calculated as follows:

$$E_{cont} = m_{cont} c_{p_{cont}} (T_{cont} - T_{cont}(t = 0\text{s})) \quad (85)$$

Where $c_{p_{cont}}$ corresponds to the thermal capacity of steel, Its value is considered constant, $c_{p_{cont}} = 542.8 \text{ J} \cdot \text{kg}^{-1} \cdot \text{K}^{-1}$. The symbol m_{cont} represents the mass of individual solid components. For instance, the shell has an overall mass of 678 kg, each of the two collectors carries a weight of 140 kg and both plates contribute to 45 kg each. Eventually, the total energy accumulated in solid constituents is obtained by summing the contributions from each element, as derived from Equation (85).

Finally, the energy stored within the HTF itself is minimal; therefore, its contribution is disregarded. The total energy accumulated in the tube's wall, fins, active and passive PCM volume is deduced as follows:

$$E_{acc} = E_{tot} - E_{loss} - E_{cont} \quad (86)$$

Figure 63 illustrates the evolution of different energy factions described above throughout the charging of the storage system. The energy level within the storage is set at zero at initial stage. As the charging progresses, the total energy released by steam progressively increases. However, the rate at which energy changes (i.e. the thermal power of the storage), as represented by the slope of the curve in Figure 63, decreases as the charging progresses. This is related to the fact that steam is injected at constant pressure. Regarding the PCM, tube and

fins regions, the stored energy curve exerts a similar shape to the total energy curve. However, the gap between the two curves expands as the charging phase proceeds. This discrepancy results from the increase in lost energy and in the accumulated energy in other solid components of the storage. Indeed, the lost energy to the surroundings follows a linear evolution with respect to time during the charging phase, signifying a uniform heat loss rate from the storage. After $t = 8$ h, the ratios to the total energy of each the lost energy, the energy accumulated in solid parts and the energy accumulated in PCM, tube + fins regions are 18.6 %, 2.8 % and 78.6 %, respectively.

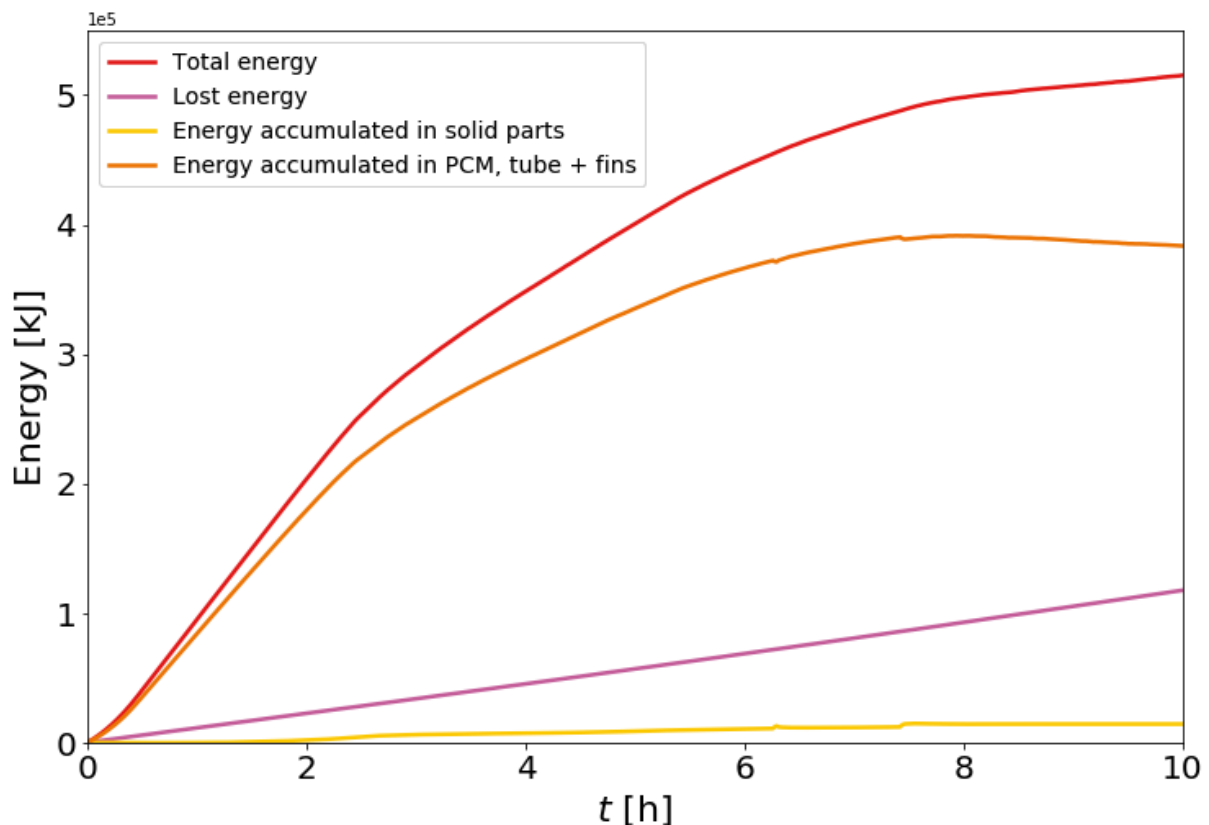


Figure 63. Evolution in time of the energy accumulated in various parts of the prototype module

III.5.2.2. System models

As previously mentioned, the whole various solid containment parts, including collectors, plates and shell are not represented in none of the system models. Furthermore, the heat lost to the surroundings is not considered, and instead, an adiabatic condition is imposed at the external domain boundary. As a result, the stored energy within the system corresponds to the accumulated energy in the tube's wall, fins, and PCM regions. Consequently, all results from the two system models (1D and 0D) will be compared to this latter.

For the heat transfer tube, the accumulated energy corresponds to the sensible increase of each elementary volume:

$$E_{tube}(t) = \rho_{tube} c_{p_{tube}} \sum_{i=0}^l V_{tube_i} (T_{tube_i}(t) - T_0) \quad (87)$$

Where T_0 is the temperature at initial stage. In this case, ρ_{tube} and $c_{p_{tube}}$ are the temperature independent density and specific heat capacity of steel. V_{tube_i} and T_{tube_i} are respectively the volume and temperature of the corresponding cell. Finally, l denotes the number of meshes representing the tube's wall.

For the 1D radial model, the domain is discretized in radial direction. Therefore, the total accumulated energy is obtained by summing the contributions of each elementary volume. For the active PCM + fins region, it is calculated as follows:

$$E_{PCM+fins}(t) = \sum_{i=1}^m \rho_{h_i} V_i \left(x_{m_i} \int_{T_0}^{T_{h_i}} c_{p_{PCM}}(T) dT + (1 - x_{m_i}) c_{p_{fins}} (T_{h_i}(t) - T_0) \right) \quad (88)$$

Here, m represents the number of cells in the radial direction. The density of the homogenous PCM + fins material in a particular mesh is ρ_{h_i} , defined by Equation (47). x_{m_i} is the PCM mass fraction, calculated using Equation (55). Finally, $c_{p_{fins}}$ is the specific heat capacity of fins, and $c_{p_{PCM}}$ is the equivalent temperature dependent specific heat capacity of PCM that accounts for the latent heat of phase change, as expressed in Equation (56).

Finally, for the passive PCM volume represented in the 1D radial model for peripheral tubes, the accumulated energy at a given instant during the charging process is expressed as follows:

$$E_{passive\ PCM}(t) = \rho_{PCM} \sum_{i=1}^n V_i \left(\int_{T_0}^{T_{PCM_i}} c_{p_{PCM}}(T) dT \right) \quad (89)$$

In the 1D radial model, a central tube is formed by the HTF tube and active PCM + fins domain. A peripheral tube is the equivalent of a central tube with an additional passive PCM layer. Therefore, the accumulated energies in central and peripheral tubes are respectively calculated as follows:

$$E_{acc,central}(t) = E_{tube}(t) + E_{PCM+fins}(t) \quad (90)$$

$$E_{acc,peripheral}(t) = E_{acc,central}(t) + E_{passive\ PCM}(t) \quad (91)$$

Finally, for the complete storage, the total energy accumulated with the 1D radial approach is calculated as follows:

$$E_{acc_{1D}}(t) = N_{tube,central}E_{acc,central}(t) + N_{tube,peripheral}E_{acc,peripheral}(t) \quad (92)$$

Where $N_{tube,central}$ and $N_{tube,peripheral}$ correspond to the number of central and peripheral tubes present in the storage module. For the prototype module described in section III.2, the values of $N_{tube,central}$ and $N_{tube,peripheral}$ are 7 and 12, respectively.

The calculation of the accumulated energy is relatively simpler for the 0D radial model, wherein the passive PCM volume is unaccounted for. As a result, the accumulated energy corresponds to the sum of energy stored in the tube's wall and the overall energy transferred to the equivalent PCM + fins region. The value of the later can be directly determined through the integration of the total heat flux exchanged at the tube's outer wall ($\varphi_{t,ext}$). Therefore, we have:

$$E_{acc_{0D}}(t) = E_{tube}(t) + \int_0^t \varphi_{t,ext} dt \quad (93)$$

III.5.2.3. Comparison of the energy stored predicted by the 'system' model with the experimental case

Figure 64 compares the temporal evolution of the accumulated energy in the storage, as predicted by both system models, with the outcome derived from the experimental trial. To ensure a fair evaluation, the experimental data curve corresponds to the accumulated energy in the tubes, fins and PCM regions only, as calculated using Equation (86). For $t < 2$ h, the charging phase is at initial stages where steam energy melts the active PCM surrounding the fins. At this phase, the influence of natural convection and fin geometry on the thermal power of the storage are accounted for in the numerical models by involving the heat transfer correlation derived from CFD simulations. As a result, both numerical models effectively replicate the same results obtained with the experiment. After the 2 h mark, the melting of the active PCM concludes, the charging phase continues where steam energy melts the remaining passive PCM at the shell's periphery. Consequently, the experimental data curve continues growing until eventually achieving stability at around $t = 8$ h. For numerical models, the stored energy evolves asymptotically after $t = 2$ h in the 0D radial model. This is because the passive

PCM volume is not represented in this model. For the 1D radial model, the consideration of the passive PCM region enables the stored energy to continuously grow for $t > 2$ h.

However, by comparing this model's predictions with the experimental data curve, it is observed that, within the time interval of $4.5 \text{ h} < t < 9 \text{ h}$, the stored energy values projected by the 1D radial model slightly lag behind those obtained from experimentation. This disparity can be attributed to the movements generated by natural convection in the liquid-phase that enhance the heat transfer rate within the storage system. In the absence of available CFD simulation data regarding the heat transfer mechanisms in this region (passive PCM volume), the numerical model overlooks the impact of natural convection on the storage behavior by supposing that heat is solely transferred by conduction through this region. This assumption leads to a marginal underestimation of the storage's thermal power. Notably, the discrepancy becomes less pronounced as the charging phase ends (around $t = 9.5 \text{ h}$), where the 1D radial model curve converges toward the experimental data curve, ultimately resulting in an equivalent average thermal power to that obtained through experimentation on the prototype module. The 0D radial model stores approximately 61% of the total energy compared to both the 1D radial model and the results from experimental trials. The remaining energy is attributed to the phase change process within the passive PCM volume, which accounts for 40% of the available PCM in the storage system (as described in Section III.2).

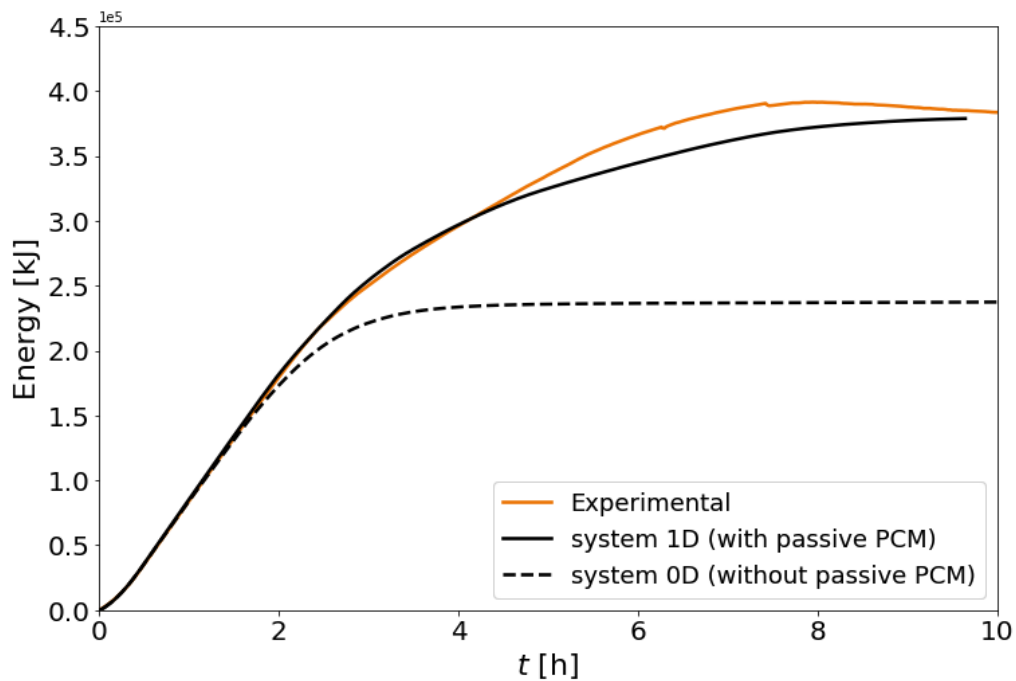


Figure 64. Evolution in time of the stored energy predicted by both numerical models compared to experimental data curve

To conclude, integrating heat transfer correlations extrapolated from comprehensive CFD simulations into simplified system models affords a precise prediction of the storage system's behavior at a global scale. Notably, even though the 0D radial model involved additional simplifications, its predictions remained accurate in comparison to the discretized model, particularly during the active stage of the charging phase.

III.5.3. Water level

Examining the stored energy throughout the charging process of the storage systems allows for a thorough analysis of the system's overall performance and behavior. From a global perspective, where the total energy stored in the PCM and fins region serves as the main criterion for assessing the accuracy of numerical models, both 0D and 1D approaches have effectively replicated the experimental data curve throughout the primary phase of the charging process. However, a comprehensive validation of the numerical model's outcomes involves the examination of the local phenomena occurring within the storage.

In this section, the evolution of the water level inside the tubes during the charging process is examined. The results obtained from both 0D and 1D approaches are compared to experimental data. The water level inside the tubes corresponds to the height of the free surface that separates the liquid water zone from the two-phase flow zone where steam condensation takes place during the charging process. Considering that steam condensation follows a film condensation regime, a condensed water film is created in contact with the inner wall of the tube. Therefore, it is essential to establish precise definitions for calculating the water level to facilitate the comparison of numerical results with experimental data.

Experimentally, the water level inside the tubes (WL_{exp}) can be determined by measuring the pressure difference (ΔP), between the exit at the bottom of the module and a water column of height H , maintained at ambient temperature:

$$WL_{exp} = \frac{\rho_l g H - \Delta P}{\rho_l^{sat} g} \quad (94)$$

With ρ_l^{sat} corresponds to the liquid saturation density according to the pressure and temperature levels in the tubes. For the numerical models, both the 0D and 1D approaches are coupled with the same two-phase flow model, where the inside of the tubes is discretized along axial direction. In this model, the implementation of the mass balance (Equation (41))

determines the flow rates entering and leaving each cell. Considering that steam condenses during the charging process and that the water level decreases within the tubes, the mass flow rate of liquid water at the module's exit exceeds that of steam entering the tube.

Figure 65 illustrates the methodology employed to determine the water level in the system models. Considering the homogenous approach adopted and outlined in section III.4.1 for the two-phase flow, the representation of film condensation regime, as shown in Figure 65(a), is not directly incorporated within the numerical model. Instead, each elementary volume contains a homogenous mixture of liquid water and steam medium. Therefore, by determining the vapor fraction x_{vap} which is calculated from the specific enthalpy within each volume, it becomes possible to compute the mass of liquid water present with the corresponding elementary volume (Figure 65(b)):

$$m_{lw} = \sum_{i=1}^{nb \text{ volumes}} \rho_{lw_i} V_i (1 - x_{vap_j}) \quad (95)$$

Consequently, the water level (WL_{system}) is determined by considering that the entire water mass accumulates in the lower section of the tube:

$$WL_{sys} = \frac{m_{lw}}{\pi R_{t,int}^2 \rho_l^{sat}} \quad (96)$$

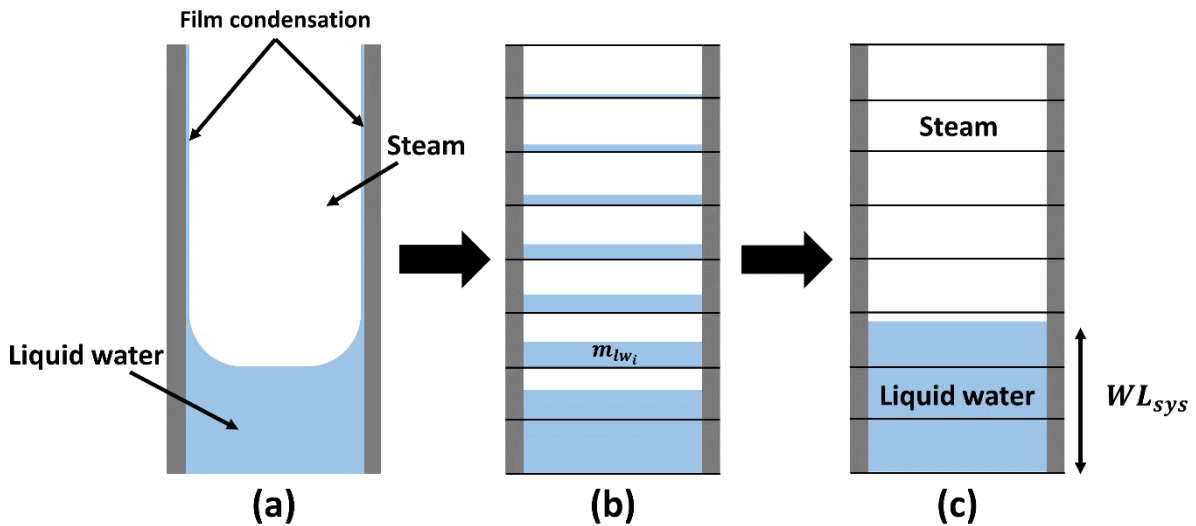


Figure 65. Illustration of the water level within the tubes (a) film condensation (b) water content in each elementary volume (c) calculated water level using Equation (96)

Figure 66 illustrates the temporal evolution of the water level, with comparisons between the data derived from experimental measurements and the results obtained through system simulations. As previously discussed, in a charging phase conducted under constant steam

pressure, the water level decreases throughout the process. During the initial stages of the charging process (for $t < 0.5$ h), both system models successfully replicate the experimental data curve. As the charging progresses (for $0.5 \text{ h} < t < 1.7$ h), the predictions of the 0D radial model remain consistent, showing minimal deviations from the experimental data. However, the precision of the 1D radial model in predicting the water level decreases. On average, the water level predicted by the 1D radial model is 0.8 m higher than that obtained from the 0D radial model and experimental data. Finally, at approximately $t = 1.9$ h, the water level curve obtained by the 1D radial model aligns with the other two curves, the water level reaches the bottom of the tubes, allowing only superheated steam to flow inside.

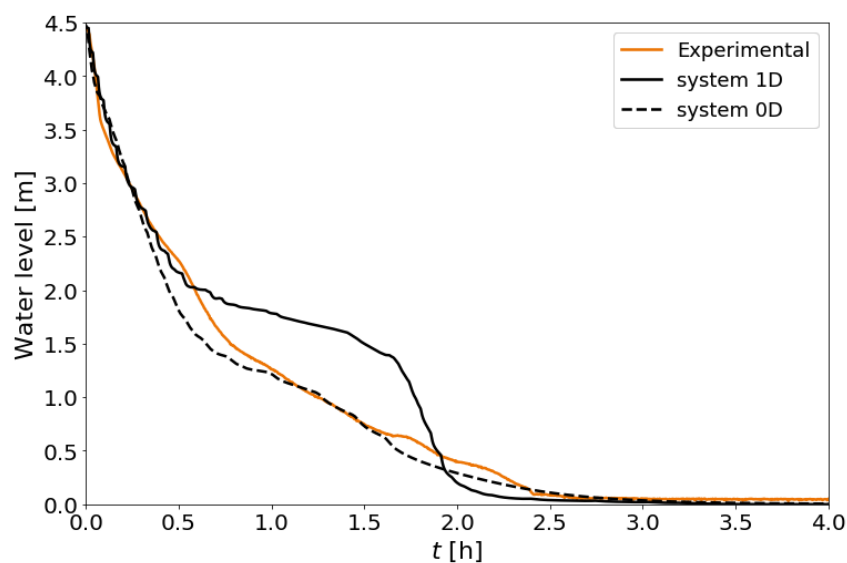


Figure 66. Evolution in time of the water level predicted by both system models compared to the experimental data curve

The elevated water level predicted by the 1D radial model implies that a shorter length of the heat transfer tube is required to completely condense the steam by transferring its energy to the surrounding PCM. This may result from a local overestimation of the heat transfer rate exchanged between the steam and the PCM at the tube's wall. To comprehend the distinctions between the two models, the states of the HTF and PCM within the storage are illustrated at various instants in Figure 67. In each graph, the water level obtained through numerical simulations, and calculated using Equation (96), is represented by a horizontal line that separates the liquid water volume from steam inside the tubes. On the PCM side, the shape of the melting front, which distinguishes the solid from the liquid PCM, is determined by the local values of the characteristic length l_c within each sub-domain. According to its definition, l_c represents the average thickness of the liquid PCM layer and is calculated using Equation (35).

Lastly, the water level derived from experimental data is illustrated in each graph as a horizontal dashed line within the tube.

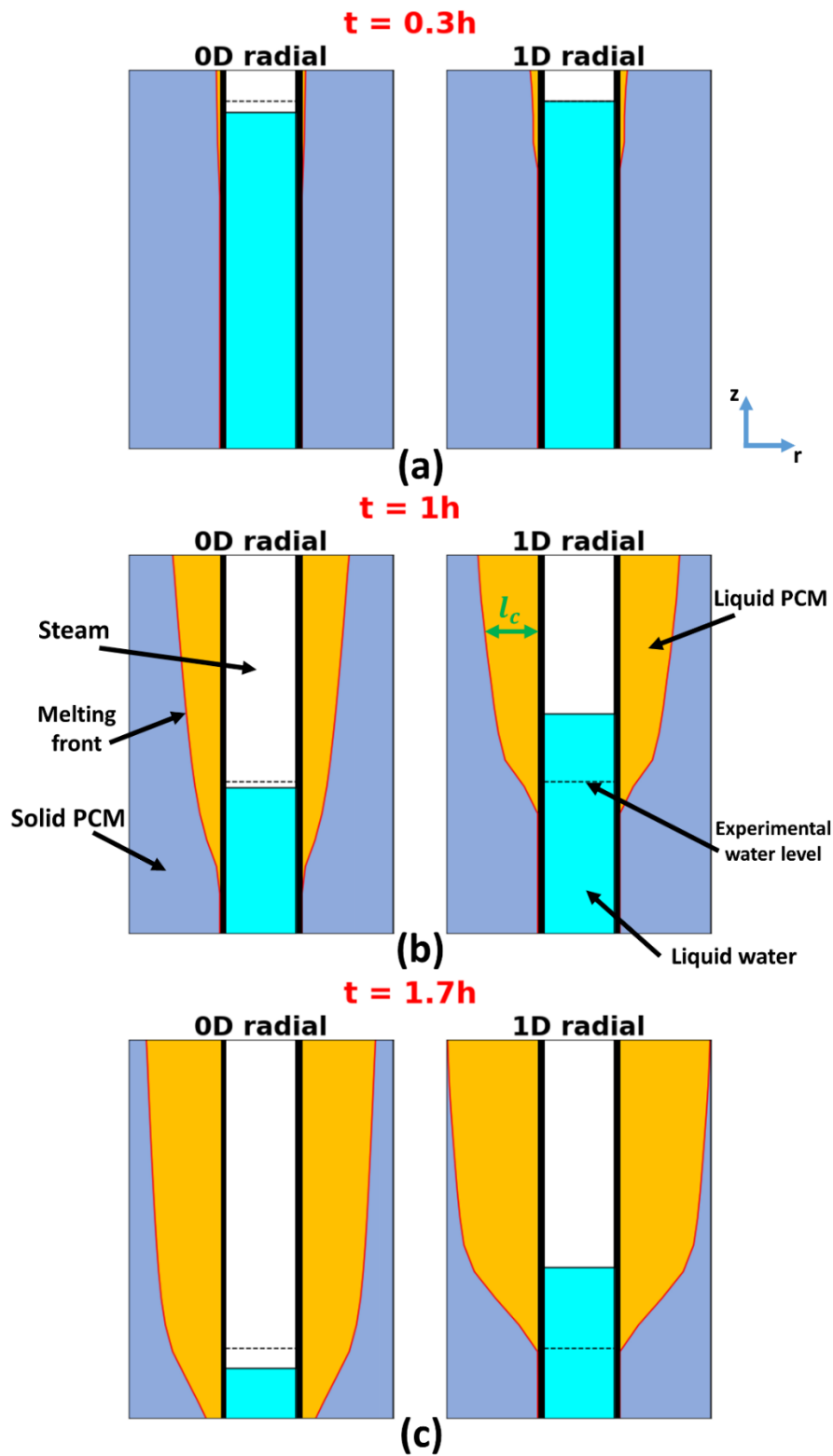


Figure 67. Illustrations of the water level inside the tubes and the PCM's melting front predicted by both 0D and 1D radial models at three instants (a) $t = 0.3 h$ (b) $t = 1 h$ (c) $t = 1.7 h$

At the start of the charging phase, at $t = 0.3$ h (Figure 67(a)), the steam energy injected in the tubes initiates the melting of the PCM at the top of the domain. However, the majority of the PCM is still in solid phase and the tiny melted layer is confined in the region between the circular bases of the fins, preventing the formation of natural convection loops during this stage. Consequently, heat is primarily transferred by pure conduction through the PCM. As a result, the water level, as predicted by both system models, is in consistent agreement with the experimental results. For $t = 1$ h, Figure 67(b) illustrates the disparities between the outcomes of the two numerical models. Regarding the water level inside the tubes, the 0D radial model aligns closely with the experimental results, while the 1D radial model yields a slightly higher level. The primary distinction between the results of the two models lies in the shape of the melting front on the PCM side. In the case of the 1D radial model, a larger portion of the PCM is melted at the upper region of the domain. Conversely, in the 0D radial model, the liquid fraction of PCM is more evenly distributed along the length of the heat transfer tube. The same pattern is observed at $t = 1.7$ h (as shown in Figure 67(c)). In the 1D radial model, the melting front has extended to the external boundary at the upper region of the domain, whereas the melting process has not yet commenced at the bottom. Inversely, for the 0D model, the melting front has not achieved the frontier and the lower part of the PCM has begun to melt. This is consistent with the above discussed results.

Figure 68 shows the evolution of the heat flux exchanged between the HTF and the PCM as a function of the melted fraction within a specific sub-domain along a single heat transfer tube for both system models. For a given melted fraction, the 1D radial model, on average, yields a heat flux approximately 25 % higher than that of the corresponding 0D radial model. The increased heat flux for the same state of PCM (i.e. identical melted fraction) suggests that a larger proportion of the steam's energy content is rapidly dissipated upon entry into the tubes. Consequently, the resulted water level is higher inside the tubes.

In the adopted multi-scale modelling approach, the overall heat transfer rate exchanged between HTF and PCM at the tube's wall is calculated according to heat transfer correlations obtained from CFD results. However, the accuracy of the correlations described in section III.3.2 relies on the accurate prediction of the characteristic parameters l_c and T_{cold} according to their respective definitions (Equations (35) and (36)).

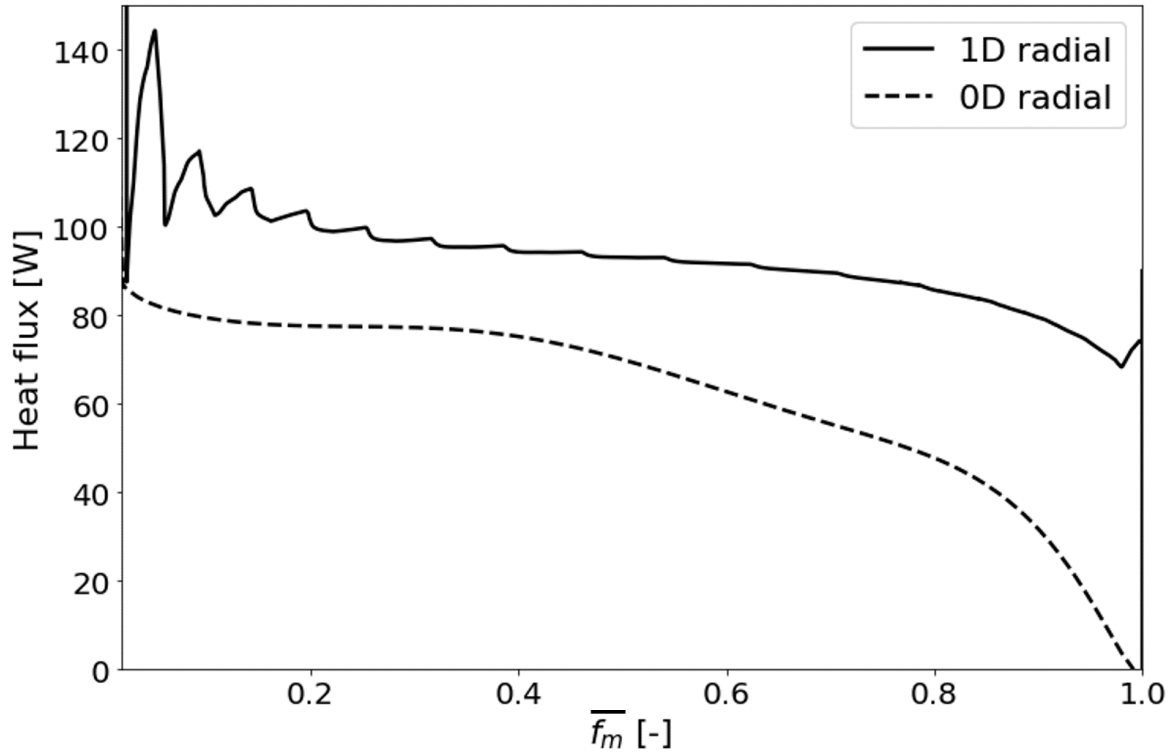


Figure 68. Variation of the heat flux of the two models according to the PCM's melted fraction

In order to investigate the distinction in outcomes between the two numerical models and gain insight into why the 0D radial model produces more accurate results at the local scale than 1D radial model, Figure 69 illustrates the evolution of the average temperature of the PCM liquid phase $\overline{T_{PCM_l}}$ according to the melted fraction \bar{f}_m . For the 1D radial model, $\overline{T_{PCM_l}}$ is calculated according to the temperatures in each elementary volume corresponding to the equivalent material of PCM + fins. In the 0D radial approach, an additional correlation was required to estimate $\overline{T_{PCM_l}} = f(\bar{f}_m)$ according to CFD simulations. As a result, Figure 69 shows that, at the beginning of the melting process, when $\bar{f}_m < 0.4$, the 1D radial model predicts an average temperature values approximately 1 °C lower than those obtained with the 0D radial model. As the melting progresses ($0.1 < \bar{f}_m < 1$), a discrepancy emerges between the predictions of the two models. Specifically, the values of $\overline{T_{PCM_l}}$ remain relatively constant in the 1D radial results, while they steadily increase in the 0D model until reaching the threshold temperature of 315 °C. According to the definitions of the dimensionless numbers Rayleigh and Nusselt (Equations (33) and (34)), the lower values of $\overline{T_{PCM_l}}$ in the discretized 1D radial model result in a greater temperature gradient between the tube's outer wall and the PCM region ($T_{t,ext} - \overline{T_{PCM_l}}$), leading to higher Rayleigh values and, accordingly, increased Nusselt number. Consequently,

the equivalent thermal conductivity introduced to the 1D radial approach to account for the effects of natural convection and the geometry of fins is overestimated. Therefore, the overestimation of the local heat flux in the 1D radial model arises from the challenge of accurately estimating the average temperature of the liquid phase. In fact, in the CFD model, $\overline{T_{PCM_l}}$ values are influenced by natural convection circulations within the liquid phase, making it challenging to replicate using a purely conductive numerical approach. On the other hand, the 0D radial model addressed this issue by incorporating an additional correlation that enables the calculation of $\overline{T_{PCM_l}}$ at any instant during the charging phase. It is thus obvious that better results are obtained since this latter is not strictly speaking predicted, a correlation being used.

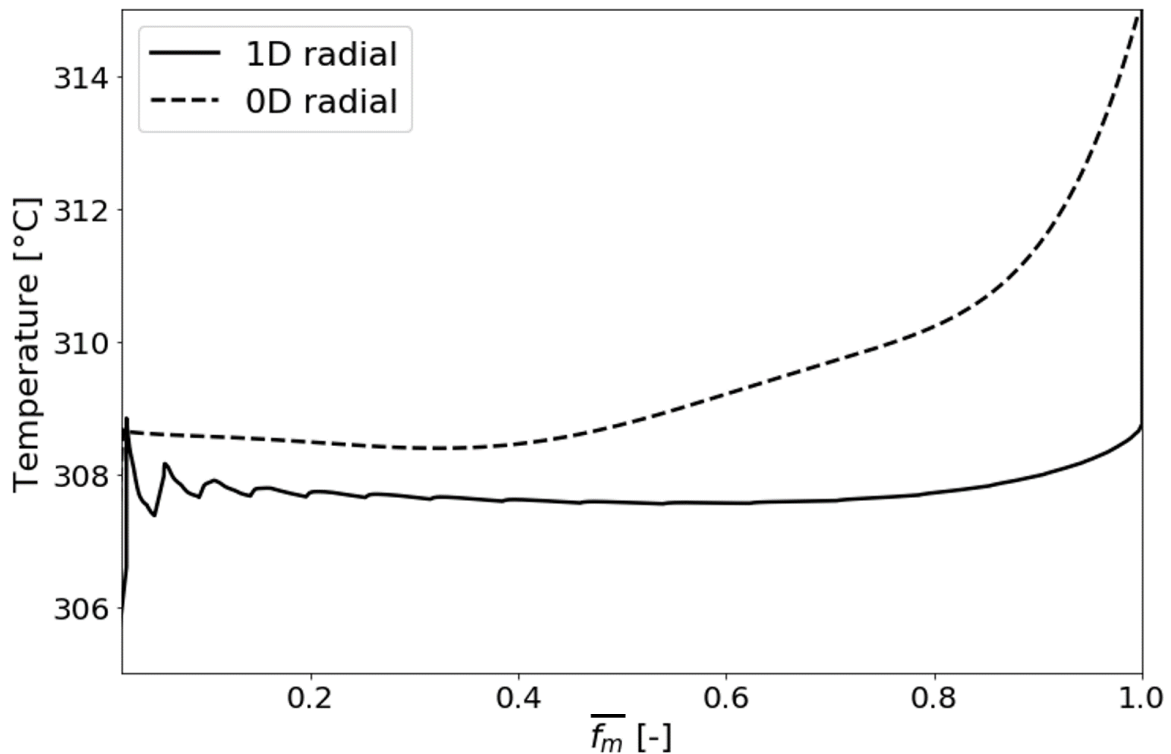


Figure 69. Variation of the average temperature of the liquid PCM phase of the two models according to the PCM's melted fraction

III.6. Conclusion

In this chapter, numerical approaches were developed to model the dynamic behavior of shell-and-tube LHTES systems. Generally, employing CFD to simulate various physical phenomena, such as the phase change of PCM and natural convection within the liquid phase, and within a representative geometry of the storage system — encompassing heat transfer tubes, fins, and the PCM domain — requires substantial computational costs. Therefore, the primary objective

of the investigations conducted in this chapter was to develop reduced numerical models capable of accurately predicting the behavior of the storage system while maintaining efficient computational costs for sizing requirements.

In the numerical models, a homogenous approach was employed to represent the two-phase flow of liquid water and steam inside the tubes. This approach assumed that both the liquid and gaseous phases shared the same temperature and velocity. Discretization in the axial direction was applied to the inside of the tubes, with each elementary volume connected to a mesh representing the thickness of the heat transfer tube. For the modelling of heat transfer within the PCM and fins domain, two distinct approaches were developed. The first approach involved the radial discretization of the domain, resulting in a 1D radial model. Within each mesh segment, an equivalent material with homogenous temperature represented the presence of fins and PCM in the volume. The effects of geometry and natural convection on the heat transfer rate were considered by modifying the thermal conductivity of the equivalent material, based on data obtained from more detailed CFD simulations in the form of dimensionless heat transfer correlations. In contrast, a second approach was formulated, where the fins and PCM region were not discretized in the radial direction. Instead, a 0D approach was retained, allowing for the direct calculation of the heat transfer rate from the HTF using CFD correlations. However, this latter approach also imply to provide an additional correlation, for the evolution of the liquid phase of the PCM with the molten fraction. Table 5 summarizes both the commonalities and distinctions between these two approaches.

	1D radial model	0D radial model
Two-phase flow	Homogeneous approach, discretized in axial direction	
Tube's wall	Discretized in radial direction	
Active PCM + fins	Discretized in radial direction	Not discretized in radial direction
Passive PCM	Represented and discretized in radial direction	Not represented
Influence of natural convection and geometry of fins	Equivalent thermal conductivity technique	Heat flux directly calculated from CFD correlations
Average temperature of the PCM liquid phase	Calculated from local temperatures in each mesh	Calculated using an additional correlation

Table 5. Summary of the shared characteristics and distinctions between the 1D radial and the 0D radial models

Following the description of the numerical models, testing and validation procedures were conducted, according to data acquired from experimental trials involving a shell-and-tube

LHTES prototype module designed and operated at CEA Grenoble. This prototype featured 19 finned tubes surrounded by sodium nitrate, serving as the PCM. The specific testing case under examination consisted of the charging phase of the module, wherein superheated steam was introduced from the top at a fixed pressure and temperature.

To comprehensively assess the performance of the numerical models, both global and local outcomes resulting from the two numerical approaches were thoroughly investigated and analyzed. On a global scale, both models effectively replicated the changes in stored energy within the tube's wall, active PCM, and fins domains throughout the charging process. Nevertheless, employing a radial discretization approach enabled the inclusion of an extra PCM layer, representing the passive PCM located beyond the reach of the fins at the shell's periphery. It is important to remind that this PCM volume had not been taken into account in the CFD simulations that served in the calculation of the heat transfer correlations. Consequently, a pure conductive heat transfer mechanism was adopted in this region.

Conversely, when examining the internal dynamics of the storage system at a more localized scale, disparities appeared in the results obtained from the two numerical models. Upon comparing the variation of liquid water within the tubes with experimental data, it was noted that the 0D radial model produced results that closely matched the observations. However, at a specific moment during the charging process, a relatively higher water level was observed in the 1D radial model in comparison to both the 0D radial model and the experimental findings. An exhaustive investigation was undertaken to identify the source of this disagreement. In summary, the 1D radial model overestimated the heat transfer rate transferred to the PCM region for a specific position of the melting front. This overestimation, in turn, accelerated the dissipation of steam energy upon its entry into the tubes. Consequently, steam condensation occurred over a shorter length of the tube, ultimately leading to a higher water level. As part of the investigation, it was found that the 1D radial model underestimated the average temperature of the liquid phase, used in the calculation of the equivalent thermal conductivity through the heat transfer correlations. This problem was not present in the 0D radial model, mainly because this latter contained an additional correlation to derive the average temperature of the liquid phase of PCM. This correlation ensured an accurate temperature gradient that is required for calculating the dimensionless numbers Rayleigh and Nusselt, thus ensuring precise heat transfer rate calculations.

In conclusion, the 0D radial model demonstrated superior accuracy in replicating the localized behavior of the storage when contrasted with the 1D radial model. However, achieving this heightened accuracy necessitated the incorporation of supplementary data regarding heat transfer within the storage, making it less straightforward to generalize. Furthermore, it is worth reminding that the 1D radial model effectively predicted the overall thermal power of the storage system while accounting for the presence of the passive PCM volume in the shell. Furthermore, these aforementioned discrepancies on the liquid PCM temperature and water level remains reasonable and consistent with the general evolution of the problem. This aspect highlights the model's ability to provide a comprehensive view of the thermal performance of the entire system. It is essential to bear in mind that expecting perfect predictions would be unrealistic (otherwise, CFD simulations would serve no purpose, which is not the case). The overarching objective is to develop a rapid, simplified model for assessing numerous design configurations, and that this model is achieved using minimal correlations.

Finally, this chapter was centered on the dynamic modelling of the storage at the reduced system scale for given working conditions and a given geometry of the module. The following chapter will involve CFD investigations to gain a deeper insight into how the storage system's performance is influenced by natural convection and the characteristics of the fins, including their geometry and material properties.

Chapter IV – CFD investigations on the effects of natural convection and fin parameters of a LHTES

IV.1. Introduction

In the preceding chapter, the studies highlighted the capability of simplified system models to accurately replicate the performance of shell-and-tube LHTES system. These models involved a special consideration of the impact of crucial physical phenomena, including the PCM solid-liquid phase transition, and the occurrence of natural convection in the liquid phase, as well as the influence of the presence of fins on the charging rate of the storage. The consideration of the impact of each of these factors was made possible through the utilization of heat transfer data obtained from detailed CFD simulations conducted on a representative geometry of the storage system in question.

As a result, the heat transfer correlations employed in the previous chapter are unique to the prototype module available at CEA Grenoble (Section III.2). In fact, any slight variation in the fin type, their spatial distribution within the PCM domain, or the material composition from which they are constructed can have a substantial impact on the thermal behavior of the storage system. Consequently, the Nusselt correlations employed in the last study may not provide highly relevant insights in such cases, given the sensitivity of the system to these variables. Therefore, to extend the applicability of the multi-scale modelling approach of shell-and-tube LHTES systems, encompassing various geometric parameters and material properties of the fins, it is essential to return to CFD scale. The primary objective of this chapter is to provide a comprehensive analysis and insights into how different fins configurations and materials impact the thermal performances of the storage, including heat transfer efficiency to the PCM region and potential enhancements due to natural convection circulation in the liquid phase.

The examination of the impact of natural convection on the charging rate of the storage system will be inspired from previous studies available in literature (Section II.2.2.2). In these studies, the investigations revolve around the outcome of simulations derived from two distinct numerical models. In the first model, heat is solely transferred through pure conduction within

the PCM volume, while in second model, liquid movements are incorporated to simulate the convective heat transfer. Nonetheless, in these studies, the primary focus was on quantifying the impact of accounting for natural convection on the melting and solidification rates of the PCM, often without delving into a comprehensive analysis of how fluid movements within the liquid phase contribute to the enhancements of the overall performance of the storage system.

Therefore, before examining the role that different fins configurations and materials play in a shell-and-tube LHTES system, an investigation is undertaken to comprehend the role of natural convection in evolving the melting process in a smooth-tube configuration (a heat transfer tube without fins added to its external surface). This endeavor involves a parametric CFD study, where the domain length is systematically varied across a wide range of values. The outcomes of these simulations are expected to provide invaluable insights that can subsequently increase the design optimization of such systems by maximizing the contribution of each heat transfer mechanism influencing heat exchange within the storage.

Subsequently, a comparative study is performed, focusing on the effect of fin orientation on the PCM's melting process within a vertical-layout storage system. The types of fins under consideration are axial and radial, with two numerical simulations performed for each fin type. These simulations allow for the distinction of the impact of each fin type on both heat transfer mechanisms, namely, heat conduction and natural convection.

Then, the main objective of this chapter comprises a series of studies focused on the parametric analysis of radial fin configurations and their material properties. Regarding the geometry, the parameters under investigation include fin length, thickness, and pitch. The goal is to gain a comprehensive understanding of how each parameter affects heat transfer mechanisms, especially the corresponding transient and the local behaviors, with the aim of optimizing the thermal performance of the storage system. Furthermore, an in-depth analysis is conducted by examining temperature distributions with the heat transfer tube, fins, and PCM regions, along with heat flux distributions on the tube's outer wall and fin surfaces. This analysis provides insights into how the circulations in the liquid phase affect the charging process. Finally, following a thorough exploration of geometric parameters on natural convection and the thermal power of the storage, a novel alternative geometric of radial fins is proposed. This new design is intended to enhance heat transfer mechanisms within the storage, outperforming the base circular radial fins in terms of thermal power for a given fin volume ratio and length.

Finally, a coupled parametric study encompassing geometric and material properties aspects is conducted to assess the impact of the thermal conductivity of the metallic components comprising the heat transfer tube and radial fins on the storage system's behavior during the charging phase. Different geometric fin configurations are considered in these evaluations. The significance of fin geometry and their constituent materials was underscored by the literature review. Notably, previous parametric studies within the literature predominantly focus on one-dimensional optimization, concentrating either on fin geometric shapes or material properties. This investigation, however, facilitates a comprehensive understanding of the contributions made by each element to the overall performance of the storage system. Consequently, the knowledge acquired through this study holds the potential to facilitate the formulation of heat transfer laws. These laws, in turn, enable the prediction of storage system behavior through the utilization of less computationally intensive numerical models, reducing computational cost and time.

IV.2. Description of the CFD model

IV.2.1. Physical model

The CFD model developed in this chapter is derived from prior studies conducted by Beust et al. [35]. In the context of steam storage systems under investigation, steam flows downward within the cylindrical body, this led to the consideration of a vertical tube layout for the system. Furthermore, in the case of steam storage applications, the two-phase flow inside the tubes leads to a notably high heat transfer coefficient with the tube's inner wall. Consequently, thermal resistances on the PCM side govern the thermal dynamics of the storage system. Thus, this study concentrates exclusively on investigating the heat transfer mechanism within the PCM + fins region, without directly simulating the two-phase liquid water/steam flow in the CFD model. Instead, a temperature boundary condition will be imposed on the tube's inner wall. In all examined cases, whether fins are present within the PCM domain or not, the heat transfer tube maintains uniform characteristics, including the internal radius, denoted as $R_{t,int}$ (Figure 70), a thickness represented as e_{tube} and the external radius indicated as $R_{t,ext}$. The PCM volume surrounds the heat transfer tube, making direct contact and extending to a radius denoted as R_{ext} . Various metallic fins of different types and configurations can be added to the tube's outer wall to enhance the heat transfer rate within the storage system. The subsequent sections of this chapter will provide a detailed overview of fin geometries under investigation.

Finally, to reduce the computational costs, the 3D geometry implemented in the CFD modelling is reduced to an angular sector θ as shown in Figure 70. The values of these generic geometric parameters used in the CFD studies are grouped in Table 6. These selected values align with the geometry of the prototype module considered in the previous chapter and detailed in Section III.2.

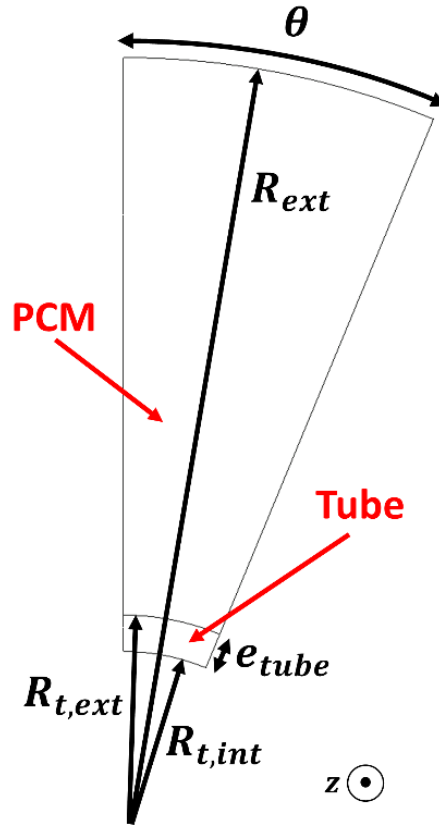


Figure 70. Cross-sectional view of the basic geometry for the CFD model

Parameter	Value
$R_{t,int}$ [mm]	13.585
$R_{t,ext}$ [mm]	15.875
e_{tube} [mm]	2.29
R_{ext} [mm]	51
θ [°]	22.5

Table 6. General design parameters of the CFD model

Finally, sodium nitrate (NaNO_3) serves as the chosen PCM for all the studies. In the preliminary studies conducted in this chapter, both the cylindrical tube and the fins are made from carbon steel SA344 Grade 6. The thermos-physical properties of both NaNO_3 and carbon steel are identical to the ones used in the previous chapter, as depicted in Table 3.

IV.2.2. Governing Equations

In the metallic part, formed by the heat transfer tube and the fins, only the transient heat equation by conduction applies with constant density, specific heat capacity and thermal conductivity:

$$\rho c_p \frac{\partial T}{\partial t} = \lambda \Delta T \quad (97)$$

To investigate the effect of natural convection on the thermal performances of the PCM, two numerical models have been developed. The first model, called the ‘CC’ model, accounts for fluid circulations on the melted phase and considers both heat conduction and convection as heat transfer mechanisms within the PCM. The second model assumes the PCM to be still and considers only heat conduction as the heat mechanism. This model will be referred to as the ‘C’ model.

In the ‘CC’ model, the PCM is considered as a homogeneous, Newtonian fluid, flowing in a laminar regime. The phase change problem is then modelled using the enthalpy-porosity method [72] where a term is added to the energy equation to account for the PCM’s latent heat. The volume expansion of the PCM is neglected. However, the effect of the PCM’s density variation on the fluid motion in the melted phase is handled through the Boussinesq approximation in the momentum equation (see Section II.2.2.1.3). Consequently, the mass, momentum and energy balance are the following:

$$\nabla \cdot \mathbf{u} = 0 \quad (98)$$

$$\rho \left(\frac{d\mathbf{u}}{dt} + \mathbf{u} \cdot \nabla \mathbf{u} \right) = -\nabla P + \mu \nabla (\nabla \mathbf{u}) - \rho \beta (T - T_{ref}) \mathbf{g} - A \mathbf{u} \quad (99)$$

$$\rho c_p \left(\frac{dT}{dt} + \mathbf{u} \cdot \nabla T \right) = \nabla (\lambda \nabla T) - \rho L \left(\frac{df_m}{dt} + \mathbf{u} \cdot \nabla f_m \right) \quad (100)$$

Where \mathbf{u} is the velocity vector and P is the pressure. f_m is the PCM’s melted fraction. It is defined according to the local temperature as follows:

$$f_m = \begin{cases} 0 & \text{if } T < T_{sol} \\ \frac{T - T_{sol}}{T_{liq} - T_{sol}} & \text{if } T_{sol} < T < T_{liq} \\ 1 & \text{if } T > T_{liq} \end{cases} \quad (101)$$

Where T_{sol} and T_{liq} are respectively the PCM’s solidus and liquidus temperatures. Since the PCM is modelled as a fluid, the term A added to the momentum equation annihilates its velocity while in solid state. It is defined based on the melted fraction as follows (see section II.2.1.2.3.7):

$$A = A_{mush} \frac{(1 - f_m)^2}{f_m^3 + b} \quad (102)$$

With $b = 10^{-3}$, a small value added to prevent division by zero. A_{mush} is the mushy zone constant which has to be large enough to stop the flow in the solid phase. In this study, we consider it at 10^8 [35], [73].

In the model without natural convection (the ‘C’ model), heat conduction within the PCM volume is the sole heat transfer mechanism simulated. Therefore, the only equation to solve is the heat equation (in presence of phase change):

$$\rho c_p \frac{dT}{dt} = \nabla(\lambda \nabla T) - \rho L \frac{df_m}{dt} \quad (103)$$

The conducted studies concentrate on the charging phase of the storage. Therefore, the heat transfer tube, the fins and the PCM region are initially at the same temperature of 290 °C:

$$T_{ini} = 290 \text{ °C} \quad (104)$$

Consequently, the PCM is initially in solid state:

$$f_m = 0 \quad (105)$$

As the CFD model does not directly simulate the two-phase flow inside the tube, simulating the charging process of the storage involves applying a constant and uniform temperature of 315 °C to the inner wall of the heat transfer tube, exceeding the melting temperatures of the PCM (which range between 303.3 °C and 306.6 °C):

$$T_{t,int} = 315 \text{ °C} \quad (106)$$

Adiabatic condition is imposed on the upper, lower, external and lateral boundaries.

Finally, the 3D geometry is discretized using hexahedral elements. To ensure the independence of the results on the grid, the characteristic length of the mesh elements was kept below 0.9 mm. This value was chosen and validated based on the work of Beust et al. [35], who had a similar base geometry. The CFD simulations are then performed with the ANSYS Fluent 2022R1 software. For the ‘CC’ model, an adaptive time step with a Courant-Friedrichs-Lewy (CFL) of one is considered. While a fixed time step of 2 s is used in the ‘C’ model. PRESTO! scheme is used for spatial discretization of pressure equation. PISO scheme is adopted for the pressure-velocity coupling: a second-order upwind scheme is used for the convective term. The under-relaxation factors for the melted fraction update, pressure correction, momentum and energy

are set respectively at 0.9, 0.9, 0.7 and 1. For the convergence criteria, a relative decrease value of 10^3 is required for the continuity and momentum equations, and 10^{11} for the energy equation. [135]

IV.3. Smooth-tube TES

Before exploring the effect that different fin types, configurations and properties have on the thermal behavior of shell-and-tube LHTES system, an investigation is first conducted to study the influence of the length of natural convection loops on the system's behavior. Throughout the charging phase, as the PCM undergoes a solid-liquid phase transition, the growing liquid fraction leads to vertical movements within the liquid phase, driven by the buoyancy differences. In order to gain a deeper understanding of how these vertical movements affect the thermal performance of the storage system, this section delves into the investigation of natural convection's impact in a vertical smooth-tube LHTES configuration (without fins on the PCM side). In fact, a smooth-tube configuration corresponds to a scenario with radial fins extended along the radial domain, excluding their heat conduction and thermal inertia. These hypothetical fins would be situated at the base and top of the domain. Consequently, simulating various domain heights without fins is equivalent to investigating the influence of the gap between fins solely in the context of natural convection, while disregarding the conductive effects of the fins.

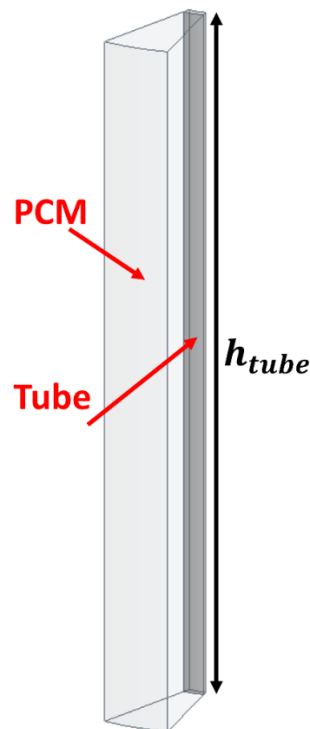


Figure 71. Smooth-tube domain represented in the CFD

Figure 71 shows the basic geometric configuration containing the heat transfer tube where a uniform and constant temperature is imposed on its inner surface, as described in section IV.2, as well as the PCM domain around the tube. The top, bottom, external and lateral boundaries are adiabatic.

The examination of how the length of the tube, labeled as h_{tube} in Figure 71, impacts the enhancements in heat transfer rate during the charging phase involves the study of eight values ranging from 0.25 cm to 54 cm. The set of different tested cases are grouped in Table 7.

h_{tube} [cm]	0.25	0.5	1	2.5	5	10	20	54
-----------------	------	-----	---	-----	---	----	----	----

Table 7. Domain height values studied in the case of a smooth-tube TES

For each configuration, two simulations were conducted using the ‘CC’ and ‘C’ models described in the previous sections (IV.2.2). Then, these configurations will be utilized as references to estimate the improvements of the storage’s thermal performances due to the addition of fins.

The evolution in time of the PCM’s melted fraction calculated using Equation (101) for all the studied configurations is shown in Figure 72. Since a uniform boundary condition is imposed on the tube’s inner wall, the ‘C’ model predicts an identical behavior of the storage regardless of the tube’s height. Therefore, a single curve is depicted.

The enhancement of the PCM melting rate attributed to the consideration of convective heat transfers within the liquid phase can be demonstrated by comparing the data resulted from the ‘CC’ model simulations with those obtained from the ‘C’ model. In Figure 72, when the melted fraction is low, below 0.05, both numerical models yield similar curves. At this phase, the majority of PCM is still in a solid state, meaning that natural convection has minimal impact on the system’s thermal power and heat transfer primarily occurs through pure conduction within the PCM. However, with the melting progress ($\overline{f_m} > 0.1$), the improvements resulting from the consideration of natural convection become increasingly evident, as it is well known. As a result, at any given moment, the melted fractions produced by the ‘CC’ model simulations surpass those obtained from the ‘C’ model simulations, regardless of the domain length.

The reduction in melting time when accounting for natural convection in the melted phase is highly anticipated and firmly established outcome the field. Nevertheless, the examination of the ‘CC’ model curves shown in Figure 72 implies that the improvements due to natural

convection are dependent on the domain length h_{tube} . Indeed, each configuration results in a distinct melted fraction at any given moment throughout the charging process. The variation in h_{tube} have a considerable influence on the slope of the melted fraction curve, thereby resulting in distinct overall thermal power for the system. Toward the end the charging process, when $\overline{f_m} \approx 1$, the configurations with the shortest and longest domain length, namely 0.25 cm and 54 cm, respectively, exhibit the slowest melting process (illustrated by the red and orange curves in Figure 72). Notably, the rate at which the PCM melts experiences enhancement as h_{tube} increases from 0.25 cm to 1 cm. However, any further increase in h_{tube} beyond 1 cm extends the time required to melt the PCM, consequently reducing the thermal performances of the storage system.

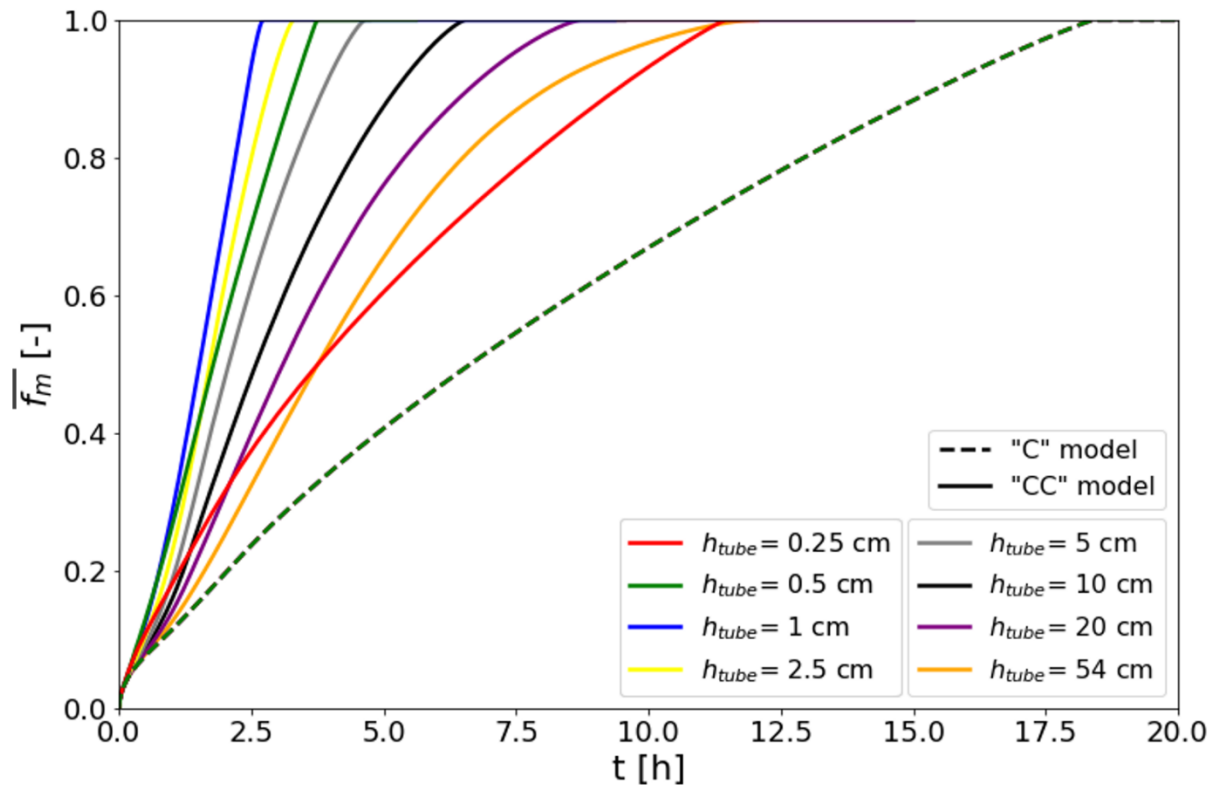


Figure 72. Evolution in time of the PCM's melted fraction for smooth-tube configurations

This is further demonstrated in Figure 73, which shows how the time required to melt a specific PCM fraction ($\overline{f_m}$), varies in relation to the domain length h_{tube} . To enhance the visibility of smaller domain heights, the values on the x-axis are presented using a logarithmic scale with a base of 10 (\log_{10}). In order to melt 20% of the PCM (as represented by the red curve in Figure 73), the time required is nearly identical for all configurations, with a slightly shorter melting time for those featuring h_{tube} values of 0.5 cm and 1 cm. As the melting process advances, the

discrepancies in the time needed to melt a specific volume of PCM become more pronounced. Notably, when aiming to completely charge the storage by melting 98 % of the PCM (as indicated by the black curve in Figure 73), the melting time diminishes from 11 h to approximately 2.8 h as h_{tube} increases from 0.25 cm to 1 cm. However, beyond 1 cm, an increase in h_{tube} results in an extended melting time, leading to a melting duration of around 10.5 h for $h_{tube} = 54$ cm.

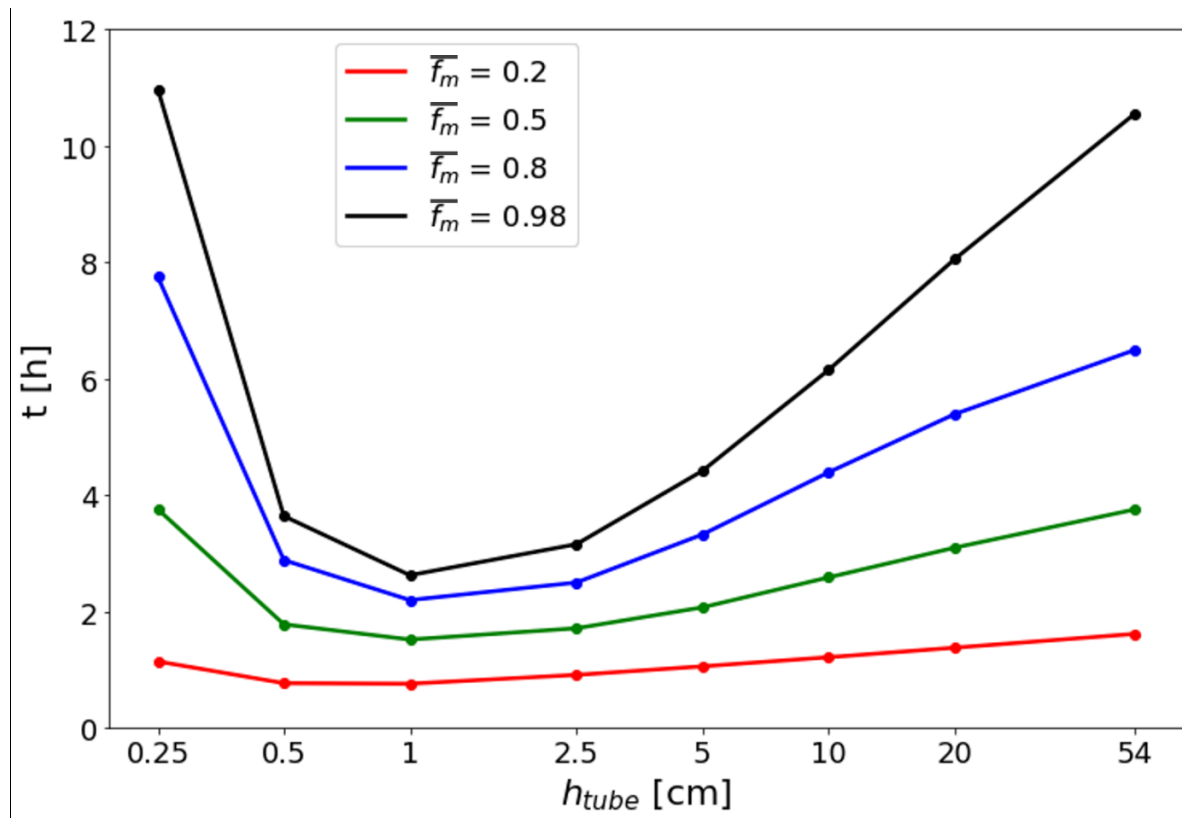


Figure 73. Variation of the melting time of a given PCM's fraction according to the tube's height

To further investigate the dependence of the enhancements due to natural convection on the height h_{tube} , Figure 74 shows a comparison of the temperature distributions within the heat transfer tube and the PCM region obtained during the charging phase, as obtained by both numerical models. The temperature scale ranges between the solidus temperature of the PCM (303.3 °C) and the threshold temperature (315 °C) imposed as a boundary condition on the internal tube's wall. For the 'C' model simulations, only the result with a tube height h_{tube} of 54 cm is presented, as the tube's height has no effect on the temperature distribution in this case. The 'C' model simulations result in a vertically uniform distribution that progresses gradually in the radial direction between the tube's outer wall and the outer limit of the PCM domain, this is due to the uniform temperature imposed as a boundary condition on the tube's

inner wall. At $t = 1$ h (Figure 74 (a)), most of the PCM is still in solid state, at a temperature below 303 °C (represented in blue within the temperature contour). In the ‘CC’ model, fluid motion initiates within the melted PCM volume, resulting in a distortion of the temperature distribution along the domain's height. Consequently, melted PCM at a relatively higher temperature accumulates at the uppermost portion of the domain. This phenomenon is more noticeable in configurations with greater domain heights. In contrast, shorter domains (h_{tube} of 0.25 cm and 0.5 cm) experience less pronounced natural convection effects at this stage, leading to a nearly uniform temperature distribution along the axial direction.

At $t = 2$ h, the melting progresses away from the heat transfer tube in the radial direction, and the influence of natural convection according to the domain height becomes more evident. As a result, an optimal configuration is observed among the studied cases. Indeed, increasing the domain height from 0.25 cm to 1 cm accelerates the melting process, directly attributed to enhancements in natural convection. However, further increases in the domain height decelerate the melting process. In fact, for configurations with h_{tube} values exceeding 1 cm, a liquid PCM volume at the threshold temperature of 315 °C accumulates at the top of the domain, where the melting front has already reached the external boundary of the PCM domain. The melting process then proceeds both radially away from the heat transfer tube and axially downward. The gradual rise in temperature at the domain's upper region diminishes the temperature gradient between the heat transfer tube and the PCM volume, and consequently reducing the heat flux exchanged within the storage system. In addition, the upper part of the domain, where the hottest fluid particles move, do not encounter any solid PCM to melt and to exchange energy with. This is only the descending streamlines that will perform this task, yet with less efficiency since they are colder.

In summary, as the domain height increases, the system's thermal power improves, thanks to the emergence of natural convection currents within the liquid phase, reaching its peak at a specific domain height. However, the benefits derived from natural convection diminish as the domain height exceeds this optimal value. Consequently, to benefit from the advantages of natural convection, the domain configuration must strike a balance, ensuring it possesses a sufficient height to induce movements within the liquid phase while also encouraging the recirculation of hot liquid particles towards the PCM in the natural convection loop, thereby facilitating efficient heat exchange renewal.

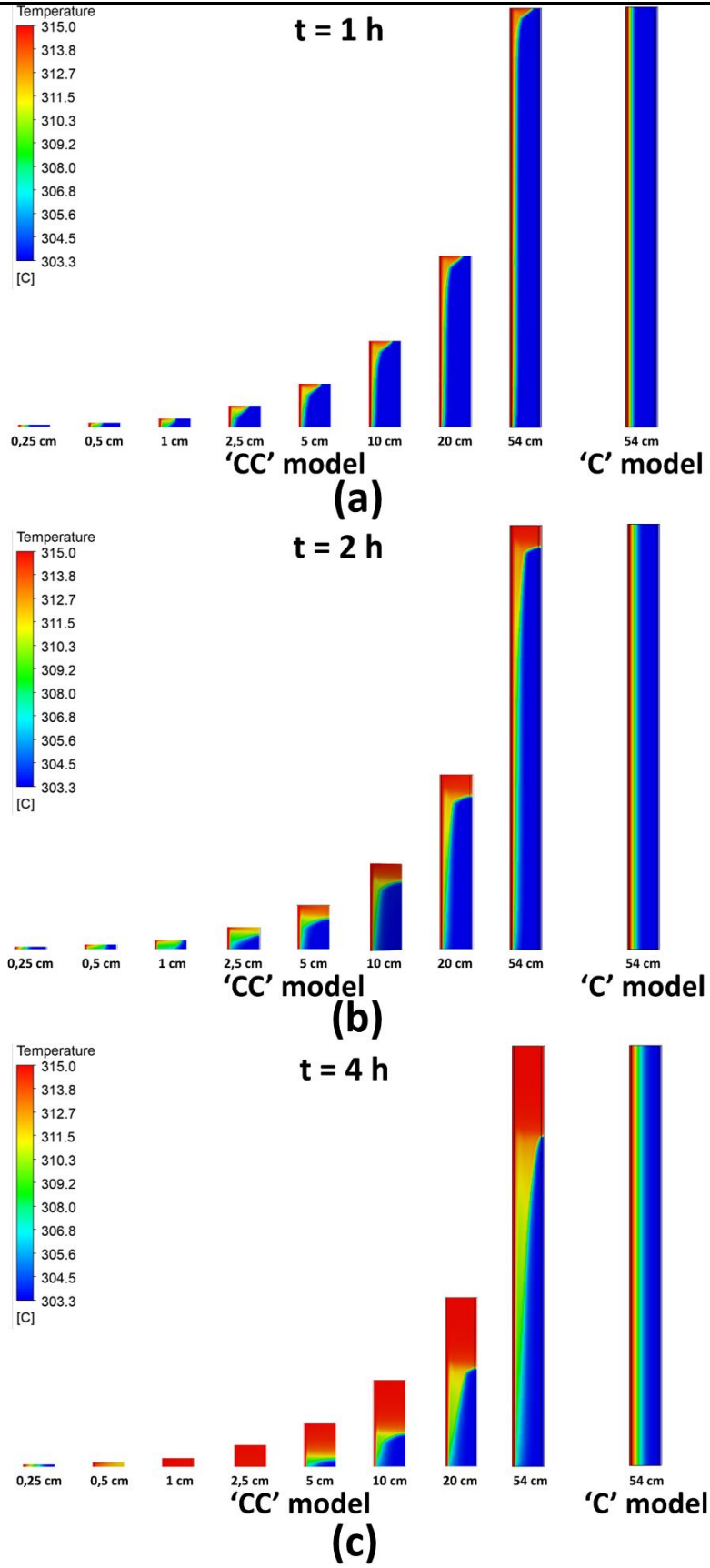


Figure 74. Temperature distribution within the tube + PCM domains for different smooth-tube heights

IV.4. Tube with fins: effect of fin type (radial vs longitudinal)

For steam storage applications, the thermal power of the storage primarily depends on the rate of heat transfer through the PCM. However, the PCM's low thermal conductivity results in increased thermal resistance, thereby impacting the dynamics of the storage system. Therefore, the addition of fins on the PCM side is a crucial element to improve and regulate the heat transfer mechanisms within the storage. Various shapes and configurations of fins can be employed, each offering distinct advantages, as discussed in Chapter II (Section II.2.3). In this section, a comparative numerical study is performed to investigate the effect of fin type on both, natural convection enhancements and the overall thermal behavior of a vertical shell-and-tube LHTES. For this reason, two distinct types of fins are considered, namely, circular radial fins and longitudinal axial fins.

Figure 75 illustrates the 3D geometric configurations employed in the CFD model. In both cases, the heat transfer tube and the PCM domain share identical geometric parameters and material properties as outlined in section IV.2, which were also applied in the simulations involving a smooth-tube TES (section IV.3). Furthermore, a domain length of 54 cm is maintained in both scenarios. In the first case, a range of circular fins are added to the external surface of the heat transfer tube within the PCM domain. These fins are characterised by specific parameters, including a length ' l_{fin} ' in the radial direction, a thickness ' e ' and a pitch ' p ' denoting the space between the centers of two consecutive fins in the axial direction. For longitudinal fins, a rectangular metallic shape is extended along the length of the domain in the axial direction. Both fins share the same length l_{fin} of 30 mm. Nevertheless, the values of the pitch ' p ' for circular fins and the thicknesses ' e ' are carefully selected to ensure an equal fin volume fraction in both fin types. Consequently, longitudinal fins result in a higher overall heat transfer surface with the PCM region. Table 8 groups the different geometric parameters for both configurations.

In order to assess the influence of the fin shape on the enhancements due to natural convection in the melted phase, two simulations of the charging phase using both the 'C' model and the 'CC' model described in section IV.2 are performed for each fin type.

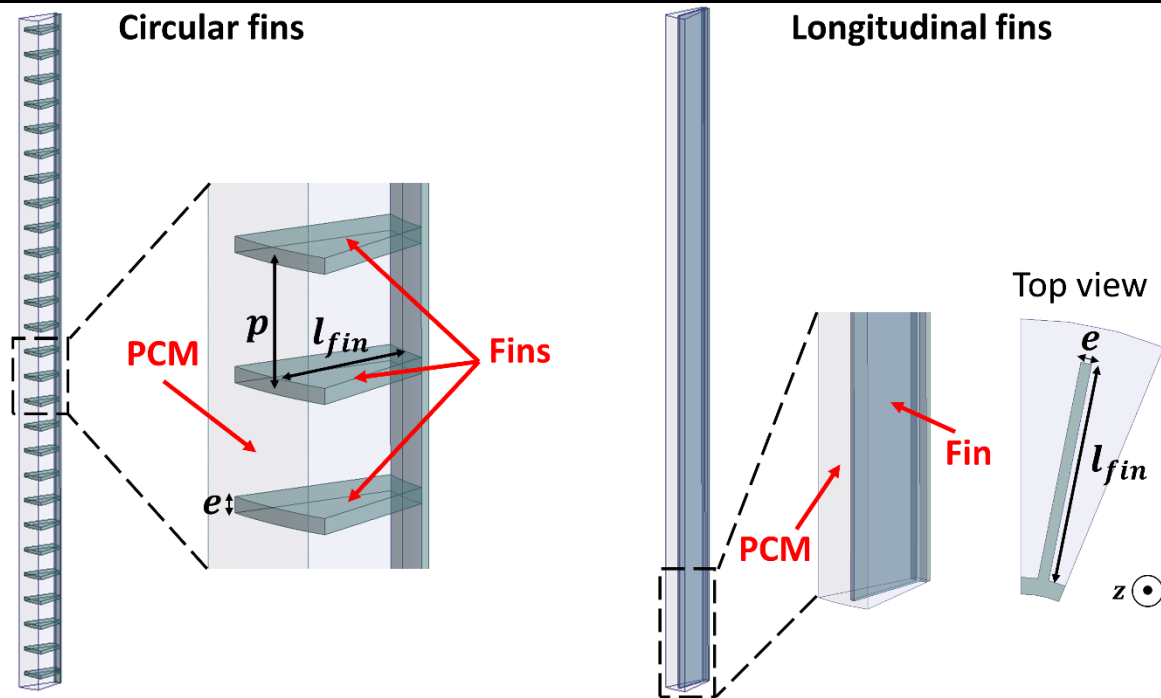


Figure 75. Geometric domains for circular and longitudinal fins used in the CFD model

Parameter		Circular fins	Longitudinal fins
l_{fin} [mm]			30
Fin volume fraction [%]			9.85
e [mm]		2.5	1.5
p [mm]		20	-
Fin number		27 (50 fin/m)	16 (around the tube)
Fin inclination [°]		11.3	-
Heat transfer surface	Area [m ² / 1 m of tube]	0.708	1.059
	Ratio to the smooth-tube area	7.1	10.6

Table 8. Design parameters for circular and longitudinal fins

IV.4.1. Validation of the domain reduction for radial fins: 22.5° vs 360°

In the case of radial fins, their circular shape follows a helical pattern along the heat transfer tube, causing the fins to be inclined at an angle relative to the tube's main axis. Consequently, the constraint of restricting the computational domain to a 22.5° angular sector (section IV.2.1) can potentially influence the system's performance. In fact, reducing the angular sector to 22.5° may eliminate potential circular motion of the liquid PCM, which is induced by the titles orientation of the fins. To ensure the independence of the results with regard to the domain's

angular sector, a validation is carried out between the results of a simulation conducted on a reduced domain with those on a complete geometry, which considers a 360° angular section. Both geometric configurations are illustrated in Figure 76.

In both scenarios, a pitch value between the centers of the fins of 25 mm is considered, which corresponds to the largest pitch among all the studied cases in this chapter, resulting in the most pronounced fin inclination. This inclination angle is denoted as ' γ ' in Figure 76(b) and measures approximately 14.3° for a 25 mm pitch. Additionally, the fins maintain a consistent thickness of 6.25 mm throughout the simulations.

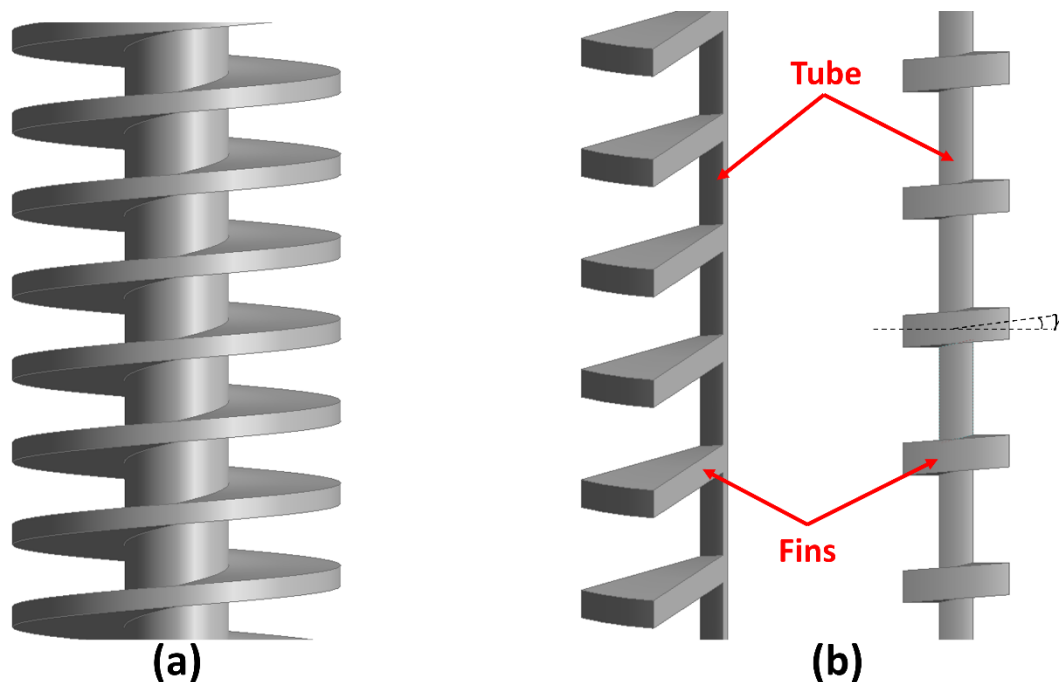


Figure 76. Geometries of circular fins following a helical pattern for different angular sectors. (a) 360° (b) 22.5°

The simulations employ the 'CC' model to ensure accurate modelling of fluid flow within the liquid phase. Figure 77 shows the evolution in time during the charging phase of the PCM's melted fraction for both geometric configurations. It can be observed that both simulations yield identical results, as evidenced by the overlapping curves. From a global point of view, simplifying the geometry by constraining the angular sector of the represented domain has no noticeable impact on thermal exchange within the storage system. Moreover, this reduction in the domain fraction represented in the CFD simulations results in a substantial decrease in computational costs by reducing the number of mesh elements used for domain discretization. Consequently, the influence of fin inclination on the thermal performance of the storage system

can be sufficiently assessed through CFD simulations without the need for modelling the entire geometry of the heat transfer tube, fins, and PCM domain.

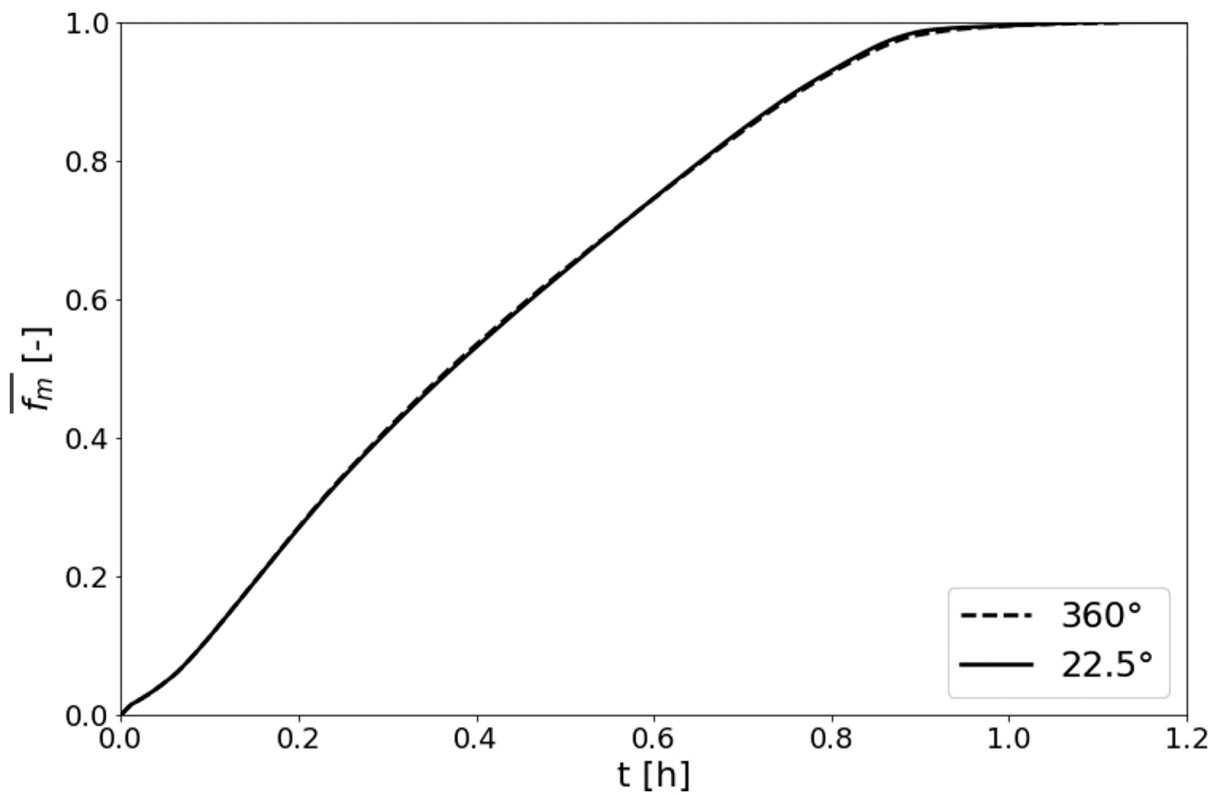


Figure 77. Evolution in time of the PCM's melted fraction for different angular sectors

IV.4.2. Melted fraction

Figure 78 shows the evolution in time of the PCM's melted fraction resulted for both circular and longitudinal fins with and without the consideration of natural convection in the melted phase. When natural convection is neglected (as indicated by the dashed-curves in Figure 78), longitudinal fins yield superior performances. At any given instant during the process, they achieve a higher melted fraction compared to the case with circular fins. As a result, the time required to completely melt the PCM volume was reduced from 2.14 h to 1.86 h when employing longitudinal fins instead of circular fins, resulting in a reducing of the melting time by approximately 13 %. This improvement is primarily due to the higher heat transfer area of the longitudinal fins, which enhances heat conduction from the heat transfer tube to the PCM region.

This trend shifts when the influence of natural convection within the liquid PCM phase is considered. The curves obtained from the 'CC' model simulations reveal that during the initial

stages of the charging phase, a faster melting process is achieved by longitudinal fins, owing to their superior heat conduction abilities, which represents the dominant heat transfer mechanism at this stage and is mainly governed by the surface area as seen above. However, upon comparing the curves obtained from both numerical models for each type of fin, it becomes evident that as the melting progresses, the influence of natural convection becomes increasingly pronounced for circular fins. Consequently, at approximately $t = 1.15$ hours, the melted fraction achieved with circular fins surpasses that attained with longitudinal fins. As a result, the total melting time achieved with circular fins is reduced by 18.4 % compared to longitudinal fins.

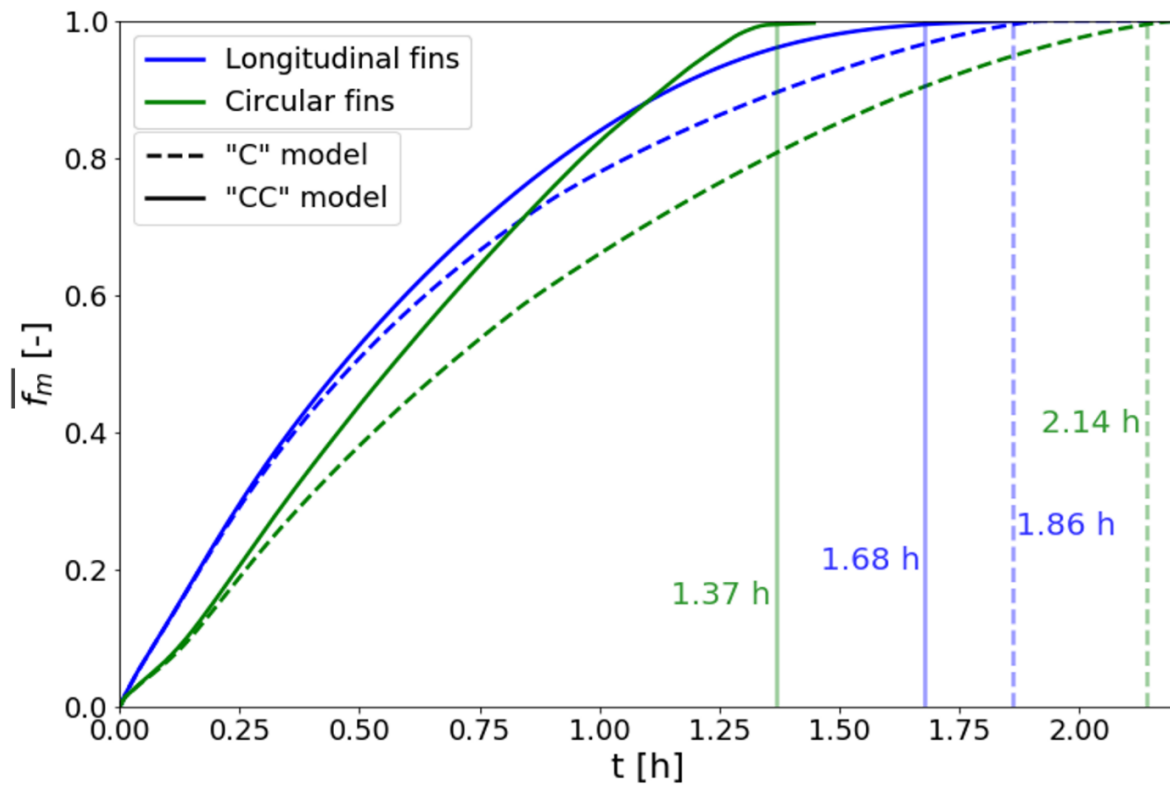


Figure 78. Evolution in time of the PCM's melted fraction for circular and longitudinal fins

The comparison between the outcomes of the 'C' model and the 'CC' model simulations reveals that the consideration of natural convection leads to a reduction in the total melting time. Specifically, for longitudinal fins, the total melting time decreases from 1.86 hours to 1.68 hours, representing a reduction of 9.6%. In the case of circular fins, the reduction is more pronounced, with the total melting time decreasing from 2.14 hours to 1.37 hours, amounting to a substantial 35.9% decrease.

The relatively lower impact of natural convection in the case of longitudinal fins may be related to the observations discussed in the previous section regarding smooth-tube systems. Despite

facilitating movement in the liquid phase and a higher surface exchange, the extensive convection loops that extend throughout the entire PCM volume do not promote the rapid recirculation of the PCM, as is the case with circular fins. This limitation may constrain the enhancements resulting from natural convection. This observation will be further explored in the following subsection by analyzing temperature distributions in the storage for both types of fins.

IV.4.3. Temperature distribution

The temperature distributions within the heat transfer tube, PCM region and fins are displayed in Figure 79 for circular and longitudinal fins, as obtained by both ‘C’ model and ‘CC’ model simulations. Similar to the smooth-tube cases, the temperature scale ranges between the PCM’s solidus temperature of 303.3 °C and the constant threshold temperature set at the tube’s inner wall of 315 °C. For the circular radial fins, the presented temperature profiles correspond to a vertical plane intersecting the center of three consecutive fins situated in the center of the domain. In the case of longitudinal fins, horizontal planes crossing the tube’s wall, PCM and fin volumes are considered. In the ‘CC’ model simulations, temperature profiles at three distinct levels along the domain height are presented. This approach allows the assessment of the impact of natural convection on the localized progression of the melting process. These three levels are situated at 10%, 50%, and 90% of the domain height, resulting in heights of 5.4 cm, 27 cm, and 48.6 cm with reference to the bottom of the domain, respectively. In the ‘C’ model simulations, temperature is distributed uniformly in the axial direction; hence, the temperature profile is provided solely at 27 cm height.

At $t = 0.25$ h (Figure 79 (a)), the temperature of the tube’s wall is at the peak level of 315 °C. The initial stage of the PCM melting commence near the external surface of the heat transfer tube. Nevertheless, the majority of the PCM remains in a solid state, with temperatures below the designated solidus temperature of 303.3 °C. In contrast, the temperature levels across the fin volumes are notably higher, primarily attributed to the significantly higher thermal conductivity of the metallic material used for the fins. As a result, the temperature profile assumes a shape conforming to the geometry of the fins in each case. In the case of circular radial fins, when natural convection is not considered (‘C’ model), a symmetrical temperature distribution forms around the fins. In this distribution, the PCM temperature decreases as one moves away from the fins in the vertical direction. The same observation applies for the

temperature distribution in the horizontal direction in the case of longitudinal fins. When natural convection is taken into account (using the ‘CC’ model), small convective loops develop within the PCM’s melted volume, located between two circular fins. These movements result in a more advanced melting front beneath the bottom surface of each fin, where relatively hotter PCM accumulates. This accumulation is represented by small red spots (high temperature) below the circular fins, as shown in the ‘CC’ model plot in Figure 79 (a)). For longitudinal fins, the influence of natural convection on the temperature distribution is less pronounced at this stage of the charging process. Additionally, nearly identical temperature profiles are observed at various heights within the domain.

As the charging process continues, by the time $t = 0.75$ h (Figure 79 (b)), the entire surfaces of the fins are surrounded by melted PCM. In the case of circular fins, the melting progresses in both radial and axial directions, and the impact of natural convection on the temperature profile intensifies. A comparison of the temperature contours generated by both the ‘CC’ model and the ‘C’ model simulations reveals that the melting of the PCM is more advanced when natural convection is considered. Furthermore, the melting front (indicated by blue spots on the contour) resulting from the ‘CC’ model appears sharper in contrast to the more rounded front obtained in the ‘C’ model. For longitudinal fins, natural convection contributes primarily to the distortion of the temperature distribution along the height of the domain. At the bottom of the domain ($h = 5.4$ cm), the melting of the PCM resulted from the ‘CC’ model simulations is less advanced compared to that one obtained from purely conductive calculations. Conversely, at the top of the domain ($h = 48.6$ cm), the melting front has already extended beyond the fins tip in the radial direction. At this stage, the overall melted fraction of the PCM is 0.7 for the model with convection and 0.66 for the one without convection. Despite the significant disparity in temperature contours at various positions along the tube, the actual impact of natural convection on the storage’s overall performance is limited.

At $t = 1.25$ h (Figure 79 (c)), in the presence of natural convection, the entire PCM volume has melted in the case of circular fins. The charging process now continues in the form of sensible heat in the liquid PCM volume until its temperature reaches the maximum value of 315 °C. For longitudinal fins, at the top of the domain, the tube’s wall, fins and PCM region have all reached the threshold temperature of 315 °C. However, the melting process is ongoing, with a portion of the PCM yet to melt at the bottom.

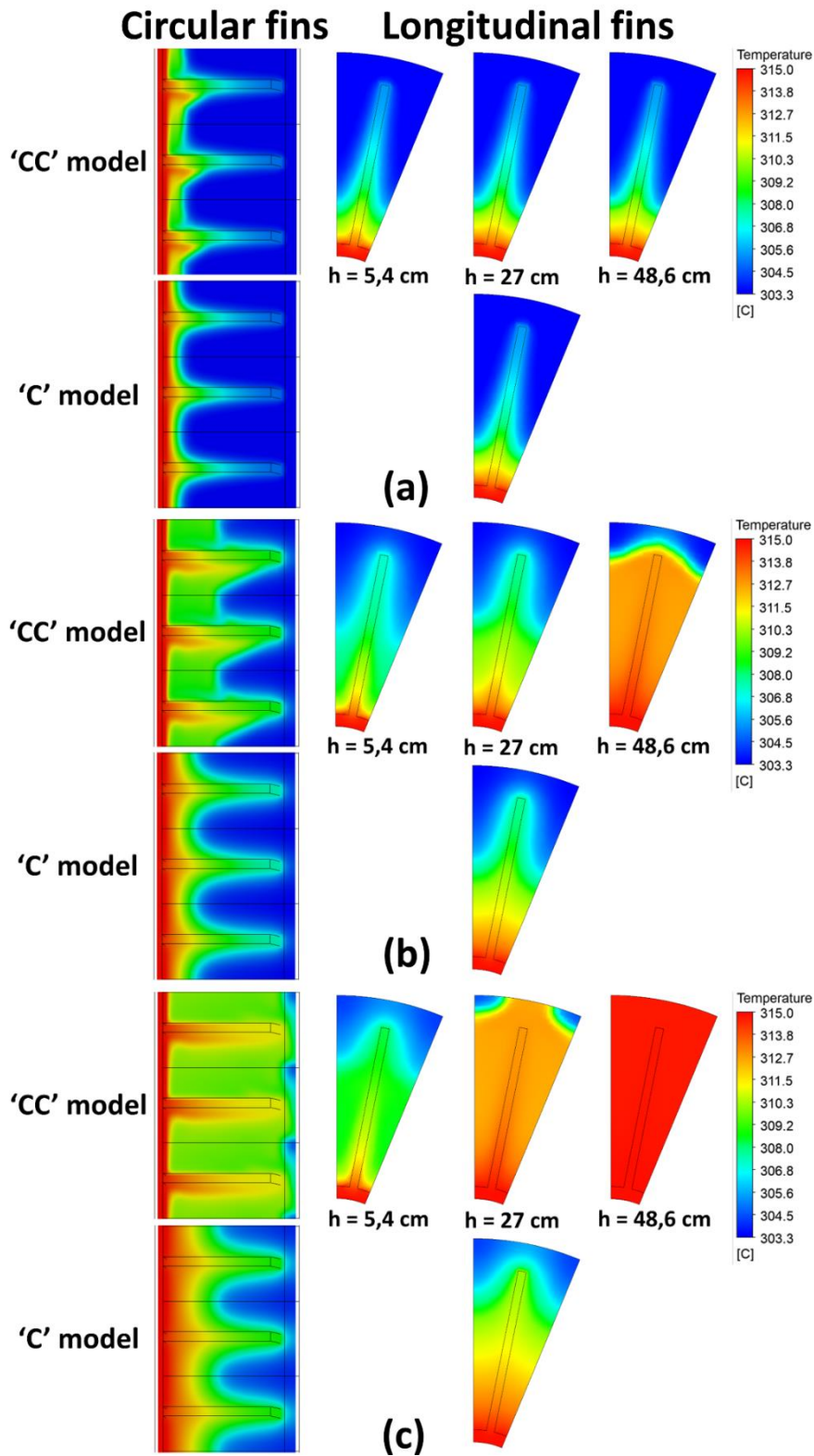


Figure 79. Temperature distribution within the tube, fins and PCM regions for circular and longitudinal fins at three instants (a) $t = 0.25 h$ (b) $0.75 h$ (c) $1.25 h$

In summary, axial longitudinal fins exhibit superior heat conduction compared to circular radial fins, primarily due to their higher heat transfer area per unit volume. However, in the case of

shell-and-tube storages using PCM, natural convection plays a crucial role in determining the system's thermal performance. Comparing the outcomes with these two fin types revealed that the use of circular fins amplifies the influence of natural convection on the overall heat exchange within the storage system. This aligns with the results obtained from simulations on smooth-tube configurations, where the excessive increase in the length of natural convection loops restricted the total heat transfer rate in the storage. Hence, in order to maximize the heat exchange and optimize the thermal power of the storage, it is essential to cut large natural convection loops along the vertical tube and to force the recirculation of the liquid PCM through smaller convective loops.

In the following section, a detailed parametric study concerning the influence of key geometric factors and material properties of circular radial fins on the thermal behavior of LHTES systems is conducted. Additionally, an in-depth analysis of how the fluid circulation in the liquid phase affects the charging process is performed using the 'C' and 'CC' numerical models.

IV.5. Tube with circular fins: effect of the geometry

The studies conducted in the previous section have established the crucial role of natural convection and circular radial fins in improving the thermal performance of vertical LHTES systems. In this section, a series of parametric studies will be conducted to examine the influence of different geometric parameters and material properties that constitute circular fins on the behavior of the storage during the charging phase.

Figure 80 illustrates the base 3D geometry containing the heat transfer tube, circular fins and PCM domain used in CFD simulations. The geometric parameters under investigation are the fin length ' l_{fin} ', thickness ' e ' and the pitch ' p ' corresponding to the distance between the centers of two consecutive fins. Following that, the influence of the properties of the constituent material forming the heat transfer tube and fins on the heat exchange mechanisms inside the storage will be investigated.

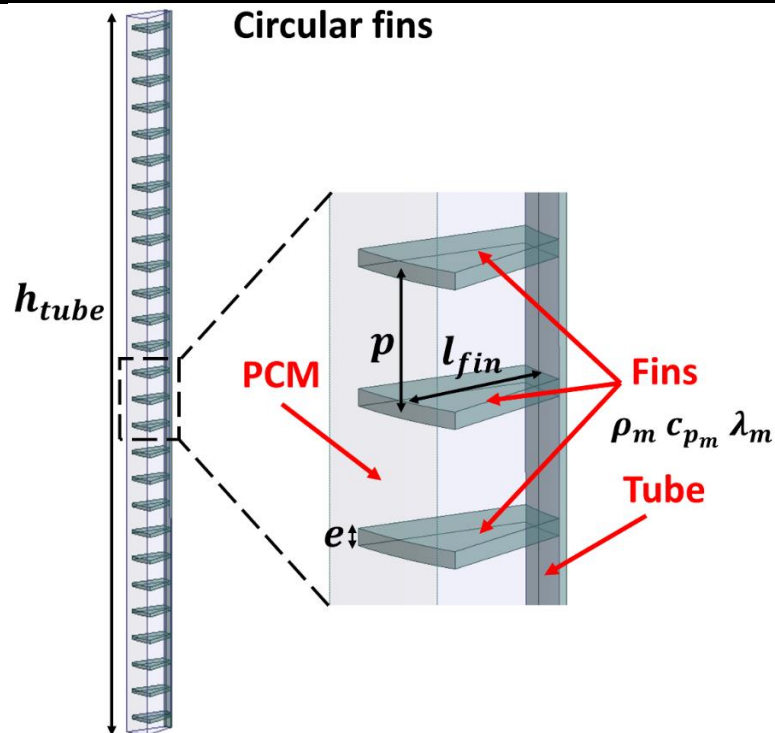


Figure 80. Geometric domain with circular fins used in the CFD model

IV.5.1. Effect of fin length

To examine the impact of fin length on the thermal performance of the storage system, three configurations are considered with l_{fin} values of 26 mm, 30 mm and 34 mm, respectively. For all cases, the fin thickness and pitch remain constant at 3 mm and 20 mm, respectively. The tube length h_{tube} is maintained at 50 cm, resulting in 25 fins arranged on the tube's external surface. Both the heat transfer tube and the fins are constructed from the same steel material as in the previous sections. Detailed material properties for the steel and the PCM can be found in Table 3. The influence of fin length on convective heat exchanges within the melted phase is studied by performing two simulations for each configuration, using the 'C' and 'CC' models described earlier in this chapter.

Figure 81 shows the evolution of the PCM's melted fraction during the charging process for different fin length values, as obtained from the two numerical models. Regardless of the consideration of natural convection in the liquid phase, increasing the fin length enhances the thermal power of the storage by reducing the time required to melt the entire PCM volume. In the case of pure conductive simulations (represented by dashed curves in Figure 81), the total melting time decreases from 2.7 h to 1.97 h and 1.7 h as the fin length increases from 26 mm to 30 mm and 34 mm, respectively. Meanwhile, when natural convection is accounted for, the

total melting time decreases from 1.74 h to 1.26 h and 1.12 h for the same configurations. In both cases, the improvement is similar for the ‘C’ and ‘CC’ model, with an increase of 27% and 37% in the first case for 27.6% and 35.6% in the convective case. Therefore, improvement of the thermal power of the storage as fin length increases is attributed to the expansion of the heat transfer area between the fins and the PCM domain. The elongation of the fins facilitates the melting of the PCM volume located further away from the heat transfer tube, near the external boundary of the domain.

The influence of natural convection varies depending on the state of the PCM within the storage system. In the initial stages of the melting process, when most of the PCM is still solid, both the ‘C’ and ‘CC’ models yield similar predictions. However, the impact of natural convection becomes increasingly significant as the melting progresses. Consequently, accounting for natural convection reduces the total melting time by 35.5 %, 36 % and 34.1 % for l_{fin} values of 26 mm, 30 mm and 34 mm, respectively. In conclusion, concerning circular radial fins, the enhancements in the thermal power of the storage system due to natural convection are not primarily dependent on the length of the fins in the radial direction. Nevertheless, it is important to note that the influence of natural convection on the system's power remains significant and cannot be disregarded when sizing a similar storage system.

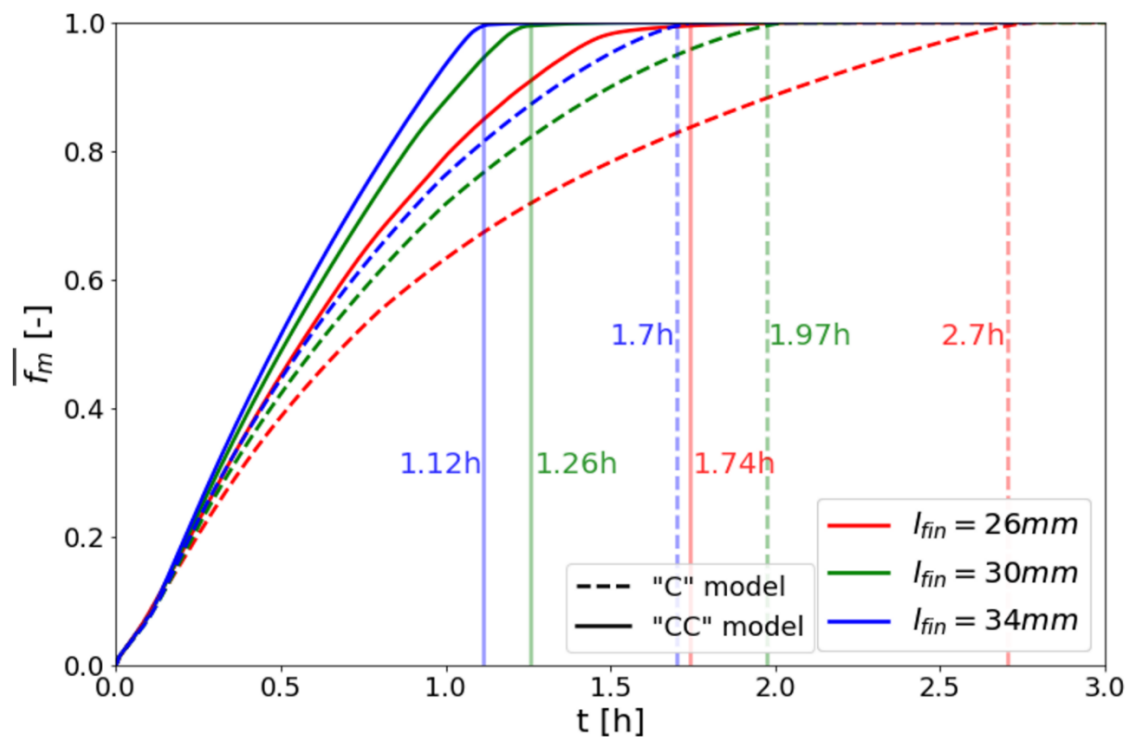


Figure 81. Evolution in time of the PCM's melted fraction for different fin length values

From a global point view, the reduction in fin length affects the overall thermal performance of the storage system, primarily because it constrains the fins' capacity to efficiently conduct heat within the PCM volume. Moreover, diminishing the fin length can influence the uniformity of heat transfer across various levels along the domain's height. Figure 82 shows the distribution of the local melted fraction of PCM along the axial height of the domain for various fin length values. The dashed vertical lines indicate the average melted fraction of the PCM. When 10 % of the PCM has melted, the volume is evenly distributed along the height of the domain, regardless of the specific fin length under consideration. At the midpoint of the charging process, with f_m equal to 0.5, the influence of fin length on the local progression of the melting process remains minimal. However, a relatively advanced / delayed local melted fraction is observed at the extreme top / bottom section of the domain. At this stage, with the liquid PCM confined between the fins, the occurrence of the phenomenon is attributed to natural convection movements in the liquid PCM, which forces heat to traverse the surfaces of the fins in an upward direction, resulting in vertical heat exchange within the storage. A more comprehensive analysis of the heat exchange distribution at the fin surfaces will be provided in the forthcoming sections. The main difference in the heat distribution along the height of the domain, among different fin length values, becomes evident during the later phases of the melting process. At $\overline{f_m} = 0.95$, the distribution of the local melted fraction is less uniform for the shortest fin length, with $l_{fin} = 26$ mm. In fact, as the melting front advances beyond the fin tips, natural convection loops are no longer constrained within the space between two adjacent fins. Instead, these smaller loops interconnect to form a larger loop extending the entire length of the domain. This phenomenon can lead to an accelerated or decelerated melting process at the upper or lower boundaries of the domain, as observed in the case of longitudinal fins or for smooth-tubes with high domain heights.

In summary, when considering circular radial fins, the improvements attributed to natural convection are independent on the radial length of the fins. However, the fin length does play a direct role in enhancing heat conduction, thereby contributing to an overall improvement in the thermal power of the storage system. Moreover, shorter fins that do not extend to the external boundary of the domain can result in a distorted progression of the melting process along the axial direction when it surpasses the fin tips. In the upcoming sections, the influence of fin pitch and thickness on the thermal behavior of the storage will be examined. During these studies, a fixed fin length of 34 mm will be retained.

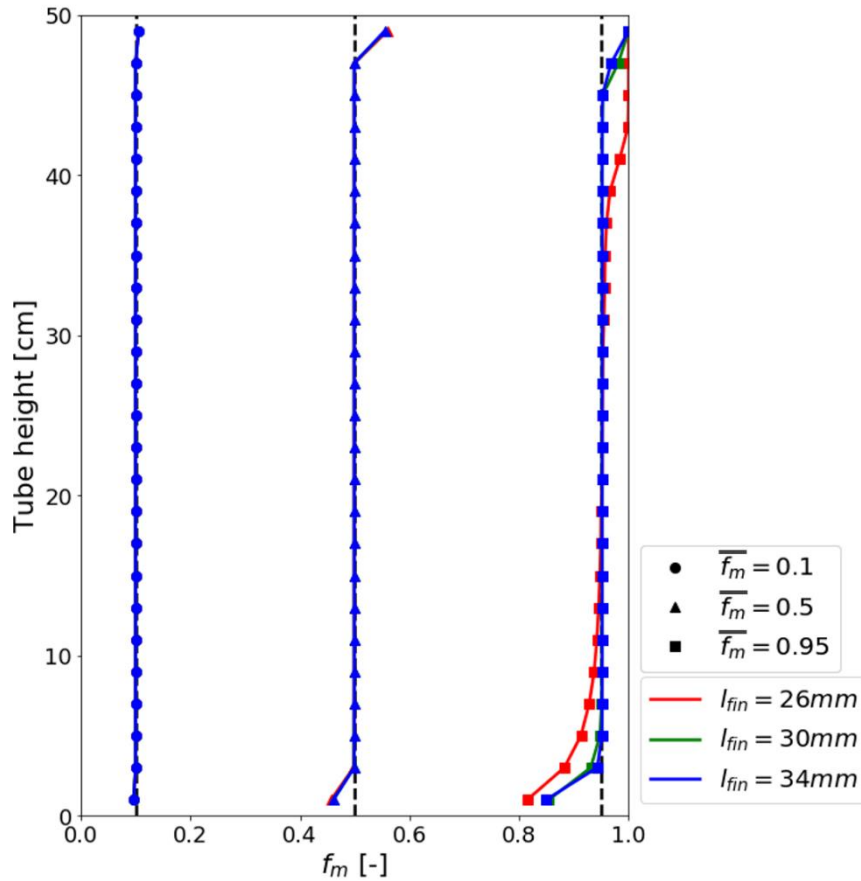


Figure 82. Distribution of the PCM's melted fraction along the domain for different fin length values

IV.5.2. Effect of fin pitch and thickness

In this section, the focus shifts to different geometric parameters of the fins, specifically the fins' pitch ' p ' and thickness ' e ' (Figure 80). All other geometric parameters regarding the heat transfer tube and the PCM domain remain identical with the descriptions provided in section IV.2.1. Throughout the analysis, a constant fin length of 34 mm is maintained. Both the heat transfer tube and the fins are constructed from steel. The PCM in use is still sodium nitrate, with all thermo-physical properties matching the descriptions provided in Table 3.

In total, a set of 50 distinct geometric configurations will be examined (Figure 83 and Table 9). To achieve this, ten evenly distributed values of the pitch ' p ', ranging from 2.5 mm to 25 mm, have been considered. For each pitch value, the fins' thickness ' e ' is adjusted based on a fixed thickness-to-pitch ratio ' e/p '. Five ratios are considered by uniformly incrementing ' e/p ' between 5 % and 25 %. The selected ratios are chosen to fulfil specific constraints. For instance, decreasing ' e/p ' reduces the presence of fins in the storage, leading to a significant decrease in the thermal power of the system. Conversely, excessively increasing the volumetric fraction of

the fins may restrict the amount of energy that can be stored within a given geometric domain. Moreover, fixing the ‘ e/p ’ ratio within each set is essential to maintain a consistent mass fraction of PCM during the evaluation of the storage performance. To ensure an integer number of fins, the tube’s height h_{tube} is slightly adjusted and varies across cases. Table 9 summarizes the design parameters of all the configurations of fins studied. Lastly, as in previous studies, the influence of natural convection on the melting progress in the storage is investigated by performing two simulations using the ‘C’ and the ‘CC’ models in each case.

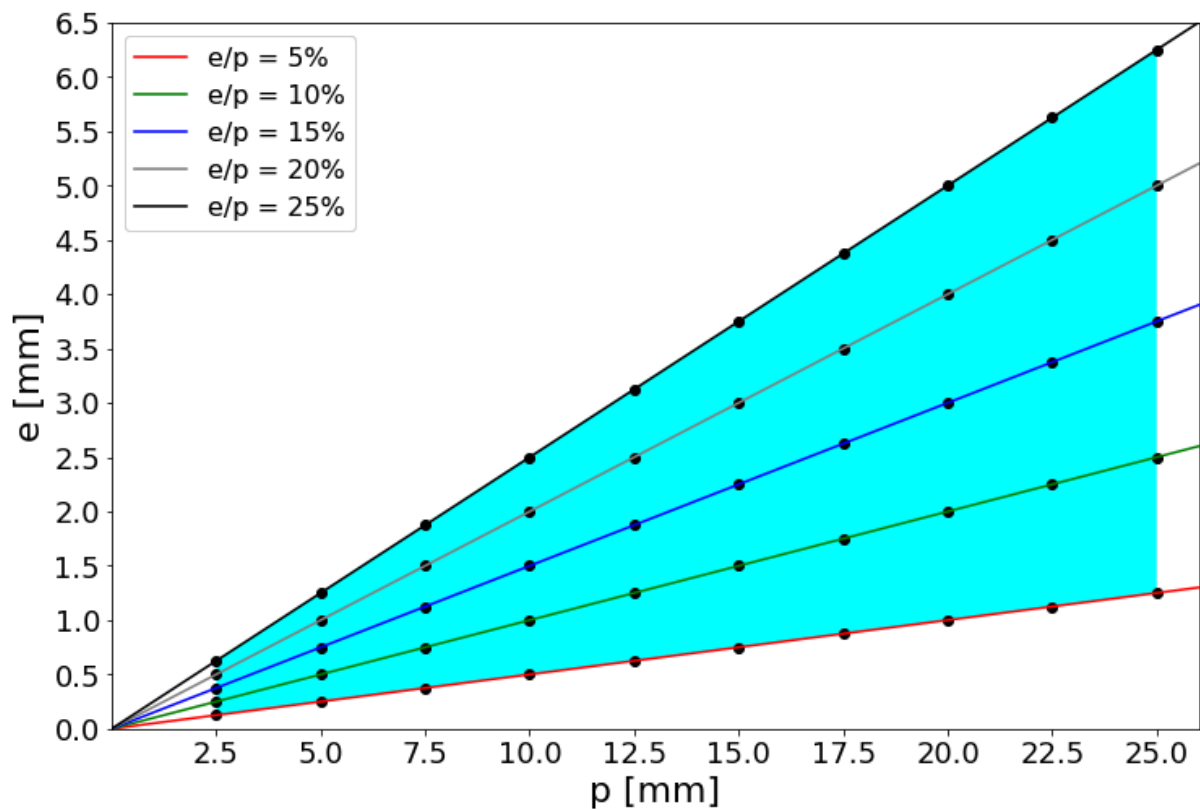


Figure 83. Studied fin configurations, e : thickness, p : pitch

Case n°	p [mm]	e [mm]	Number of fins	Tube’s height [cm]
1	2.5	0.125	200	50
2		0.25		
3		0.375		
4		0.5		
5		0.625		
6	5	0.25	100	50
7		0.5		
8		0.75		
9		1		
10	7.5	1.25	66	49.5
11		0.375		
12		0.75		
13		1.125		

Teddy CHEDID – 2023

14		1.5		
15		1.875		
16	10	0.5	50	50
17		1		
18		1.5		
19		2		
20		2.5		
21	12.5	0.625	40	50
22		1.25		
23		1.875		
24		2.5		
25		3.125		
26	15	0.75	33	49.5
27		1.5		
28		2.25		
29		3		
30		3.75		
31	17.5	0.875	28	49
32		1.75		
33		2.625		
34		3.5		
35		4.375		
36	20	1	25	50
37		2		
38		3		
39		4		
40		5		
41	22.5	1.125	22	49.5
42		2.25		
43		3.375		
44		4.5		
45		5.625		
46	25	1.25	20	50
47		2.5		
48		3.75		
49		5		
50		6.25		

Table 9. Study parameters

IV.5.2.1. Melted fraction

The substantial number of tested cases presents a challenge in terms of representing and drawing comprehensive conclusions from the PCM's melted fraction curves throughout the entire charging process. As an alternative approach, specific instants during the process are selected. At these instances, the melted fraction values resulting from the two numerical models are presented in the form of heatmaps in Figure 84. The melted fraction curves for the 50 configurations can be found in Appendix A.

During the initial stages of the charging process, at $t = 0.3$ h, both models predict similar results with a limited difference in the $\overline{f_m}$ values that does not exceed 3 % at most. Indeed, at this stage, the PCM's melted volume is still insignificant to generate movements within the liquid phase. Therefore, the heat is mainly transferred by conduction. However, the impact of the geometric configuration of the fins on the melted fraction is already noticeable. By decreasing the pitch ' p ' (i.e., moving from right to left on the x-axis in Figure 84), the number of fins used per unit length of the tube increases, resulting in a larger heat transfer surface between the fins and the PCM which, in turn, enhances the system's thermal power. In addition, for any given pitch value, increasing the ' e/p ' ratio (i.e., moving from bottom to top on the y-axis in Figure 84) increases the melted fraction. At $t = 0.6$ h, the impact of the pitch ' p ' and the ratio ' e/p ' on the $\overline{f_m}$ values in the 'C' model continues to exhibit the trend just mentioned hereinbefore. However, at this time, the melting process has already finished for the configuration with lowest ' p ' value of 2.5 mm and the highest ' e/p ' value of 25 %. For the 'CC' results, maximum $\overline{f_m}$ values are appearing along the ' p ' range for any given ' e/p ' ratio. In other words, as the pitch decreases from 25 mm, the $\overline{f_m}$ values increase until reaching a peak at a particular pitch value, beyond which further decreases in pitch lead to a drop in the $\overline{f_m}$ values. At $t = 0.9$ h, nearly all the PCM has melted for ' e/p ' values of 20 % and 25 % in the 'CC' model. For lower ' e/p ' ratios of 5 %, 10 % and 15 %, the configurations with a pitch value of 7.5 mm give the highest melted fraction along the corresponding p-axis, with values of 0.55, 0.79 and 0.98 respectively. By 1.2 h, almost all the PCM has melted for ' e/p ' ratios greater than 5 % in the 'CC' model. Moreover, the disparity between the results obtained from both models continues to widen. For example, for $e/p = 5$ %, the 'C' model's melted fraction ranges from 0.43 to 0.52 along the p-axis, while the 'CC' model's melted fraction peaks at 0.72 for $p = 10$ mm. Finally, after 1.5 h, the charging process has ended for all configurations with $e/p > 5$ % in the 'CC' model simulation. In comparison to a smooth-tube TES (refer to section IV.3), around 25 % of the PCM only had melted after the same period of 1.5 h (Figure 72). This indicates that adding fins, regardless of their volume and distribution, results in a considerable reduction of the melting time, leading to an improvement of the storage's thermal power.

To sum up, in a LHTES system with circular radial fins, increasing the thickness of fins for a given pitch consistently enhances the thermal power of the storage, regardless of the heat transfer mechanism within the liquid PCM. Additionally, reducing the pitch for a given ' e/p '

ratio (i.e. given fin volume), promotes better conduction of the heat through the PCM, despite the decrease of the fins thickness to maintain the ‘ e/p ’ ratio. However, this reduction in pitch limits natural convection contribution, resulting in a competition between both mechanisms and therefore the existence of an optimal configuration. The contribution of natural convection to the storage behavior will be further detailed in the following sections.

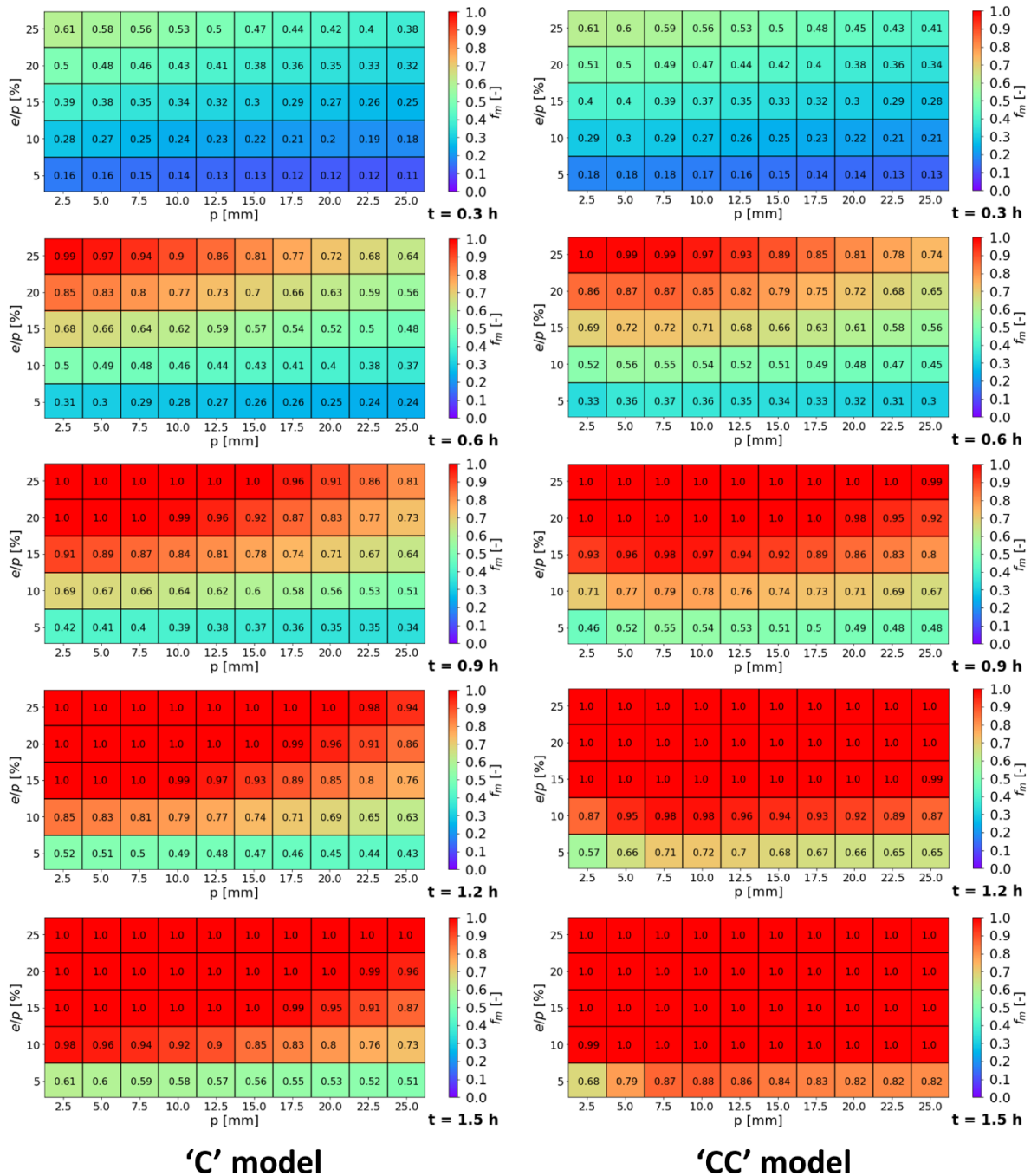


Figure 84. Comparison of the PCM's melted fraction, \bar{f}_m , at different instants for the two models, 'C' (on the left) and 'CC' (on the right)

IV.5.2.2. Influence of natural convection: melting time ratio

To quantitatively elaborate the influence of natural convection on the melting process of a vertical LHTES for different geometric parameters of circular radial fins, the time ratio to melt a given fraction of the PCM with and without the consideration of natural convection is presented in this section. It is defined as follows:

$$t_{cc/c}|_{\bar{f}_m} = \frac{t_{cc}|_{\bar{f}_m}}{t_c|_{\bar{f}_m}} \quad (107)$$

Figure 85 illustrates, using heatmaps the $t_{cc/c}$ values for all the tested geometric configurations at several values of the melted fraction \bar{f}_m during the charging process. Since natural convection always speeds up the melting process, leading to a ratio $t_{cc/c}|_{\bar{f}_m} < 1$, the heatmaps use a color scale ranging from 0.45 to 1. Cooler colors on the scale indicate a significant difference between the model predictions, while warmer colors indicate good agreement between the two models. When $\bar{f}_m = 0.2$, most of the PCM is still in solid state, $t_{cc/c}$ is greater than 85% in almost all cases. This indicates that, at this stage, a ‘C’ model can be used without significant error, regardless of the configuration. Then, for $\bar{f}_m = 0.5$, i.e. when half of the PCM has already melted, the dependence of $t_{cc/c}$ on the geometric configuration of the fins becomes more noticeable. The tendency of improvement due to natural convection goes toward increasing the pitch and decreasing the fins’ thickness to pitch ratio. For instance, for the configuration ($p = 25$ mm and $e/p = 5$ %), the inclusion of natural convection reduces the time needed to melt half of the PCM to 65 % compared to a purely conductive heat transfer mechanism. This time ratio increases all the way to 99 % for the configuration ($p = 2.5$ mm and $e/p = 25$ %). For $\bar{f}_m = 0.8$ and 0.98 , the values $t_{cc/c}$ keep decreasing, indicating that the significance of natural convection on the charging process grows with increasing melted fraction. Therefore, the prediction of the behavior of the storage system using the ‘C’ model would become less precise. Nevertheless, the inaccuracy on the charging time due to the neglect of natural convection remains below 20 % for several configurations (17/50 for $\bar{f}_m = 0.98$ and 38/50 for $\bar{f}_m = 0.8$). Consequently, this result can serve to estimate the storage’s over-sizing if the dimensioning was based on a pure conductive heat transfer mechanism in the liquid PCM. In fact, pure conductive models offer a substantial reduction in computational costs. This is primarily due to the fact that only the energy equation is solved, with no consideration of velocities in the liquid

phase. Consequently, evaluating the impact of neglecting natural convection becomes essential in determining when the ‘C’ model can provide an accurate and relatively fast sizing of the storage system.

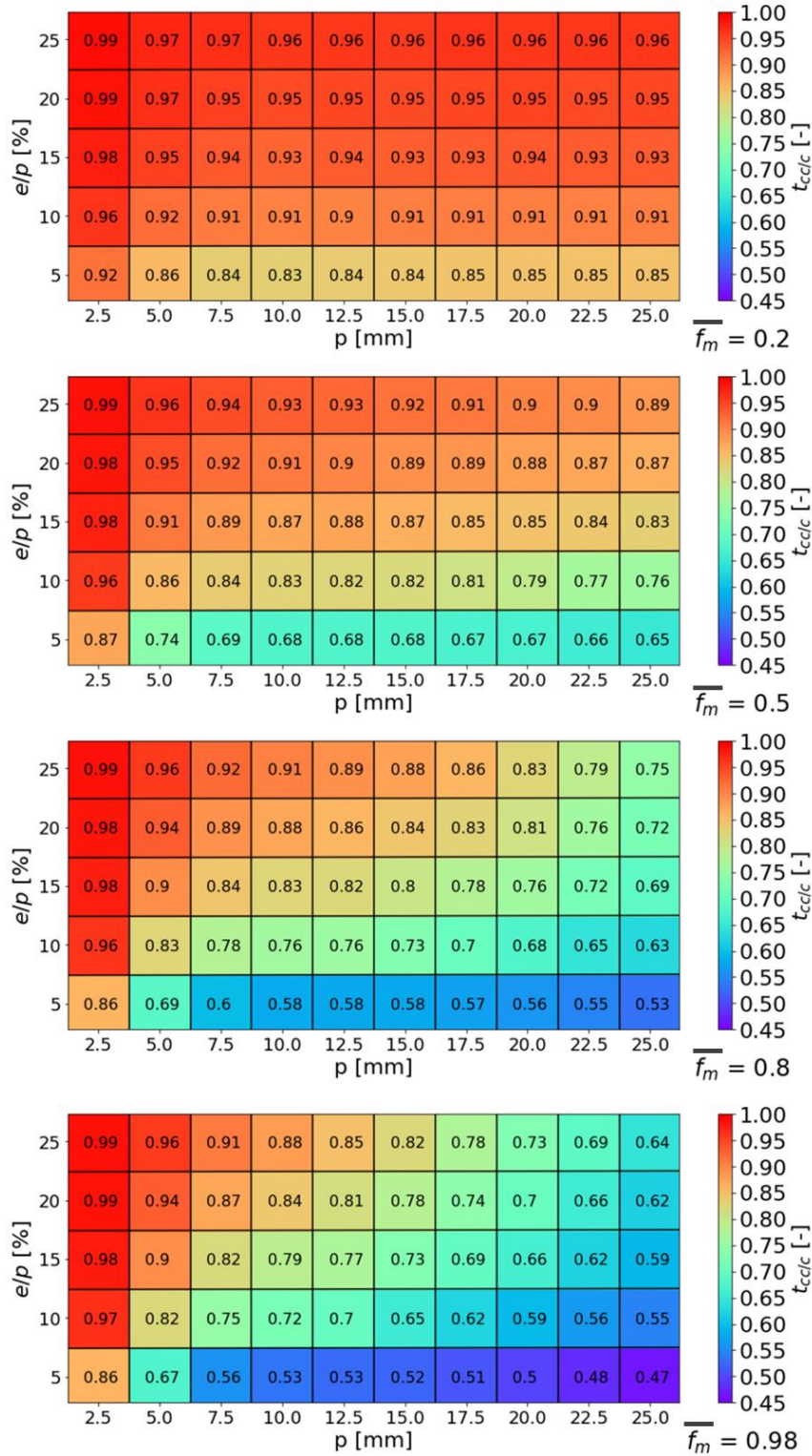


Figure 85. Distribution of the time ratio to melt a PCM fraction with and without natural convection

IV.5.2.3. Temperature and velocity distributions

To better understand the impact of the thickness of fins on the PCM’s melting, Figure 86 shows the temperature distribution and velocity vectors on a vertical plane crossing the tube, fins and PCM domains. The results presented correspond to cases 46, 48 and 50 in Table 9 where ‘ p ’ is the same at 25 mm and ‘ e/p ’ is respectively 5 %, 15 % and 25 %. These particular configurations were selected because at this pitch, the charging process of the storage system is most impacted by natural convection. Moreover, the three selected configurations have nearly identical heat transfer surface between the metallic components (tube + fins) and the PCM region of around 0.66 m² per unit length of tube. Three instants during the charge phase are considered where in each; the results obtained from both numerical models are presented.

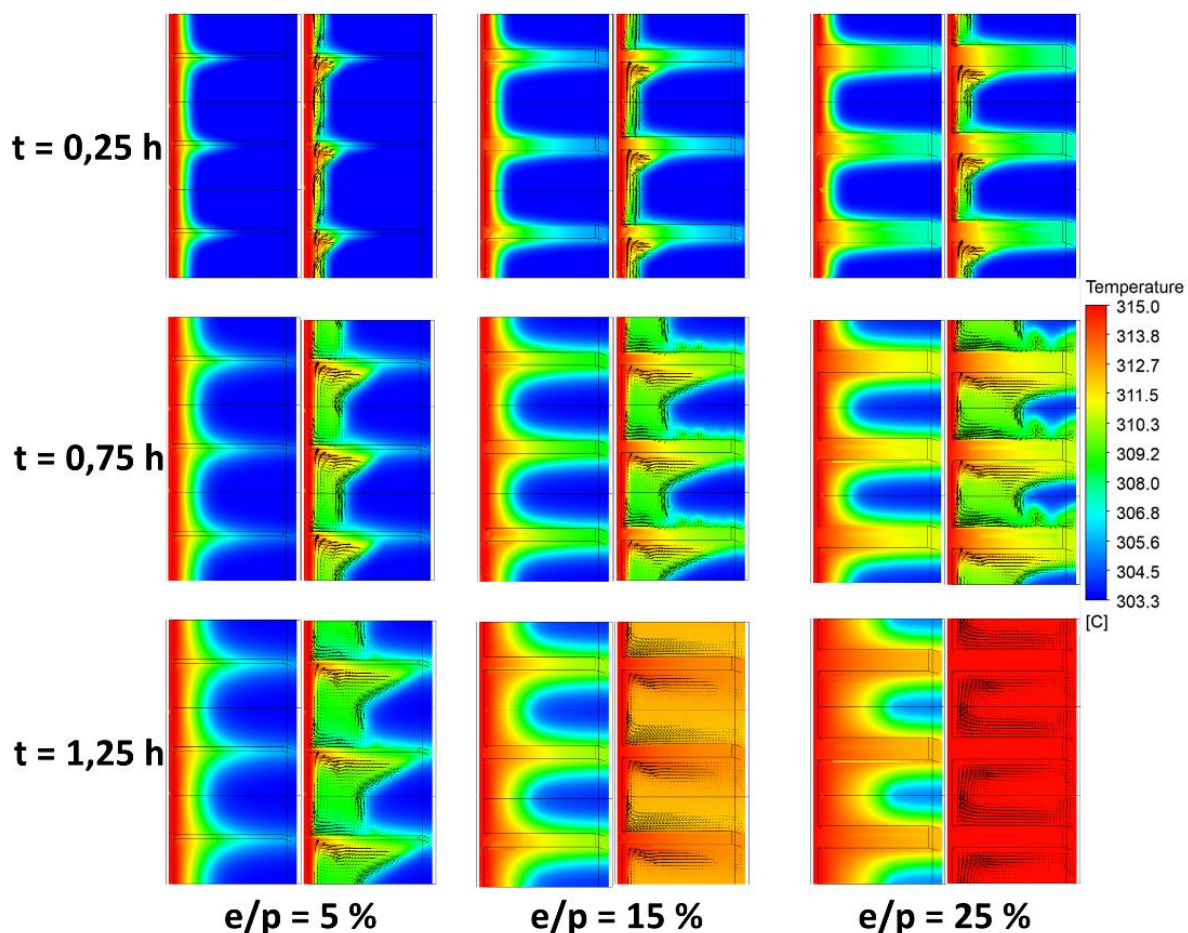


Figure 86. Comparison of the temperature and velocity distributions in the tube + fins + PCM domains for different fins’ thickness for a given pitch of 25 mm. ‘C’ model (left), ‘CC’ model (right)

At $t = 0.25$ h, the melting process is at initial stages and starts propagating radially away from the hot heat transfer tube, leading to a temperature gradient in that direction. However, the

influence of the fins' thickness on the temperature distribution is already significant. In the case of the thinnest fins ($e/p = 5\%$), the temperature is almost uniform in the vertical direction. Despite being highly conductive relatively to the PCM, a significant part of the fins remains at the same temperature as the PCM. The heat transferred to the PCM is mainly at the tube's external wall. Hence, the contribution of the fins to the heat exchange process is not that significant. By increasing the thickness of the fins (for $e/p = 15\%$ and 25%), the temperature at the tip of the fins becomes relatively higher with respect to thinner fins. Consequently, a higher fins' area is contributing to the heat conducted to the PCM region leading to a greater melted fraction at any given instant, and accordingly a better thermal power of the storage. Table 10 groups the melted fraction values resulted from both numerical models at the three instants as well as the maximum velocity of the liquid PCM in the 'CC' model. Although u_{max} reaches 3.43 mm/s for $e/p = 25\%$, the impact of considering natural convection in the liquid phase is still insignificant at this stage. The melted fractions obtained by both models differ by less than 1% . Consequently, at earlier stage the heat transfer in the storage is primarily driven by the fins configuration, rather than natural convection movements.

At $t = 0.75\text{ h}$, the temperature level within the fins has increased compared to the temperature at 0.25 h . The 'C' model predicts a symmetric temperature distribution around the fins, with thicker fins leading to higher temperature values. In the 'CC' model, the behavior is quite different, for $e/p = 5\%$, the circulations in the liquid phase carry the hot PCM to the bottom surface of the fins, leading to a non-uniform temperature distribution. As a result, the highest temperatures of the PCM are located below the fins. For thicker fins with an ' e/p ' ratio of 15% and 25% , when natural convection is taken into account, the remaining solid PCM is surrounded by melted PCM in both horizontal and vertical directions. This creates smaller loops above and below the solid phase, leading to an additional contribution of natural convection to the improvement of thermal performances compared to 'C' simulations. As listed in Table 10, after 0.75 h of the charging process, the melted fraction for $e/p = 15\%$ and 25% increases from 0.56 and 0.72 , respectively, to 0.68 and 0.88 , respectively, when natural convection is considered.

After 1.25 h , the temperature in the 'C' simulations consistently increases. Additionally, as the ' e/p ' ratio increases, the rate of melting accelerates: the melted fraction $\overline{f_m}$ for $e/p = 5\%$, 15% and 25% is respectively 0.44 , 0.78 and 0.95 (Table 10). For the calculations with natural

convection, the melting process is over for $e/p = 25\%$ ($\overline{f_m} = 1$), the temperature throughout the tube's wall, the fins and the PCM region is at uniform at $315\text{ }^\circ\text{C}$. For $e/p = 15\%$, the majority of the PCM has melted ($\overline{f_m} = 0.99$), the charging of the sensible heat in the liquid PCM continues until its temperature reaches the threshold value of $315\text{ }^\circ\text{C}$. For thinner fins with $e/p = 5\%$, a single natural convection loop in the liquid PCM is present, leading to higher temperature values beneath the fins. As the melting front evolves radially, the remaining solid fraction also melts from the top causing a non-uniform temperature distribution. However, in comparison to ' e/p ' ratios of 15% and 25% , only 67% of the PCM has melted at this stage, resulting in a significantly slower charging process. The influence of natural convection on the melted fraction of PCM keeps increasing as time goes by.

		Time [h]		0.25	0.75	1.25
e/p [%]	5	Conduction Only	$\overline{f_m}[-]$	0.09	0.29	0.44
		Conduction + Convection	$\overline{f_m}[-]$	0.1	0.38	0.67
			$u_{max}[mm/s]$	1.66	2.25	2.08
	15	Conduction Only	$\overline{f_m}[-]$	0.2	0.56	0.78
		Conduction + Convection	$\overline{f_m}[-]$	0.22	0.68	0.99
			$u_{max}[mm/s]$	2.78	3.07	2.74
	25	Conduction Only	$\overline{f_m}[-]$	0.31	0.72	0.95
		Conduction + convection	$\overline{f_m}[-]$	0.34	0.88	1
			$u_{max}[mm/s]$	3.43	2.45	0.41

Table 10. PCM's melted fraction and maximum velocity for different fins' thickness for a given pitch of 25 mm

IV.5.2.4. Heat Flux distribution

To grasp more thoroughly on how the movements in the liquid phase enhance the thermal performances of a LHTES, the heat flux distribution in the storage is investigated in this section. The previous results showed that for a given geometric configuration of circular radial fins, the performance of the storage varies during the melting progress. It was also shown that, for cases with radial fins, natural convection enhancements become more significant as the liquid phase volume develops (refer to Figure 85). Figure 87 shows the evolution of the total heat flux per unit length of tube exchanged at the inner tube wall for a fins' pitch of 20 mm and thickness of 3 mm (case 38 in Table 9). Since a fixed temperature is imposed as boundary condition on the tube's inner wall, the total thermal power of the storage system drops during charging phase. By comparing the results obtained from both numerical models, it can be observed that for a very small melted fraction ($\overline{f_m} < 5\%$), both curves overlap. As the melting progresses, the 'CC' simulations results in a higher thermal power with respect to the 'C' model. Additionally, the

difference between the two curves increases as the charging process continues. The maximum difference observed at $\bar{f}_m = 98\%$, where the ‘CC’ model predicts a heat flux that is 2.25 times greater than that predicted by the ‘C’ model.

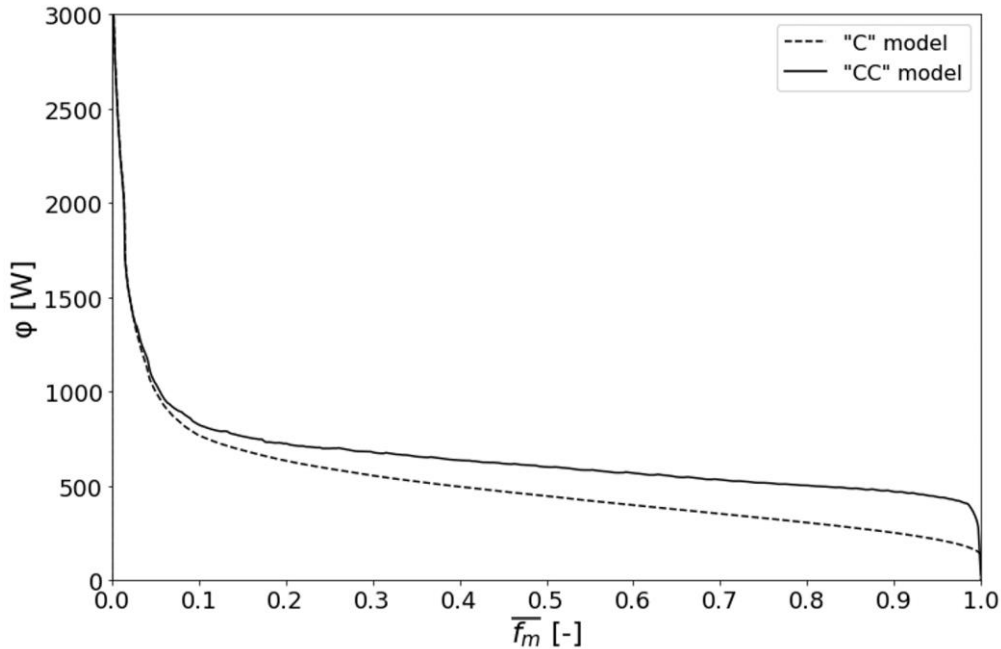


Figure 87. Variation of the total heat flux per meter of tube with respect to the melted fraction for case 38

Figure 88 allows us to understand how the heat flux transferred to the PCM is distributed on the heat transfer surface formed by the external tube’s wall in contact with the PCM region and the surface of the fins. Top and bottom views of the same fin are shown at four instants during the process. A corresponding color scale is considered for each model to enhance the visualization of the heat flux distribution. Additionally, the melting front separating the PCM’s liquid and solid phases, defined here as the isosurface of $f_m = 0.5$, is shown on the graphs (semi-transparent gray surfaces).

At $t = 0.25$ h, the melted fractions obtained from the ‘CC’ model and the ‘C’ model are respectively 0.24 and 0.22. Despite this small difference, the heat flux distribution differs notably. Moreover, we observe that when natural convection is considered, a negative heat flux results on the fin’s bottom surface in contact with the liquid phase. This can be explained as follows: despite the fin being highly conductive, with a thermal conductivity factor of about a hundred relative to the PCM (Table 3), with the melting progress, liquid PCM at a higher temperature compared to the fin is driven toward its bottom surface leading to a heat transferred from the PCM to the metallic fins. On the other hand, a relatively colder liquid PCM flows

toward the fin's upper surface, enhancing significantly the heat flux exchanged by the tube's wall above the fins and the upper fin surface compared to the corresponding without natural convection.

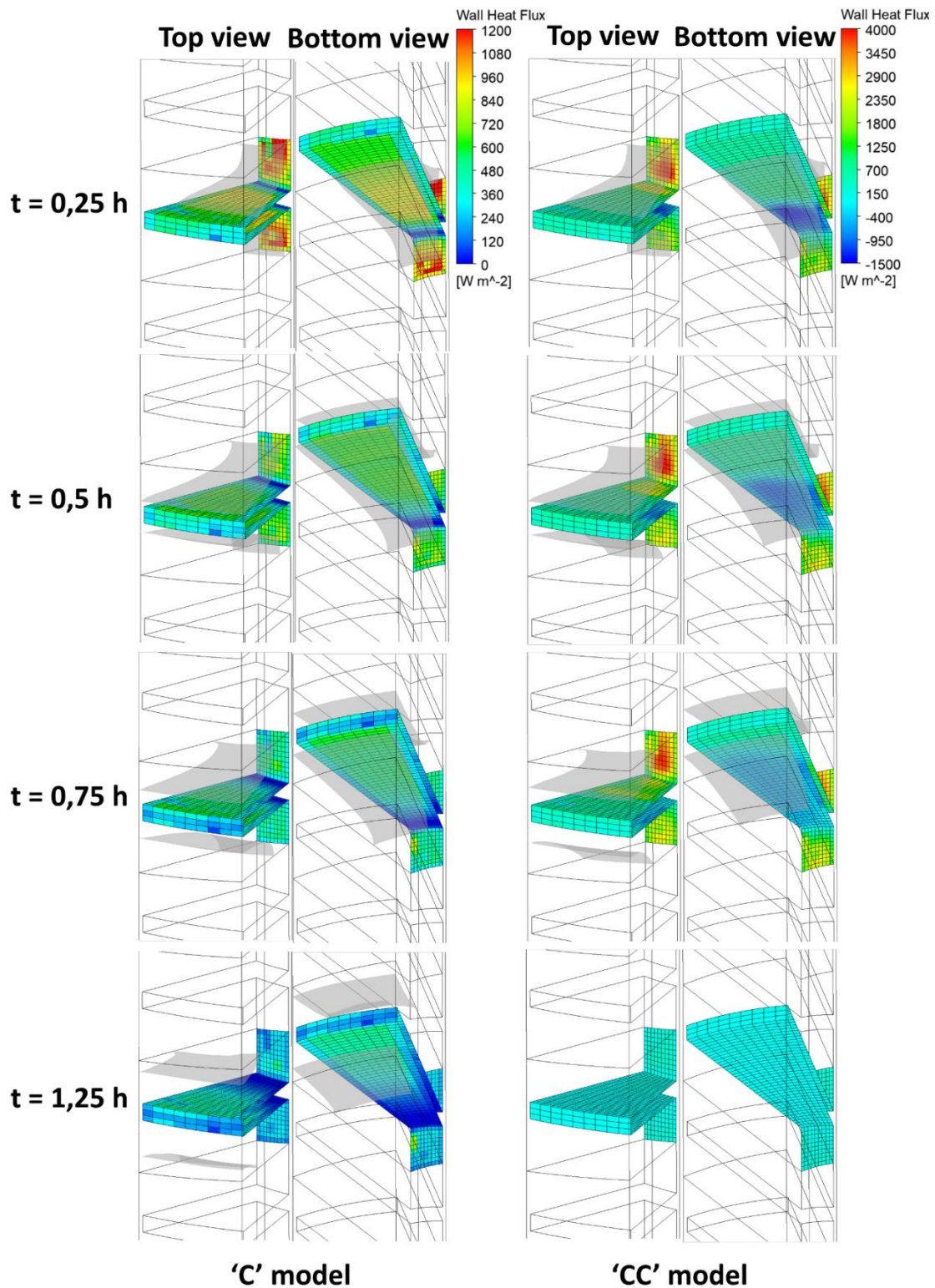


Figure 88. Heat flux distribution on the tube's outer wall and fins surface for case 38. Semi-transparent gray surfaces correspond to the isosurface of $f_m = 0.5$. Different scales are used in each case.

At $t = 0.5$ h, the entire surface of the fin is in contact with melted PCM. The effect that natural convection has on the flux distribution increases and we can observe a greater area with negative heat flux on the fin's bottom. The melted fraction is at 0.51 for the case with natural convection and at 0.44 for the purely conductive case. Then, the difference of the results obtained by both models keeps building up. At $t = 1.25$ h, the storage's charging has ended in 'CC' model simulation. Meanwhile, 14 % of the PCM is still in solid phase in the 'C' model simulation.

An additional interesting finding is how the heat flux distribution on the fins' surface evolve with the melting front. At initial stages, the heat is mainly transferred via the base of the fins near the tube. This stage corresponds to the highest storage's power level as seen in Figure 87. Then, with the melting progress, the heat flux distribution spreads out on the surface of the fins following the advancement of the melting front. Finally, by combining this observation with the results obtained in previous sections, an important question arises: could there be an alternative fin geometry capable of enhancing the flux distribution and thereby enhancing the storage system's performance? Additional information about this proposed optimization is elaborated upon in the subsequent section.

IV.5.2.5. Enhanced fin design: Triangular-shaped fin

IV.5.2.5.1. Design proposal

The results discussed in this section showed the importance that the geometry of radial fins could play on the performance of a LHTEs system. In IV.5.2.3, the temperature distributions through the fins showed that, at initial stage of the melting process, the thinner fins struggled to carry the heat to their tip, leading to a large part of the fin that did not contribute to the heat transfer towards the PCM. Moreover, in section 0, the heat flux distribution along the tube's outer wall and fins surface showed that for an important period during the melting process, the fraction of fins' geometry contributing to heat exchange in the storage is the one near the tube. Given that, we test in this section an alternative fins' geometry where the thickness of the fins varies in the radial direction resulting in a triangular section following a helical pattern (Figure 89). The tube's height h_{tube} is at 50 cm. $R_{t,int}$, e_{tube} , R_{fin} and R_{ext} are identical with the one described in section IV.2.1. The pitch value ' p ' chosen is 20 mm and the fins' thickness is varied to maintain an identical fins volume as the corresponding configuration of $p = 20$ mm and $e/p = 15\%$.

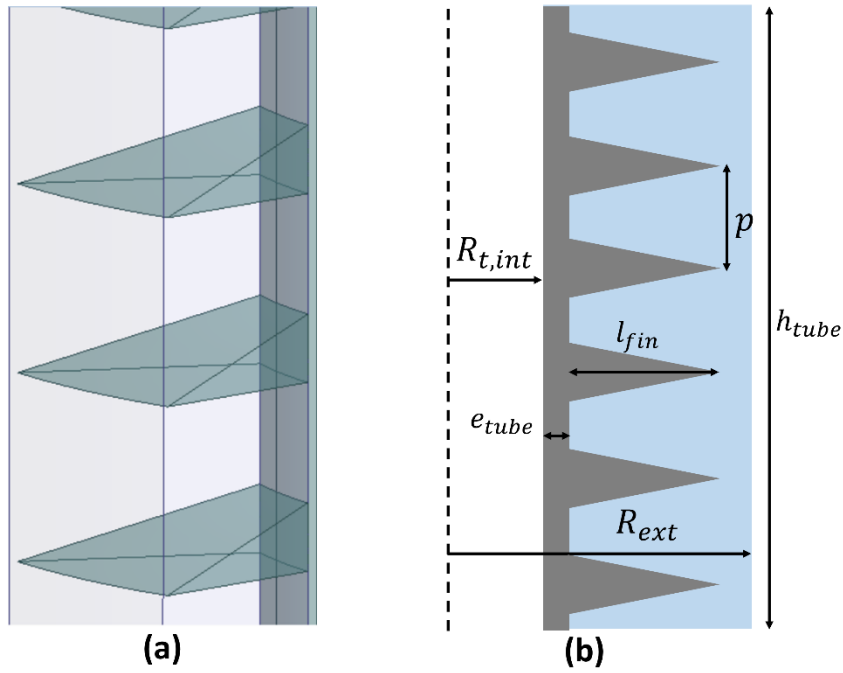


Figure 89. Description of triangular fins geometry. (a) Fraction domain represented in CFD modelling pattern (b) Computational domain

IV.5.2.5.2. Melted fraction

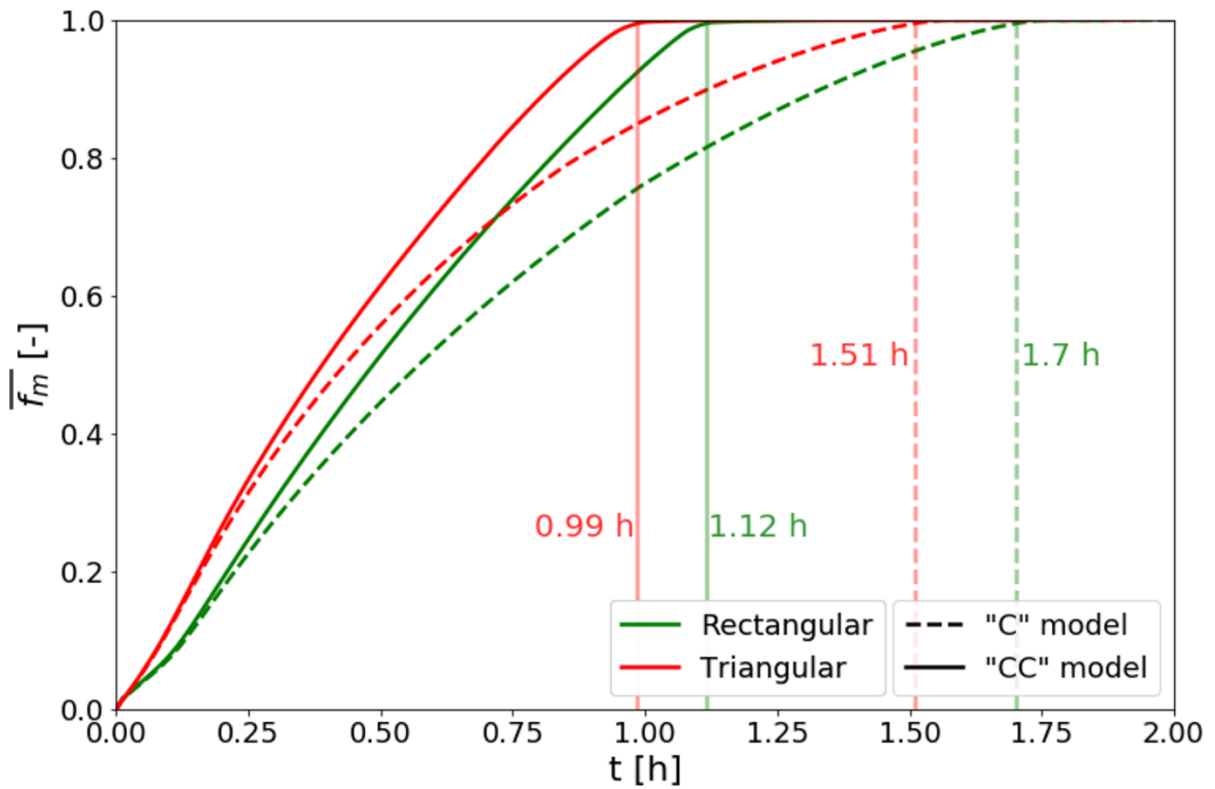


Figure 90. Evolution in time of the PCM's melted fraction for triangular and rectangular fins

Two simulations were performed on this geometry using the ‘C’ model and the ‘CC’ model described in section IV.2.2 for the PCM. Figure 90 shows the evolution in time of the melted fraction obtained by using fins with triangular section compared to the previous geometry of radial fins with rectangular section for the same pitch and fins volume.

For circular fins with a rectangular cross-section, the incorporation of natural convection in the liquid phase reduces the total melting time from 1.7 h to 1.12 h. This represents a 34% reduction in the melting duration. Conversely, when considering circular fins with a triangular cross-section, the inclusion of natural convection diminishes the PCM's melting time from 1.51 hours to 0.99 hours, also resulting in a 34% reduction. Therefore, for this configuration, the enhancements in thermal power of the storage are not primarily influenced by the shape of the circular fins, but rather by the selection of key parameters, such as pitch and thickness.

Finally, irrespective of whether or not natural convection is accounted for or not, triangular fins consistently yield a higher rate of PCM melting at any given point during the charging process, leading to an improvement in the overall thermal power of the storage system. By employing triangular fins, the time required to completely melt the entire PCM volume is reduced from 1.12 hours to 0.99 hours when natural convection is considered. Even when heat transfer occurs solely through conduction within the PCM, the melting time is still decreased from 1.7 hours to 1.51 hours. This results in an overall enhancement of approximately 13% in the total thermal power of the energy storage system.

IV.5.2.5.3. Temperature and velocity distributions

Figure 91 compares the temperature and velocity distributions within the heat transfer tube, fins and PCM regions for the two fins geometry, as obtained from the ‘CC’ model simulations. At $t = 0.25$ h, the temperature distribution difference inside the fins is already noticeable. While the temperature at the tip of the triangular fins is already around 309 °C, the rectangular fins struggle in spreading the heat toward the tip resulting in relatively colder temperature of around 305 °C. The temperature differences inside the fins between both geometries remains the same as time goes by leading to complete melted PCM at $t = 1$ h for triangular fins while a small solid fraction remains to be melted for rectangular fins.

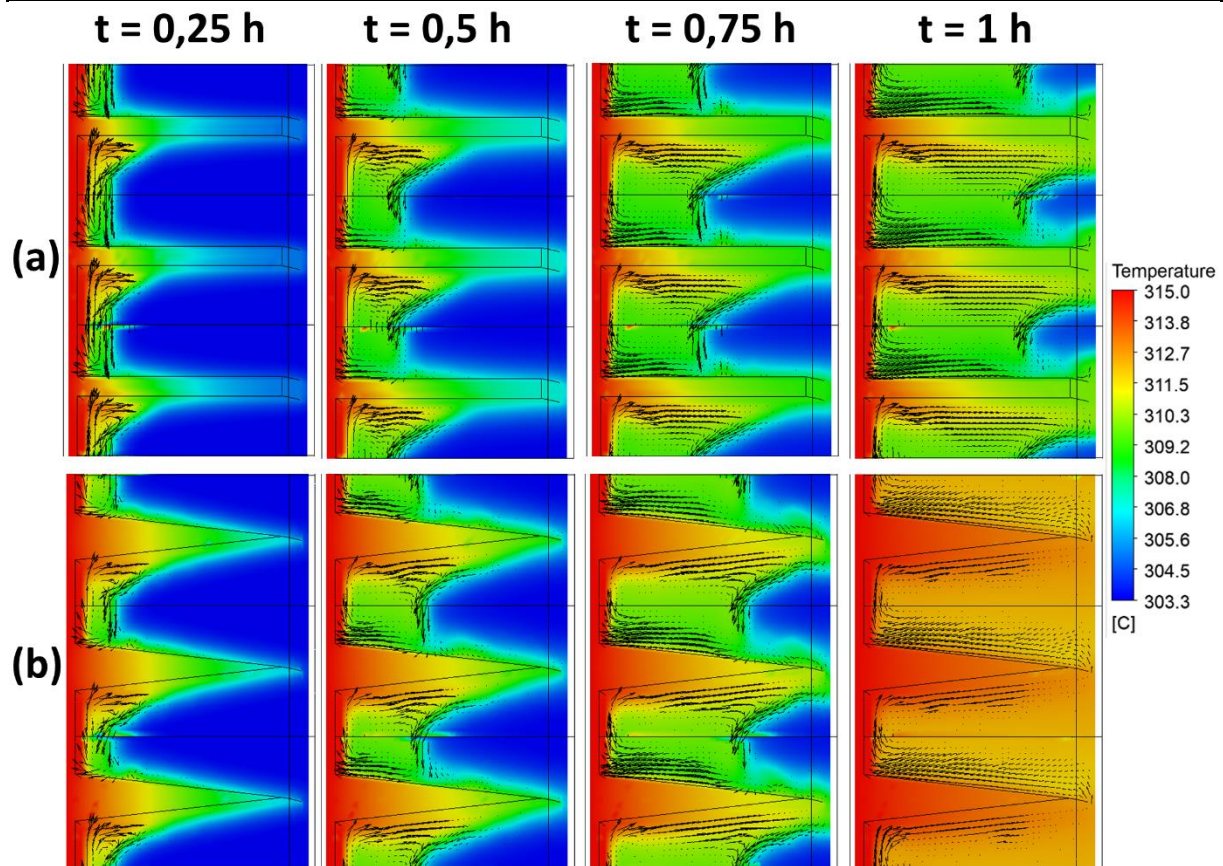


Figure 91. Comparison of the temperature and velocity distributions in the tube + fins + PCM domains for two fins geometries (a) rectangular section (b) triangular section

IV.5.3. Effect of fin material

Previous studies have consistently demonstrated that the thermal performance of LHTES system during the charging phase is significantly influenced by the type and arrangement of the fins employed on the PCM side. As a result, the optimal selection is the one that strikes a balance between facilitating efficient heat conduction through the highly conductive fins and promoting natural convection enhancements within the liquid phase, all with the ultimate goal of maximizing heat transfer to the PCM region. This objective can also be attained by enhancing fin efficiency, achieved through the selection of a constituent material possessing a notably high thermal conductivity. In this section, the influence of the thermo-physical properties of the metallic material forming the heat transfer tube and the fins on the behavior of the storage is investigated.

The constituent metallic material forming the tube's wall and the fins is characterized by three properties: the density ρ , the specific heat capacity c_p and the thermal conductivity λ .

For a given fin configuration, the product of the tube and fin material's density and specific heat ρc_p represents the thermal inertia, which refers to the material's resistance to changes in temperature. The impact of fin thermal inertia on the behavior of the storage system was examined by comparing the outcomes of two simulations with distinct ρc_p values. In the first case, the density and specific heat capacity of steel were retained by the metallic fins, while in the second case, the properties of aluminum were adopted by the metallic fins, with the thermal conductivity remaining constant at the steel value. The material properties are detailed in Table 11.

Material	Case 1 : $(\rho * c_p)_{steel}$	Case 2 : $(\rho * c_p)_{aluminum}$
λ [W.m ⁻¹ .K ⁻¹]	50.33	
ρ [kg.m ⁻³]	7764	2719
c_p [J.kg ⁻¹ .K ⁻¹]	542.8	871
ρc_p [kJ.m ⁻³ .K ⁻¹]	4214	2368

Table 11. Material properties to study the influence of the thermal inertia of fins on the behavior of the storage

These investigations were conducted using the 'CC' model, which incorporates natural convection in the liquid phase. The fin geometry selected for this study corresponds to case number 38 in Table 9, with a fin pitch of 20 mm between the centers of the fins and a fin thickness of 3 mm.

Figure 92 shows the evolution of the energy stored throughout the tube's wall, fins and PCM domain for the equivalent of 1 m of tube length in both cases. The curves in the figure reveal that varying the thermal inertia of the fins has no noticeable impact on the charging rate of the storage. In fact, for nearly the entire charging phase, the energy curves overlap. The primary distinction between both scenarios lies in storage capacity. Using fins with a ρc_p value equivalent to steel results in relatively higher stored energy at the end of the charging process. This difference arises from the greater thermal inertia of steel compared to aluminum, leading to energy stored in the form of sensible heat within the fins.

In the subsequent studies, a fixed ρc_p product is maintained, with the steel value being retained. The focus of the investigations will be on the examination of the influence of the thermal conductivity of the fins.

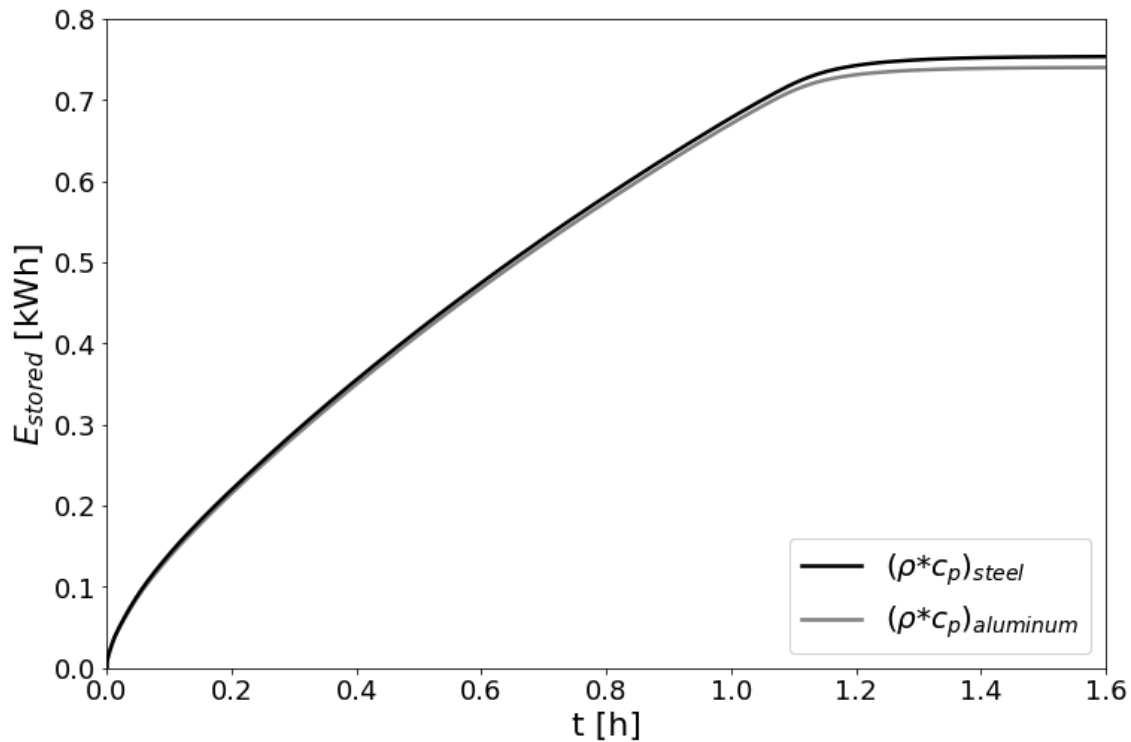


Figure 92. Evolution in time of the energy stored in the tube's wall, fins and PCM regions for different ρc_p values

The influence of thermal conductivity in the metallic components formed by the heat transfer tube and fins is investigated through a parametric study that couples thermal conductivity with the geometric configuration of the fins. Figure 93 displays the geometric configurations of fins selected for this investigation from among all the previously examined configurations (Table 9), as indicated by the red dots. Three levels of the fin thickness-to-pitch ratio ' e/p ' are chosen, with respective values of 5%, 15%, and 25%. For each level, four pitch values are considered: 2.5 mm, 10 mm, 17.5 mm, and 25 mm. The values of the pitch ' p ' and the ratio ' e/p ' are carefully chosen to represent the entire domain (depicted as the blue zone in Figure 93). Then, for each configuration, the thermal conductivity is varied across a range from $50.33 \text{ W}\cdot\text{m}^{-1}\cdot\text{K}^{-1}$ to $400 \text{ W}\cdot\text{m}^{-1}\cdot\text{K}^{-1}$. The retained values are grouped in Table 12. Altogether, the combination between various geometric configurations and thermal conductivity values yields a total of 48 distinct combinations. For each of these cases, two simulations are executed, employing both the 'CC' and 'C' models.

The temporal evolution of the melted fraction of the PCM across the 48 configurations derived from simulations conducted using both the 'C' model and the 'CC' model can be found in Appendix B. To gain insight into the influence of thermal conductivity on heat exchange within

the storage, Figure 94 shows the variations in the time required to melt 98% of the PCM volume for all examined cases. Each graph corresponds to a distinct thermal conductivity value of the tube and fins region. To facilitate cross-graph comparisons, the charging time axis (y-axis) scale is consistently maintained across all graphs.

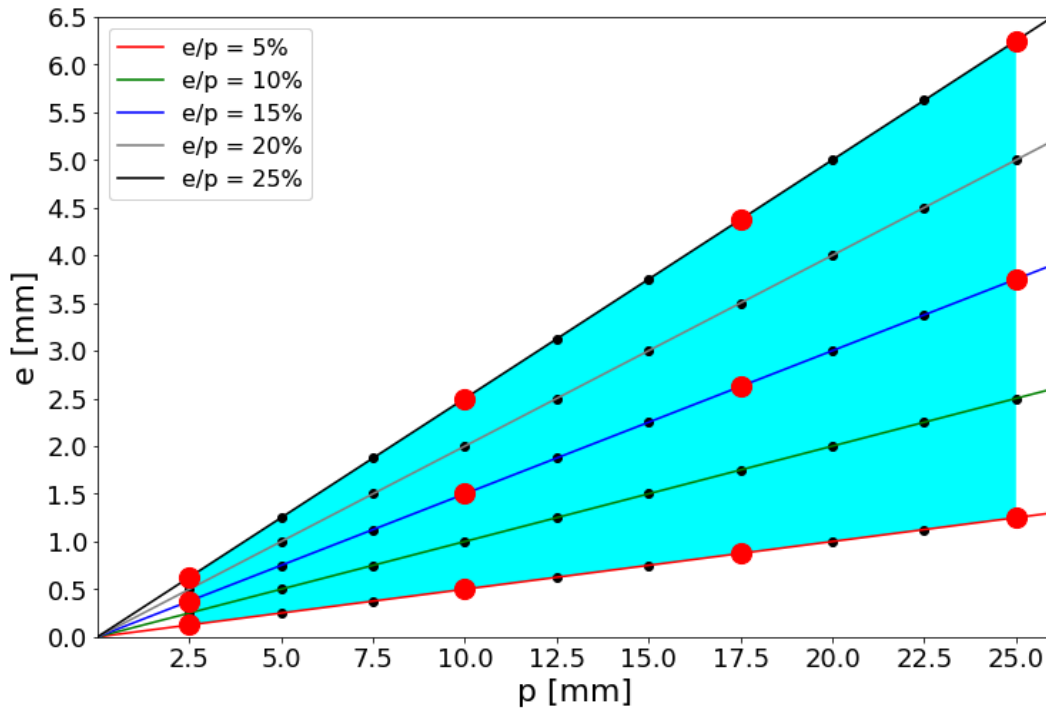


Figure 93. Retained geometric configurations for study of the influence of the thermal conductivity

λ [$\text{W}\cdot\text{m}^{-1}\cdot\text{K}^{-1}$]	50.33	100	200	400
--	-------	-----	-----	-----

Table 12. Values of the studied thermal conductivity

Irrespective of the fins' geometric configuration, an increase in the thermal conductivity of both the tube and fins materials leads to a reduction in the time required for PCM melting. For $\lambda = 50.33 \text{ W}\cdot\text{m}^{-1}\cdot\text{K}^{-1}$ (Figure 94(a)), the presented values align with those obtained in the study presented in section IV.5.2. For this specific conductivity value, the incorporation of natural convection results in an optimal pitch value (in this case, 10 mm), leading to the fastest melting process. Several observations hold true across all cases. For instance, decreasing 'p' for any 'e/p' ratio enhances the thermal conduction within the storage, as indicated by the 'C' model curves. Furthermore, for a given pitch 'p', increasing fin thickness by augmenting 'e/p' results in a quicker melting process, thereby enhancing the overall thermal power of the storage (notably, blue curves consistently fall below green curves, which, in turn, are below red curves). Additionally, the influence of natural convection is proportional to the pitch 'p', with the gap between 'C' model curves and 'CC' model curves widening as 'p' increases.

The primary distinction among various cases lies in the relative contributions of two heat transfer mechanisms: heat conduction and natural convection, which collectively determine the overall heat transfer rate within the storage. In the case of $\lambda = 100 \text{ W}\cdot\text{m}^{-1}\cdot\text{K}^{-1}$ (Figure 94(b)), unlike the scenario with $\lambda = 50.33 \text{ W}\cdot\text{m}^{-1}\cdot\text{K}^{-1}$, the presence of an optimal pitch value, where melting occurs most rapidly, is only applicable for $e/p = 5\%$. Conversely, for 'e/p' values of 15% and 25%, the configurations with the smallest pitch value of 2.5 mm yield the fastest melting times. This trend becomes more pronounced with higher thermal conductivities, such as $\lambda = 200 \text{ W}\cdot\text{m}^{-1}\cdot\text{K}^{-1}$ and $400 \text{ W}\cdot\text{m}^{-1}\cdot\text{K}^{-1}$ (Figure 94(c) and (d)). In these instances, the melting time is directly proportional to the pitch and inversely proportional to the 'e/p' ratio. Consequently, even though the contribution of natural convection remains relatively constant, the substantial increase in thermal conductivity significantly amplifies the portion of heat transferred through conduction, establishing it as the predominant heat transfer mechanism dictating the thermal behavior of the storage. In simpler terms, elevating thermal conductivity accentuates the influence of heat conduction, favoring geometric configurations that promote efficient heat – conduction, thereby resulting in the fastest melting process. Such observation is only possible through a coupled geometric-conductivity study.

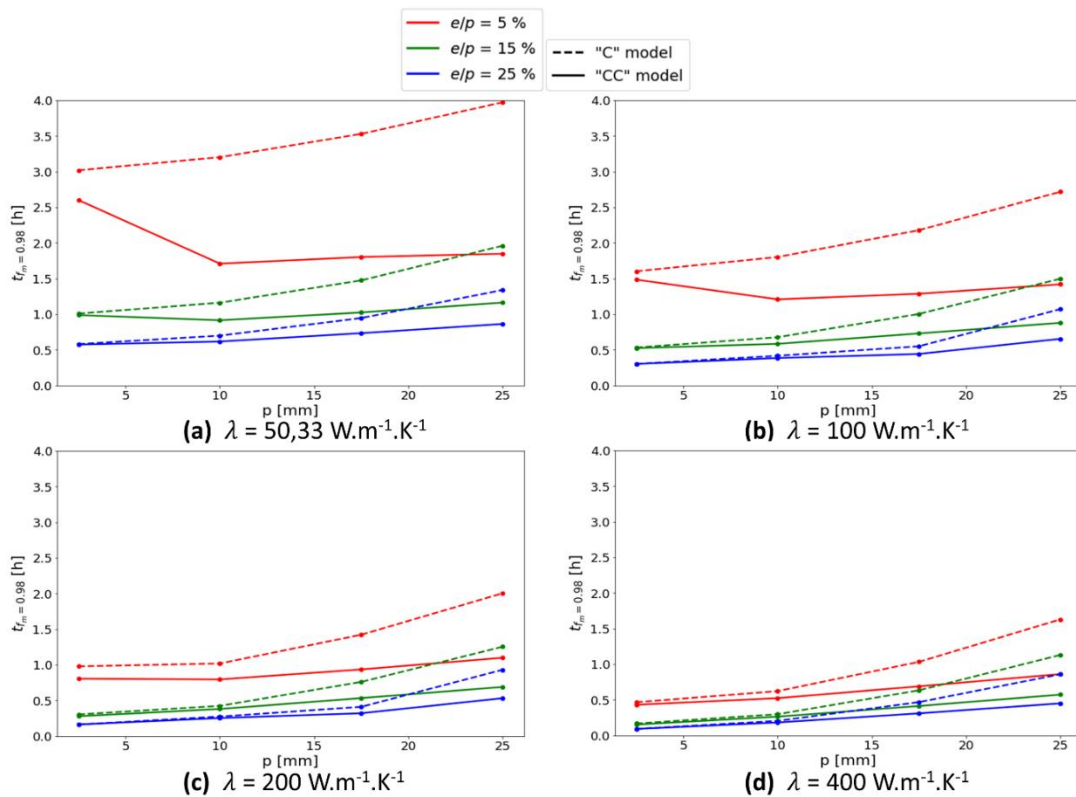


Figure 94 variation of the time required to melt 98 % of the PCM volume according to the pitch p for different e/p ratios and thermal conductivities. $\lambda =$ (a) $50 \text{ W}\cdot\text{m}^{-1}\cdot\text{K}^{-1}$ (b) $100 \text{ W}\cdot\text{m}^{-1}\cdot\text{K}^{-1}$ (c) $200 \text{ W}\cdot\text{m}^{-1}\cdot\text{K}^{-1}$ (d) $400 \text{ W}\cdot\text{m}^{-1}\cdot\text{K}^{-1}$.

IV.6. Conclusion

In this chapter, the influence of physical phenomena involved within the storage and geometric configurations on the behavior of a shell-and-tube LHTES system was studied through the utilization of CFD simulations. The effects of natural convection within the liquid phase on the melting progress were investigated through the use of two distinct numerical models. The first model, denoted as the ‘C’ model, focused solely on heat transfer via pure conduction throughout the PCM, regardless of its state. In contrast, the second model, referred to as the ‘CC’ model, incorporated the effects of natural convection within the liquid phase in addition to heat conduction. To simulate the PCM’s phase change phenomenon, the enthalpy-porosity approach was adopted. In the ‘CC’ model, the PCM was treated as a fluid with zero velocity during its solid state, while fluid movements in the liquid state, driven by buoyancy, were accounted for using the Boussinesq approximation.

The influence of natural convection on the melting process was initially examined on vertical smooth-tube configurations. In these cases, the geometry of the storage represented in the CFD simulations consisted of the cylindrical tube wall surrounded by an annular PCM region. To comprehensively explore the impact of convective heat transfer, a parametric investigation was conducted, focusing on variations in the domain height ranging from 0.25 cm to 54 cm. Remarkably, the primary finding of this study revealed a non-linear relationship between domain height and natural convection enhancements within the storage system. As the domain height increased, convective heat transfer improved, but only up to a certain threshold. Beyond this point, further increases in domain height began to diminish the effect of natural convection. In conclusion, a noteworthy approach to optimizing the thermal performance of the storage system involves inducing the recirculation of liquid particles within small convective loops. This technique promotes an efficient contribution of natural convection, thereby maximizing the fraction of the tube participating in heat exchange with the PCM region.

Subsequently, the focus shifted towards examining the impact of added fins on the performance of the storage system. Fins consist of highly conductive metallic shapes integrated into the external surface of the tube within the PCM region. Their role is to compensate the low thermal conductivity of the PCM and regulate heat transfer within the storage system. In a first investigation, the influence of the fin type on the behavior of the storage was studied. To this end, two distinct fin types were considered: axial longitudinal fins and radial circular fins. In

order to maintain a consistent fin volume ratio for both cases, the geometric parameters of each fin were precisely adjusted. The observations gathered during the charging phase, including the evolution of the PCM's melted fraction and the temperature distributions within the tube, fins and PCM region, suggested that longitudinal fins exhibited superior heat conduction capacity due to their larger heat transfer area per unit volume. However, circular radial fins excelled in enhancing convective heat transfer, enabling them to recover more efficiently with the melting progress and consequently resulting in a faster melting process.

Building on the outcome of the previous simulations, a thorough parametric study regarding the geometry of circular radial fins was conducted. The geometric parameters in question were the fin length, thickness and pitch. The primary findings can be summarized as follows:

- Compared to a smooth-tube, the addition of any fin volume ratio significantly enhances the thermal performance of the storage. This highlights the essential role of fins in LHTES systems.
- Increasing the length of the fins in the radial direction enhances the overall thermal power of the storage, thanks to the expanded heat transfer area with the PCM. Nevertheless, variations in fin length do not impact the enhancements attributed to natural convection.
- For a given fin pitch, increasing the thickness of the fins has a positive effect on the thermal power of the storage leading to a faster melting process.
- For a given fins thickness-to-pitch ratio (i.e. constant fin volume ratio), decreasing both the fins' pitch and thickness enhances thermal conduction within the storage. This means that the beneficial impact of reducing the pitch and expanding the heat transfer surface area between the fins and the PCM outweighs the detrimental effect of reducing the fins' thickness on heat conduction. However, it is important to note that decreasing both parameters diminishes the contribution of natural convection, which predominantly relies on the pitch between the fins. By balancing these two opposite effects, an optimal combination of pitch and thickness is obtained, resulting in the fastest melting process.
- Using the same computational resources, neglecting natural convection reduces the computational costs by approximately 95 % when compared to a model that includes both conduction and convection. Hence, in certain configurations (as shown in Figure

85), using a simplified model based solely on heat conduction can be sufficient for an accurate and relatively fast sizing of the storage system.

- As a result, switching from rectangular section fins to triangular section fins with the same fin volume ratio, the heat flux transferred to the PCM can be improved, resulting in a 13 % reduction in the total melting time.

Last but not least, a coupled parametric study that combines considerations of both geometric factors of fins and material properties was conducted. In summary, the study highlighted the interplay between heat conduction and natural convection in shell-and-tube LHTES with radial fins.

Finally, the significance of this study resides in the comprehension of how the combination of both natural convection and geometric configuration and material properties of radial fins influences the thermal behavior of a LHTES system during its charging phase. Furthermore, using the results highlighted in this study, heat transfer laws can be obtained that could be used to ensure a fast and accurate prediction of the behavior of such systems. The generalization of the multi-scale modelling approach of shell-and-tube LHTES featuring circular fins is detailed in the following chapter.

Chapter V – Multi-scale modelling approach

V.1. Introduction

Chapter III witnessed the development of reduced numerical models capable of accurately and rapidly predicting the behavior of the storage system. Two approaches were presented for considering the PCM's phase change phenomenon and the influence of natural convection, as well as fin geometry, on the performance of a shell-and-tube LHTES system. The outcome of these models was compared and validated using experimental data obtained from a steam storage prototype available at CEA Grenoble.

In both cases, data from previously conducted CFD simulations by Beust et al. [35], in the form of dimensionless heat transfer correlations, were employed to assist in predicting the heat transfer flux between the HTF and the PCM domain within the 'system' models. However, these correlations were specifically adapted to the studied scenario, where serrated radial fins were deployed throughout the PCM region. Therefore, the primary aim of the subsequent work is to generalize these correlations for broader application across various geometric configurations of fins.

To accomplish this, the focus of the research shifted back to the CFD scale, where a series of parametric studies were conducted to assess the influence of both natural convection and radial fin geometry on the behavior of the storage system during the charging phase (Chapter IV). Circular radial fins were considered in these CFD studies. The primary investigation consisted of a comprehensive coupled parametric analysis of fin thickness and pitch. The results showcased the substantial impact of fin geometry on both heat transfer mechanisms, namely heat conduction and natural convection. As a result, the underestimation of the storage system's power due to the neglect of the influence of natural convection within the melted phase was quantified for the various studied geometric fin configurations.

The primary aim of this chapter is to establish and validate a comprehensive heat transfer correlation that encompasses a broad spectrum of geometric configurations and operational scenarios for a LHTES system equipped with radial fins. As such, a multi-scale modelling approach of the charging phase of the storage system is developed. Subsequently, the obtained correlations are integrated into the 1D radial model presented in Chapter III (section III.4.3.1),

which is adapted according to the geometric configurations of the cases studied. This model proved its accuracy in reproducing the performances of the storage without relying on an additional correlation, as did the 0D radial model (section III.4.4). Furthermore, an investigation is conducted over the formulation and the amount of data required from CFD to construct a robust heat transfer correlation. Finally, the applicability of the obtained correlations for various working conditions of the storage is assessed and validated.

V.2. Calculation of the heat transfer correlation

V.2.1. Introduction

In this section, a detailed demonstration is provided on how a heat transfer correlation, allowing for an accurate prediction of the thermal behavior of the storage, can be extracted based on insights gained from previous CFD simulations. The work is based in the parametric study performed in Chapter IV, section IV.5.2, regarding the fins' thickness and pitch. As natural convection affects the storage's behavior during the charging phase, the results obtained from the 'CC' model are employed for the establishment of the heat transfer correlation.

V.2.2. Parameters of the correlation

To incorporate the impact of natural convection on the storage behavior, Beust et al. [35] established correlations between the dimensionless Nusselt and Rayleigh numbers (Equation (40) from Chapter III). The CFD results discussed in the preceding chapter quantified the enhancements of the thermal power of the storage due to the consideration of convective heat transfer within the liquid phase of PCM. It was evident that, for the majority of fin configurations, neglecting natural convection is not advisable. Furthermore, the parametric studies conducted revealed that variations in fin thickness 'e' and pitch 'p' significantly influence both conductive and convective heat transfers within the system. Therefore, in order to account for these variables, the more general targeted correlation should adhere to the following formulation:

$$Nu = f(Ra, e, p) \quad (108)$$

The dimensionless numbers Nusselt and Rayleigh are defined as follows:

$$Nu = \frac{\varphi}{S_e(T_{t,int} - T_{PCM1})} \frac{l_c}{\lambda_{PCMl}} \quad (109)$$

$$Ra = g \left(\frac{\beta}{\mu D_{th}} \right)_{PCM} (T_{t,int} - \overline{T_{PCM_l}}) l_c^3 \quad (110)$$

Where $\lambda_{PCM,l}$ is the thermal conductivity of the liquid phase of the PCM. φ , S_e and $T_{t,int}$ are respectively the total heat flux, area and temperature of the heat transfer tube's inner wall. l_c and $\overline{T_{PCM_l}}$ represent a characteristic length and temperature, respectively. Their definition should be carefully selected in order to ensure a generalized correlation among the various parameters outlined in Equation (108). Beust et al. [35] demonstrated that, in the context of a LHTES system with radial fins, during the charging phase of the storage, l_c and T_{cold} should be defined as the average thickness in the radial direction and temperature of the liquid PCM layer.

The average temperature of the liquid PCM layer ($\overline{T_{PCM_l}}$) is calculated from the set of local temperatures in each mesh element representing the PCM domain. The same definition used in Chapter III is adopted (see Equation (36) in section III.3.2). During the charging phase, the PCM is initially in a solid state. As the charging process advances, a melting front gradually propagates in a radial direction away from the heat transfer tube. This front acts as a boundary, separating the liquid PCM surrounding the tube from the remaining solid PCM that occupies the rest of the annular volume within the shell. Consequently, the average thickness of the liquid PCM layer varies, starting from zero at the start of the charging phase and increasing as the melting progresses. In the study conducted by Beust et al. [35], as applied in the system modelling presented in Chapter III (Equation (35)), a specific definition of l_c was used. This definition assumed a cylindrical shape for the melting front, where the overall melted fraction of the PCM represented the ratio of the liquid annular volume, of thickness l_c , located between the external wall of the tube and the melting front to the total annular volume encompassing the PCM + fins domain. This definition, however, did not distinguish between the volume occupied by the PCM and that occupied by the fins.

In the CFD studies performed in Chapter 4, the geometric parameters of the fins are varied. Consequently, the definition of l_c needs to be adapted to specifically account for the volume occupied by the PCM alone, which is influenced by the parametric configuration of the fins. Figure 95 provides a visual representation of a single sub-domain, including the tube, fins, and PCM regions, and illustrates the different geometric parameters that are considered when

calculating the characteristic length l_c . As a result, the calculation of l_c depends on the PCM's melted volume and distinguishes between two distinct zones:

1. When the overall melted fraction of the PCM (\bar{f}_m) is less than the ratio between the PCM occupying the volume between the fins and the overall PCM volume (V_{PCM}), the average length of the liquid phase does not exceed the length of the fins in the radial direction (i.e. $0 < l_c < l_{fin}$). Therefore:

$$\bar{f}_m = \frac{V_{PCM_l}}{V_{PCM}} = \frac{\pi p \left(1 - \frac{e}{p}\right) \left((R_{t,ext} + l_c)^2 - R_{t,ext}^2 \right)}{V_{PCM}} \quad (111)$$

2. When the overall melted fraction of the PCM surpasses the ratio between the PCM occupying the volume between the fins and the overall PCM volume, the average length of the liquid phase extends beyond the length of the fins (i.e. $l_{fin} < l_c < R_{ext} - R_{t,ext}$). Therefore:

$$\bar{f}_m = \frac{V_{PCM_l}}{V_{PCM}} = \frac{\pi p \left[\left(1 - \frac{e}{p}\right) \left((R_{t,ext} + l_{fin})^2 - R_{t,ext}^2 \right) + \left((R_{t,ext} + l_c)^2 - (R_{t,ext} + l_{fin})^2 \right) \right]}{V_{PCM}} \quad (112)$$

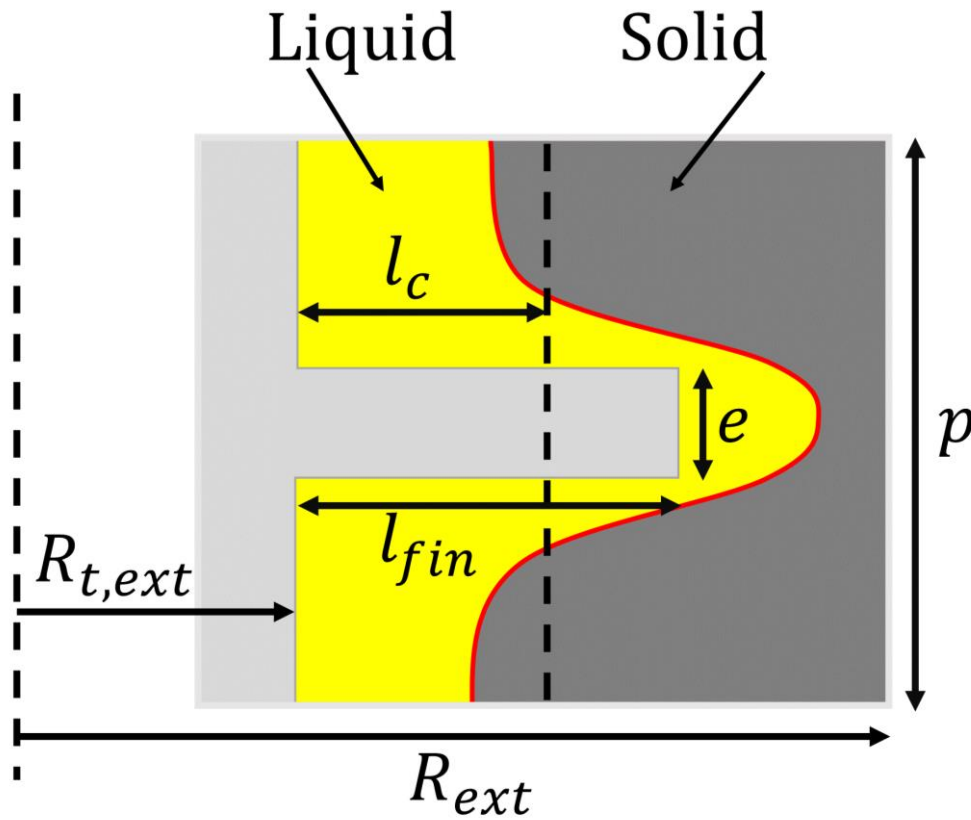


Figure 95. Illustration showing the position of l_c according to the state of the PCM

Finally, the characteristic length l_c is calculated as follows:

$$l_c = \begin{cases} -R_{t,ext} + \sqrt{R_{t,ext}^2 + \frac{V_{PCM}}{\pi p(1-\frac{e}{p})} \bar{f}_m} & \text{for } \bar{f}_m < \frac{\pi p(1-\frac{e}{p})((R_{t,ext}+l_{fin})^2 - R_{t,ext}^2)}{V_{PCM}} \\ -R_{t,ext} + \sqrt{\frac{V_{PCM}\bar{f}_m - \pi p(1-\frac{e}{p})((R_{t,ext}+l_{fin})^2 - R_{t,ext}^2)}{\pi p} + (R_{t,ext} + l_{fin})^2} & \text{for } \bar{f}_m > \frac{\pi p(1-\frac{e}{p})((R_{t,ext}+l_{fin})^2 - R_{t,ext}^2)}{V_{PCM}} \end{cases} \quad (113)$$

The adoption of such definition for l_c implies that throughout the charging phase of the storage, its values progressively increase from zero to the total thickness of the PCM domain $R_{ext} - R_{t,ext}$. Therefore, when considering the provided definitions for l_c and T_{cold} , the dimensionless numbers Rayleigh and Nusselt could be continuously calculated during the charging process rather than solely relying on average values for each geometric configuration. This notion offers an enhanced precision in predicting the behavior of the storage according to the state of the PCM within the system.

V.2.3. Influence of the geometric configuration on the dimensionless numbers

Figure 96 groups the evolution of dimensionless numbers Nusselt and Rayleigh for several fins' pitch and thickness-to-pitch ratios as function of l_c . Notably, the Nusselt number exhibits a strong dependence on the e/p ratio, featuring distinct values for different ratios, each represented by separate curves within the same graph. This variability primarily arises from enhancements in the overall thermal power of the storage system, denoted as φ in Equation (109), and resulted from the increase of the thickness of the fins, as explored in the preceding chapter. Furthermore, it is worth noting that the shape of the Nusselt number curves varies as the pitch p changes. For instance, the rate of change of the Nusselt number, reflected in the slope of the curves, is more pronounced for a pitch value of 25 mm (as illustrated in Figure 96(d)) compared to a pitch value of 2.5 mm (as shown in Figure 96(a)). This phenomenon is attributed to the growing influence of natural convection, which becomes increasingly evident as the space between two adjacent fins widens.

On the other hand, several insights can be made regarding the Rayleigh number curves. For a given pitch value, the Rayleigh number remains almost independent on the e/p ratio. However, the values of the Rayleigh number are slightly dependent on the pitch parameter. For instance, as p increases, the maximum values attained by the Rayleigh number (at around $l_c = 0.034$ m) decreases. In fact, Rayleigh values are directly dependent on the cube of the characteristic

length, l_c^3 . Consequently, as the charging process advances, the average thickness of the liquid PCM layer l_c increases. As l_c increases, the Rayleigh number also increases correspondingly. However, towards the latter stages of the charging phase, Rayleigh values reach a maximum, where a further increase in l_c results in a decrease in Ra. It is crucial to remind that the Rayleigh number depends equally on the temperature difference ($T_{t_{int}} - \overline{T_{PCM_l}}$). An excessive increase in $\overline{T_{PCM_l}}$ toward the end of the charging phase can result in a reduction in Rayleigh values.

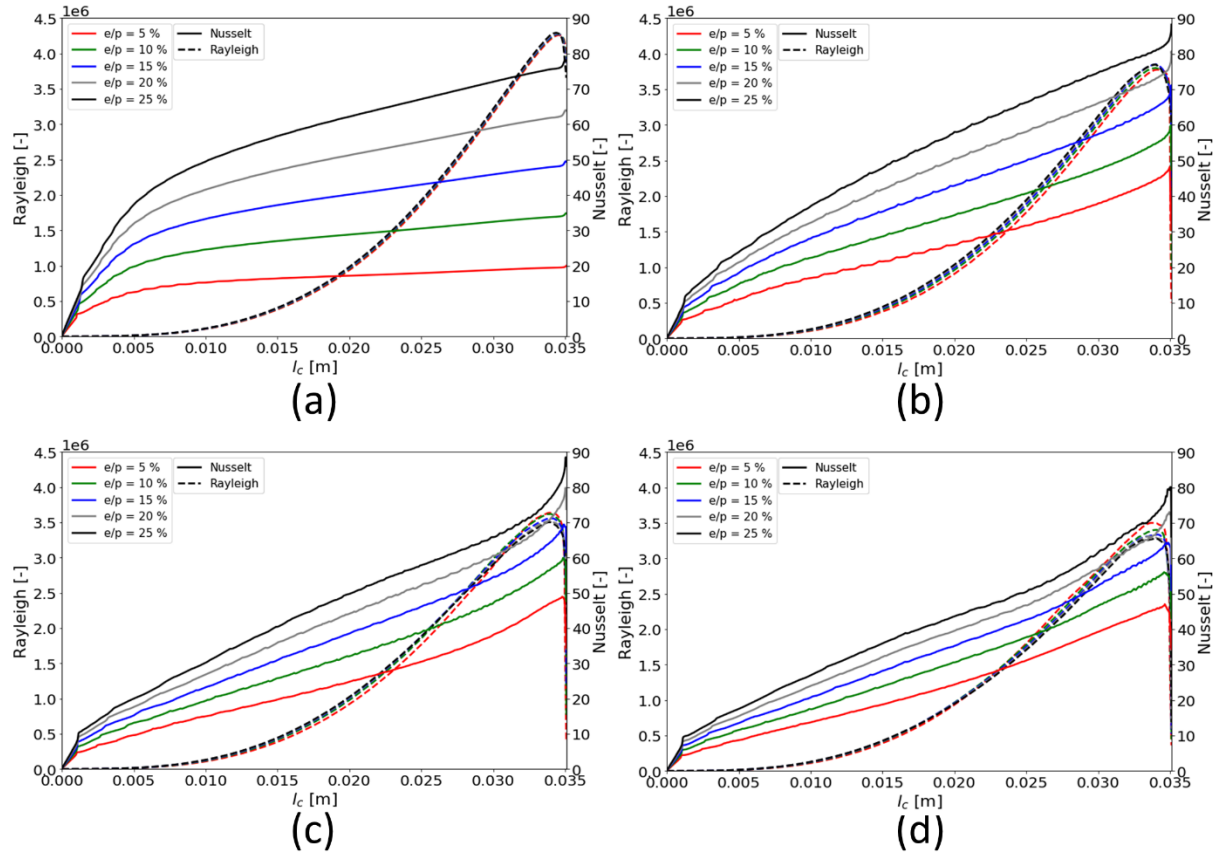


Figure 96. Evolution of the Rayleigh and Nusselt numbers with l_c . $p =$ (a) 2.5 mm (b) 10 mm (c) 17.5 mm (d) 25 mm.

These observations are validated through Figure 97, which shows the evolution of $\overline{T_{PCM_l}}$ as function of l_c for various e/p ratios at pitch values of 2.5 mm and 25 mm. Toward the end of the charging phase, $\overline{T_{PCM_l}}$ experiences a sudden increase in its value. This increase diminishes the thermal gradient ($T_{t_{int}} - \overline{T_{PCM_l}}$) directly leading to a decrease in the Rayleigh number. Additionally, as the pitch between the fins is increased, it raises the average temperature of the liquid phase during the advanced stages of the melting process. This phenomenon accounts for the decline in the maximum value attained by the Rayleigh number with an increase in pitch.

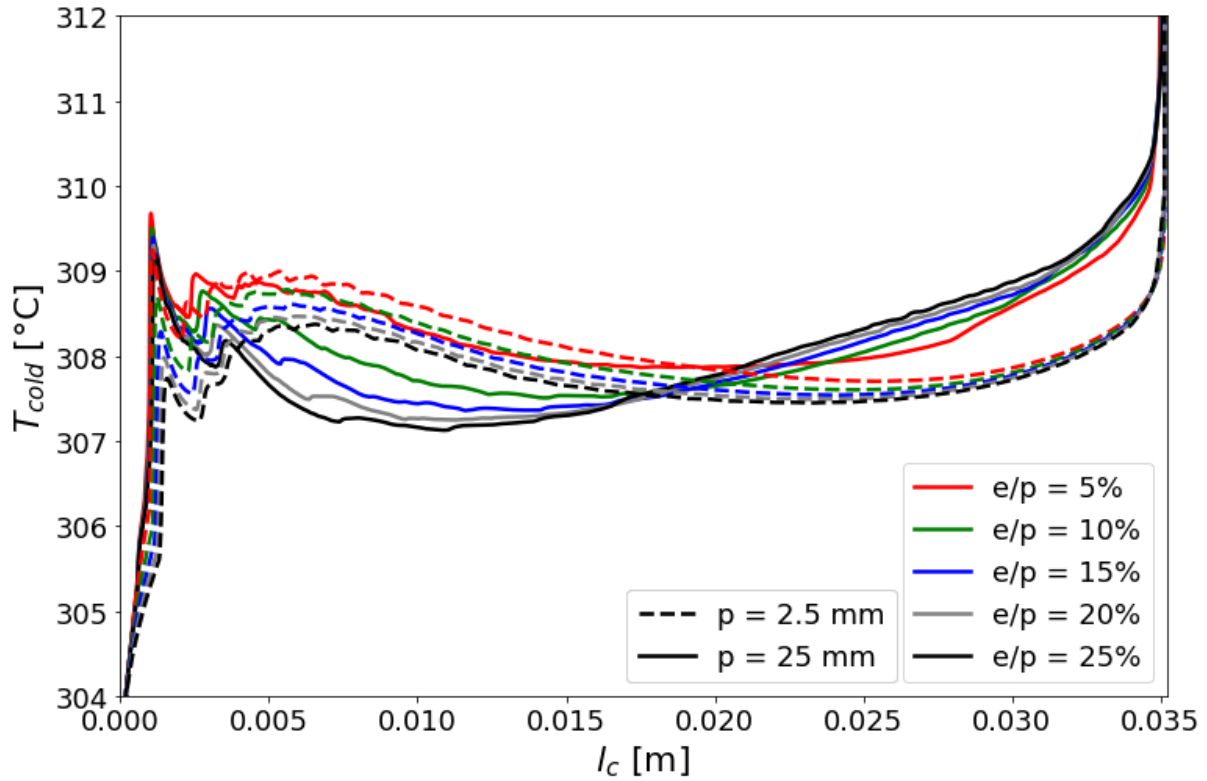


Figure 97. Evolution of the average temperature of liquid PCM as function of l_c

Overall, the set of curves shown in Figure 96 highlights the interdependence between the dimensionless numbers Nusselt and Rayleigh, and the geometric parameters e and p , confirming the choice made in equation (108) for the calculation of the heat transfer correlation.

V.2.4. Formulation of the heat transfer correlation

For $\bar{f}_m < 1$, the PCM undergoes the solid-liquid phase transition, the energy stored during this phase corresponds for a major portion of the overall storage capacity. Therefore, the accuracy of the correlation within this phase is crucial for an accurate prediction of the behavior of the storage by the ‘system’ model. Based on previous results (Figure 96), it is established that the Nusselt number is dependent on the Rayleigh number, as well as the thickness e and pitch p of the fins. However, we are yet to determine the specific form of the correlation that needs to be adapted. Therefore, several correlation structures are being tested, each differing in the number of terms it constitutes while sharing the following base structure:

$$\ln Nu_1 = \sum_{i=1}^n A_i F_i \quad (114)$$

Where A_i correspond to the correlations coefficients to be determined. F_i correspond to a combination of various parameters that influence the thermal power of the storage and are grouped in Table 13. n represents the number of terms used to construct the correlation, this parameter is being investigated by considering four formulations, each having a respective number of terms: 4, 5, 7 and 8.

i	1	2	3	4	5	6	7	8
F_i	1	$\ln e$	$\ln p$	$\ln Ra$	$\ln e \ln p$	$\ln e \ln Ra$	$\ln p \ln Ra$	$\ln e \ln p \ln Ra$

Table 13. Combination of parameters used in the Nusselt correlation (Equation (114))

Another purpose of the study is to examine the effect of the number of geometric configurations used for the construction of the correlation. The objective is to determine whether data from all 50 configurations described in section IV.5.2 are indispensable for achieving a robust correlation. In order to investigate this, six distinct test cases were conducted, with each one employing a different number of configurations in the building of the correlation. The various cases examined are shown in Figure 98 and encompass the following:

1. Case (a): 4 configurations corresponding to the extremities of the domain
2. Case (b): 10 configurations distributed on the edge of the domain with a pitch difference $\Delta p = 7.5 \text{ mm}$ and fins' thickness-to-pitch ratio difference $\Delta \frac{e}{p} = 10 \%$.
3. Case (c): 12 configurations distributed uniformly throughout the domain with $\Delta p = 7.5 \text{ mm}$ and $\Delta \frac{e}{p} = 10\%$.
4. Case (d): 20 configurations distributed uniformly throughout the domain with $\Delta p = 7.5 \text{ mm}$ and $\Delta \frac{e}{p} = 5\%$.
5. Case (e): 32 configurations corresponding to the configurations used in case (d) + the remaining 12 configurations with $\frac{e}{p} = 5 \text{ and } 25 \%$.
6. Case (f): all the 50 configurations with $\Delta p = 2.5 \text{ mm}$ and $\Delta \frac{e}{p} = 5\%$.

It is important to note that the geometric parameters e and p , as utilized in Equation (114) are expressed in meters [m]. Moreover, to avoid potential biases arising from variations in data size across different configurations, an equal number of 100 data points (Ra , Nu) were collected from each calculation. These points are uniformly distributed throughout the charging phase, allowing for a balanced representation of data across all configurations.

As a result, by combining both studies examining the number of terms used in correlation formulation and the number of geometric configurations used as input data, we were able to generate a set of 24 distinct correlations. Consequently, the coefficients A_i used in equation (114) can be found in tables Table 14, Table 15, Table 16, Table 17, Table 18, and Table 19. These correlations will be integrated to the system model, with a detailed examination of the associated errors to follow in subsequent discussions.

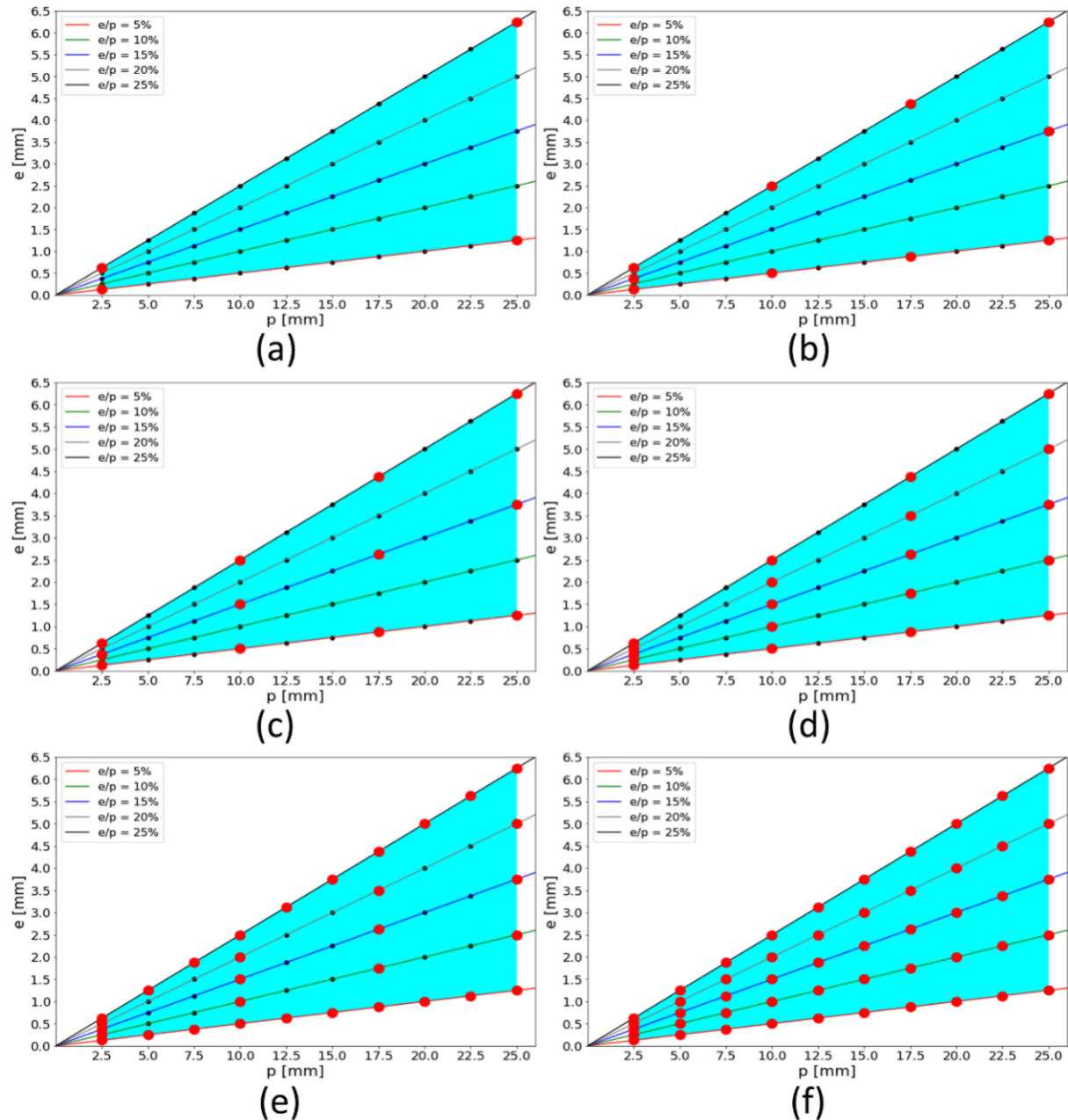


Figure 98. Combination of different sets of configurations used in the construction of the Nusselt correlation. Number of configurations: (a) 4 (b) 10 (c) 12 (d) 20 (e) 32 (f) 50

		4	5	7	8
i	F_i	A_i			
1	1	2.292	-3.983	-7.46	4.159
2	$\ln(e)$	0.578	-0.343	-0.399	1.274
3	$\ln(p)$	-0.561	-1.898	-2.566	0.062
4	$\ln(Ra)$	0.186	0.19	0.451	-0.413
5	$\ln(e) \ln(p)$	-	-0.19	-0.189	0.175
6	$\ln(e) \ln(Ra)$	-	-	0.004	-0.12
7	$\ln(p) \ln(Ra)$	-	-	0.051	-0.144
8	$\ln(e) \ln(p) \ln(Ra)$	-	-	-	-0.027

Table 14. Coefficients of Nusselt correlation when constructed using data from 4 geometric configurations

n =		4	5	7	8
i	F_i	A_i			
1	1	1.93	-3.7	-6.732	3.943
2	$\ln(e)$	0.494	-0.29	-0.233	1.252
3	$\ln(p)$	-0.481	-1.744	-2.47	-0.00346
4	$\ln(Ra)$	0.202	0.204	0.44	-0.352
5	$\ln(e) \ln(p)$	-	-0.172	-0.167	0.169
6	$\ln(e) \ln(Ra)$	-	-	-0.00289	-0.113
7	$\ln(p) \ln(Ra)$	-	-	0.0567	-0.126
8	$\ln(e) \ln(p) \ln(Ra)$	-	-	-	-0.025

Table 15. Coefficients of Nusselt correlation when constructed using data from 10 geometric configurations

n =		4	5	7	8
i	F_i	A_i			
1	1	1.886	-3.494	-6.48	3.93
2	$\ln(e)$	0.495	-0.256	-0.209	1.244
3	$\ln(p)$	-0.484	-1.679	-2.382	0.00268
4	$\ln(Ra)$	0.205	0.207	0.441	-0.332
5	$\ln(e) \ln(p)$	-	-1.634	-0.158	0.168
6	$\ln(e) \ln(Ra)$	-	-	-0.00187	-0.11
7	$\ln(p) \ln(Ra)$	-	-	0.055	-0.121
8	$\ln(e) \ln(p) \ln(Ra)$	-	-	-	-0.024

Table 16. Coefficients of Nusselt correlation when constructed using data from 12 geometric configurations

n =		4	5	7	8
i	F_i	A_i			
1	1	1.939	-3.31	-6.392	3.846
2	$\ln(e)$	0.498	-0.23	-0.189	1.23
3	$\ln(p)$	-0.476	-1.644	-2.35	-0.008
4	$\ln(Ra)$	0.204	0.206	0.451	-0.311
5	$\ln(e) \ln(p)$	-	-0.159	-0.152	0.166
6	$\ln(e) \ln(Ra)$	-	-	-0.000957	-0.107
7	$\ln(p) \ln(Ra)$	-	-	0.056	-0.117
8	$\ln(e) \ln(p) \ln(Ra)$	-	-	-	-0.024

Table 17. Coefficients of Nusselt correlation when constructed using data from 20 geometric configurations

n =		4	5	7	8
i	F_i	A_i			
1	1	1.784	-3.207	-6.036	3.933
2	$\ln(e)$	0.466	-0.222	-0.143	1.251
3	$\ln(p)$	-0.456	-1.586	-2.303	-0.01
4	$\ln(Ra)$	0.209	0.21	0.435	-0.306
5	$\ln(e) \ln(p)$	-	-0.154	-0.148	0.168
6	$\ln(e) \ln(Ra)$	-	-	-0.00405	-0.108
7	$\ln(p) \ln(Ra)$	-	-	0.057	-0.113
8	$\ln(e) \ln(p) \ln(Ra)$	-	-	-	-0.023

Table 18. Coefficients of Nusselt correlation when constructed using data from 32 geometric configurations

n =		4	5	7	8
i	F_i	A_i			
1	1	1.625	-2.74	-5.41	2.829
2	$\ln(e)$	0.465	-0.155	-0.093	1.088
3	$\ln(p)$	-0.488	-1.476	-2.132	-0.234
4	$\ln(Ra)$	0.209	0.21	0.423	-0.188
5	$\ln(e) \ln(p)$	-	-0.138	-0.132	0.137
6	$\ln(e) \ln(Ra)$	-	-	-0.0026	-0.0.9
7	$\ln(p) \ln(Ra)$	-	-	0.052	-0.088
8	$\ln(e) \ln(p) \ln(Ra)$	-	-	-	-0.0199

Table 19. Coefficients of Nusselt correlation when constructed using data from 50 geometric configurations

For $\overline{f_m} = 1$, the PCM's solid-liquid phase transition is over and all the PCM is in liquid state. However, the charging of the sensible heat continues until the PCM's temperature reaches the threshold temperature imposed as a boundary condition on the tube's inner wall. Although the energy stored as sensible heat in the liquid phase constitutes only a small fraction of the total storage capacity, it is crucial to consider it to ensure a correlation that covers the entire charging phase. At this stage, the characteristic length l_c used in the dimensionless numbers is constant at its upper limit at $R_{ext} - R_{t,ext}$. Therefore, we suppose that the total heat flux exchanged at the tube's inner wall φ used in the calculation of the Nusselt number (Equation (109)) is directly proportional to the temperature difference $T_{hot} - T_{cold}$, hence leading to an average Nusselt number for each geometric configuration of fins:

$$Nu = f(e, p) \quad (115)$$

The Nusselt correlation at this stage adapts the following formulation:

$$\ln Nu_2 = n_1 + n_2 \ln e + n_3 \ln p + n_4 \ln e \ln p \quad (116)$$

Using CFD data, the values obtained for the coefficients n_1 , n_2 , n_3 and n_4 are respectively 0.39, 0.2, -1.85 and -0.12. As a result, the distribution of the Nusselt number for the studied fins' configurations obtained by both CFD and Nusselt correlation (Equation (116)) are shown in Figure 99.

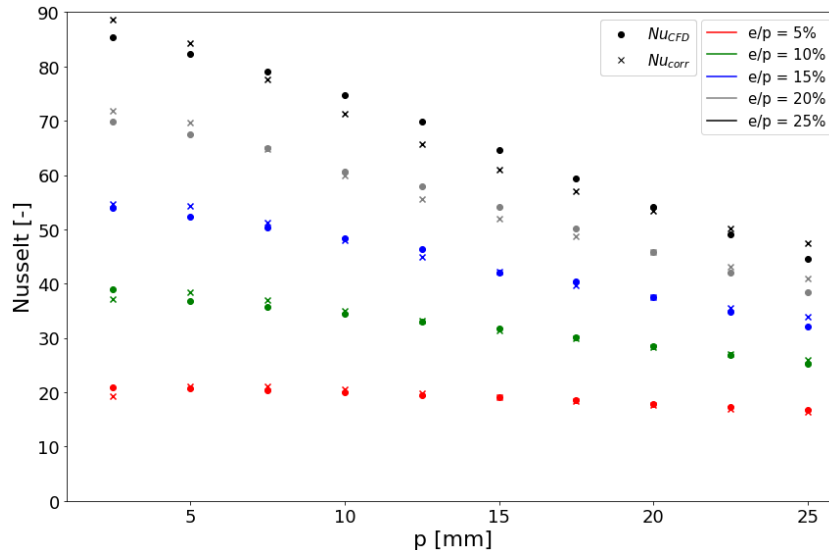


Figure 99. Distribution of the Nusselt number resulted from both CFD and heat transfer correlation

Finally, to achieve continuous correlations between different charging phases, the approach developed by Beust et al [35] is adapted where the PCM's melted fraction f_m is used to

determine the appropriate selection of the Nusselt correlation with a linear transition for $0.98 < \overline{f_m} < 1$:

$$Nu = \begin{cases} Nu_1 & \text{for } \overline{f_m} < 0.98 \\ \frac{1 - \overline{f_m}}{0.02} Nu_1 + \frac{\overline{f_m} - 0.98}{0.02} Nu_2 & \text{for } 0.98 < \overline{f_m} < 1 \\ Nu_2 & \text{for } \overline{f_m} = 1 \end{cases} \quad (117)$$

Here, Nu_1 corresponds to the Nusselt number during the charging of the latent heat of the storage defined in Equation (114) and Nu_2 corresponds to the charging of the residual sensible heat of the liquid phase at the end of the charging phase defined by Equation (116). Equation (117) is then implemented in the reduced numerical model to predict the complete behavior of the storage system. The details of the reduced model and the results obtained from investigating the formulation and the amount of data used to calculate Nu_1 are thoroughly presented in the following section.

V.3. System modelling

The geometric domain considered in the ‘system’ model consists of the metallic heat transfer tube surrounded by a homogenous material designating the PCM and fins volumes (Figure 100). Heat transfer in the axial and angular directions is neglected. Consequently, the annular space around the tube is discretized in ‘m’ elementary volume in the radial direction. The geometric parameters $R_{t,int}$, $R_{t,ext}$ and R_{ext} are identical to the ones used in the CFD model, described in section III.4.3.1.

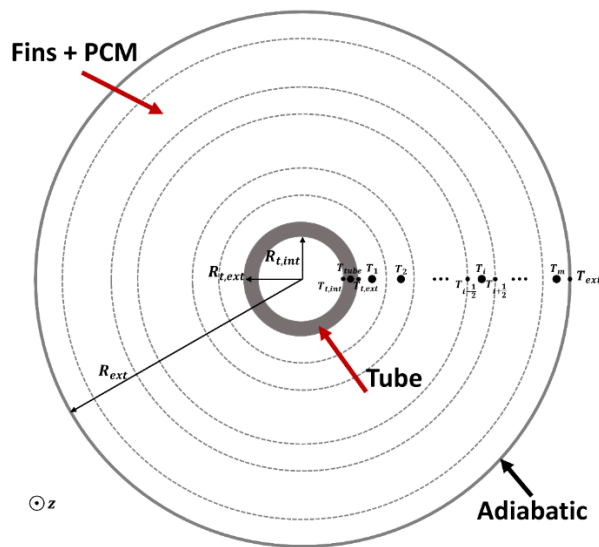


Figure 100. Computational domain represented in the “system” model

In the PCM + fins domain, the 1D radial approach developed in Chapter III for central tubes is adopted. The domain is discretized in the radial direction and heat is supposed to be transferred solely by pure conduction within an equivalent material representing the PCM and fins (refer to section III.4.3.1 in Chapter III). The key distinction from the model described in Chapter III is the utilization of circular fins with varying thickness and pitch, as opposed to serrated fins. With these circular fins, the computational domain is divided into two distinct regions based on their radial positioning (Figure 101):

1. $R_{t,ext} < R < R_{t,ext} + l_{fin}$: the domain is composed of both fins and PCM. The PCM volume fraction in this space varies according to the fins' thickness and pitch, and is calculated as follows:

$$r = 1 - \frac{e}{p} \quad (118)$$

2. $R_{t,ext} + l_{fin} < R < R_{ext}$: this region corresponds to the annular space exceeding the tip of fins, containing only the PCM, therefore:

$$r = 1 \quad (119)$$

Then, the volumetric and mass fraction of PCM are calculated in each cell using the trapezoidal method shown in Section III.4.3.1 of Chapter III.

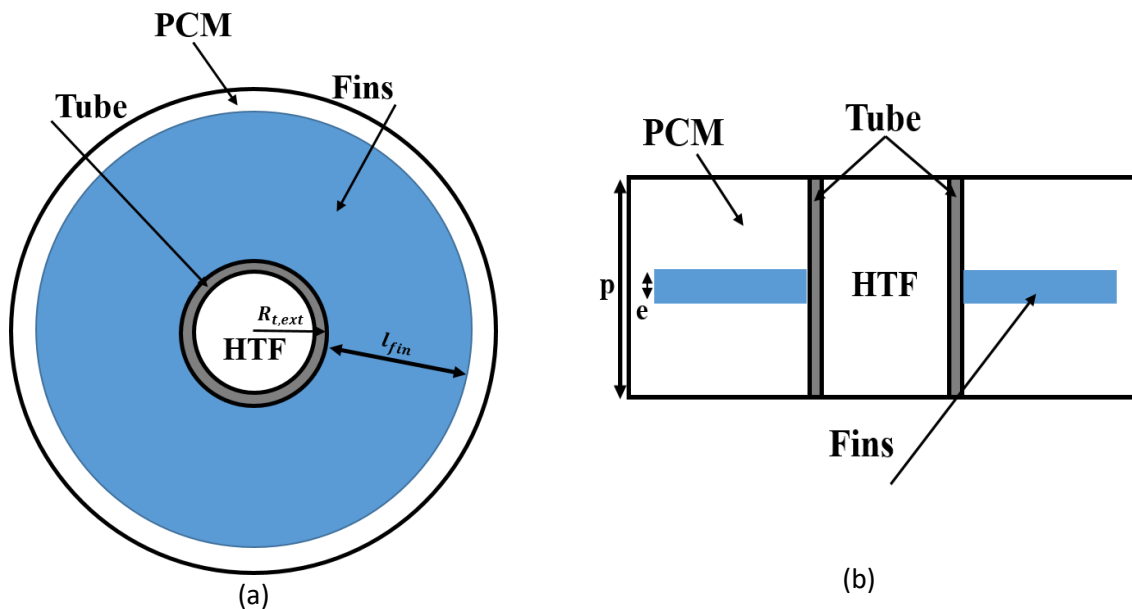


Figure 101. Illustrations of the presence of circular fins in a given sub-domain (a) radial cross-section view (b) axial cross-section view

V.3.1.Results

In section V.2.4, data from CFD were utilized to derive 24 distinct possible correlations for Equation (108), covering a range of number of parameters and number of configurations used as input data to the construction of the correlation. These 24 correlations are employed in the “system” model to calculate the equivalent thermal conductivity λ_{eq} of the homogenous material PCM + fins. To investigate the robustness of the correlations, each of the 24 cases was used to perform simulations on the 50 configurations grouped in Table 9, resulting in a total of 1200 simulations. In all of them, the annular space surrounding the tube is discretized to 25 elementary volumes in the radial direction. The simulations are performed using the DYMOLA software.

V.3.1.1. RMSE

The main objective of the “system” model is to reproduce an identical storage’s behavior as the more complete and detailed CFD model. The storage’s charging time, whether partially or totally, can be a pertinent way to examine the accuracy of the results obtained by performing fast ‘system’ simulations. As it was previously defined, the charging time of the storage corresponds to the physical time needed to melt a certain amount of PCM during the charging phase. Additionally, the storage’s charging time is an interesting parameter since it provides a direct indication of the thermal power of storage, which is an essential design criterion of LHTES systems.

Therefore, and in order to investigate the accuracy of the heat transfer correlations, the Root-mean-square deviation (RMSE) of the storage’s charging time ratio predicted by the “system” model to the one obtained by performing CFD simulations is calculated for a given melted fraction f_m by the following equation:

$$RMSE|_{\bar{f}_m} = \sqrt{\frac{1}{k} \sum_{i=1}^k \left(1 - \frac{t_{sys_i}|_{\bar{f}_m}}{t_{CFD_i}|_{\bar{f}_m}} \right)^2} \quad (120)$$

Where $t_{sys_i}|_{\bar{f}_m}$ and $t_{CFD_i}|_{\bar{f}_m}$ correspond to the time taken to melt a PCM fraction \bar{f}_m predicted by both ‘system’ and CFD models. The parameter k corresponds to the total number of configurations used in the investigation. In this case, since all the geometric configurations

covering the domain presented in Figure 98 are used in the validation of the ‘system’ model, k is equal to 50.

The values of the RMSE calculated by Equation (120) are presented for several values of the melted fraction $\overline{f_m}$ in Figure 102. In each graph, the x-axis represents the number of geometric configurations of fins used as entry data in the construction of the Nusselt correlation, while the y-axis represents the range of values of the RMSE. Additionally, several curves are plotted in each graph to represent the effect of the number of coefficients used in the formulation of the heat transfer correlation.

For $\overline{f_m} = 0.2$ (Figure 102 (a)), the charging process is at initial stages. The effect of increasing the number of configurations is not quite evident at this stage. Increasing the number of coefficients from 4 to 7 reduces RMSE values from around 18 % to around 8 % respectively. Interestingly, adding an 8th coefficient (coupling ‘e’, ‘p’ and ‘Ra’) does not improve the predictions of the system model. For $\overline{f_m} = 0.5$ (Figure 102 (b)), half of the PCM is melted. Overall, the RMSE values decrease with respect to $\overline{f_m} = 0.2$ (RMSE < 14 % for all cases). The effect of the number of coefficients maintains a similar trend as for $\overline{f_m} = 0.2$ with a reduction of the RMSE from around 13 % for 4 coefficients to around 5 % for 7 coefficients. However, the impact of the number of coefficients becomes more evident. For the curves of 5, 7 and 8 coefficients, the use of only 4 configurations as input data for the correlation leads to relatively higher errors than other cases. For $\overline{f_m} = 0.8$ (Figure 102 (c)) and $\overline{f_m} = 0.98$ (Figure 102 (d)), the impact of the number of coefficients and configurations becomes more visible. The cases with 5, 7 and 8 coefficients gives identical RMSE values which are lower than those of the cases with 4 coefficients. This means that the addition of a fifth coefficient to the heat transfer correlation is enough to lower the errors of the prediction of the ‘system’ model and the addition of more coefficients does not further improve the accuracy of the ‘system’ model. Moreover, the results demonstrate that increasing the number of configurations from 4 to 12 reduces the RMSE from 10 % to 6 % for the cases involving 5, 7 and 8 coefficients. However, further enlarging the size of the input data does not result in more precise predictions.

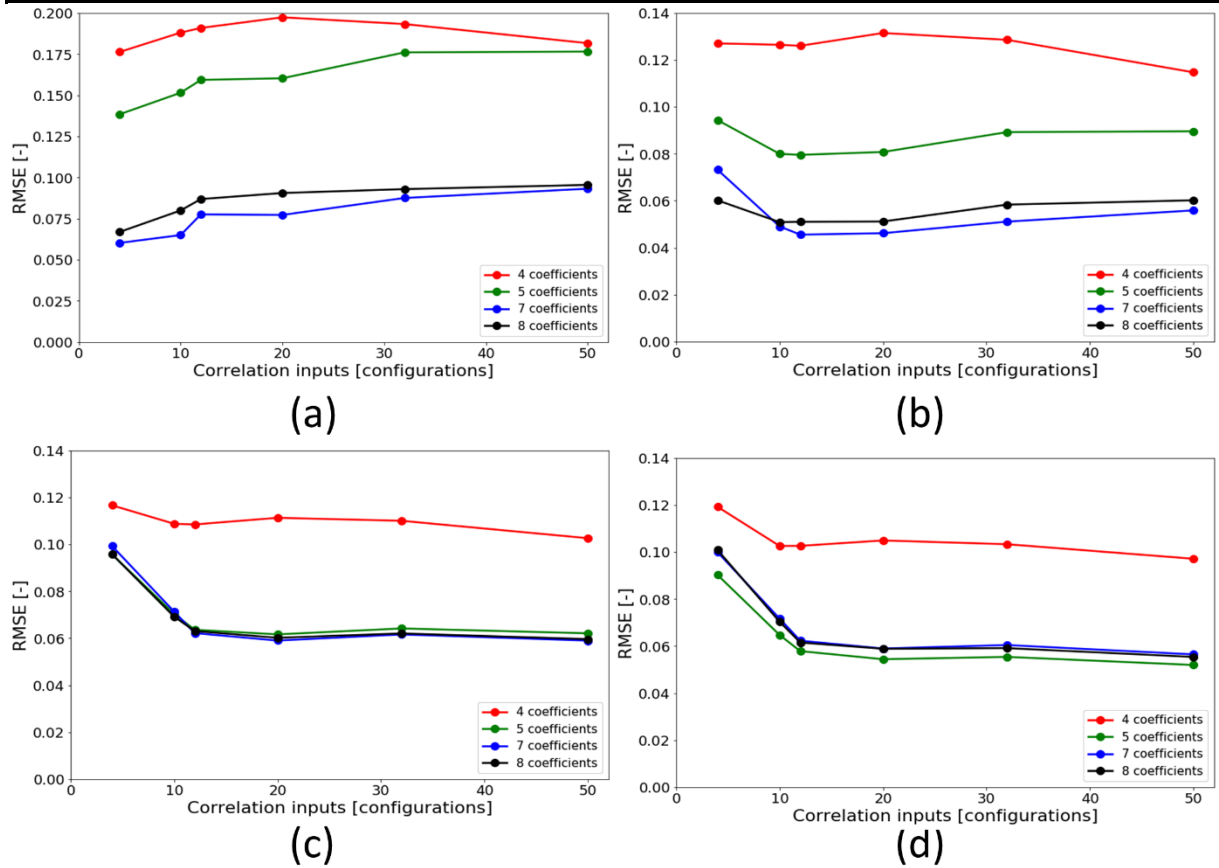


Figure 102. RMSE values for all the tested correlations. (a) for $\bar{f}_m = 0.2$ (b) $\bar{f}_m = 0.5$ (c) $\bar{f}_m = 0.8$ (d) $\bar{f}_m = 0.98$

To sum up, by analyzing the results at a global scale obtained from simulations performed on 50 configurations of circular radial fins, we can conclude that for the studied domain, there is no need for more than 12 configurations distributed as shown in Figure 102(c) to establish a robust and accurate Nusselt correlation. Moreover, the formulation of the correlations depends on the sizing criteria of the storage. For instance, 7 coefficients are indispensable to minimize the overall error if the sizing criteria is based on the time taken to partially charge the storage at 20 or 50 %. However, 5 coefficients are sufficient if the sizing is based on higher melted fraction of 80 and 98 %.

To further investigate this observation, Figure 103 shows the evolution of the RMSE with the melted fraction of the 4 formulations of the Nusselt correlation. These results are obtained by utilizing 12 configurations as input data. For all cases, the RMSE reduces with the increase of the melted fraction. The curve corresponding to the correlation formulated using 5 coefficients explains the observations made by analyzing Figure 102. At early stages of the charging process (i.e. for low PCM’s melted fraction), the addition of a fifth term in the correlation has little to no effect on the RMSE values. It takes 7 coefficients to improve the predictions of the ‘system’

model leading to lower RMSE. However, the ability of the correlation containing 5 coefficients only to lead to an accurate prediction of the behavior of the storage improves with the melting progress. The results presented in Figure 103 shows that the curve for 5 coefficients rejoins the curves obtained by using 7 and 8 coefficients around a PCM's melted fraction of 0.8. Finally, considering that using a 7-term correlation instead of a 5-term one does not require additional numerical resources in terms of CFD calculations, and given that the Nusselt values consistently outperform those obtained with 5 terms, opting for the 7-term correlation appears to be the consistently superior choice.

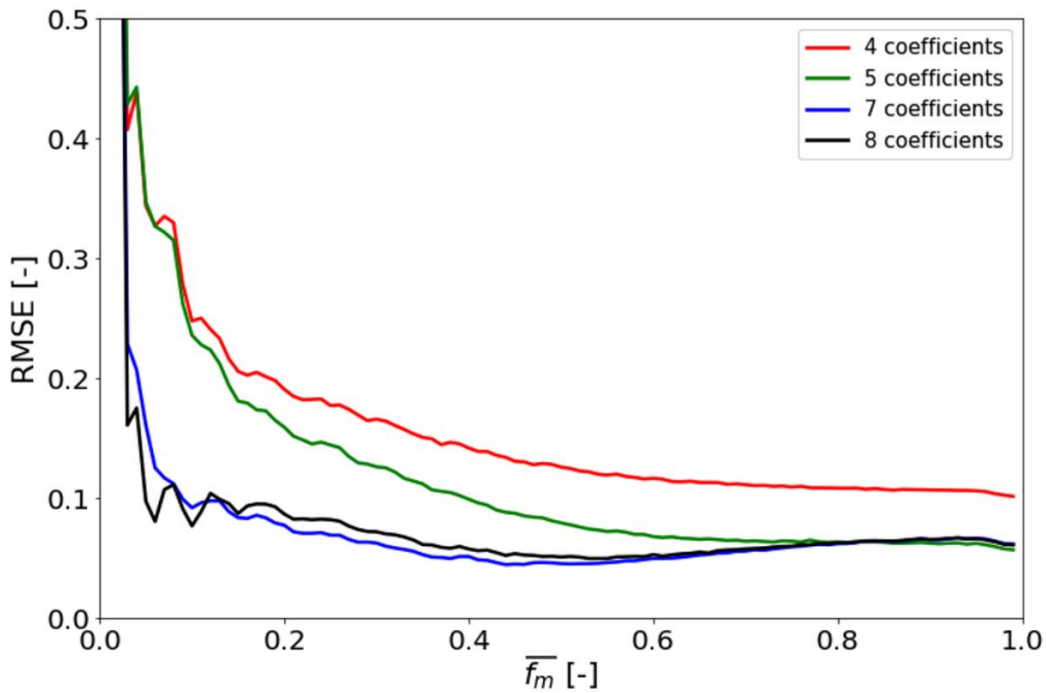


Figure 103. Evolution of the RMSE values with the melted fraction for the correlations obtained from 12 geometric configurations

The graphs presented in Figure 102 and Figure 103 demonstrated the impact of the amount of data and the number of coefficients used in the calculation of a heat transfer correlation on the predictions of the “system” model by using collective results from the 50 distinct geometric configurations of the fins. However, the accuracy of the correlations for each specific combination of design parameters (e and p) was not demonstrated. This can be achieved by calculating the distribution of charging time ratio predicted by both “system” and CFD model over the range of values of the fins’ pitch p and the fins’ thickness-to-pitch ratio e/p:

$$\frac{t_{sys}}{t_{CFD}} \Big|_{\bar{f}_m} = \frac{t_{sys} \Big|_{\bar{f}_m}}{t_{CFD} \Big|_{\bar{f}_m}} \quad (121)$$

The distributions of the values of $\frac{t_{sys}}{t_{CFD}} \Big|_{\bar{f}_m}$ are presented in Figure 104 to Figure 109. Each figure corresponds to the set of correlations based on a given number of configurations. In each figure, the results obtained from testing several formulations of the Nusselt correlation are presented in different sets where each set corresponds to a certain number of coefficients. In each set, three graphs are plotted to represent different values of the PCM's melted fraction \bar{f}_m . In each graph, the x-axis represents the fins' pitch p ranging from 2.5 to 25 mm while the y-axis represents the fins' thickness-to-pitch ratio ranging from 5 to 25 %. The time ratio $\frac{t_{sys}}{t_{CFD}} \Big|_{\bar{f}_m}$ is represented in colors between 0.7 and 1.3 around the ideal value of 1. A time ratio $\frac{t_{sys}}{t_{CFD}} \Big|_{\bar{f}_m} < 1$ (represented by the blue cells) implies that the time taken by the 'system' model so that the storage melts the corresponding fraction of the PCM is less than the one needed in the CFD model, which means that a faster charging process is predicted by the "system" which is overestimating the thermal power of the storage. Contrarily, a time ratio $\frac{t_{sys}}{t_{CFD}} \Big|_{\bar{f}_m} > 1$ (represented by the red cells) signifies that the 'systems' model underestimates the thermal power of the storage leading to a slower melting process. By considering these distributions, one can quantify the amount of error committed by simulating using a simplified 'system' model, the charging process of a LHTES system for any combination of the geometric parameters e and p .

The distribution of time ratios substantiates the observations made regarding the RMSE values. Concerning the number of coefficients employed in the correlation construction, employing only 4 coefficients (as shown in sub-figures (a)) leads to higher ratios compared to the other formulation, irrespective of the melted fraction value of the PCM. The use of 5 coefficients enhances the accuracy of the correlation within the (e,p) domain, particularly for high melted fractions (compare sub-figures (a) with sub-figures (b) at a melted fraction of 98%).

Ultimately, the key takeaway from these figures lies in the correlations' ability to predict the charging time for configurations not included in their development. In all cases, except when all 50 configurations were utilized in their construction, the heat transfer correlations were constructed based on data from specific (e,p) configurations. Once integrated into the 'system' model, the results were validated using CFD data from all 50 configurations. The distribution of time ratios depicted in these figures reveals that the correlations are not necessarily more

accurate for the cases used in their development. In most instances, errors appear to be fairly uniform across the domain, with slightly higher values for configurations having e and p values at the domain's edges.

4 configurations

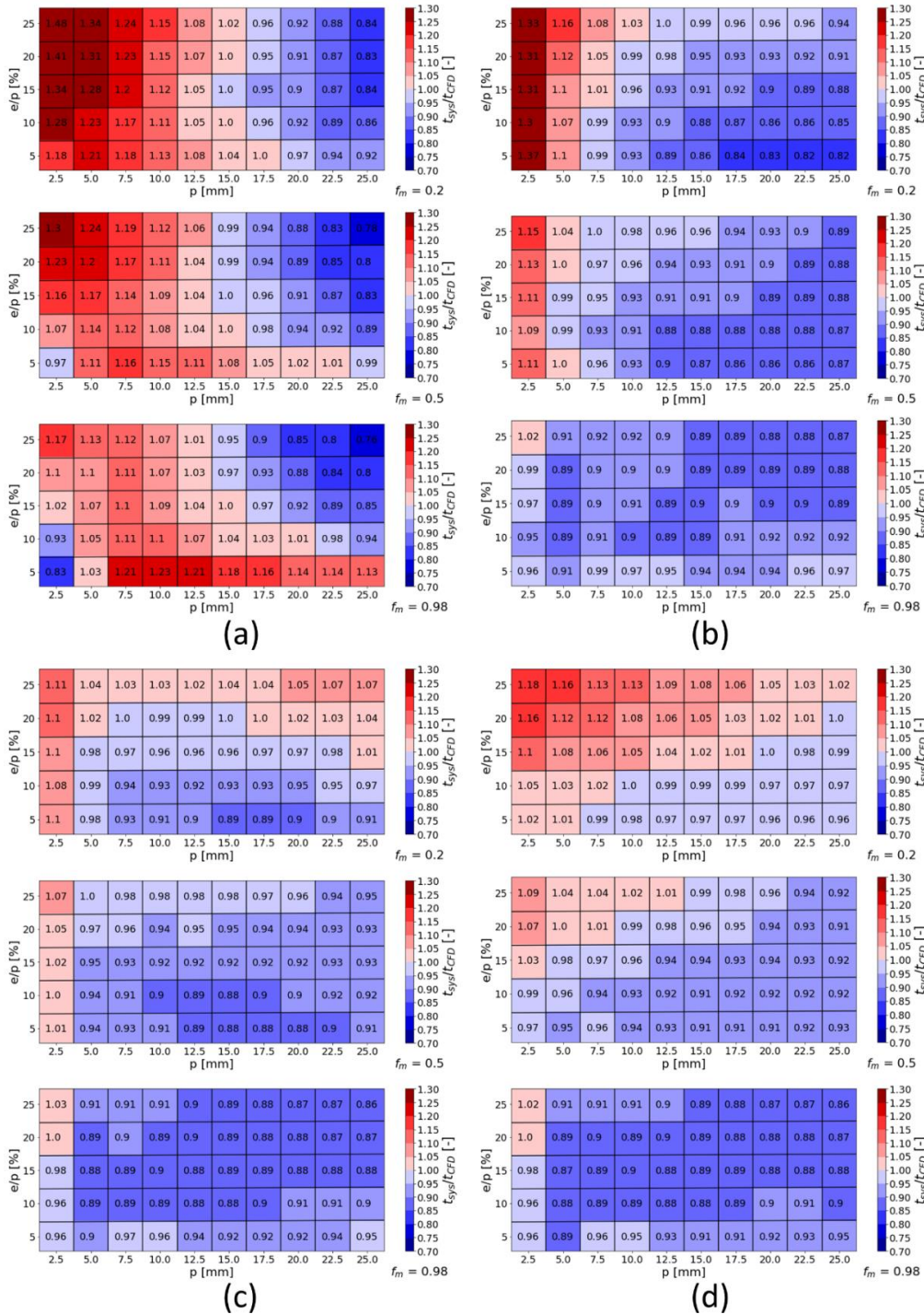


Figure 104. Distribution of the charging time ratio between both 'system' and CFD models for Nusselt correlations constructed using data from 4 geometric configurations (a) 4 coefficients (b) 5 coefficients (c) 7 coefficients (d) 8 coefficients.

10 configurations

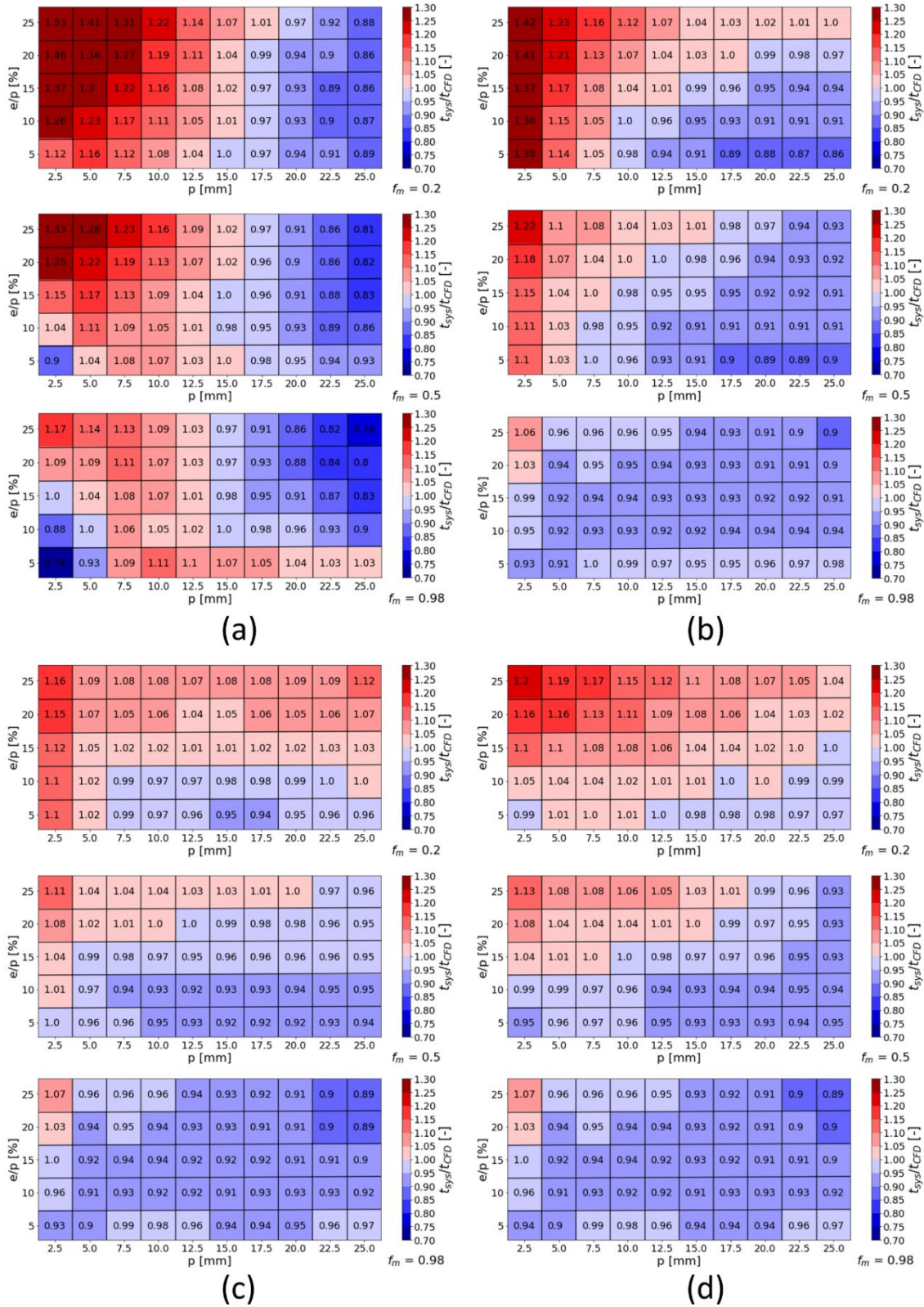


Figure 105. Distribution of the charging time ratio between both 'system' and CFD models for Nusselt correlations constructed using data from 10 geometric configurations (a) 4 coefficients (b) 5 coefficients (c) 8 coefficients (d) 8 coefficients.

12 configurations

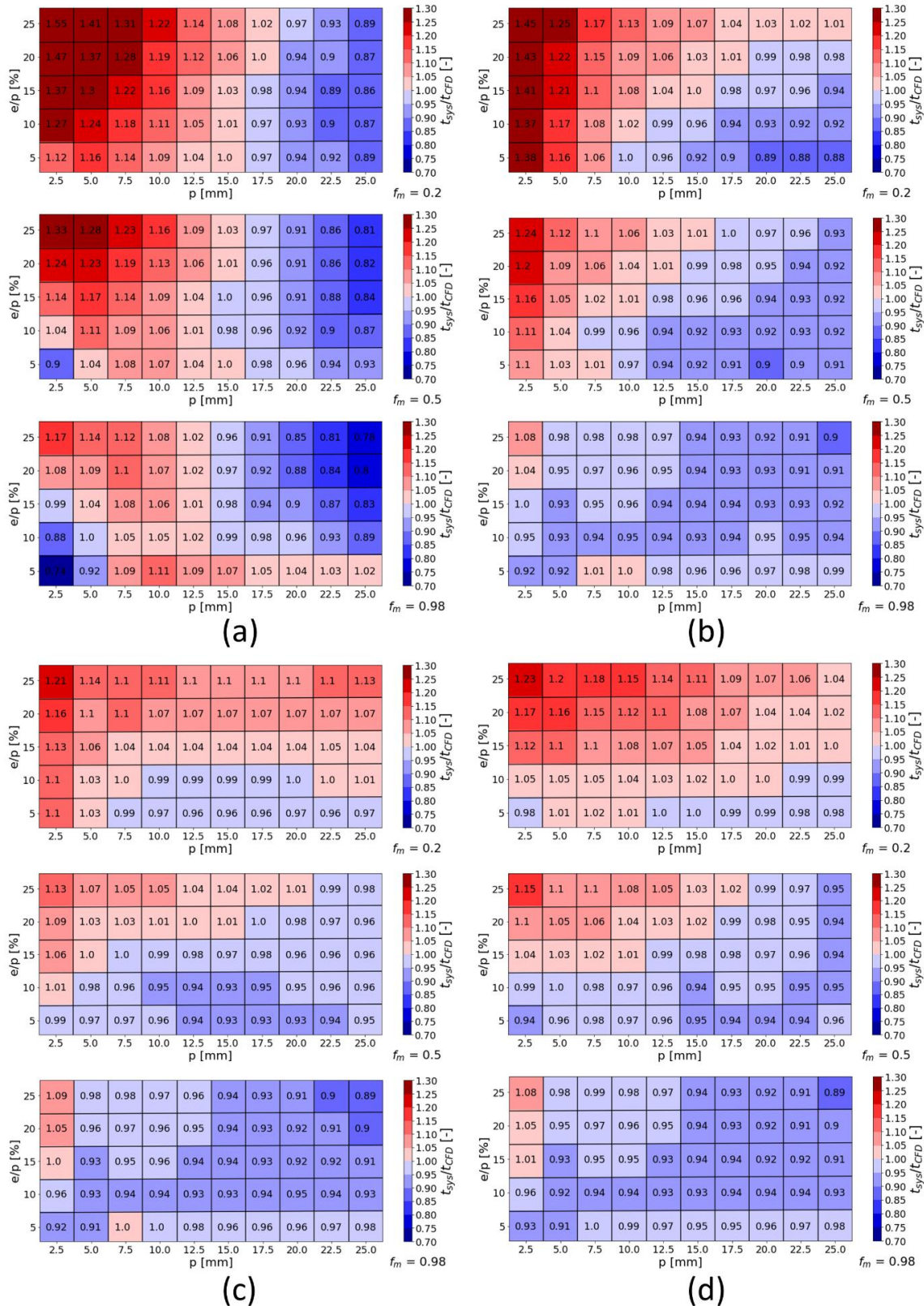


Figure 106. Distribution of the charging time ratio between both ‘system’ and CFD models for Nusselt correlations constructed using data from 12 geometric configurations (a) 4 coefficients (b) 5 coefficients (c) 7 coefficients (d) 8 coefficients.

20 configurations

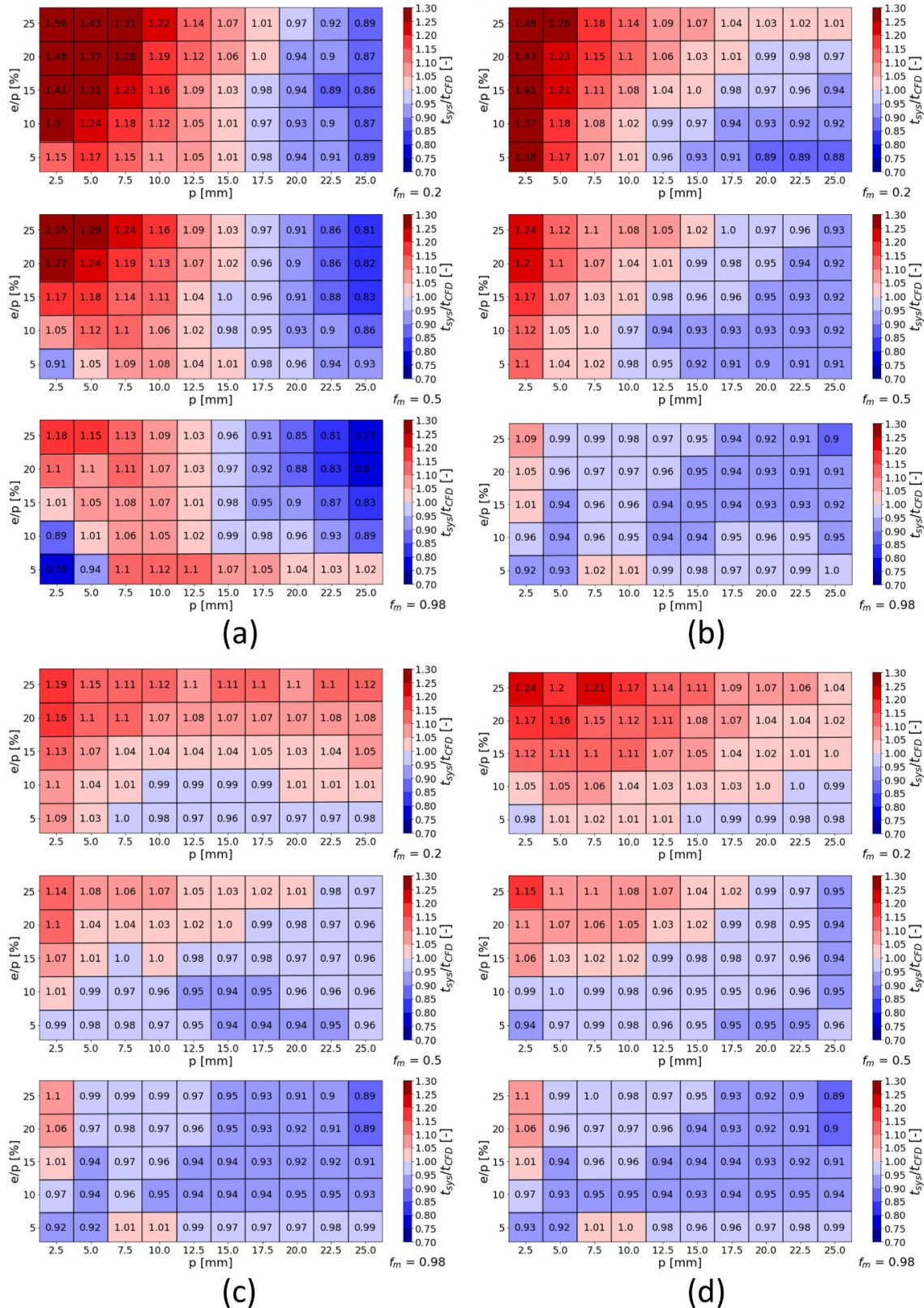


Figure 107. Distribution of the charging time ratio between both ‘system’ and CFD models for Nusselt correlations constructed using data from 20 geometric configurations (a) 4 coefficients (b) 5 coefficients (c) 7 coefficients (d) 8 coefficients.

32 configurations

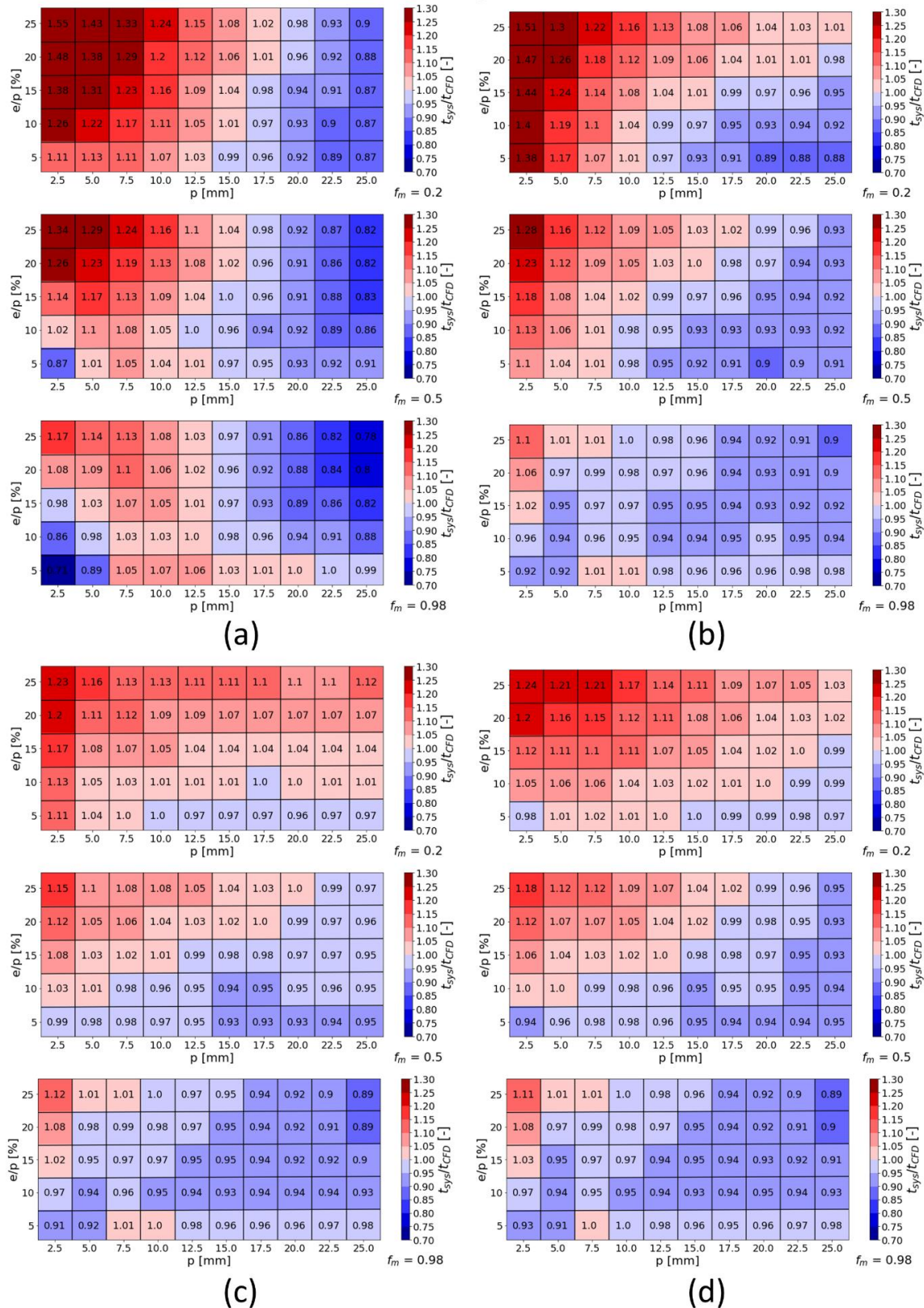


Figure 108. Distribution of the charging time ratio between both ‘system’ and CFD models for Nusselt correlations constructed using data from 32 geometric configurations (a) 4 coefficients (b) 5 coefficients (c) 7 coefficients (d) 8 coefficients.

50 configurations

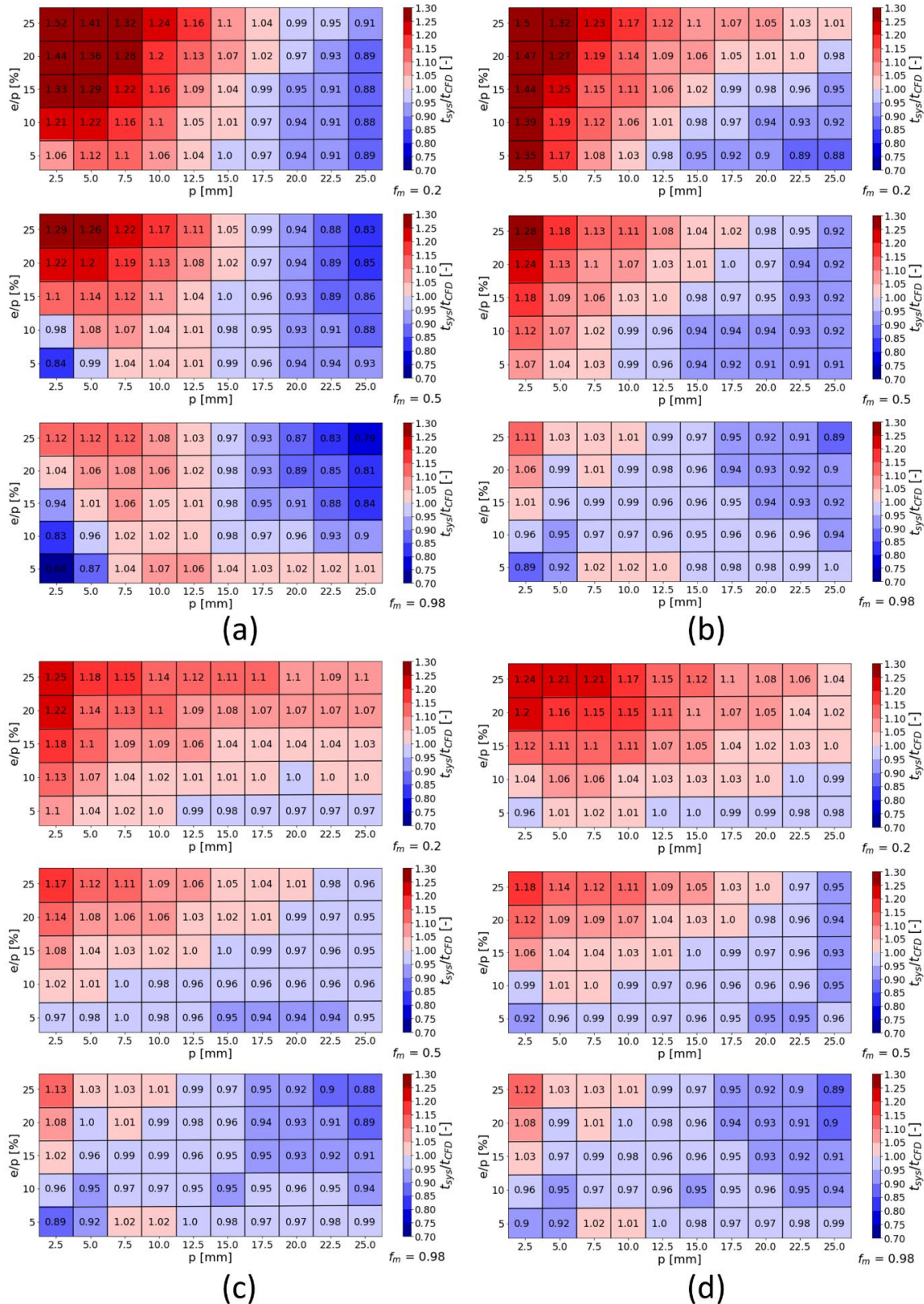


Figure 109. Distribution of the charging time ratio between both 'system' and CFD models for Nusselt correlations constructed using data from 50 geometric configurations (a) 4 coefficients (b) 5 coefficients (c) 7 coefficients (d) 8 coefficients.

V.3.1.2. Non-uniform temperature boundary condition

In the previous section, the set of correlations obtained from CFD simulations were tested on the ‘system’ scale. The investigations led to the conclusion that 12 configurations of fins with a difference in pitch Δp of 7.5 mm and difference in the fins’ thickness-to-pitch ratio $\Delta e/p$ of 10 % is sufficient to build a correlation to predict the behavior of a LHTEs system with circular fins. This is applicable for a range of pitches between 2.5 mm and 25 mm and thickness-to-pitch ratios ranging from 5 to 25 %. However, it is important to recall that for the construction of the heat transfer correlations, as well as the validation of the ‘system’ model, we carried for a single charging case of the storage system. In this specific case, a uniform and constant temperature boundary condition of 315 °C was applied to the inner wall of the tube, resulting in an axially uniform melting front along the PCM domain in the ‘system’ model. In practical applications, the temperature of the HTF may not be uniform throughout the heat transfer tube, rendering the assumptions made in both CFD and ‘system’ models incomplete in covering the complete range of operating conditions in a LHTEs system. In order to validate the obtained correlation for various charging modes, simulations were performed in which a non-uniform temperature was imposed at the tube’s inner wall. The chosen fin configuration was number 38 in Table 9 with a pitch of 20 mm and a thickness of 3 mm (e/p ratio of 15 %). All other geometric parameters and material properties used in the previous study remained unchanged. The temperature at the tube’s inner wall increases linearly from bottom to top of the tube, as follows:

$$T_{t,int} = 310 + 50z \quad (122)$$

Where z denotes the axial position of the tube ranging from 0 to 0.5 m. This temperature range may not align with real-world scenarios encountered in two-phase steam storage systems. Nevertheless, it is intentionally exaggerated to assess the robustness of the numerical model's predictions under extreme conditions.

The CFD simulation was performed using the ‘CC’ model. The correlation, which was formulated using 7 parameters and constructed from the data obtained through 12 configurations, is used in the ‘system’ model to predict the behavior of the storage system.

Figure 110 shows the evolution of the energy stored in the storage elements formed by the heat transfer tube, fins and PCM during the charging phase. The values on the y-axis correspond to

the energy stored in a complete tube (i.e. angular sector of 360°) with a length of 1 m. At a global scale, the curves resulted from both models overlap for a significant part of the charging phase leading to a successful reproduction by the ‘system’ model of the CFD results. Consequently, the ‘system’ model employing the correlation previously mentioned is reliable to predict the evolution of the energy stored over time, and therefore, the thermal power of the storage, without the need to account directly for the effects of the geometry and natural convection.

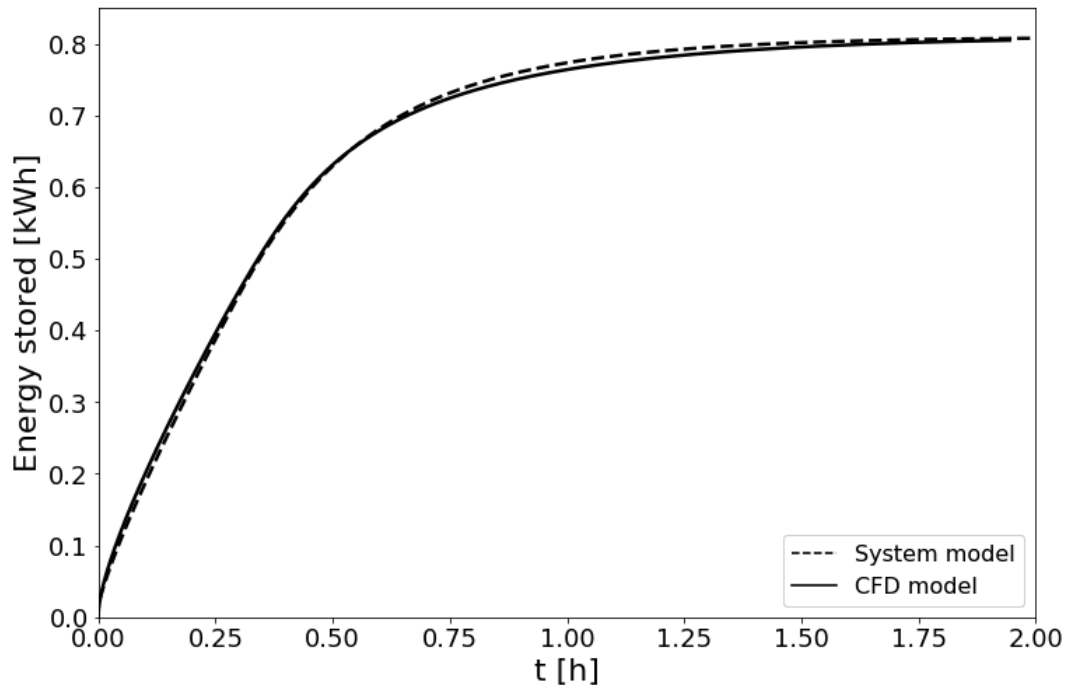


Figure 110. Evolution with time of the energy stored in the storage predicted by both the ‘system’ and CFD models for a charge with a non-uniform temperature along the tube’s height.

Figure 111 shows the liquid PCM layer thickness distribution, defined by l_c in Equation (113), at different instants during the charging phase along the height of the tube. Here again, an excellent agreement is observed. At $t = 0.05$ h, the charging phase is still in its initial stages, resulting in small values of l_c . However, the impact of the non-uniform boundary condition is already noticeable, leading to a thicker liquid PCM layer at the top of the domain. The ‘system’ model reproduces the evolution of l_c accurately. As the charging process advances, the difference in l_c values between the top and the bottom of the domain increases. Nevertheless, the predictions of the ‘system’ model remain pertinent. A small difference between the results of both models is observed in the first sub-domain at the top, where the CFD model predicts an advanced melting process relative to the ‘system’ model. This difference is due to the

accumulations of a small volume of liquid PCM at the top of the domain due to the heat transferred vertically through of fins. These axial heat exchanges are not considered in the ‘system’ model. For circular radial fins, their effect on the predictions of the “system” model, on both local (Figure 111) and global (Figure 110) scales remains negligible. Finally, the success of the ‘system’ model to reproduce the CFD results, even when considering a non-uniform temperature at the tube’s inner wall, is attributed to the definition of the characteristic length l_c and temperature T_{cold} used in the dimensionless numbers Rayleigh and Nusselt.

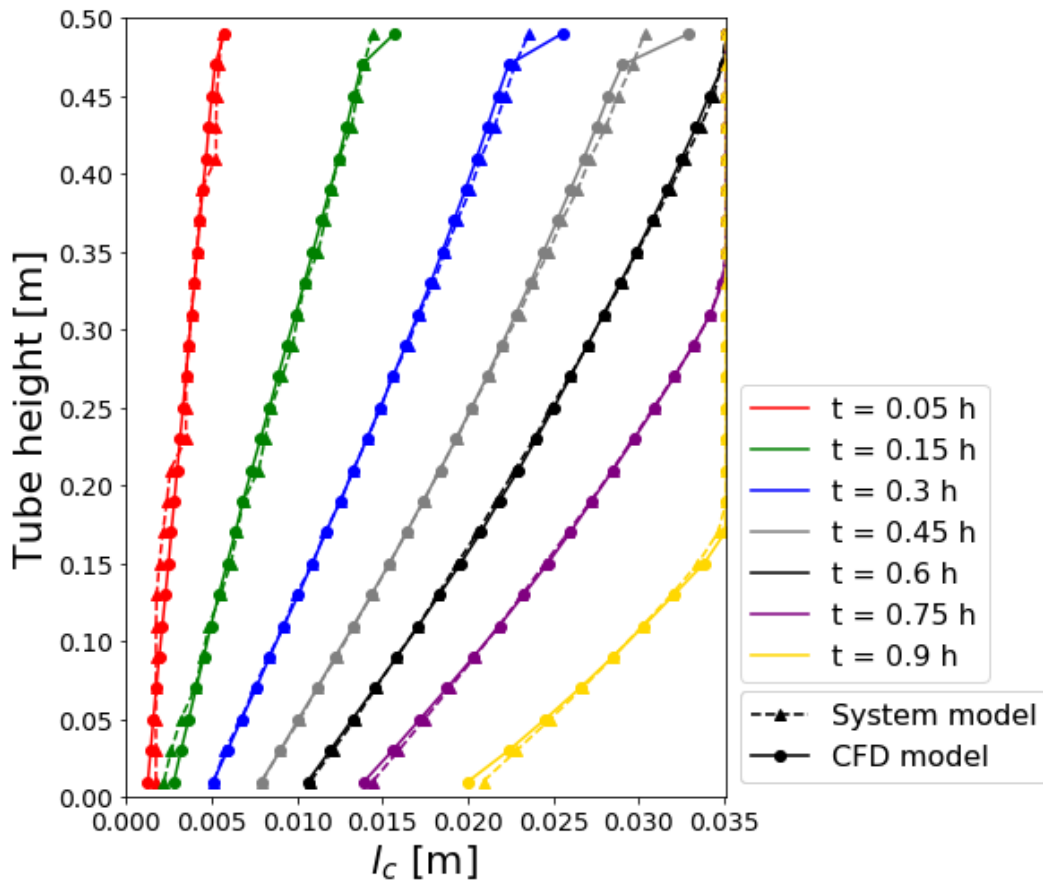


Figure 111. Distribution of the liquid PCM layer along the domain obtained by both ‘system’ and CFD models at different instants for a charge with a non-uniform temperature along the tube’s height.

V.4. Conclusion

The primary objective of this chapter was to develop a comprehensive multi-scale modelling approach for predicting the behavior of a LHTES system equipped with circular fins during the charging phase. This approach involves the construction of heat transfer correlations derived from numerical data obtained through CFD simulations. These correlations are then integrated into a simplified ‘system’ model, facilitating both accurate and rapid predictions of the storage

system's performance. The goal was to construct a heat transfer correlation that accounts for the influence of natural convection and fin geometry on the overall thermal behavior of the storage. To achieve this, a thorough investigation was conducted to evaluate the correlation's formulation and the amount of CFD data required to establish a robust correlation.

As a result, it was demonstrated that utilizing seven coefficients and twelve configurations, evenly distributed across the fin pitch and thickness domain ($\Delta p = 7.5$ mm and $\Delta e/p = 10\%$), are sufficient to generate a correlation that enables accurate predictions by the reduced model, with an average error of less than 6% (see RMSE values in Figure 102) within the studied range of (e, p) values. Furthermore, these findings underscored the utility of the derived correlation and the reduced numerical model in predicting the storage behavior across various operational conditions. This was verified by comparing the outcomes of the 'system' model with those of CFD simulations that featured non-uniform temperature boundary conditions imposed on the tube's inner wall.

Looking ahead, future research endeavors should aim at further generalizing the heat transfer correlation. This can be accomplished by considering the material properties of the metallic components, including both the heat transfer tube and the fins. This extension aligns with the outcomes of the CFD simulations conducted in the previous chapter, as detailed in section IV.5.3. Additionally, the multi-scale modelling approach can be expanded to encompass the discharging phase of the storage, particularly when the PCM undergoes solidification within the shell.

Finally, the significance of this study lies in the substantial reduction in computational cost. The time required to simulate a complete charging phase of the storage has been significantly reduced, from 2-3 days when using the 3D CFD model to just a few seconds with the reduced 'system' 1D model.

Chapter VI – General conclusion and perspectives

VI.1. Conclusions

In this concluding chapter, a comprehensive overview is provided of the work undertaken, focusing on the generalization of a multi-scale modelling approach for shell-and-tube LHTES systems for steam storage applications. The primary objective throughout this research endeavor has been the development of a powerful computational tool for the efficient sizing of a storage system while accounting for the influence of various physical phenomena. These include the PCM's solid-liquid phase transition, heat conduction throughout the different components of the storage system, and natural convection within the liquid phase of the PCM. Furthermore, investigations were conducted into how the geometry and material composition of the metallic components influence these phenomena, and, consequently, the overall thermal performances of the storage system. Fine 3D CFD simulations were employed as the primary tool for this multidimensional investigation. Additionally, novel heat transfer correlations including the role of geometrical parameters were developed, based on the insights gained from the outcomes of CFD simulations. Besides, a painstaking sensitivity analysis was performed to show the best form for this correlation, as well as the best and/or minimal size of the tests sample. These correlations have been subsequently integrated in a 'system' model, enabling the calculation of an equivalent thermal conductivity for a homogeneous PCM + fins material. This calculation allows an accurate prediction of the heat flux exchanged occurring between the HTF and PCM within the storage. The 'system' simulations represent an efficient computational solution for reproducing the storage system's behavior, while accounting for the impact of various influencing factors.

In **Chapter II**, a state-of-the-art research on thermal energy storages applied for steam storage applications was presented. Steam is extensively utilized as a HTF in various industrial processes, as well as for electricity generation from renewable resources in CSP plants based on direct steam generation. The integration of steam storage technologies is deemed essential to address the discrepancy between supply and demand while also enabling the recovery of waste heat. The most mature technology for steam storage involves steam accumulators, where

steam energy is stored under pressure in the form of sensible heat within a volume of saturated liquid. However, strong limitations exist with this technology, notably regarding the temperature and pressure levels of the steam produced during discharge and the mechanical constraints associated with designing large-capacity storage systems.

An alternative method for steam storage entails the utilization of PCM that undergo a solid-liquid phase transition. This phase transition is accompanied by a significant absorption/release of energy over a narrow temperature range. Various approaches based on PCM for storing steam energy already exist, with the shell-and-tube technology being particularly noteworthy. In these systems, a volume of PCM occupies a metallic shell and is traversed by a stack of tubes through which steam flows. Notably, this technology has advanced to the pre-industrial scale, with several prototype modules constructed for potential industrial applications and CSP plants. To facilitate the integration of this technology into industry practices, the development of an efficient and reliable numerical tool becomes imperative. Such a tool is required to accurately size industrial-scale storage systems, thereby justifying the objectives pursued in this thesis.

Accurately modelling the behavior of shell-and-tube LHTES systems necessitates the utilization of fine 3D CFD models. These models enable the comprehensive consideration of various factors that influence the thermal performance of the storage system. Through a detailed literature review, each of these influential factors and the corresponding mathematical methodologies for simulating the storage system's behavior were identified. Regarding the modelling of the solid-liquid phase transition of PCM, the enthalpy-porosity method introduced by Voller [72] was adopted. In this approach, PCM is considered a homogeneous Newtonian fluid flowing in a laminar regime. To account for the latent heat of phase change, a source term is introduced into the energy equation. Furthermore, given that PCM is treated as a fluid, a source term is introduced into the momentum equation to effectively impose zero velocity for the solid phase. In the course of this thesis, the Darcy source term method has been selected. These methods are widely adopted in the literature and seamlessly integrated into the commercial CFD software ANSYS Fluent, which serves as the primary tool for conducting CFD simulations.

Another pivotal factor influencing the storage behavior is natural convection. Natural convection arises due to density variations between the solid and liquid phases, as well as buoyancy-driven forces within the liquid phase. The literature review presented various

techniques for addressing this phenomenon in a mathematical model. In the studies performed during the thesis, the Boussinesq approximation was chosen, which accounts for the effects of the buoyancy-driven flow within the liquid phase without varying the density of PCM.

Finally, to regulate and enhance heat transfer within the storage, metallic fins are commonly added to the external surface of the heat transfer tubes within the PCM domain. A multitude of fin types and shapes are documented in the literature, each accompanied by its own set of advantages and disadvantages. The parametric studies detailed in Chapter II, focusing on the configurations of fins and their material properties, served as the foundational groundwork for the investigations carried out in this thesis.

In **Chapter III**, two distinct reduced numerical approaches were developed for modelling the dynamic behavior of shell-and-tube LHTES system. The primary differentiation between the two models is found in the dimensionality of the PCM and fins domain representation. In the first approach, the domain was discretized in the radial direction (1D radial model), while in the second approach, the PCM and fins domain was treated as a whole volume without radial discretization (0D radial model). Both models were coupled with a 1D homogeneous model, which was utilized to represent the two-phase liquid water/steam flow inside the tubes. The models were tested and validated according to experimental data obtained from trials involving a shell-and-tube LHTES prototype module designed and operated at CEA Grenoble. Regarding the heat transfer mechanisms within the storage, a purely conductive approach was employed. The influences of natural convection and the geometry of the fins on the thermal exchange within the storage were taken into consideration through the incorporation of heat transfer correlations derived from CFD simulations conducted by Beust et al. [35] for the same geometry of the prototype module under consideration.

The numerical models were tested according to a charging phase of the prototype module, where superheated steam was introduced at fixed temperature and pressure conditions. The performance of the two numerical approaches was examined at both local and a global scales. On the global scale, the evolution of the energy accumulated in the storage during the charging phase, as predicted by the numerical models, was compared to the experimental data. During the active phase of charging, where the melting front of the PCM had not yet extended beyond the tips of the radial fins, the thermal power of the storage was effectively predicted by both numerical models. The primary distinction between both approaches became evident when

comparing their outcomes at a more localized scale. During a charging phase, conducted under fixed pressure conditions, the water level that separates the condensed liquid water at the bottom of the tubes from the steam above moves downward within the tubes. The 0D radial model closely aligned with observed data, whereas the 1D radial model resulted in a relatively higher water level. A thorough investigation revealed that the source of disagreement between both approaches originated from the distribution of heat flux along the heat transfer tube. For a given state within the PCM, the 1D radial model overestimated the heat transfer rate from the HTF to the PCM. Consequently, a shorter length of tube was required for steam condensation. However, the superior ability of the 0D radial model to replicate the heat flux distribution along the tube came at a cost. In fact, an additional correlation was incorporated into this model to precisely calculate the heat flux. Generalizing this correlation to accommodate various geometrical configurations of fins can be challenging, posing a significant obstacle to generalizing the 0D approach for the future research conducted during this thesis. On the other hand, the 1D radial model remained effective in predicting the overall thermal power of the storage while considering the entire geometric domain of the system.

Chapter IV was dedicated to CFD investigations. The heat transfer correlation developed by Beust et al. [35] and integrated into the numerical approaches developed in Chapter III is specific to the shell-and-tube prototype module available at CEA Grenoble. Therefore, to generalize the applicability of the multi-scale modelling approach for such systems, encompassing various geometric parameters and material properties of the fins, a return to the CFD scale was necessary. The objective of this chapter was to provide comprehensive insights into how different fin shapes, configurations, and material properties impact the thermal performance of the storage during the charging phase. The impact of natural convection in the liquid phase was examined in detail, and two models were described for this purpose. In the first one, denoted as the ‘C’ model, heat was assumed to be transferred by pure conduction within the liquid PCM phase. In contrast, the second model, denoted as the ‘CC’ model, considered natural convection in addition to heat conduction through the liquid phase.

Before investigating the role of adding fins on the thermal behavior of the storage, the influence of natural convection was initially examined on vertical smooth-tube configurations (tubes without added fins on their exterior surfaces). A first parametric study was conducted based on the tube's domain height. The results revealed the existence of an optimal tube height at which

the contribution of natural convection was maximized, resulting in the fastest melting process. For the studied cases, the optimal domain height was found to be 1 cm. Optimizing convective heat exchanges within the storage is achieved by prioritizing the breaking of large convection loops in favor of smaller, more efficient ones.

Then, metallic fins were incorporated into the PCM domain. In an initial examination, the impact of the type of fins employed on the behavior of a vertically arranged storage system during the charging phase was investigated. Accordingly, two types of fins were compared: axial longitudinal fins and radial circular fins. The findings revealed that longitudinal fins exhibit superior heat conduction capabilities. However, radial circular fins outperformed in enhancing convective heat transfer, allowing for more efficient recovery as the melting phase progressed, consequently leading to a relatively accelerated melting process.

Subsequently, a comprehensive parametric study regarding the geometry of circular radial fins was conducted. The geometric parameters under investigation were the fin length, thickness, and pitch. By comparing the outcomes with those obtained from simulations involving smooth-tube configurations, it was demonstrated that the addition of any fin volume significantly improves the thermal power of the storage, emphasizing the role of metallic fins in such systems. Additionally, the fin length was found to have no direct impact on the enhancements attributed to natural convection. Nevertheless, an increase in fin length, given fixed fin thickness and pitch values, improved heat conduction to the PCM, thereby reducing the time required for complete PCM volume melting. Furthermore, the reduction of fin thickness and pitch, while maintaining a fixed thickness-to-pitch ratio, improved thermal conduction within the storage. However, this reduction in both parameters limited the contribution of natural convection. Therefore, it was shown that here again competitive effects are present, and optimal combinations of pitch and thickness were achieved by balancing these two opposing effects. Finally, an assessment of the error associated with neglecting natural convection on the charging time of the storage was conducted for the configurations presented in the study. This enabled the determination of when it is more advantageous to utilize the 'C' model (which offers a 95% reduction in computational cost relative to the 'CC' model).

Utilizing the insights gained from these observations, a novel fin geometry was proposed and tested. This geometry consisted of radial fins with a triangular section. For the same fin volume

ratio as conventional circular fins, triangular-section fins improved heat conduction to the PCM domain and resulted in a 13% reduction in the total melting time.

Finally, a coupled parametric study that combined both geometric factors of fins and material properties was conducted. Twelve geometric configurations were selected from the extensive list used in the previous study. For each configuration, the thermal conductivity of the fins was varied from $50.33 \text{ W}\cdot\text{m}^{-1}\cdot\text{K}^{-1}$ to $400 \text{ W}\cdot\text{m}^{-1}\cdot\text{K}^{-1}$. Simulations were then performed using both the ‘C’ model and the ‘CC’ model. The results illustrated the interplay between heat conduction and natural convection in shell-and-tube LHTES with radial fins. They indicated that an increase in the thermal conductivity of fins improved heat conduction in the storage, leading to a decreased contribution of natural convection, which is solely dependent on the system's geometry. The combination of the effects of both heat conduction and natural convection is essential for understanding the behavior of the storage and optimizing it in the future.

In **Chapter V**, the knowledge acquired from CFD investigations served as the foundation for developing a multi-scale modelling approach to predict the behavior of a shell-and-tube LHTES system with circular fins during the charging phase. Data obtained from CFD simulations using the ‘CC’ model were utilized to construct heat transfer correlations. These correlations aimed to establish a relationship between the heat transfer rate within the storage and various influencing factors, including the PCM solid-liquid phase change, natural convection within the melted phase, and the geometry of the fins, represented by fin thickness and pitch. Two dimensionless numbers, the Nusselt and Rayleigh numbers, were selected for this purpose. The desired correlations took the following form: $Nu = f(Ra, e, p)$. A comprehensive investigation was undertaken to assess the impact of correlation formulations and the quantity of CFD data required to establish a robust correlation. Subsequently, the resulting correlations were integrated into the 1D radial ‘system’ model, enabling accurate and rapid predictions of the storage system's performance.

As a result, it was demonstrated that by employing seven coefficients and twelve configurations, evenly distributed across the fin pitch and thickness domain ($\Delta p = 7.5 \text{ mm}$ and $\Delta e/p = 10\%$), it is possible to generate a correlation that allows accurate predictions by the reduced model, with an average error of less than 6% within the studied range of (e, p) values. Furthermore, these findings emphasized the practicality of the derived correlation and the reduced numerical model in predicting storage behavior across various operational conditions.

This was confirmed by comparing the results of the ‘system’ model with those of CFD simulations featuring non-uniform temperature boundary conditions applied to the tube's inner wall.

VI.2. Perspectives

In this final section, attention is shifted towards the future, and potential avenues for further research and development in the field of shell-and-tube LHTES systems are reflected. The insights acquired from the present studies open doors for various possibilities and areas that merit more profound investigation.

In **Chapter III**, both 0D radial and 1D radial approaches were developed to represent the heat transfer mechanisms within the PCM + fins domain. In the 0D radial model, the calculation of the heat transfer flux exchanged at the tube's wall between the HTF and PCM + fins region was directly based on the Nusselt correlation. However, using these correlations required knowledge of the average temperature of the PCM's liquid phase. Given that this parameter was unknown to the model, calculating its values necessitated the integration of an additional correlation. This supplementary correlation involved recovering the temperature variation according to the PCM's average melted fraction throughout the charging process. Notably, this correlation is specific to the studied case under the considered working condition, and its applicability remains suitable for this particular case. Consequently, generalizing the use of the 0D radial approach requires finding a generic method to estimate this parameter. This estimation can be achieved by correlating the heat flux exchanged at the melting interface with various factors related to the state of the storage.

Another limitation of the 0D radial approach relates to simulating heat transfer within the passive PCM volume. These volumes were not considered in the CFD simulations used to establish the heat transfer correlations. Consequently, representing them in a 0D radial approach, where the heat transfer rate is directly calculated from the correlations derived from CFD, presents some challenges. Therefore, if a 0D radial approach is to be adopted at the ‘system’ level, adjustments to the CFD model should be made to account for the presence of a passive PCM volume near the periphery of the shell. These latter must be precisely defined and their precision duly estimated.

Additionally, both the 0D radial and 1D radial approaches were tested and validated based on experimental data provided by the prototype module installed at CEA Grenoble. The testing case corresponds to a charging phase at a fixed pressure and temperature. However, as described in Chapter III section III.2, the storage may operate under different working conditions. During the charging phase, steam may be injected at a sliding pressure and temperature. The increase in steam pressure, along with its corresponding saturation temperature, compensates for the increase in thermal resistance within the storage and ensures a uniform thermal power throughout the charging phase. Consequently, the entire length of the tube is required to condense the steam, and the water level is maintained at the bottom of the tube throughout the charging phase. On the PCM side, the melting front exhibits greater uniformity in the axial direction compared to the case with steam injected at a fixed pressure and temperature. Testing the two numerical approaches for a charging phase with sliding pressure can offer an interesting perspective for validating these models.

In **Chapter IV**, CFD simulations were conducted to evaluate the influence of the length of a vertical smooth-tube domain on enhancements due to natural convection. The results demonstrated that a domain height of 1 cm resulted in the fastest melting process. This study can be further advanced by verifying this outcome for different thicknesses of the domain in the radial direction. Consequently, correlations can be derived to enable the prediction of the charging time as a function of the domain's height and the thickness of the PCM domain.

Additionally, the influence of fin types, configurations, and material properties on the storage behavior during the charging phase was investigated. An important prospect lies in simulating the discharging phase. During discharge, liquid water is injected from the bottom of the tubes. The PCM, initially in a liquid state, transfers its heat to the liquid water, producing steam for the process. On the PCM side, a solidification front forms and progresses away from the tube in the radial direction. During discharge, heat is primarily transferred by pure conduction within the PCM. The influence of the fin geometry and material properties is expected to resemble the observations made from the 'C' model simulations during the charging phase.

In **Chapter V**, the calculated Nusselt correlation considered the influence of natural convection, fin thickness 'e', and pitch 'p'. However, prior studies in Chapter IV revealed that the thermal power of the storage also depends on the thermal conductivity of the metallic components ' λ .' An interesting perspective involves expanding the applicability of the Nusselt correlation based

on the CFD data. Thus, a new, more generalized correlation of the form $Nu = f(Ra, e, p, \lambda)$ can be computed and integrated into the ‘system’ model. Furthermore, the Nusselt correlations can be assessed across various PCM with distinct thermo-physical properties.

Finally, another physical phenomenon occurring within the PCM can be represented in the CFD model. During phase change, the density of the PCM varies, typically becoming denser in its solid state. This results in the PCM expanding as it transitions from a solid to a liquid phase. The PCM's volume expansion was not considered in the CFD model, as it assumed a constant PCM density. The expansion of the PCM during the charging phase serves two roles. First, it generates movements within the melted phase, which the Boussinesq approximation in the studies accounts for due to buoyancy-driven forces within the liquid phase. However, it does not consider the velocity gradient that can occur due to density variations at the interface. Second, PCM expansion increases the heat transfer area between the HTF and the PCM. As the PCM expands, the height of the tube in contact with it increases, potentially leading to an overall increase in heat transfer rate and a reduction in the charging time of the storage. Accounting for variable PCM density presents several challenges, especially when some of the PCM volume is confined between the radial fins. In such scenarios, the melted PCM is enclosed by radial fins vertically, while the metallic heat transfer tube and the solid PCM volume encase it horizontally. These solid volumes restrict the expansion of the PCM during the melting process. Consequently, addressing this situation demands a careful examination of the underlying physical phenomena and the adoption of distinctive numerical techniques.

In conclusion, this thesis work has provided new insights into understanding the role of various heat transfer mechanisms as well as geometric and material components in the thermal performance of shell-and-tube LTHES systems. The correlations and ‘system’ models developed can serve as valuable tools for accurately and efficiently sizing such systems.

Appendix A

This appendix groups the PCM's melted fraction curves throughout the charging phase of the storage for the different circular radial fins configurations studied in Section IV.5.2. Each graph contains the curves obtained from both the 'C' model and the 'CC' model simulations for different fin thickness-to-pitch ratios ' e/p ' for a given fin pitch value ' p '.

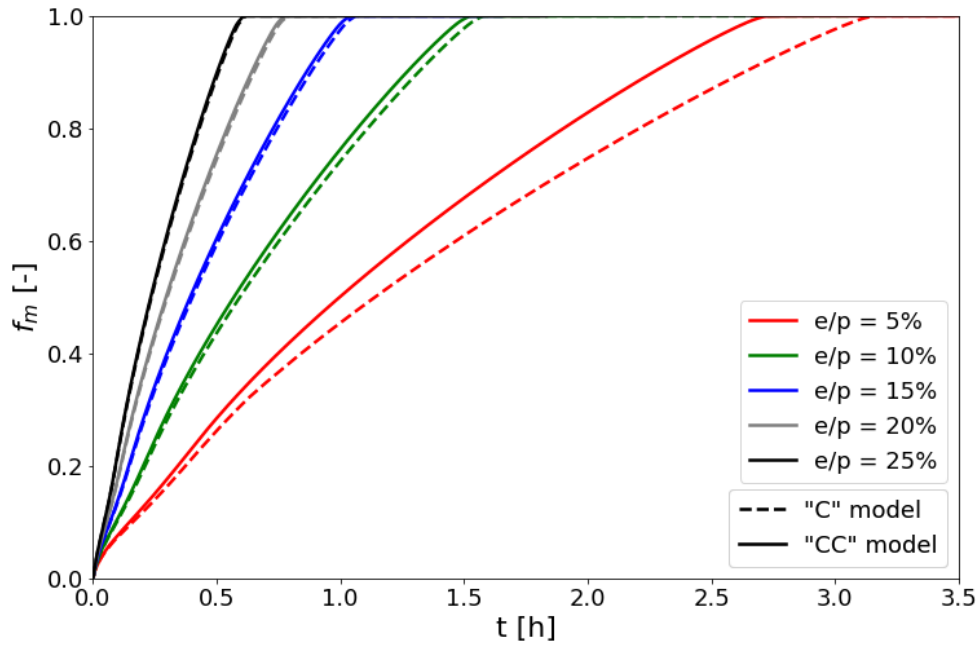


Figure 112. Evolution in time of the PCM's melted fraction for circular radial fins with a pitch of 2.5 mm.

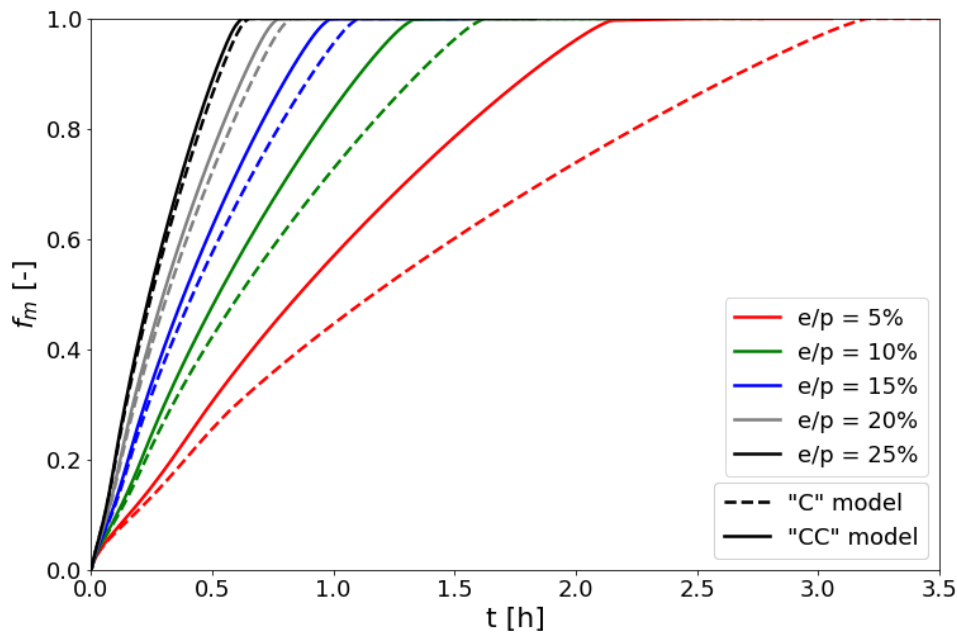


Figure 113. Evolution in time of the PCM's melted fraction for circular radial fins with a pitch of 5 mm.

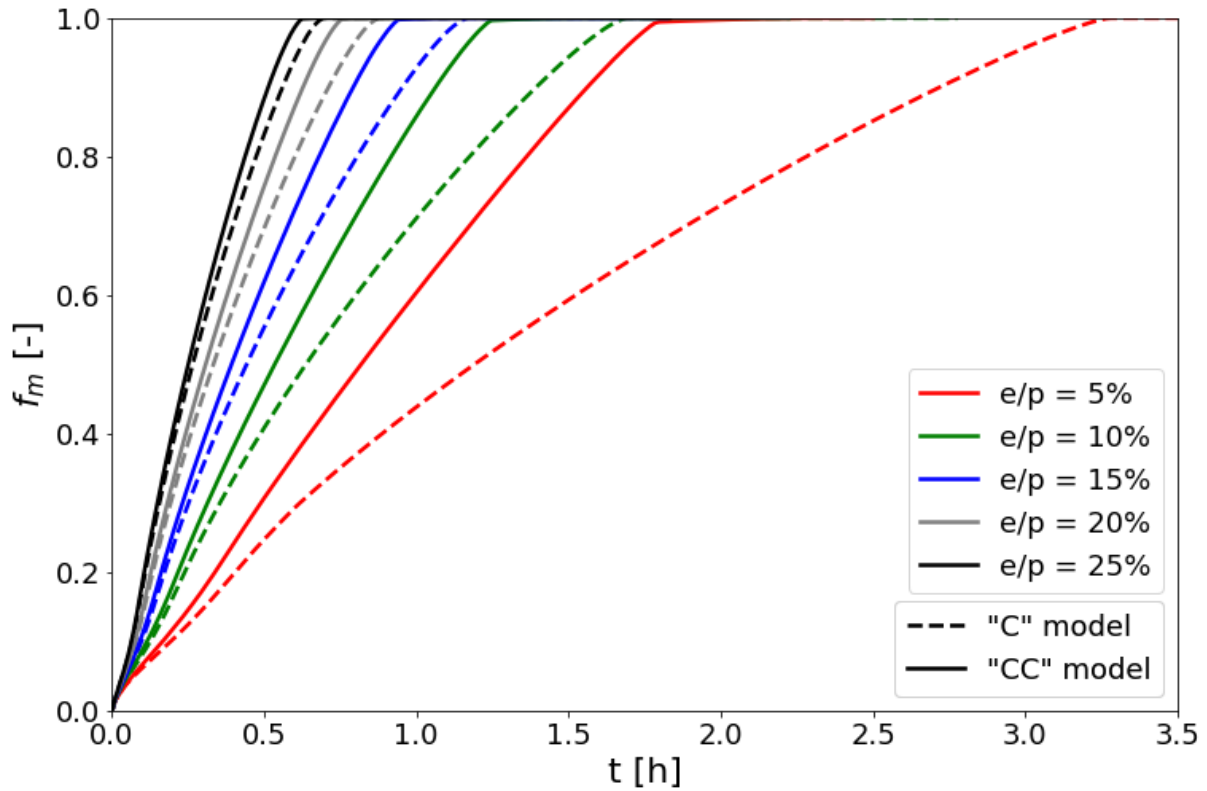


Figure 114. Evolution in time of the PCM's melted fraction for circular radial fins with a pitch of 7.5 mm.

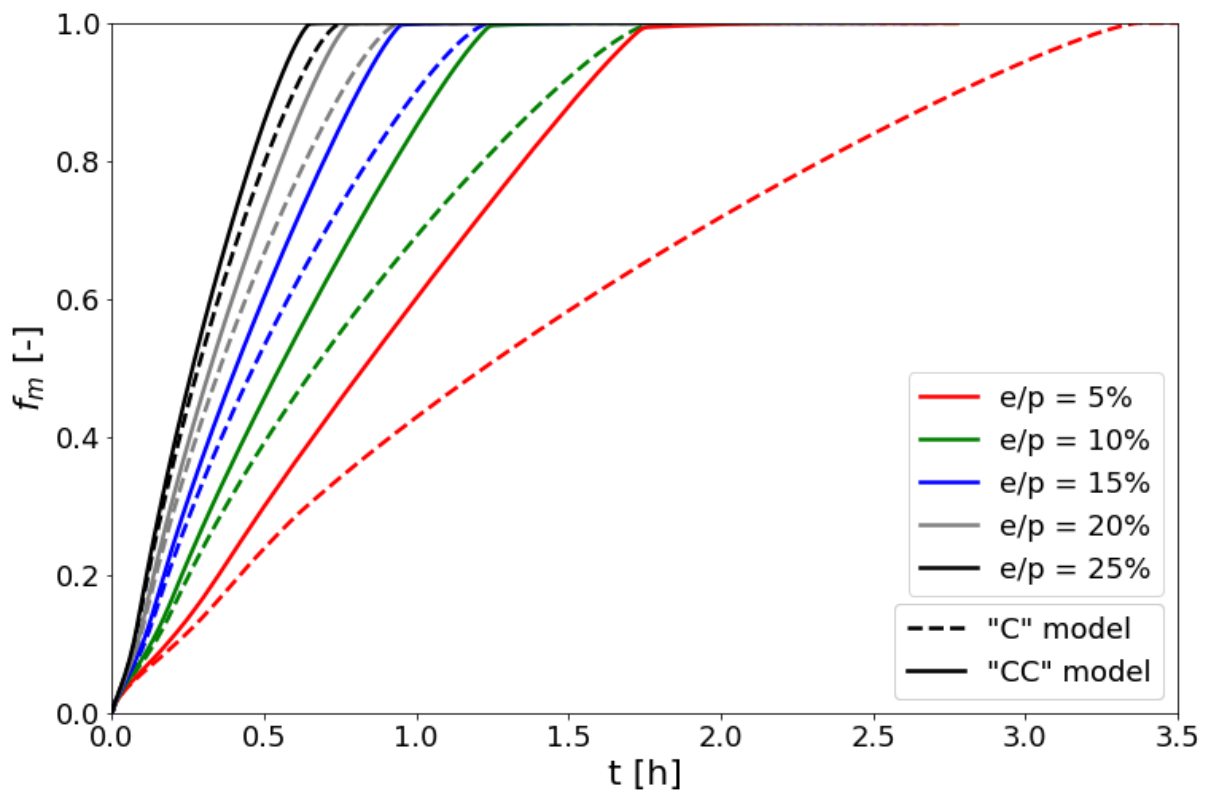


Figure 115. Evolution in time of the PCM's melted fraction for circular radial fins with a pitch of 10 mm.

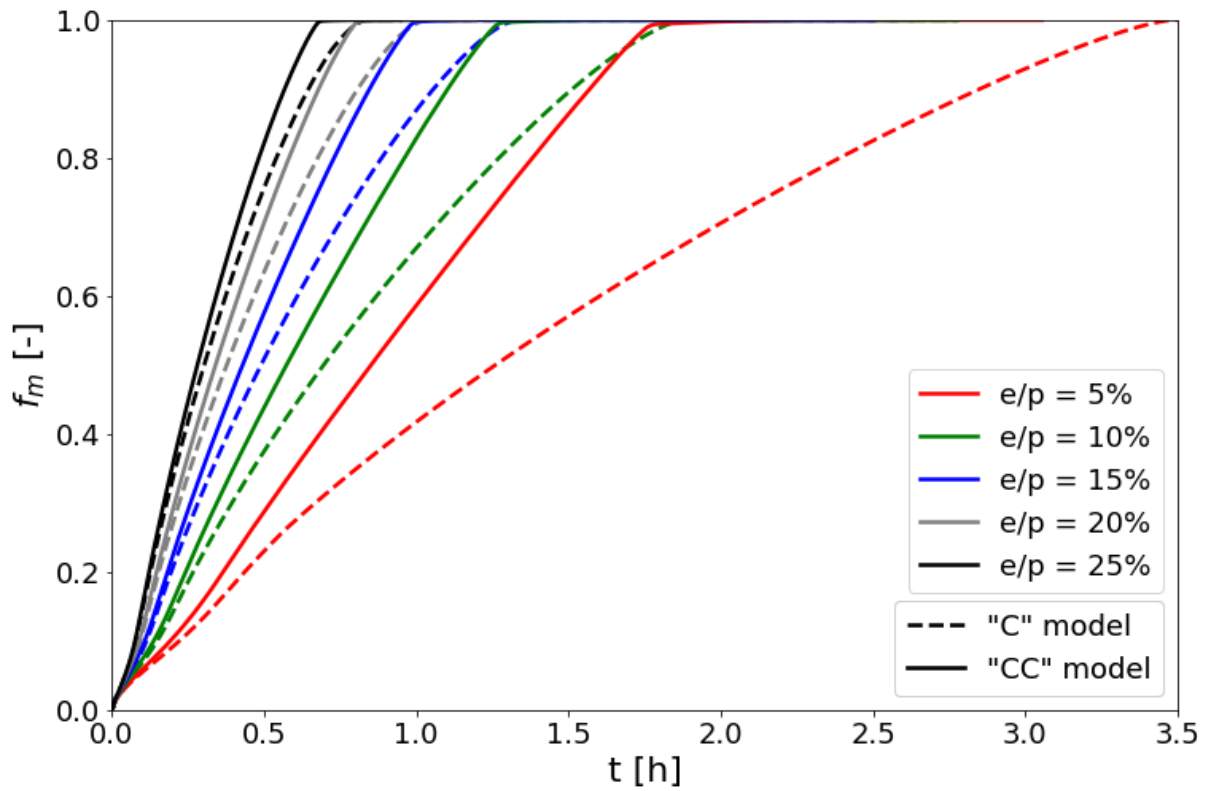


Figure 116. Evolution in time of the PCM's melted fraction for circular radial fins with a pitch of 12.5 mm.

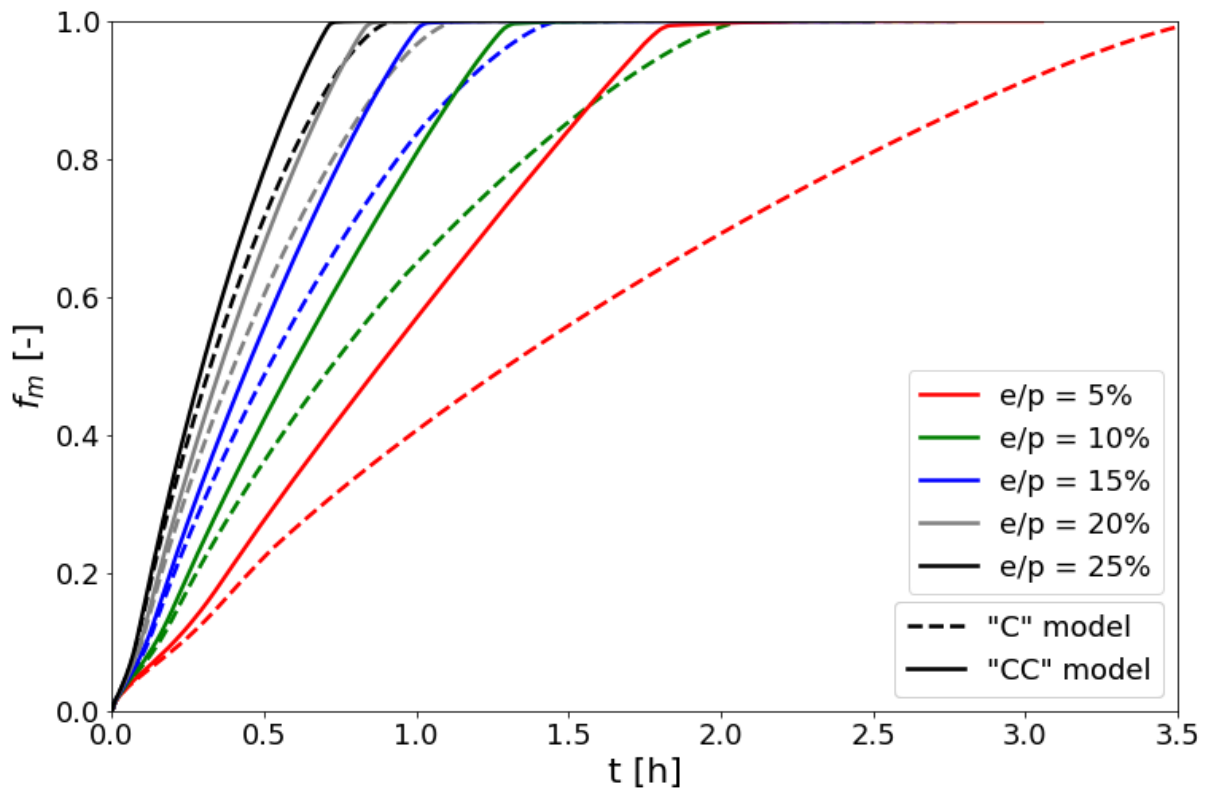


Figure 117. Evolution in time of the PCM's melted fraction for circular radial fins with a pitch of 15 mm.

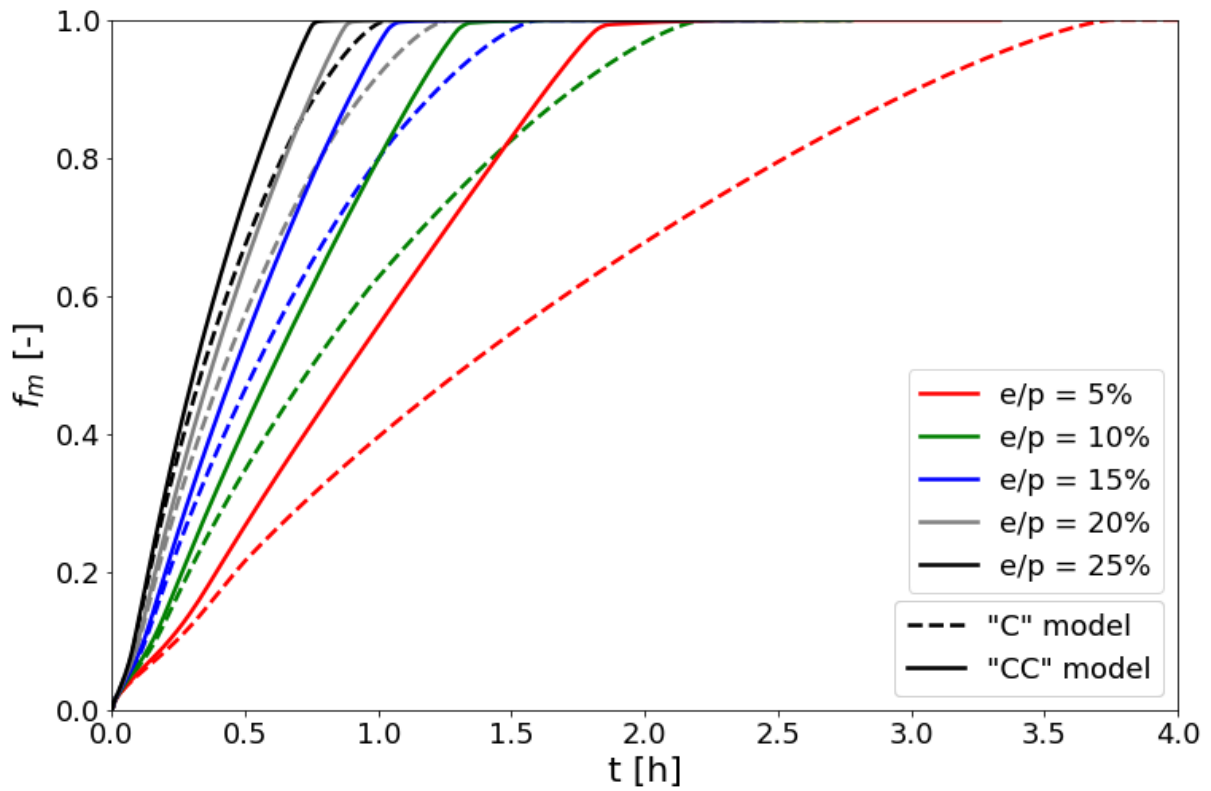


Figure 118. Evolution in time of the PCM's melted fraction for circular radial fins with a pitch of 17.5 mm.

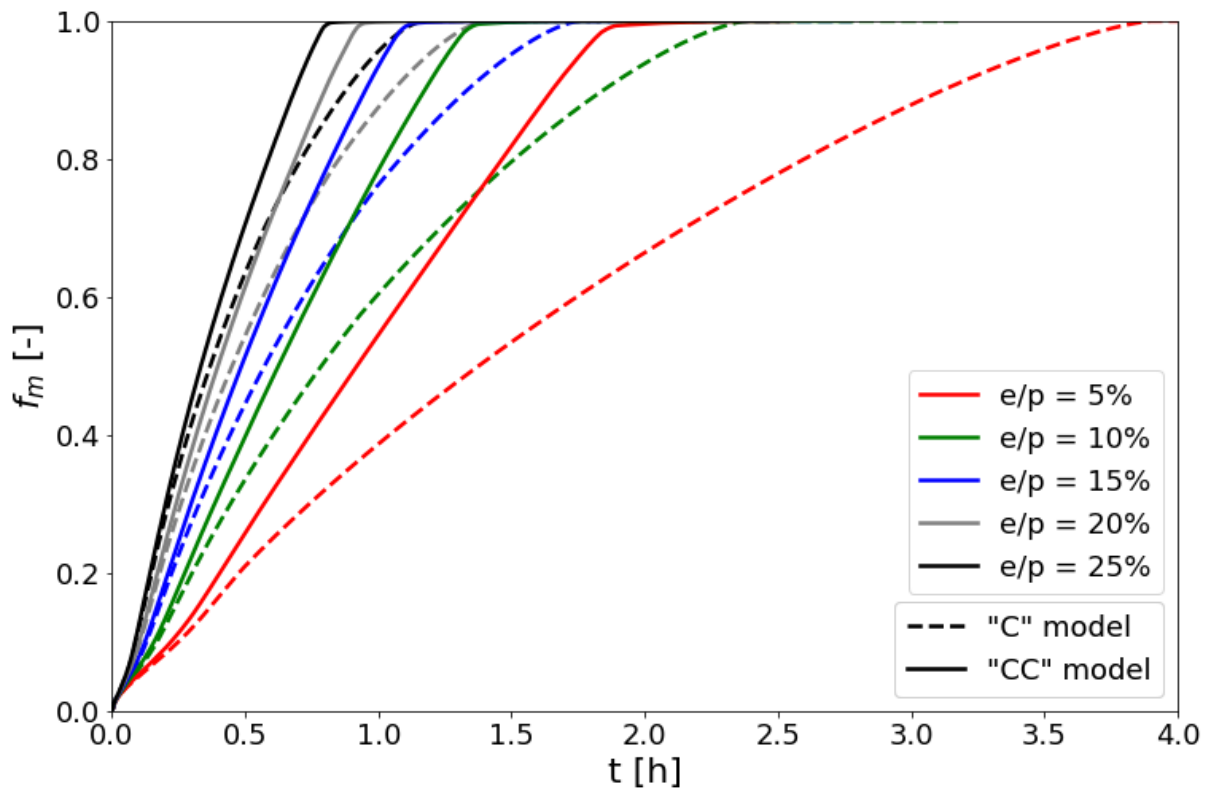


Figure 119. Evolution in time of the PCM's melted fraction for circular radial fins with a pitch of 20 mm.

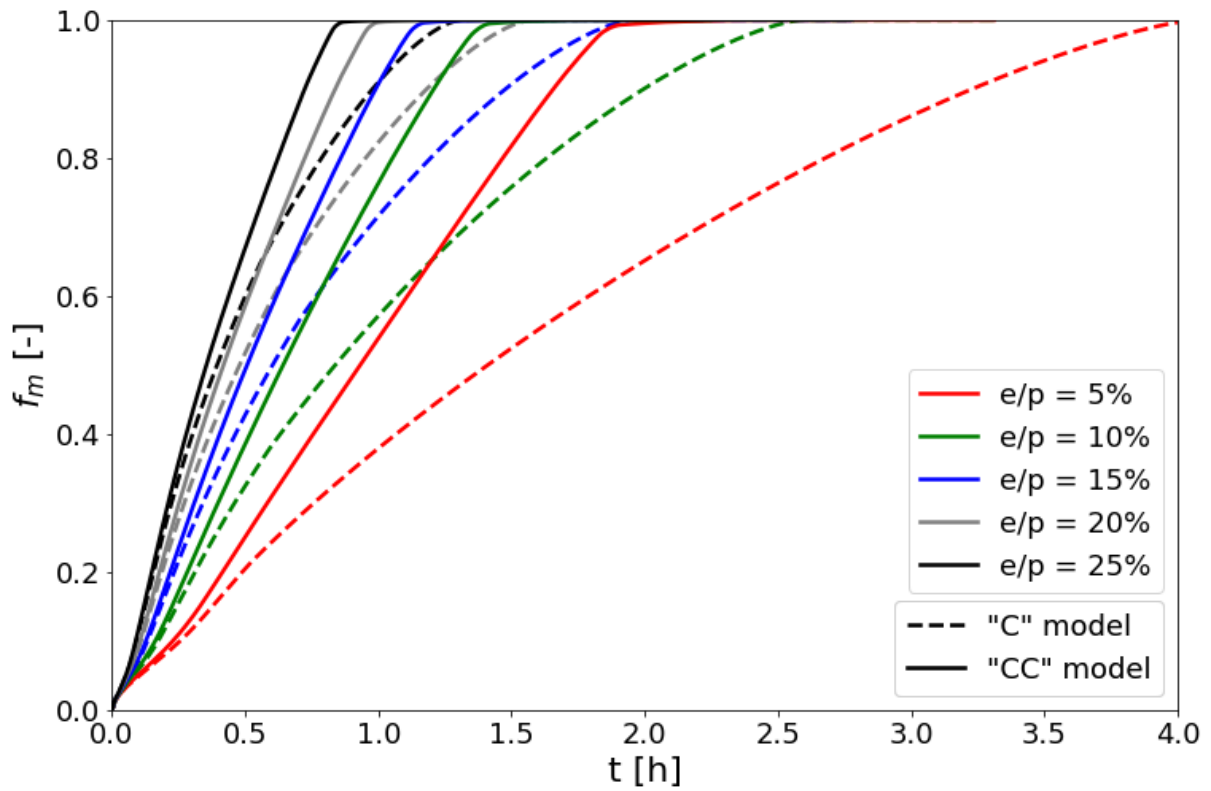


Figure 120. Evolution in time of the PCM's melted fraction for circular radial fins with a pitch of 22.5 mm.

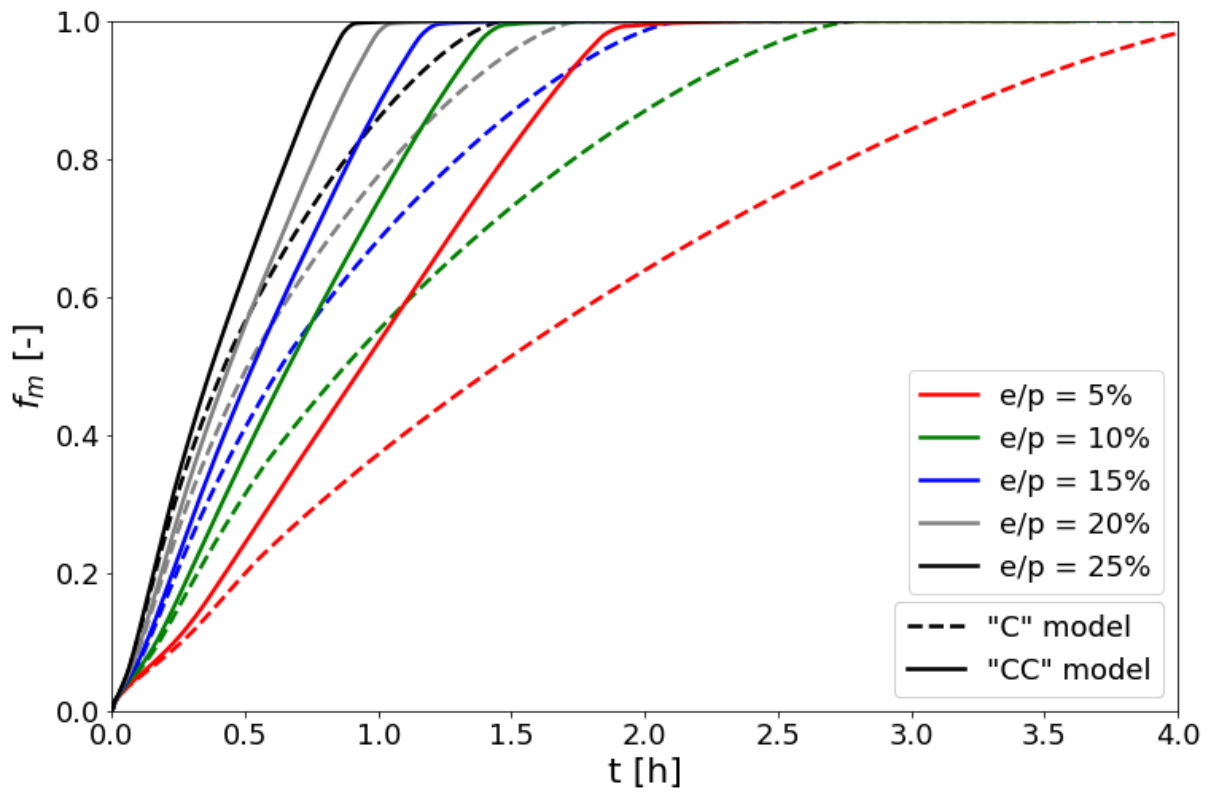


Figure 121. Evolution in time of the PCM's melted fraction for circular radial fins with a pitch of 25 mm.

Appendix B

This appendix groups the PCM's melted fraction curves throughout the charging phase of the storage for the different circular radial fins configurations studied in Section IV.5.3. Each graph contains the curves obtained from both the 'C' model and the 'CC' model simulations for the different thermal conductivity values studied.

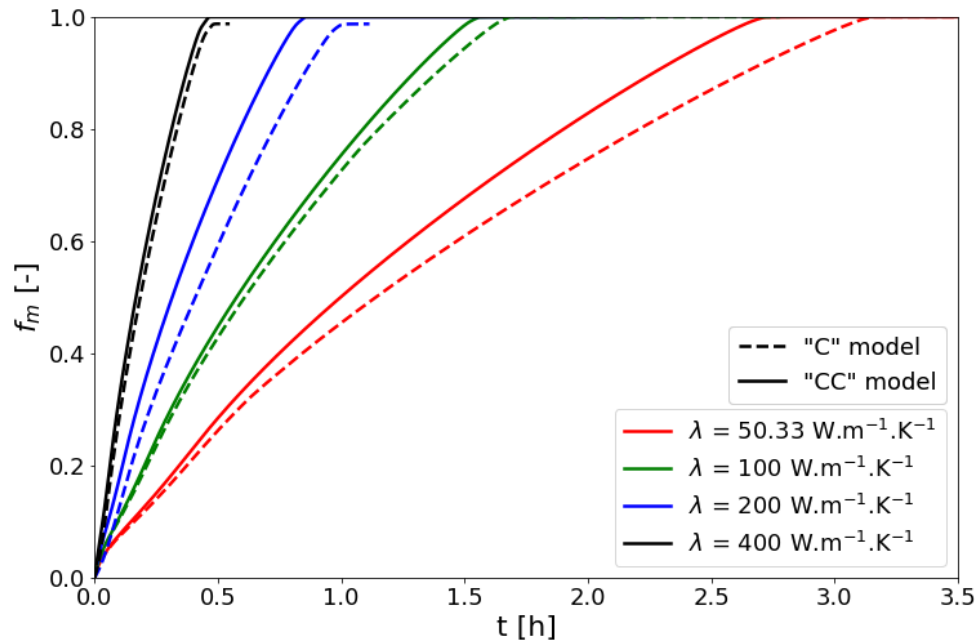


Figure 122. Evolution in time of the PCM's melted fraction for circular radial fins with $p=2.5$ mm and $e/p=5\%$

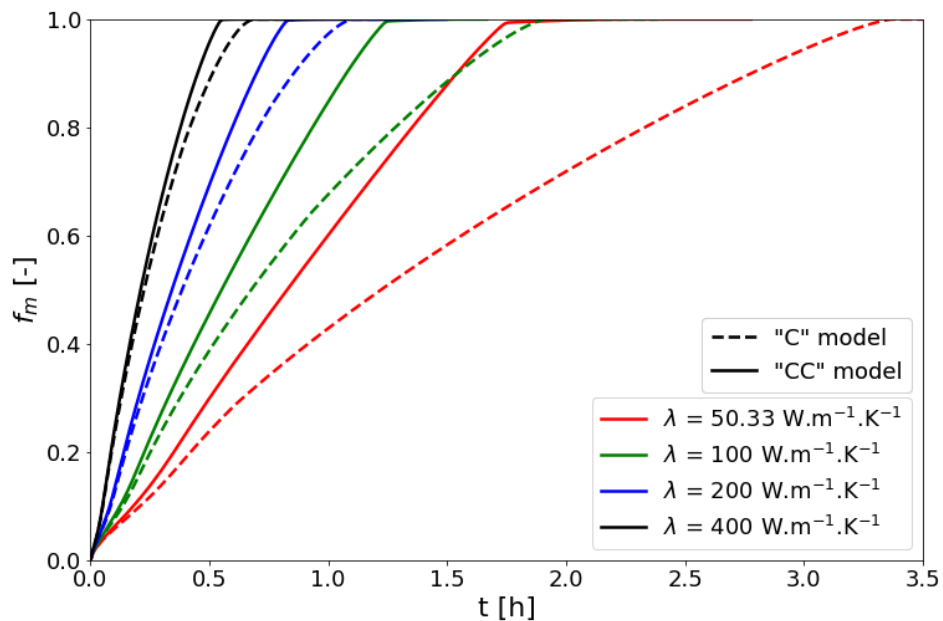


Figure 123. Evolution in time of the PCM's melted fraction for circular radial fins with $p=10$ mm and $e/p=5\%$

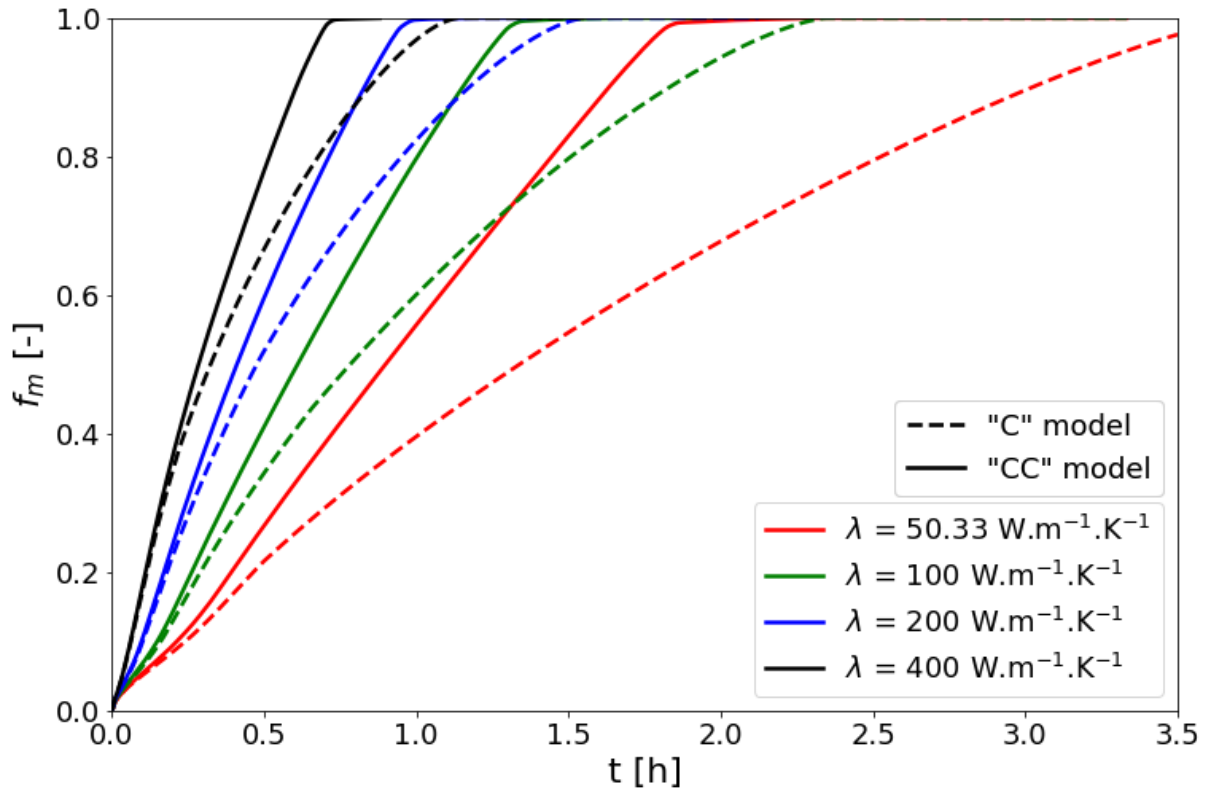


Figure 124. Evolution in time of the PCM's melted fraction for circular radial fins with $p=17.5$ mm and $e/p=5\%$

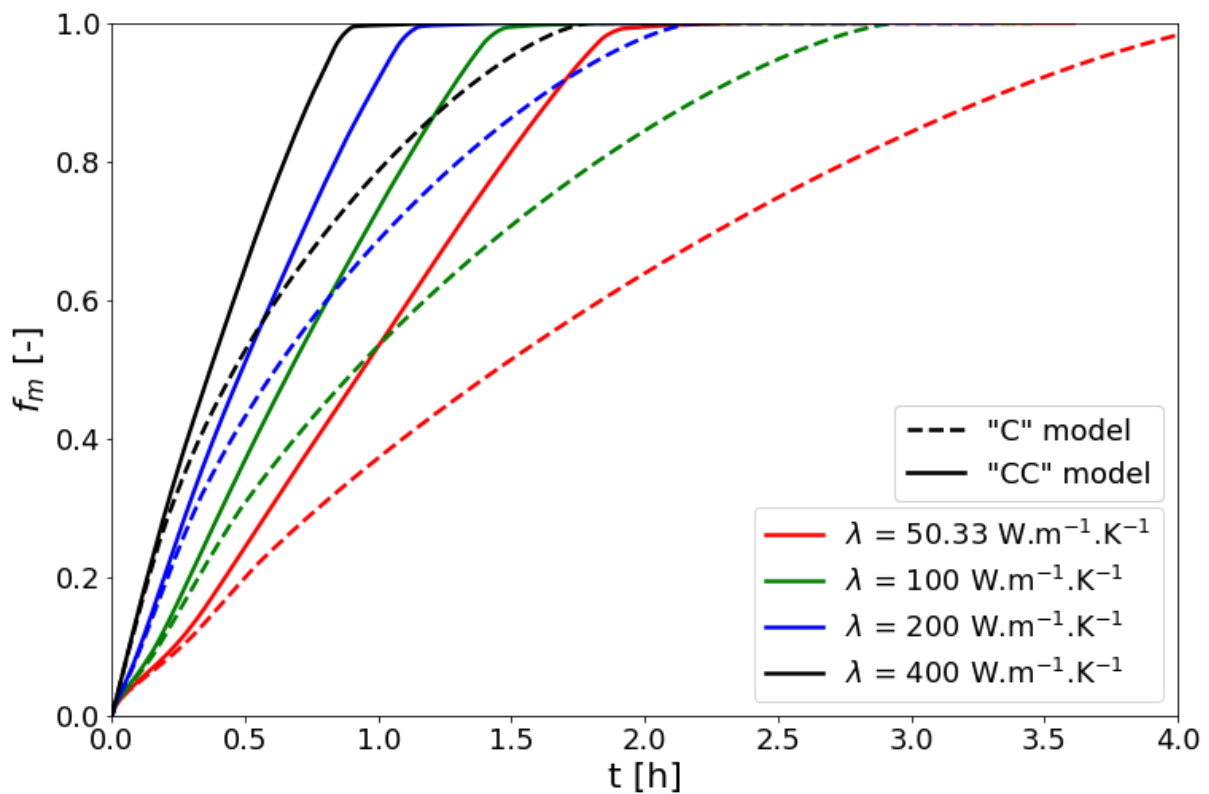


Figure 125. Evolution in time of the PCM's melted fraction for circular radial fins with $p=25$ mm and $e/p=5\%$

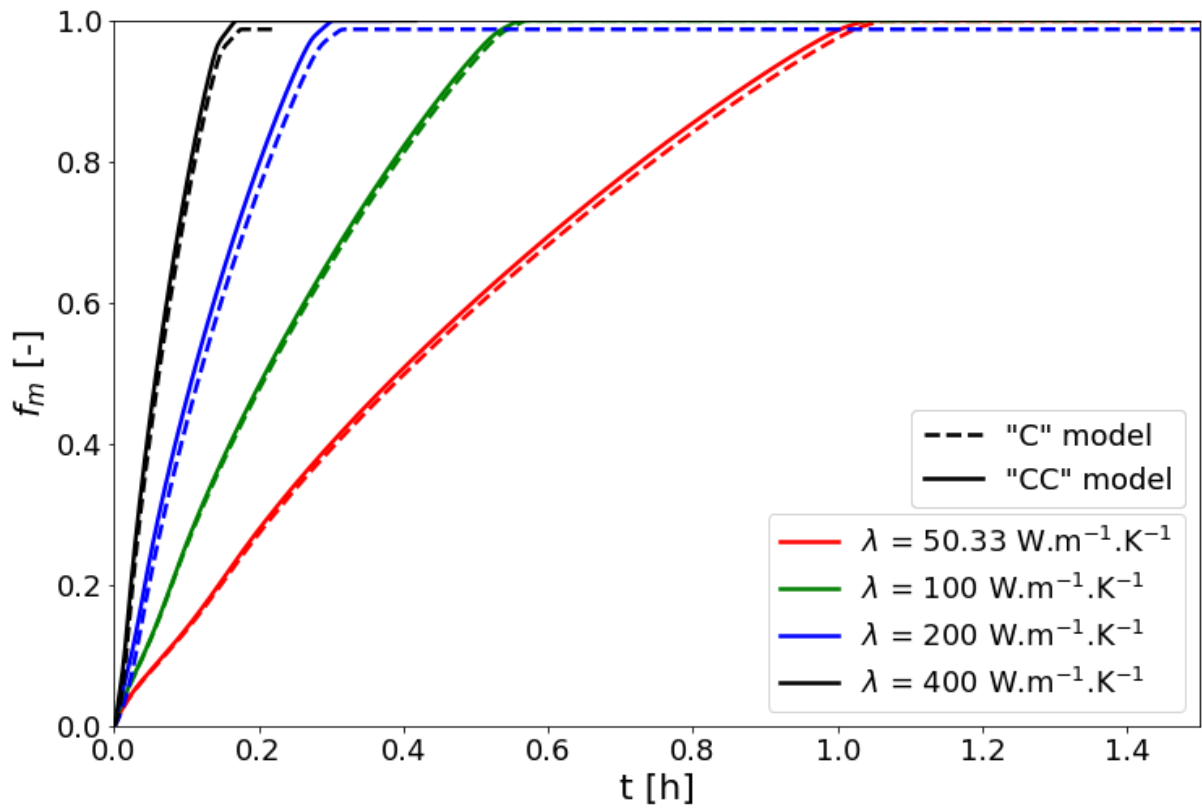


Figure 126. Evolution in time of the PCM's melted fraction for circular radial fins with $p=2.5\text{mm}$ and $e/p=15\%$

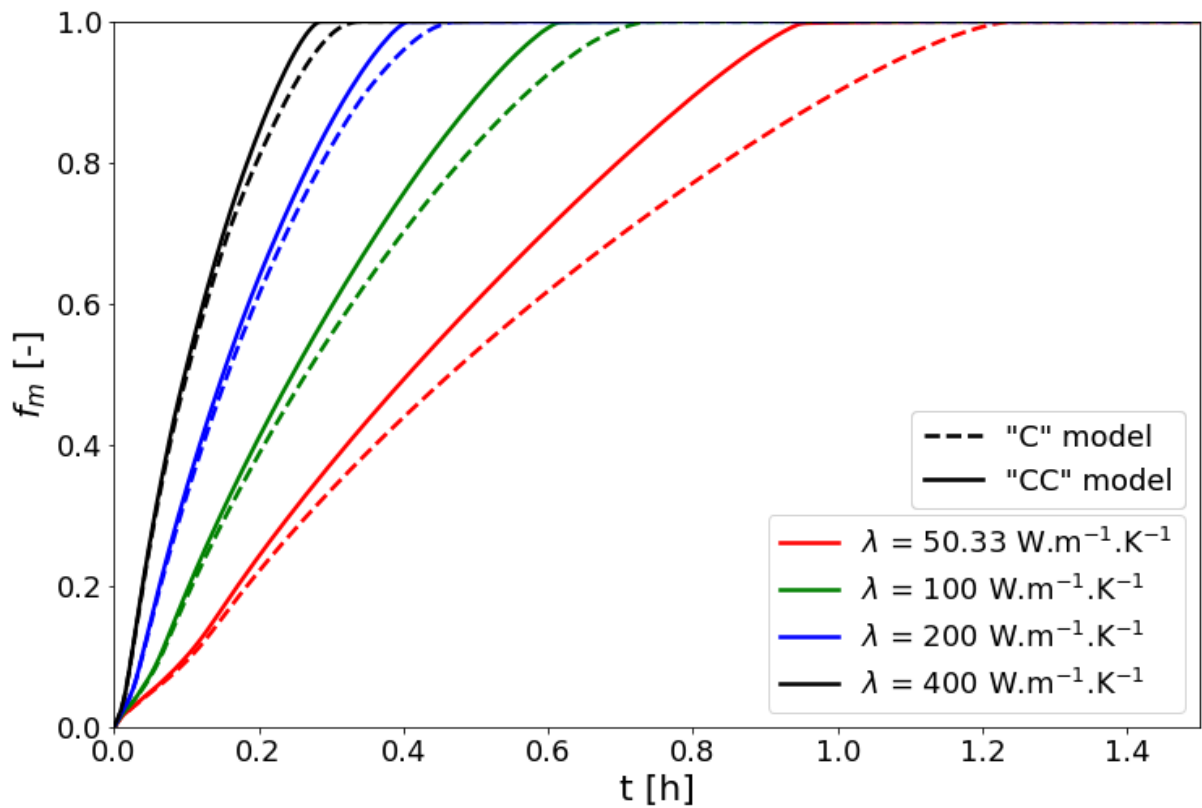


Figure 127. Evolution in time of the PCM's melted fraction for circular radial fins with $p=10\text{mm}$ and $e/p=15\%$

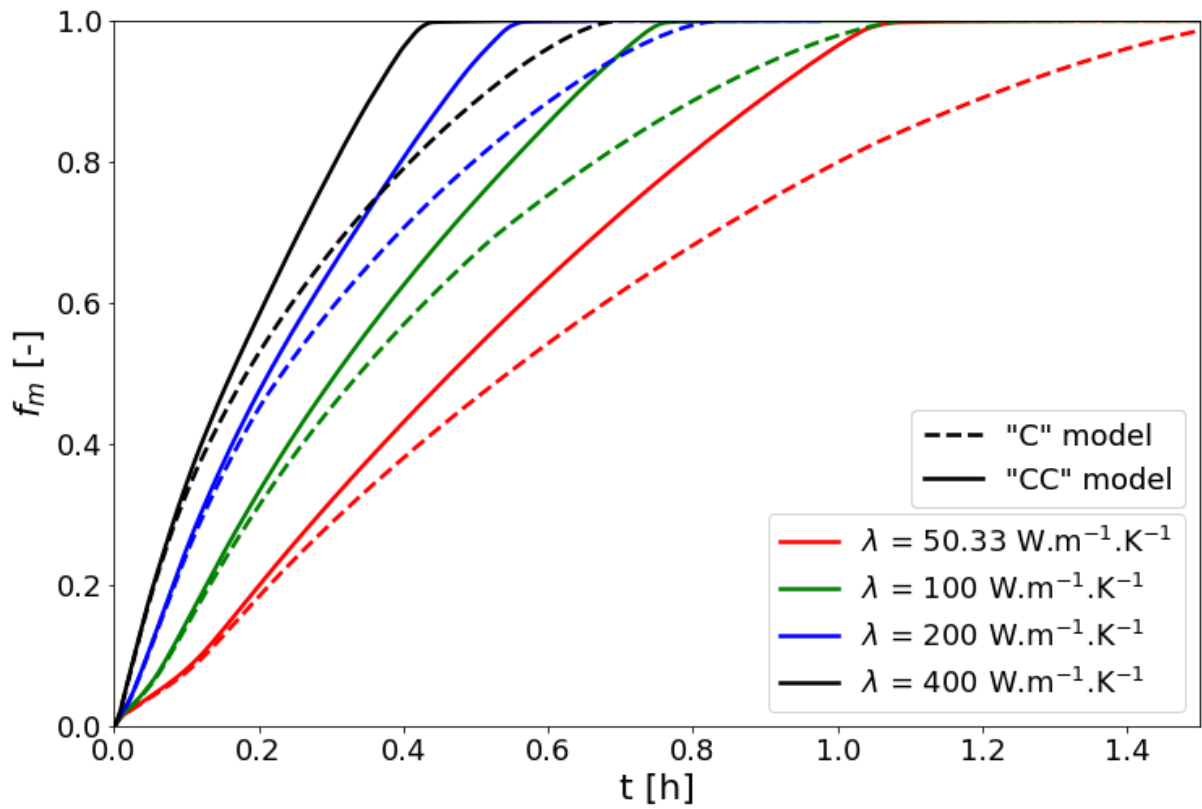


Figure 128. Evolution in time of the PCM's melted fraction for circular radial fins with $p=17.5\text{mm}$ and $e/p=15\%$

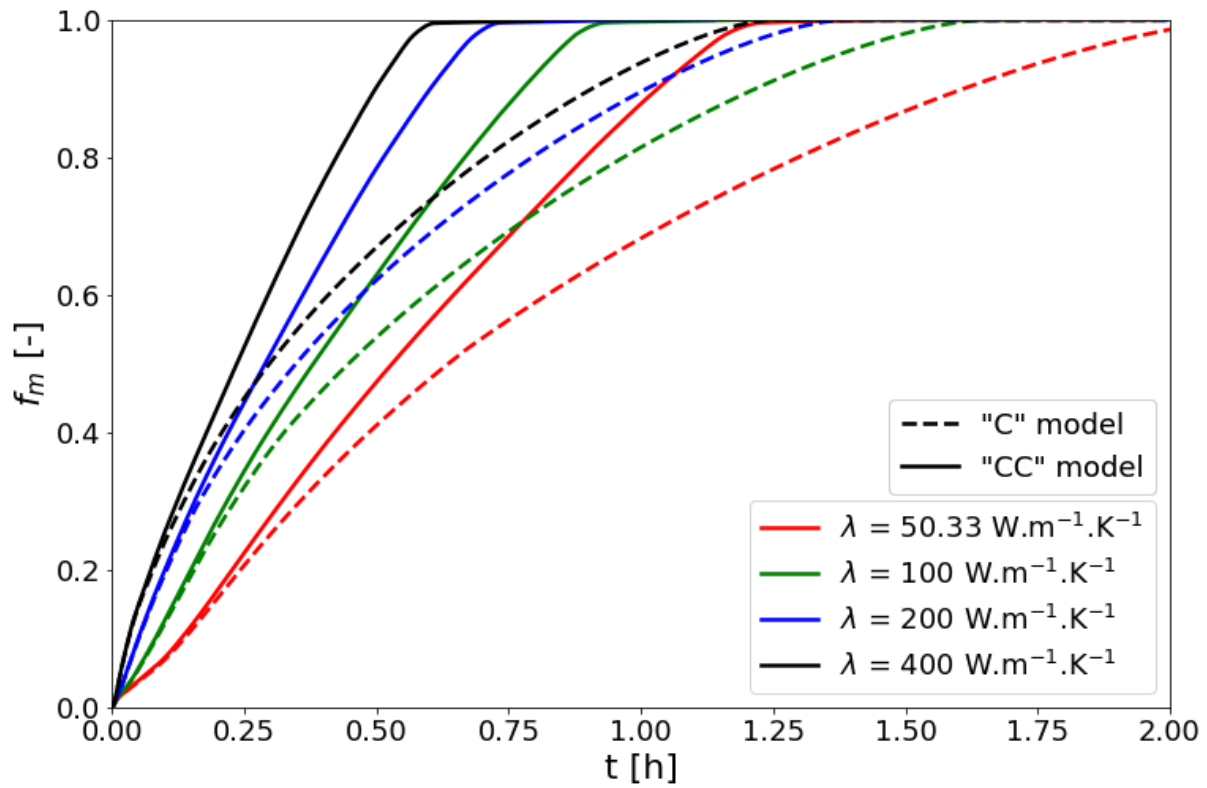


Figure 129. Evolution in time of the PCM's melted fraction for circular radial fins with $p=25\text{mm}$ and $e/p=15\%$

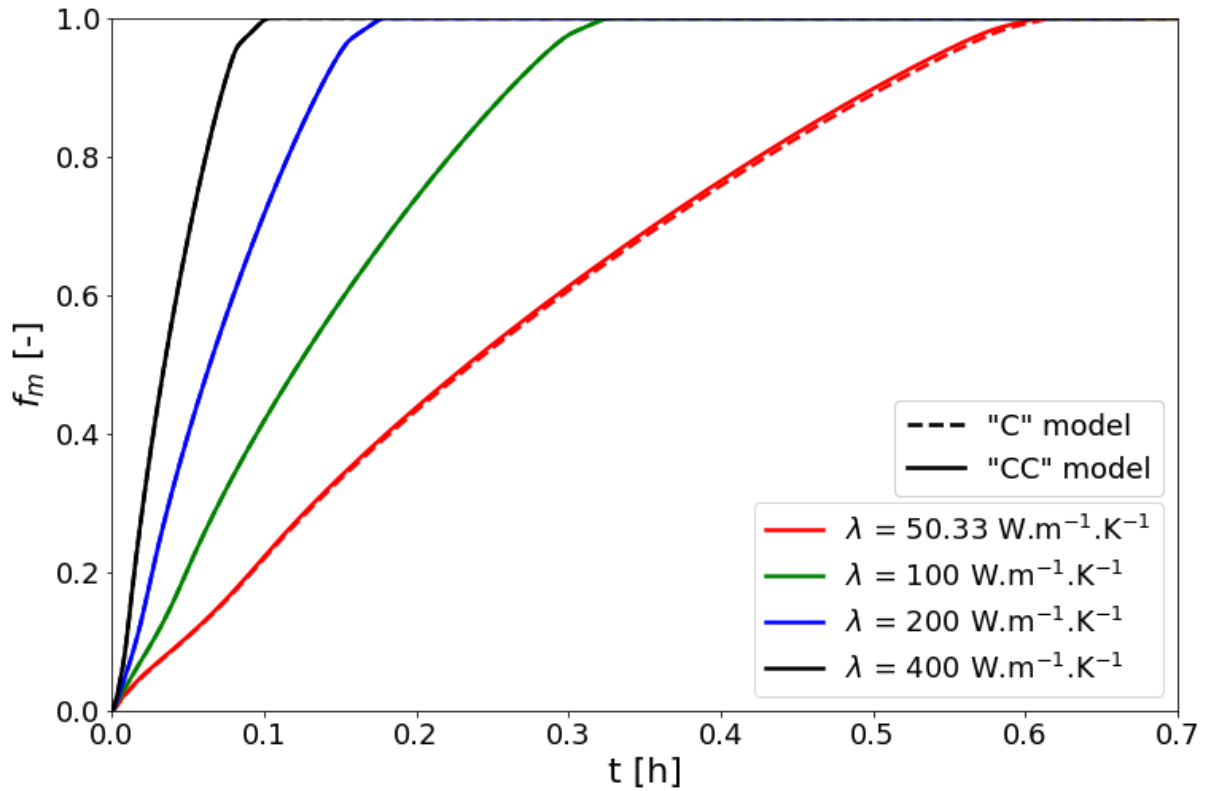


Figure 130. Evolution in time of the PCM's melted fraction for circular radial fins with $p=2.5\text{mm}$ and $e/p=25\%$

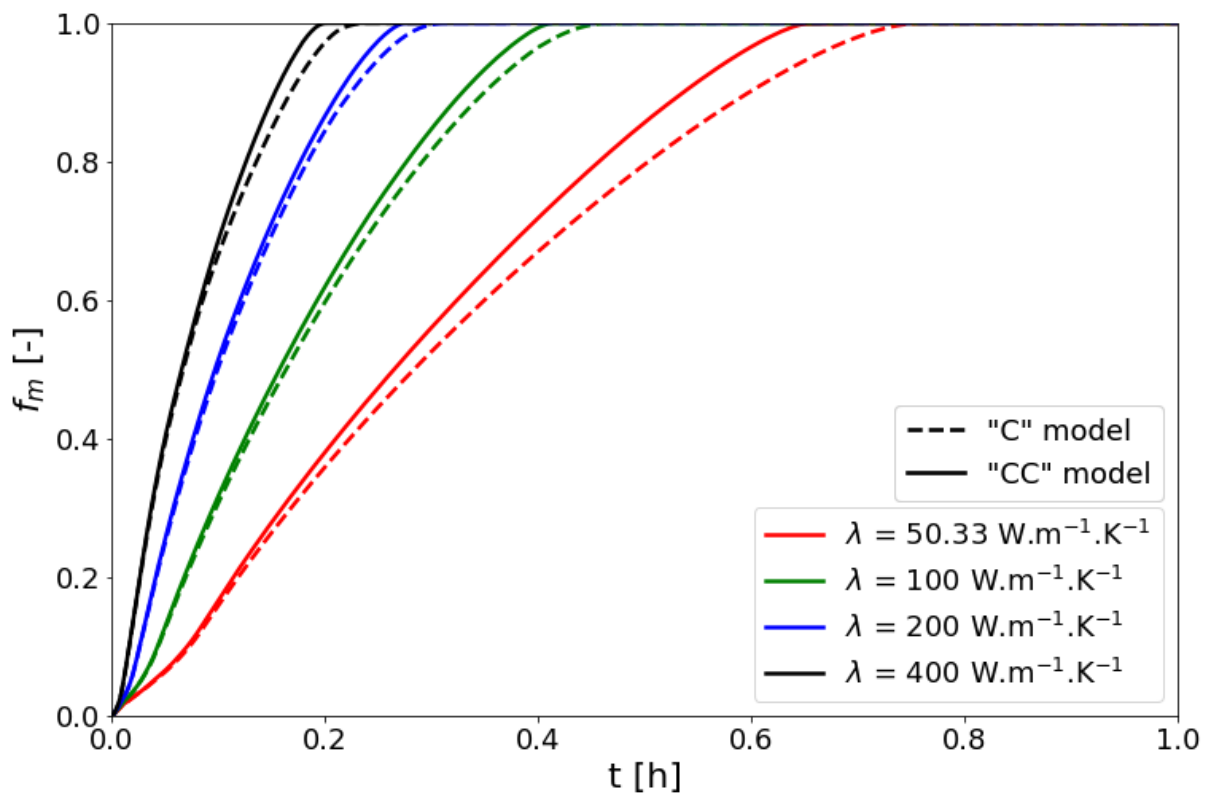


Figure 131. Evolution in time of the PCM's melted fraction for circular radial fins with $p=10\text{mm}$ and $e/p=25\%$

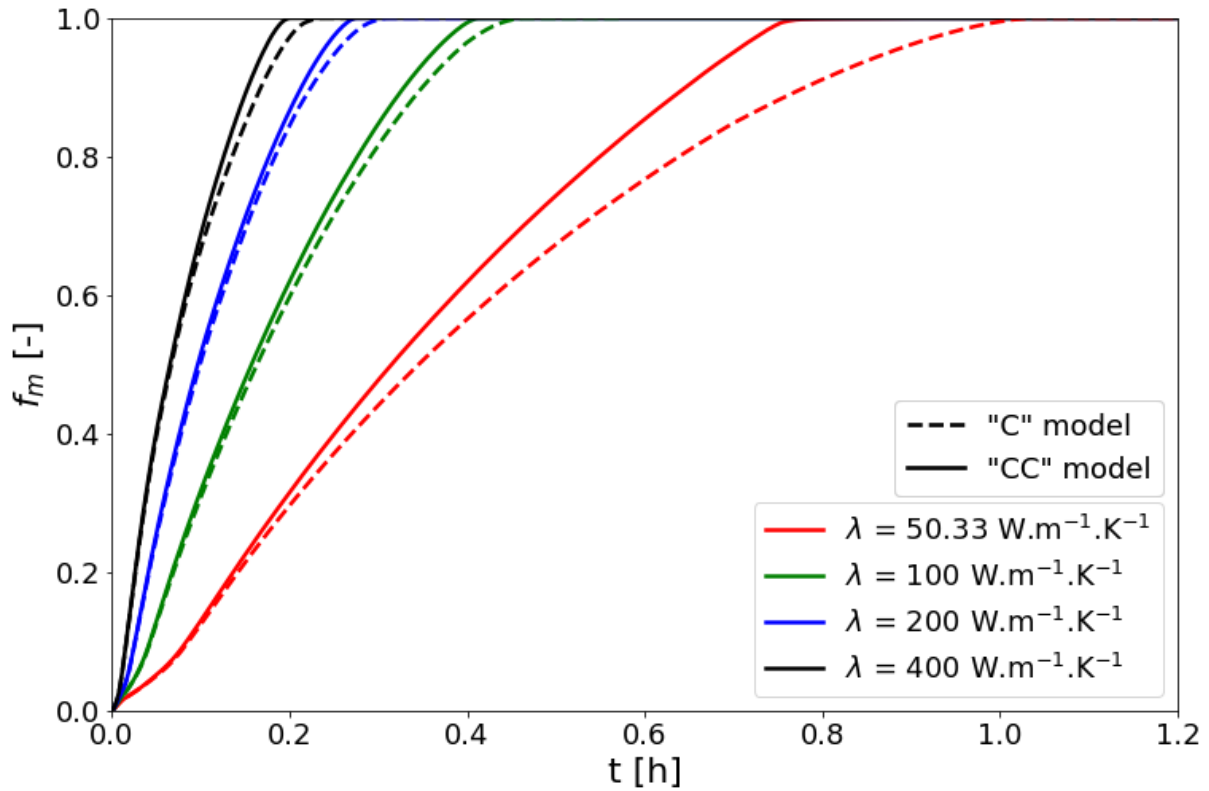


Figure 132. Evolution in time of the PCM's melted fraction for circular radial fins with $p=17.5\text{mm}$ and $e/p=25\%$

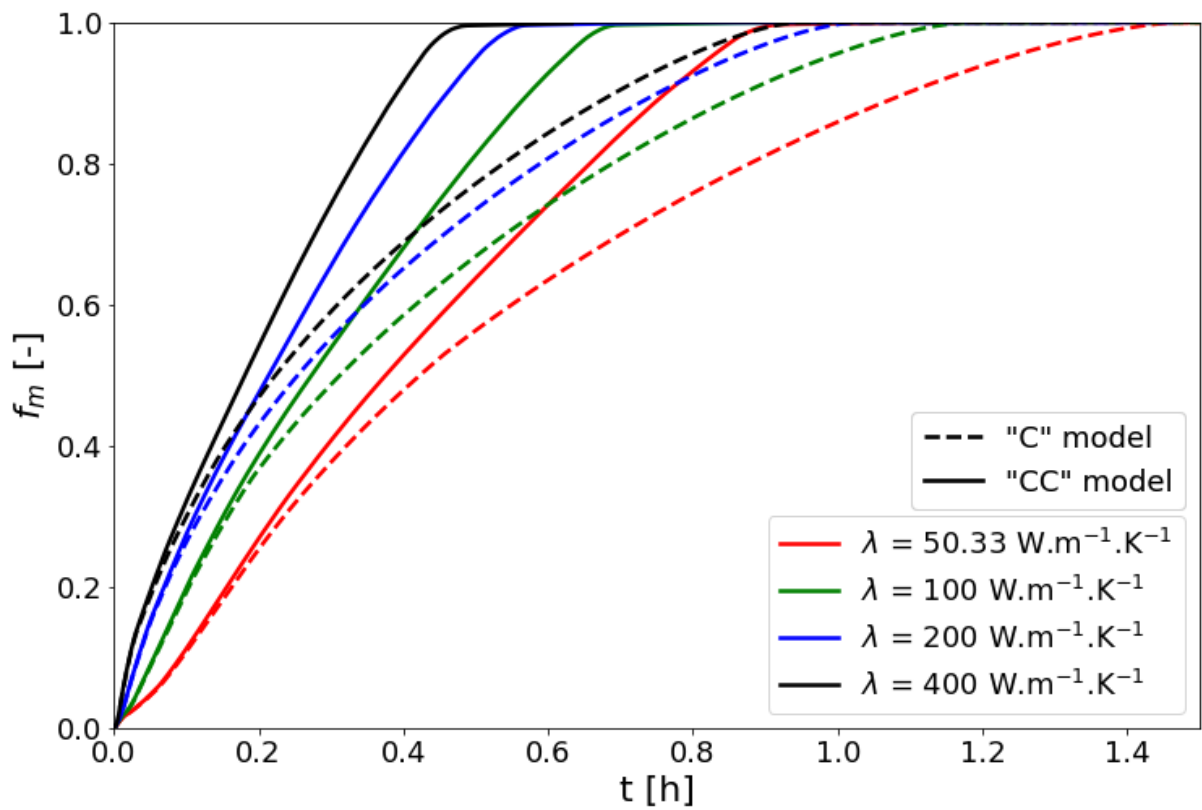


Figure 133. Evolution in time of the PCM's melted fraction for circular radial fins with $p=25\text{mm}$ and $e/p=25\%$

References

- [1] « Climate change Synthesis Report 2023 ». Intergovernmental Panel on Climate Change ipcc. [En ligne]. Disponible sur: <https://www.ipcc.ch/report/sixth-assessment-report-cycle/>
- [2] Ministère de la Transition écologique et solidaire, « Loi de transition énergétique pour la croissance verte ». [En ligne]. Disponible sur: <https://www.ecologie.gouv.fr/loi-transition-energetique-croissance-verte>
- [3] « Energie fatale : de la récupération à la revalorisation », EDF France. Consulté le: 27 août 2019. [En ligne]. Disponible sur: <https://www.edf.fr/entreprises/le-mag/le-mag-entreprises/conseils-energie-competitivite/energie-fatale-de-la-recuperation-a-la-revalorisation>
- [4] « Le réseau vapeur et condensats », Service Public de Wallonie, sept. 2010. [En ligne]. Disponible sur: <https://energie.wallonie.be/fr/cahier-technique-le-reseau-de-vapeur-et-condensats.html?IDC=8038&IDD=97658>
- [5] M. Medrano, A. Gil, I. Martorell, X. Potau, et L. F. Cabeza, « State of the art on high-temperature thermal energy storage for power generation. Part 2—Case studies », *Renewable and Sustainable Energy Reviews*, vol. 14, n° 1, p. 56-72, janv. 2010, doi: 10.1016/j.rser.2009.07.036.
- [6] A. Fernández-García, E. Zarza, L. Valenzuela, et M. Pérez, « Parabolic-trough solar collectors and their applications », *Renewable and Sustainable Energy Reviews*, vol. 14, n° 7, p. 1695-1721, sept. 2010, doi: 10.1016/j.rser.2010.03.012.
- [7] M. Jiménez-Arreola, R. Pili, F. Dal Magro, C. Wieland, S. Rajoo, et A. Romagnoli, « Thermal power fluctuations in waste heat to power systems: An overview on the challenges and current solutions », *Applied Thermal Engineering*, vol. 134, p. 576-584, avr. 2018, doi: 10.1016/j.applthermaleng.2018.02.033.
- [8] T. Nomura, N. Okinaka, et T. Akiyama, « Waste heat transportation system, using phase change material (PCM) from steelworks to chemical plant », *Resources, Conservation and Recycling*, vol. 54, n° 11, p. 1000-1006, sept. 2010, doi: 10.1016/j.resconrec.2010.02.007.
- [9] A. Biglia, L. Comba, E. Fabrizio, P. Gay, et D. Ricauda Aimonino, « Steam batch thermal processes in unsteady state conditions: Modelling and application to a case study in the food industry », *Applied Thermal Engineering*, vol. 118, p. 638-651, mai 2017, doi: 10.1016/j.applthermaleng.2017.03.004.
- [10] J. H. Carr, P. J. Hurley, et P. J. Martin, « Applications of thermal energy storage to process heat storage and recovery in the paper and pulp industry », U.S. Department of Energy, sept. 1978. Consulté le: 6 janvier 2017. [En ligne]. Disponible sur: <https://ntrs.nasa.gov/search.jsp?R=19790022630>
- [11] D. A. Shnaider, P. N. Divnich, et I. E. Vakhromeev, « Modeling the dynamic mode of steam accumulator », *Autom Remote Control*, vol. 71, n° 9, Art. n° 9, sept. 2010, doi: 10.1134/S0005117910090225.

- [12] M. Berger, M. Meyer-Grünefeldt, D. Krüger, K. Hennecke, M. Mokhtar, et C. Zahler, « First Year of Operational Experience with a Solar Process Steam system for a Pharmaceutical Company in Jordan », *Energy Procedia*, vol. 91, p. 591-600, juin 2016, doi: 10.1016/j.egypro.2016.06.209.
- [13] W.-D. Steinmann et M. Eck, « Buffer storage for direct steam generation », *Solar Energy*, vol. 80, n° 10, Art. n° 10, oct. 2006, doi: 10.1016/j.solener.2005.05.013.
- [14] J. Buschle, W.-D. Steinmann, et R. Tamme, « Latent heat storage for process heat applications », in *The Tenth International Conference on Thermal Energy Storage, Atlantic City, New Jersey*, 2006. Consulté le: 14 décembre 2016. [En ligne]. Disponible sur: http://talon.stockton.edu/eyos/energy_studies/content/docs/FINAL_PAPERS/14B-4.pdf
- [15] E. González-Roubaud, D. Pérez-Osorio, et C. Prieto, « Review of commercial thermal energy storage in concentrated solar power plants: Steam vs. molten salts », *Renewable and Sustainable Energy Reviews*, vol. 80, p. 133-148, déc. 2017, doi: 10.1016/j.rser.2017.05.084.
- [16] C. Prieto, A. Rodríguez, D. Patiño, et L. F. Cabeza, « Thermal energy storage evaluation in direct steam generation solar plants », *Solar Energy*, vol. 159, p. 501-509, janv. 2018, doi: 10.1016/j.solener.2017.11.006.
- [17] D. Laing, C. Bahl, T. Bauer, D. Lehmann, et W.-D. Steinmann, « Thermal energy storage for direct steam generation », *Solar Energy*, vol. 85, n° 4, Art. n° 4, avr. 2011, doi: 10.1016/j.solener.2010.08.015.
- [18] R. Osuna *et al.*, « PS10, Construction of a 11MW Solar Thermal Tower Plant in Seville, Spain », in *13th International Symposium on Concentrated Solar Power and Chemical Energy Technologies*, Seville (Spain): IEA SolarPACES, juin 2006.
- [19] « Concentrating Solar Power Projects - Khi Solar One | Concentrating Solar Power | NREL ». Consulté le: 19 mai 2017. [En ligne]. Disponible sur: https://www.nrel.gov/csp/solarpaces/project_detail.cfm/projectID=244
- [20] F. Agyenim, N. Hewitt, P. Eames, et M. Smyth, « A review of materials, heat transfer and phase change problem formulation for latent heat thermal energy storage systems (LHTESS) », *Renewable and Sustainable Energy Reviews*, vol. 14, n° 2, p. 615-628, févr. 2010, doi: 10.1016/j.rser.2009.10.015.
- [21] L. Willwerth *et al.*, « Commissioning and tests of a mini CSP plant », in *AIP Conference Proceedings*, AIP Publishing, 2018, p. 180012.
- [22] D. Laing, T. Bauer, N. Breidenbach, B. Hachmann, et M. Johnson, « Development of high temperature phase-change-material storages », *Applied Energy*, vol. 109, p. 497-504, sept. 2013, doi: 10.1016/j.apenergy.2012.11.063.
- [23] P. Garcia, M. Olcese, et S. Rougé, « Experimental and Numerical Investigation of a Pilot Scale Latent Heat Thermal Energy Storage for CSP Power Plant », *Energy Procedia*, vol. 69, p. 842-849, mai 2015, doi: 10.1016/j.egypro.2015.03.102.

- [24] H. Pointner et W.-D. Steinmann, « Experimental demonstration of an active latent heat storage concept », *Applied Energy*, vol. 168, p. 661-671, avr. 2016, doi: 10.1016/j.apenergy.2016.01.113.
- [25] R. Adinberg, D. Zvegilsky, et M. Epstein, « Heat transfer efficient thermal energy storage for steam generation », *Energy Conversion and Management*, vol. 51, n° 1, Art. n° 1, janv. 2010, doi: 10.1016/j.enconman.2009.08.006.
- [26] V. Zipf, A. Neuhäuser, D. Willert, P. Nitz, S. Gschwander, et W. Platzer, « High temperature latent heat storage with a screw heat exchanger: Design of prototype », *Applied Energy*, vol. 109, p. 462-469, sept. 2013, doi: 10.1016/j.apenergy.2012.11.044.
- [27] M. Johnson, J. Vogel, M. Hempel, A. Dengel, M. Seitz, et B. Hachmann, « High Temperature Latent Heat Thermal Energy Storage Integration in a Co-gen Plant », *Energy Procedia*, vol. 73, p. 281-288, juin 2015, doi: 10.1016/j.egypro.2015.07.689.
- [28] M. Johnson, A. Dengel, B. Hachmann, M. Fiß, et D. Bauer, « Large-scale high temperature and power latent heat storage unit development », *AIP Conference Proceedings*, vol. 2126, n° 1, Art. n° 1, juill. 2019, doi: 10.1063/1.5117738.
- [29] R. Tamme, T. Bauer, J. Buschle, D. Laing, H. Müller-Steinhagen, et W.-D. Steinmann, « Latent heat storage above 120°C for applications in the industrial process heat sector and solar power generation », *International Journal of Energy Research*, vol. 32, n° 3, Art. n° 3, mars 2008, doi: 10.1002/er.1346.
- [30] W.-D. Steinmann et R. Tamme, « Latent heat storage for solar steam systems », *Journal of Solar Energy Engineering, Transactions of the ASME*, vol. 130, n° 1, Art. n° 1, 2008, doi: 10.1115/1.2804624.
- [31] K. Pielichowska et K. Pielichowski, « Phase change materials for thermal energy storage », *Progress in Materials Science*, vol. 65, p. 67-123, août 2014, doi: 10.1016/j.pmatsci.2014.03.005.
- [32] H. Pointner, W. D. Steinmann, M. Eck, et C. Bachelier, « Separation of Power and Capacity in Latent Heat Energy Storage », *Energy Procedia*, vol. 69, p. 997-1005, mai 2015, doi: 10.1016/j.egypro.2015.03.189.
- [33] R. Guédez, M. Arnaudo, M. Topel, R. Zanino, Z. Hassar, et B. Laumert, « Techno-economic performance evaluation of direct steam generation solar tower plants with thermal energy storage systems based on high-temperature concrete and encapsulated phase change materials », présenté à AIP Conference Proceedings, 2016. doi: 10.1063/1.4949158.
- [34] P. Garcia, V. Vuillerme, M. Olcese, et N. El Mourchid, « Design and modelling of an innovative three-stage thermal storage system for direct steam generation CSP plants », *AIP Conference Proceedings*, vol. 1734, p. 050015, 2016, doi: 10.1063/1.4949113.
- [35] C. Beust, E. Franquet, J.-P. Bédécarrats, et P. Garcia, « Predictive approach of heat transfer for the modelling of large-scale latent heat storages », *Renewable Energy*, vol. 157, p. 502-514, sept. 2020, doi: 10.1016/j.renene.2020.04.135.

- [36] P. G. Kroeger et S. Ostrach, « The solution of a two-dimensional freezing problem including convection effects in the liquid region », *International Journal of Heat and Mass Transfer*, vol. 17, n° 10, p. 1191-1207, oct. 1974, doi: 10.1016/0017-9310(74)90120-3.
- [37] Dhaidan, Nabeel S. et J. M. Khodadadi, « Melting and convection of phase change materials in different shape containers: A review », *Renewable and Sustainable Energy Reviews*, vol. 43, p. 449-477, 2015, doi: <http://dx.doi.org/10.1016/j.rser.2014.11.017>.
- [38] P. Jany et A. Bejan, « Scaling theory of melting with natural convection in an enclosure », *International Journal of Heat and Mass Transfer*, vol. 31, n° 6, p. 1221-1235, juin 1988, doi: 10.1016/0017-9310(88)90065-8.
- [39] J. Hua et D. Mortensen, « A front tracking method for simulation of two-phase interfacial flows on adaptive unstructured meshes for complex geometries », *International Journal of Multiphase Flow*, vol. 119, p. 166-179, oct. 2019, doi: 10.1016/j.ijmultiphaseflow.2019.07.011.
- [40] V. R. Voller et S. Peng, « An enthalpy formulation based on an arbitrarily deforming mesh for solution of the Stefan problem », *Computational Mechanics*, vol. 14, n° 5, p. 492-502, août 1994, doi: 10.1007/BF00377601.
- [41] A. Datas, *Ultra-High Temperature Thermal Energy Storage, Transfer and Conversion*. Woodhead Publishing, 2020.
- [42] D. Juric et G. Tryggvason, « A Front-Tracking Method for Dendritic Solidification », *Journal of Computational Physics*, vol. 123, n° 1, p. 127-148, janv. 1996, doi: 10.1006/jcph.1996.0011.
- [43] T. V. Vu, G. Tryggvason, S. Homma, et J. C. Wells, « Numerical investigations of drop solidification on a cold plate in the presence of volume change », *International Journal of Multiphase Flow*, vol. 76, p. 73-85, nov. 2015, doi: 10.1016/j.ijmultiphaseflow.2015.07.005.
- [44] G. H. Meyer, « The numerical solution of Stefan problems with front-tracking and smoothing methods », *Applied Mathematics and Computation*, vol. 4, n° 4, p. 283-306, oct. 1978, doi: 10.1016/0096-3003(78)90001-2.
- [45] P. Zhao et J. C. Heinrich, « Front-Tracking Finite Element Method for Dendritic Solidification », *Journal of Computational Physics*, vol. 173, n° 2, p. 765-796, nov. 2001, doi: 10.1006/jcph.2001.6911.
- [46] O. Gloth, D. Hänel, L. Tran, et R. Vilsmeier, « A front tracking method on unstructured grids », *Computers & Fluids*, vol. 32, n° 4, p. 547-570, mai 2003, doi: 10.1016/S0045-7930(02)00014-2.
- [47] W. DeLima-Silva et L. C. Wrobel, « A front-tracking BEM formulation for one-phase solidification/melting problems », *Engineering Analysis with Boundary Elements*, vol. 16, n° 2, p. 171-182, janv. 1995, doi: 10.1016/0955-7997(95)00053-4.
- [48] M. Dehghan et M. Najafi, « Numerical solution of a non-classical two-phase Stefan problem via radial basis function (RBF) collocation methods », *Engineering Analysis with Boundary Elements*, vol. 72, p. 111-127, nov. 2016, doi: 10.1016/j.enganabound.2016.07.015.

- [49] S. L. Mitchell et M. Vynnycky, « An accurate finite-difference method for ablation-type Stefan problems », *Journal of Computational and Applied Mathematics*, vol. 236, n° 17, p. 4181-4192, nov. 2012, doi: 10.1016/j.cam.2012.05.011.
- [50] S. L. Mitchell et M. Vynnycky, « Finite-difference methods with increased accuracy and correct initialization for one-dimensional Stefan problems », *Applied Mathematics and Computation*, vol. 215, n° 4, p. 1609-1621, oct. 2009, doi: 10.1016/j.amc.2009.07.054.
- [51] S. L. Mitchell et M. Vynnycky, « On the numerical solution of two-phase Stefan problems with heat-flux boundary conditions », *Journal of Computational and Applied Mathematics*, vol. 264, p. 49-64, juill. 2014, doi: 10.1016/j.cam.2014.01.003.
- [52] S. Kutluay, A. R. Bahadir, et A. Özdeş, « The numerical solution of one-phase classical Stefan problem », *Journal of Computational and Applied Mathematics*, vol. 81, n° 1, p. 135-144, juin 1997, doi: 10.1016/S0377-0427(97)00034-4.
- [53] H. Song, « Spectral Method for the Black-Scholes Model of American Options Valuation », *JMS*, vol. 47, n° 1, p. 47-64, juin 2014, doi: 10.4208/jms.v47n1.14.03.
- [54] E. M. Rønquist et A. T. Patera, « A Legendre spectral element method for the Stefan problem », *Int. J. Numer. Meth. Engng.*, vol. 24, n° 12, p. 2273-2299, déc. 1987, doi: 10.1002/nme.1620241204.
- [55] M. Longeon, A. Soupart, J.-F. Fourmigué, A. Bruch, et P. Marty, « Experimental and numerical study of annular PCM storage in the presence of natural convection », *Applied Energy*, vol. 112, p. 175-184, déc. 2013, doi: 10.1016/j.apenergy.2013.06.007.
- [56] M. Iten, S. Liu, et A. Shukla, « Experimental validation of an air-PCM storage unit comparing the effective heat capacity and enthalpy methods through CFD simulations », *Energy*, vol. 155, p. 495-503, juill. 2018, doi: 10.1016/j.energy.2018.04.128.
- [57] H. Niyas et P. Muthukumar, « Novel encapsulation technique to upscale latent heat storage capacity in steam accumulators », présenté à ISES Solar World Congress 2015, Conference Proceedings, 2015, p. 1560-1566. doi: 10.18086/swc.2015.02.17.
- [58] C. Bonacina, G. Comini, A. Fasano, et M. Primicerio, « Numerical solution of phase-change problems », *International Journal of Heat and Mass Transfer*, vol. 16, n° 10, Art. n° 10, oct. 1973, doi: 10.1016/0017-9310(73)90202-0.
- [59] D. Poirier et M. Salcudean, « On Numerical Methods Used in Mathematical Modeling of Phase Change in Liquid Metals », *Journal of Heat Transfer*, vol. 110, n° 3, Art. n° 3, 1988, doi: 10.1115/1.3250529.
- [60] M. Salcudean et Z. Abdullah, « On the numerical modelling of heat transfer during solidification processes », *Int. J. Numer. Meth. Engng.*, vol. 25, n° 2, Art. n° 2, juin 1988, doi: 10.1002/nme.1620250212.
- [61] E. Javierre, C. Vuik, F. J. Vermolen, et S. van der Zwaag, « A comparison of numerical models for one-dimensional Stefan problems », *Journal of Computational and Applied Mathematics*, vol. 192, n° 2, Art. n° 2, août 2006, doi: 10.1016/j.cam.2005.04.062.

- [62] F. Gibou, R. Fedkiw, R. Caflisch, et S. Osher, « A Level Set Approach for the Numerical Simulation of Dendritic Growth », *Journal of Scientific Computing*, vol. 19, n° 1-3, Art. n° 1-3, déc. 2003, doi: 10.1023/A:1025399807998.
- [63] L. Tan et N. Zabaras, « A level set simulation of dendritic solidification with combined features of front-tracking and fixed-domain methods », *Journal of Computational Physics*, vol. 211, n° 1, Art. n° 1, janv. 2006, doi: 10.1016/j.jcp.2005.05.013.
- [64] S. Chen, B. Merriman, S. Osher, et P. Smereka, « A Simple Level Set Method for Solving Stefan Problems », *Journal of Computational Physics*, vol. 135, n° 1, Art. n° 1, juill. 1997, doi: 10.1006/jcph.1997.5721.
- [65] M. Fabbri et V. R. Voller, « The Phase-Field Method in the Sharp-Interface Limit: A Comparison between Model Potentials », *Journal of Computational Physics*, vol. 130, n° 2, Art. n° 2, janv. 1997, doi: 10.1006/jcph.1996.5585.
- [66] V. R. Voller, M. Cross, et N. C. Markatos, « An enthalpy method for convection/diffusion phase change », *Int. J. Numer. Meth. Engng.*, vol. 24, n° 1, p. 271-284, janv. 1987, doi: 10.1002/nme.1620240119.
- [67] E. Assis, L. Katsman, G. Ziskind, et R. Letan, « Numerical and experimental study of melting in a spherical shell », *International Journal of Heat and Mass Transfer*, vol. 50, n° 9-10, p. 1790-1804, mai 2007, doi: 10.1016/j.ijheatmasstransfer.2006.10.007.
- [68] A. R. Darzi, M. Farhadi, et K. Sedighi, « Numerical study of melting inside concentric and eccentric horizontal annulus », *Applied Mathematical Modelling*, vol. 36, n° 9, p. 4080-4086, sept. 2012, doi: 10.1016/j.apm.2011.11.033.
- [69] V. R. Voller, M. Cross, et N. C. Markatos, « An enthalpy method for convection/diffusion phase change », *Int. J. Numer. Meth. Engng.*, vol. 24, n° 1, Art. n° 1, janv. 1987, doi: 10.1002/nme.1620240119.
- [70] Z. Ma et Y. Zhang, « Solid velocity correction schemes for a temperature transforming model for convection phase change », *International Journal of Numerical Methods for Heat and Fluid Flow*, vol. 16, n° 2, Art. n° 2, 2006, doi: 10.1108/09615530610644271.
- [71] D. K. Gartling, « Finite element analysis of convective heat transfer problems with change of phase », présenté à Numer Methods in Laminar and Turbul Flow, Swansea, Wales, 1978, p. 489-500.
- [72] V. R. Voller et C. Prakash, « A fixed grid numerical modelling methodology for convection-diffusion mushy region phase-change problems », *International Journal of Heat and Mass Transfer*, vol. 30, n° 8, Art. n° 8, août 1987, doi: 10.1016/0017-9310(87)90317-6.
- [73] C. Beust, E. Franquet, J.-P. Bédécarrats, et P. Garcia, « A numerical investigation of some key factors for the simulation of convection-dominated melting », *International Journal of Thermal Sciences*, vol. 161, p. 106687, mars 2021, doi: 10.1016/j.ijthermalsci.2020.106687.
- [74] S. S. Mostafavi Tehrani, G. Diarce, et R. A. Taylor, « The error of neglecting natural convection in high temperature vertical shell-and-tube latent heat thermal energy storage

- systems », *Solar Energy*, vol. 174, p. 489-501, nov. 2018, doi: 10.1016/j.solener.2018.09.048.
- [75] M. Faden, A. König-Haagen, E. Franquet, et D. Brüggemann, « Influence of density change during melting inside a cavity: Theoretical scaling laws and numerical analysis », *International Journal of Heat and Mass Transfer*, vol. 173, p. 121260, juill. 2021, doi: 10.1016/j.ijheatmasstransfer.2021.121260.
- [76] E. Assis, L. Katsman, G. Ziskind, et R. Letan, « Numerical and experimental study of melting in a spherical shell », *International Journal of Heat and Mass Transfer*, vol. 50, n° 9-10, p. 1790-1804, mai 2007, doi: 10.1016/j.ijheatmasstransfer.2006.10.007.
- [77] E. Assis, G. Ziskind, et R. Letan, « Numerical and Experimental Study of Solidification in a Spherical Shell », *Journal of Heat Transfer*, vol. 131, n° 2, p. 024502, févr. 2009, doi: 10.1115/1.2993543.
- [78] M. Zeneli *et al.*, « Numerical simulation of a silicon-based latent heat thermal energy storage system operating at ultra-high temperatures », *Applied Energy*, vol. 242, p. 837-853, mai 2019, doi: 10.1016/j.apenergy.2019.03.147.
- [79] S. F. Hosseinizadeh, A. A. Rabienataj Darzi, F. L. Tan, et J. M. Khodadadi, « Unconstrained melting inside a sphere », *International Journal of Thermal Sciences*, vol. 63, p. 55-64, janv. 2013, doi: 10.1016/j.ijthermalsci.2012.07.012.
- [80] M. Bechiri et K. Mansouri, « Study of heat and fluid flow during melting of PCM inside vertical cylindrical tube », *International Journal of Thermal Sciences*, vol. 135, p. 235-246, janv. 2019, doi: 10.1016/j.ijthermalsci.2018.09.017.
- [81] H. Shmueli, G. Ziskind, et R. Letan, « Melting in a vertical cylindrical tube: Numerical investigation and comparison with experiments », *International Journal of Heat and Mass Transfer*, vol. 53, n° 19-20, Art. n° 19-20, sept. 2010, doi: 10.1016/j.ijheatmasstransfer.2010.05.028.
- [82] J. H. Dymond et R. Malhotra, « The Tait equation: 100 years on », *Int J Thermophys*, vol. 9, n° 6, p. 941-951, nov. 1988, doi: 10.1007/BF01133262.
- [83] J. Dallaire et L. Gosselin, « Various ways to take into account density change in solid-liquid phase change models: Formulation and consequences », *International Journal of Heat and Mass Transfer*, vol. 103, p. 672-683, déc. 2016, doi: 10.1016/j.ijheatmasstransfer.2016.07.045.
- [84] A. R. Archibold, M. M. Rahman, D. Y. Goswami, et E. K. Stefanakos, « Analysis of heat transfer and fluid flow during melting inside a spherical container for thermal energy storage », *Applied Thermal Engineering*, vol. 64, n° 1-2, Art. n° 1-2, mars 2014, doi: 10.1016/j.applthermaleng.2013.12.016.
- [85] F. L. Tan, « Constrained and unconstrained melting inside a sphere », *International Communications in Heat and Mass Transfer*, vol. 35, n° 4, p. 466-475, avr. 2008, doi: 10.1016/j.icheatmasstransfer.2007.09.008.
- [86] T. K. Aldoss et M. M. Rahman, « Comparison between the single-PCM and multi-PCM thermal energy storage design », *Energy Conversion and Management*, vol. 83, p. 79-87, juill. 2014, doi: 10.1016/j.enconman.2014.03.047.

- [87] M. Veerappan, S. Kalaiselvam, S. Iniyan, et R. Goic, « Phase change characteristic study of spherical PCMs in solar energy storage », *Solar Energy*, vol. 83, n° 8, p. 1245-1252, août 2009, doi: 10.1016/j.solener.2009.02.006.
- [88] Z. Gao, Y. Yao, et H. Wu, « Validation of a melting fraction-based effective thermal conductivity correlation for prediction of melting phase change inside a sphere », *International Journal of Thermal Sciences*, vol. 142, p. 247-257, août 2019, doi: 10.1016/j.ijthermalsci.2019.04.029.
- [89] F. Fornarelli *et al.*, « CFD analysis of melting process in a shell-and-tube latent heat storage for concentrated solar power plants », *Applied Energy*, vol. 164, p. 711-722, févr. 2016, doi: 10.1016/j.apenergy.2015.11.106.
- [90] A. Trp, « An experimental and numerical investigation of heat transfer during technical grade paraffin melting and solidification in a shell-and-tube latent thermal energy storage unit », *Solar Energy*, vol. 79, n° 6, p. 648-660, déc. 2005, doi: 10.1016/j.solener.2005.03.006.
- [91] X. Yang, Z. Lu, Q. Bai, Q. Zhang, L. Jin, et J. Yan, « Thermal performance of a shell-and-tube latent heat thermal energy storage unit: Role of annular fins », *Applied Energy*, vol. 202, p. 558-570, sept. 2017, doi: 10.1016/j.apenergy.2017.05.007.
- [92] M. Longeon, A. Soupart, J.-F. Fourmigué, A. Bruch, et P. Marty, « Experimental and numerical study of annular PCM storage in the presence of natural convection », *Applied Energy*, vol. 112, p. 175-184, déc. 2013, doi: 10.1016/j.apenergy.2013.06.007.
- [93] S. Zhang, L. Pu, L. Xu, et M. Dai, « Study on dominant heat transfer mechanism in vertical smooth/finned-tube thermal energy storage during charging process », *Applied Thermal Engineering*, vol. 204, p. 117935, mars 2022, doi: 10.1016/j.applthermaleng.2021.117935.
- [94] F. He, B. Yan, J. Zou, C. Hu, X. Meng, et W. Gao, « Experimental evaluation of the effect of perforated spiral fins on the thermal performance of latent heat storage units », *Journal of Energy Storage*, vol. 58, p. 106359, févr. 2023, doi: 10.1016/j.est.2022.106359.
- [95] R. Karami et B. Kamkari, « Experimental investigation of the effect of perforated fins on thermal performance enhancement of vertical shell and tube latent heat energy storage systems », *Energy Conversion and Management*, vol. 210, p. 112679, avr. 2020, doi: 10.1016/j.enconman.2020.112679.
- [96] N. H. S. Tay, F. Bruno, et M. Belusko, « Comparison of pinned and finned tubes in a phase change thermal energy storage system using CFD », *Applied Energy*, vol. 104, p. 79-86, avr. 2013, doi: 10.1016/j.apenergy.2012.10.040.
- [97] F. He, R. Bo, C. Hu, X. Meng, et W. Gao, « Employing spiral fins to improve the thermal performance of phase-change materials in shell-tube latent heat storage units », *Renewable Energy*, vol. 203, p. 518-528, févr. 2023, doi: 10.1016/j.renene.2022.12.091.
- [98] A. Rozenfeld, Y. Kozak, T. Rozenfeld, et G. Ziskind, « Experimental demonstration, modeling and analysis of a novel latent-heat thermal energy storage unit with a helical fin », *International Journal of Heat and Mass Transfer*, vol. 110, p. 692-709, juill. 2017, doi: 10.1016/j.ijheatmasstransfer.2017.03.020.

- [99] F. He, B. Yan, J. Zou, C. Hu, X. Meng, et W. Gao, « Experimental evaluation of the effect of perforated spiral fins on the thermal performance of latent heat storage units », *Journal of Energy Storage*, vol. 58, p. 106359, févr. 2023, doi: 10.1016/j.est.2022.106359.
- [100] T. Rozenfeld, Y. Kozak, R. Hayat, et G. Ziskind, « Close-contact melting in a horizontal cylindrical enclosure with longitudinal plate fins: Demonstration, modeling and application to thermal storage », *International Journal of Heat and Mass Transfer*, vol. 86, p. 465-477, juill. 2015, doi: 10.1016/j.ijheatmasstransfer.2015.02.064.
- [101] F. Agyenim, P. Eames, et M. Smyth, « Experimental study on the melting and solidification behaviour of a medium temperature phase change storage material (Erythritol) system augmented with fins to power a LiBr/H₂O absorption cooling system », *Renewable Energy*, vol. 36, n° 1, p. 108-117, janv. 2011, doi: 10.1016/j.renene.2010.06.005.
- [102] M. Kirincic, A. Trp, et K. Lenic, « Influence of natural convection during melting and solidification of paraffin in a longitudinally finned shell-and-tube latent thermal energy storage on the applicability of developed numerical models », *Renewable Energy*, vol. 179, p. 1329-1344, déc. 2021, doi: 10.1016/j.renene.2021.07.083.
- [103] A. Sciacovelli, F. Gagliardi, et V. Verda, « Maximization of performance of a PCM latent heat storage system with innovative fins », *Applied Energy*, vol. 137, p. 707-715, janv. 2015, doi: 10.1016/j.apenergy.2014.07.015.
- [104] P. Yan, W. Fan, Y. Yang, H. Ding, A. Arshad, et C. Wen, « Performance enhancement of phase change materials in triplex-tube latent heat energy storage system using novel fin configurations », *Applied Energy*, vol. 327, p. 120064, déc. 2022, doi: 10.1016/j.apenergy.2022.120064.
- [105] J. Vogel et M. Johnson, « Natural convection during melting in vertical finned tube latent thermal energy storage systems », *Applied Energy*, vol. 246, p. 38-52, juill. 2019, doi: 10.1016/j.apenergy.2019.04.011.
- [106] F. Ren *et al.*, « Study on thermal performance of a new optimized snowflake longitudinal fin in vertical latent heat storage », *Journal of Energy Storage*, vol. 50, p. 104165, juin 2022, doi: 10.1016/j.est.2022.104165.
- [107] F. Agyenim, P. Eames, et M. Smyth, « A comparison of heat transfer enhancement in a medium temperature thermal energy storage heat exchanger using fins », *Solar Energy*, vol. 83, n° 9, p. 1509-1520, sept. 2009, doi: 10.1016/j.solener.2009.04.007.
- [108] M. Medrano, M. O. Yilmaz, M. Nogués, I. Martorell, J. Roca, et L. F. Cabeza, « Experimental evaluation of commercial heat exchangers for use as PCM thermal storage systems », *Applied Energy*, vol. 86, n° 10, p. 2047-2055, oct. 2009, doi: 10.1016/j.apenergy.2009.01.014.
- [109] J. Zhang *et al.*, « Improving the melting performance of phase change materials using novel fins and nanoparticles in tubular energy storage systems », *Applied Energy*, vol. 322, p. 119416, sept. 2022, doi: 10.1016/j.apenergy.2022.119416.
- [110] S. Zhang, L. Pu, L. Xu, et M. Dai, « Study on dominant heat transfer mechanism in vertical smooth/finned-tube thermal energy storage during charging process », *Applied*

-
- Thermal Engineering*, vol. 204, p. 117935, mars 2022, doi: 10.1016/j.applthermaleng.2021.117935.
- [111] A. Shahsavari, A. Goodarzi, H. I. Mohammed, A. Shirneshan, et P. Talebizadehsardari, « Thermal performance evaluation of non-uniform fin array in a finned double-pipe latent heat storage system », *Energy*, vol. 193, p. 116800, févr. 2020, doi: 10.1016/j.energy.2019.116800.
- [112] L. Pu, S. Zhang, L. Xu, et Y. Li, « Thermal performance optimization and evaluation of a radial finned shell-and-tube latent heat thermal energy storage unit », *Applied Thermal Engineering*, vol. 166, p. 114753, févr. 2020, doi: 10.1016/j.applthermaleng.2019.114753.
- [113] A. K. Hassan, J. Abdulateef, M. S. Mahdi, et A. F. Hasan, « Experimental evaluation of thermal performance of two different finned latent heat storage systems », *Case Studies in Thermal Engineering*, vol. 21, p. 100675, oct. 2020, doi: 10.1016/j.csite.2020.100675.
- [114] S. Zhang, L. Pu, L. Xu, R. Liu, et Y. Li, « Melting performance analysis of phase change materials in different finned thermal energy storage », *Applied Thermal Engineering*, vol. 176, p. 115425, juill. 2020, doi: 10.1016/j.applthermaleng.2020.115425.
- [115] A. Erek, Z. ?lken, et M. A. Acar, « Experimental and numerical investigation of thermal energy storage with a finned tube », *Int. J. Energy Res.*, vol. 29, n° 4, p. 283-301, mars 2005, doi: 10.1002/er.1057.
- [116] E. Guelpa, A. Sciacovelli, et V. Verda, « Entropy generation analysis for the design improvement of a latent heat storage system », *Energy*, vol. 53, p. 128-138, mai 2013, doi: 10.1016/j.energy.2013.02.017.
- [117] M. Parsazadeh et X. Duan, « Numerical study on the effects of fins and nanoparticles in a shell and tube phase change thermal energy storage unit », *Applied Energy*, vol. 216, p. 142-156, avr. 2018, doi: 10.1016/j.apenergy.2018.02.052.
- [118] S. Zhang, L. Pu, L. Xu, et M. Dai, « Study on dominant heat transfer mechanism in vertical smooth/finned-tube thermal energy storage during charging process », *Applied Thermal Engineering*, vol. 204, p. 117935, mars 2022, doi: 10.1016/j.applthermaleng.2021.117935.
- [119] A. Pizzolato, A. Sharma, R. Ge, K. Maute, V. Verda, et A. Sciacovelli, « Maximization of performance in multi-tube latent heat storage – Optimization of fins topology, effect of materials selection and flow arrangements », *Energy*, vol. 203, p. 114797, juill. 2020, doi: 10.1016/j.energy.2019.02.155.
- [120] S. Liu, H. Peng, Z. Hu, X. Ling, et J. Huang, « Solidification performance of a latent heat storage unit with innovative longitudinal triangular fins », *International Journal of Heat and Mass Transfer*, vol. 138, p. 667-676, août 2019, doi: 10.1016/j.ijheatmasstransfer.2019.04.121.
- [121] A. Tavakoli, M. Farzaneh-Gord, et A. Ebrahimi-Moghadam, « Using internal sinusoidal fins and phase change material for performance enhancement of thermal energy storage systems: Heat transfer and entropy generation analyses », *Renewable Energy*, vol. 205, p. 222-237, mars 2023, doi: 10.1016/j.renene.2023.01.074.

- [122] S. S. Mostafavi Tehrani, Y. Shoraka, G. Diarce, et R. A. Taylor, « An improved, generalized effective thermal conductivity method for rapid design of high temperature shell-and-tube latent heat thermal energy storage systems », *Renewable Energy*, vol. 132, p. 694-708, mars 2019, doi: 10.1016/j.renene.2018.08.038.
- [123] K. Couvreur, W. Beyne, R. Tassenoy, S. Lecompte, et M. De Paepe, « Characterization of a latent thermal energy storage heat exchanger using a charging time energy fraction method with a heat loss model », *Applied Thermal Engineering*, vol. 219, p. 119526, janv. 2023, doi: 10.1016/j.applthermaleng.2022.119526.
- [124] M. Johnson, J. Vogel, M. Hempel, B. Hachmann, et A. Dengel, « Design of high temperature thermal energy storage for high power levels », *Sustainable Cities and Society*, vol. 35, n° Supplement C, Art. n° Supplement C, nov. 2017, doi: 10.1016/j.scs.2017.09.007.
- [125] R. Waser *et al.*, « Fast and experimentally validated model of a latent thermal energy storage device for system level simulations », *Applied Energy*, vol. 231, p. 116-126, déc. 2018, doi: 10.1016/j.apenergy.2018.09.061.
- [126] H. A. Adine et H. E. Qarnia, « Numerical analysis of the thermal behaviour of a shell-and-tube heat storage unit using phase change materials », *Applied Mathematical Modelling*, p. 13, 2009.
- [127] J. Vogel, M. Keller, et M. Johnson, « Numerical modelling of large-scale finned tube latent thermal energy storage systems », *The Journal of Energy Storage*, p. 26, 2020.
- [128] M. Lacroix, « Numerical simulation of a shell-and-tube latent heat thermal energy storage unit », *Solar Energy*, vol. 50, n° 4, Art. n° 4, avr. 1993, doi: 10.1016/0038-092X(93)90029-N.
- [129] H. A. Zondag, R. de Boer, S. F. Smeding, et J. van der Kamp, « Performance analysis of industrial PCM heat storage lab prototype », *Journal of Energy Storage*, vol. 18, p. 402-413, août 2018, doi: 10.1016/j.est.2018.05.007.
- [130] C. Beust, « Modélisation multi-échelles d'un système de stockage thermique de vapeur par Matériau à Changement de Phase (MCP) », 2019.
- [131] M. Martinelli, F. Bentivoglio, A. Caron-Soupart, R. Couturier, J.-F. Fourmigue, et P. Marty, « Experimental study of a phase change thermal energy storage with copper foam », *Applied Thermal Engineering*, vol. 101, p. 247-261, mai 2016, doi: 10.1016/j.applthermaleng.2016.02.095.
- [132] V. M. B. Nunes, C. S. Queirós, M. J. V. Lourenço, F. J. V. Santos, et C. A. Nieto de Castro, « Molten salts as engineering fluids – A review: Part I. Molten alkali nitrates », *Applied Energy*, vol. 183, p. 603-611, déc. 2016, doi: 10.1016/j.apenergy.2016.09.003.
- [133] A. Caron-Soupart, J.-F. Fourmigué, P. Marty, et R. Couturier, « Performance analysis of thermal energy storage systems using phase change material », *Applied Thermal Engineering*, vol. 98, p. 1286-1296, avr. 2016, doi: 10.1016/j.applthermaleng.2016.01.016.
- [134] A. Lomonaco, D. Hailot, E. Pernot, E. Franquet, et J.-P. Bédécarrats, « Sodium nitrate thermal behavior in latent heat thermal energy storage: A study of the impact of sodium

- nitrite on melting temperature and enthalpy », *Solar Energy Materials and Solar Cells*, vol. 149, p. 81-87, mai 2016, doi: 10.1016/j.solmat.2015.12.043.
- [135] « ANSYS Fluent Theory Guide Release 17.2 ». 2016. [En ligne]. Disponible sur: <http://www.fluent.com>
- [136] W. Nusselt, *Die Oberflächenkondensation des Wasserdampfes*. VDI, 1916.
- [137] J. Bonnin, « Écoulement des fluides dans les tuyauteries », *Techniques de l'ingénieur Stockage et transfert des fluides des machines hydrauliques et thermiques*, vol. base documentaire : TIB174DUO., n° ref. article : a738, Art. n° ref. article : a738, 1983, [En ligne]. Disponible sur: <https://www.techniques-ingenieur.fr/base-documentaire/mecanique-th7/stockage-et-transfert-des-fluides-des-machines-hydrauliques-et-thermiques-42174210/ecolement-des-fluides-dans-les-tuyauteries-a738/>
- [138] S. S. Kutateladze, *Fundamentals of Heat Transfer*. Academic Press, New York, 1963.
- [139] D. A. Labuntsov, « Heat transfer in film condensation of pure steam on vertical surfaces and horizontal tubes », *Teploenergetika*, vol. 4, n° 7, Art. n° 7, 1957.
- [140] V. Gnielinski, « New equations for heat and mass transfer in turbulent pipe and channel flow », *Int. Chem. Eng.*, vol. 16, n° 2, Art. n° 2, 1976.
- [141] W. H. Mac Adams, *Transmission de la chaleur*. Dunod, 1975.
- [142] G. K. Filonenko, « Hydraulic resistance in pipes », *Teploenergetika*, vol. 1, n° 4, Art. n° 4, 1954.